SOME MAGNETO-DYNAMIC PROPERTIES OF TYPE II SUPERCONDUCTORS

Chan-Shin Chou

A Thesis Submitted for the Degree of PhD
at the
University of St Andrews

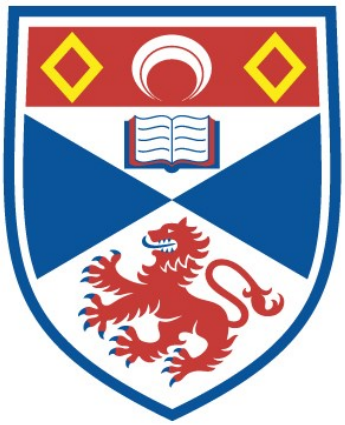

1978

Some Magneto-Dynamic Properties of Type II Superconductors

A Thesis
presented by

Chan-Shin CHOU, B.Sc.,

to the
University of St. Andrews
in application for the Degree
of Doctor of Philosophy

ABSTRACT

The possibility of making a refrigerator by mechanically induced flux flow to transfer heat in a type II superconductor has been examined. Heat generation due to flux flow was sufficient to destroy the cooling effect over most of our experimental temperature range, although some cooling was obtained near T_c.

The dissipation due to flux pinning was determined by the pinning strength of the specimen. The pinning forces in Nb and Pb-In were determined by mechanically sweeping a magnetic field over them and measuring the resulting force. Three different forces due to the interaction of the magnetic field, with (a) the trapped flux lines, (b) the Meissner screening current, and (c) the pinning sites of the specimen, were identified. The magnitude of the force due to the screening current was proportional to the field strength, and was reduced by the trapped flux lines inside the specimen. The magnitude of the bulk pinning force was in agreement with that calculated from the magnetization via the Irie-Yamafuji model; $F_p = \alpha B^{\gamma}$. The dependence of the pinning force and the magnetic properties on the temperature and on the surface treatment of the specimen was also studied. The temperature dependence of the pinning force was found to be given by $F_p(T) = F_p(o)(1 - \frac{T}{T_c})$ and it is suggested that this can be understood in terms of Anderson's flux creep model. The critical current of various specimens was obtained from the pinning force and the magnetization.

In applying the Irie-Yamafuji model, the demagnetization and the surface effects of a specimen had to be taken into account, and methods of doing these have been suggested and experimentally checked.

The role of the magneto-caloric effect on the mixed state specific heat was discussed. A 'two-fluid' type equation was proposed and used to calculate the mixed state specific heat. The results were compared with

the experimental measurements.

With the above experiments, the dissipation associated with flux flow was studied in terms of the pinning and viscous forces. It was shown that dissipation due to pinning was dominant in low fields and that viscous forces gradually became important as the field increased.

It was found that the motion of the flux lattice inside a type II superconductor could not be induced by moving the source of a uniform magnetic field. This showed that the concept of 'lines of flux' has no meaning for the case of a uniform field.

DECLARATION

I hereby certify that this thesis has been composed by me, and is a record of work done by me, and has not previously been presented for a higher Degree.

The research was carried out in the school of Physical Science in the University of St. Andrews under the supervision of Professor J.F. Allen, F.R.S., and Mr. J.G.M. Armitage.

Chan-Shin CHOU

CERTIFICATE

We certify that Chan-Shin Chou, B.Sc., has spent nine terms at research work in the school of physical science in the University of St. Andrews under our direction, that he has fulfilled the conditions of the Resolution of the University Court, 1967, No. 1, and that he is qualified to submit the accompanying thesis in application for the Degree of Doctor of Philosophy.

Research Supervisors

CAREER

I graduated from the Department of Physics of the National Taiwan University in June 1971, and obtained a Bachelor of Science degree (no classification of B.Sc. degree). From September 1971 until September 1973, I was employed by the Department of Physics there as a research assistant.

In October, 1973, I was enrolled as a research student under Resolution of the University Court, 1967, No. 1, as a candidate for the degree of Doctor of Philosophy.

ACKNOWLEDGEMENTS

The author wishes to express his gratitude to Professor J F Allen, F.R.S. and to Mr J G M Armitage for their helpful supervision.

My thanks to Mr R H Mitchell, and the workshop staff of the School of Physical Sciences for skilful technical assistance.

I am indebted to the British Council for the overseas student school fee award, and to the University of St Andrews for the award of a University scholarship for the year 1975-76.

I especially wish to thank my sisters and brothers for their encouragement and understanding.

To My Parents

"A weed may never be able to express its gratitude to the selfless-shining Sun, even not a blossom. But the Sun is always there"

The Author

C O N T E N T S

PAGE

List of symbols

A	surface area
$\underline{A}$	vector potential
B	magnetic induction
$B_{r\ max}$	maximum bulk remanence field
$B_{r\ max}$	maximum remanence field
C_{en}	normal electronic specific heat
C_{es}	superconducting electronic specific heat
$C_{\ell n}$	lattice specific heat
C_m	mixed state specific heat
C_{mT}	mixed state specific heat as determined thermally
C_{mB}	mixed state specific heat as determined from induction
C_n	normal state specific heat
C_s	superconducting state specific heat
c_{ij}	elastic constant
D	total power dissipation
$D_{e\ell}$	electrical power dissipation
D_{th}	thermal power dissipation
d	plate thickness
d	interflux line distance
E	electric field
E	internal energy
e	electron charge
e^*	2e
F	free energy
F_{pV}	pinning force per unit volume
F_s	surface pinning force
F_A	initial attractive force due to trapped flux
F_p	bulk pinning force
F_R	initial repulsive force due to trapped flux
F_{SP}	surface force on first passage over specimen
f_d	damping force per unit flux line
f_L	Lorentz force per unit flux line
f_m	Magnus force per unit flux line
f_p	pinning force per unit flux line

G	Gibbs free energy
G_m	magnetic Gibbs free energy
G_{sq}	Gibbs free energy of square flux lattice structure
G_{tri}	Gibbs free energy of triangular flux lattice structure
H	magnetic field
H_a	external applied field
$H_{a\ max}$	maximum field of a field profile
H_c	thermodynamic critical field
H_{cp}	$H_c(1 - N)$
H_p	$H_{c1}\ (1 - N)$
H_{c1}	lower critical field in type II
H_{c2}	upper critical field in type II
H_{c3}	critical field of surface superconductivity
H_o	critical field at the Absolute Zero
H_p	penetration field
H_{tr}	transition field
h	Planck's constant
$\hbar$	$h/2\pi$
J	current density
J_n	normal fluid flow current density
J_s	superfluid flow current density
J_T	transport current density
$J_o(r)$	circulation current of a stationary vortex
K_0, K_1	Hankel functions of imaginary argument of order zero and order one
k	Boltzmann's constant
k	thermal conductivity
L	latent heat
l	electron mean free path
M	magnetization
M_n	magnetization of normal state
M_s	magnetization of superconducting state
M_b	magnetization of state b
ΔM	difference in equilibrium magnetizations
m	electronic mass
m^*	$2m$

N	demagnetization factor
n	electron density
n	number of moles
p	pressure
P_s	canonical momentum
Q	Heat
Q_{el}	heat generation due to eddy current
Q_p	heat generation due to pinning
Q_{th}	heat generation due to local temperature gradient
Q_i	total of all quantities of heat
Q_{ir}	heat dissipation due to flux flow
Q_r	latent heat of transition
r	radius
r_p	penetration radius
S	entropy
S_m	mixed state entropy
S_n	normal state entropy
S_s	superconducting state entropy
S_ϕ	entropy difference between the superconducting and the normal phases per unit length of fluxon
S_i	entropy production due to a unit length of vortex added to a specimen
S_{el}	electrical entropy production due to flux flow
S_{th}	thermal entropy production due to flux flow
$\Delta_{ir}S$	irreversible entroy production
$\Delta_T S$	reversible isothermal change of entropy due to magnetization
S_v	surface area
T	temperature
T_c	critical temperature
U_{ij}	repulsive interaction energy between the vortices
V	volume
V_n	volume of normal state
V_s	volume of the superconducting state
v_F	Fermi velocity
v_ϕ	flux flow velocity
α	$V/(1 - N)$
α, β	constants of the Ginzburg-Landau theory
α	a constant describing the intensity of the interaction between the pinning sites and fluxons
β	lattice specific heat coefficient

γ	electronic specific heat coefficient
γ	a constant dependent on the density and the distribution of the pinning sites ($F_p = \alpha B^{\gamma}$)
$\delta_2(r)$	two-dimensional delta function
ε_i	strains
ε	energy of a vortex per unit length
η	viscosity
η_{th}	viscosity due to local temperature gradient
$\eta_{e\ell}$	viscosity due to eddy current heating
θ_H	Hall angle
κ	Ginzburg - Landau parameter
$\kappa_1(T)$	$H_{c2}(T)/\sqrt{2}\, H_c(T)$
$\kappa_2(T)$	$[\, 8\pi\beta(\frac{dM}{dH})_{H_{c2}}^{-1} + \frac{1}{2}\,]^{\frac{1}{2}}$
$\kappa_3(T)$	$f^{-1}\,(\frac{H_{c1}(T)}{H_c(T)})$ (see p IV 11)
λ	penetration depth
λ_L	London penetration depth
ξ	coherence length
ρ	pinning sites density
ρ_f	flux flow resistivity
ρ_n	normal state resistivity
ϕ_o	flux quantum
σ	electrical conductivity
σ_{ns}	surface energy
τ	electron transport collision time
$d\tau_v$	volume element
ψ	order parameter
ψ'	dimensionless order parameter
ω_c	cyclotron frequency

CHAPTER I

INTRODUCTION

I. Introduction

1.1 General review

Superconductivity was discovered and given that name by Kamerlingh Onnes (1911). Following his first liquefaction of helium in 1908, he began to examine the electrical behaviour of metals down to the new low temperature limit of about 1.5 K. Although he expected that the resistance of some metals might approach zero as the temperature approached zero, he was astonished to find that the resistance of mercury vanished abruptly at about 3.9 K. Other metals, such as lead and tin showed similar behaviour. Onnes also discovered that superconductivity could be destroyed by a magnetic field, and that the critical field for destruction H_c has a relation to temperature that was very nearly parabolic:

$$H_c = H_0 \, (1 - T^2/T_c^2), \qquad 1.1$$

where H_0 is the critical magnetic field at the absolute zero.

A superconductor is able to maintain its zero resistivity only up to a certain current strength such that at a point on the superconductor surface, the magnetic field due to the transport current exceeds the critical magnetic field H_c. This current is called the critical current J_c of the superconductor, an idea first suggested by Silsbee (1916).

The zero resistivity of a superconductor implies that the electrical field inside it is always zero, and that therefore $\dot{\underline{B}} = 0$, i.e the magnetic induction inside a superconductor is constant in time. If this were so, it would mean that the magnetic induction inside a superconductor would depend on the history of the state and would not be a unique function of the external conditions. In such a situation the methods of equilibrium thermodynamics

could not be applied. It was not until 1933 that Meissner and Ochsenfeld showed that a superconductor is a perfect diamagnet such that the field vanishes in all but a thin penetration region near the surface of the superconductor. This penetration region allows a screen current to flow and thus to generate a flux density that exactly cancels the flux density of the applied field. This effect is known as the Meissner-Ochsenfeld Effect, or more simply the Meissner Effect.

The Meissner Effect shows that the superconducting state in a given external magnetic field which is smaller than the critical field, is a single stable state to which the laws of thermodynamics can be applied. This justified the experimental conclusion of Keesom (1924), Rutgers (1933) and Gorter (1933) that superconductivity is associated with a phase transition, which in the absence of a magnetic field is of second order, with a discontinuity in the specific heat but no latent heat.

In the absence of a fundamental theory of superconductivity, attempts were made to develop phenomenological theories to describe superconductive behaviour. Among these were the well-known two-fluid model of Gorter and Casimir (1934, 1934a) which accounted for the thermal properties, and the famous equations given by the London brothers (1950) to account for the electromagnetic properties. Pippard (1950, 1951, 1953), modifying the London local equations to a non-local theory, successfully explained the effect of the impurities in a superconductor through a characteristic length ξ, which he called the coherence length.

Another important phenomenological theory was developed by Ginzburg and Landau (1950). It was based on the superconducting-normal transition which in the absence of the magnetic field, is a second order phase transition and a reversible process. In this theory they described the free energy of a superconductor in terms of an order parameter ψ, which was shown by Gor'kov (1958,

1959, 1960) to be related to the wavefunction of the microscopic theory of a superconductor particularly in the region near H_{c2} in a type II superconductor.

Various attempts were made to develop a microscopic theory of superconductivity, based on the electron's Coulomb interaction by Born and Cheng (1948) and others, but these proved unsuccessful. Bohm and Pines (1953) showed that the Coulomb interaction is connected with the collective oscillation of the electrons which is hardly affected by the transition. This indicated that a new mechanism was needed to describe the phenomenon.

The idea that pairs of fermions can combine to form effective bosons through Bose-Einstein condensation suggested by Ogg (1946), opened the positive approach to the mechanism of superconductivity.

The experimental discovery of the isotope effect by Reynolds et al (1950), $T_c \propto M^{-\frac{1}{2}}$, which was concurrent with its prediction by Fröhlich (1950), led the latter to suggest that the interaction of the electrons in a metal with the acoustic lattice vibrations would lead to an attraction between the electrons near the Fermi surface, and that in consequence the Fermi surface would not represent their lowest state. Although this independent electron model could not explain the cooperative features of superconductivity nevertheless this kind of interaction is now generally believed to give rise to superconductivity in most, if not all of the known superconductors.

The exponential temperature dependence of the specific heat of a superconductor at lower temperatures (Corak et al, 1954) showed that superconductivity was characterized by a 'forbidden' range of energies for the electrons, and indicated the existence of an energy gap. Following this, Cooper (1956) showed that the appearance of superconductivity was due to an instability of the normal state in the presence of an attractive interaction between the electrons. This

attraction was made possible by an interaction through the lattice which allowed electrons with opposite spin to form pairs, called Cooper pairs. Based on this mechanism, the Bardeen-Cooper-Schrieffer (1957) microscopic theory of superconductivity was produced. Although the discovery by Giaever (1960) of the tunnelling effect and by Abrikosov and Gor'kov (1961) of the gapless superconductor showed that superconductivity was not necessarily connected with an energy gap, the BCS theory was successful in calculating most of the parameters of type I superconductors.

What we have been describing above are what are now known as type I superconductors. In 1956 Abrikosov (1956) showed that in addition to the complete flux explusion characteristic of the Meissner state, there possibly existed another type of superconductor, now known as type II, in which the magnetic flux penetrates the sample in the form of separated filaments (single quantized fluxons), to form the so-called mixed state. This pattern is similar to the creation of the vortex filaments in superfluid helium II (Onsager 1949, and Feynmann 1954). The Abrikosov theory was based on a defect-free ideal specimen in which the flux lines move so as to be in an equilibrium state with the applied field, and it also predicted the existence of flux lattices as well as reversible magnetization. Metals which show this kind of behaviour are called 'ideal' type II superconductors.

Real materials nearly always exhibit some degree of magnetic irreversibility. This irreversibility has been related to lattice defects, which prevent free entry or exit of flux lines to the specimen and hinders their motion inside it. In this case the flux distribution inside the specimen will not come into equilibrium, and the density of the lines will not be uniform. The hindrance to flux motion by point or line or other dislocations or impurities is called

pinning, and it is the existence of pinned flux lines which gives rise to non-uniformity of line density, or in other words, field gradients. The application of higher transport currents or higher field gradients can cause the release of the pinning, and it is this area of phenomena which is responsible for energy dissipation and with which we are largely concerned in this thesis.

By studying the hysteresis in the magnetization curve of the specimen and assuming that the magnetization can be attributed primarily to the (finite) supercurrent induced in the specimen, one can derive the relation of the critical current and the pinning force to the magnetic induction of the specimen.

Flux flow can also be studied in the presence of a transport current (Kim et al, 1962) by means of the Lorentz force between the fluxon and the transport current itself (Anderson 1962, Gorter 1962, 1962a). By measuring critical currents in different flux densities, and temperature variations in the specimen due to flux motion (in the non-isothermal case), one can interpret the results in terms of pinning forces, driving forces on fluxons and energy dissipation due to flux flow.

One can also investigate these effects, in particular the idea of pinning, by mechanical means, by forcing the magnetic flux to flow in the specimen and measuring the resulting torque on it (Houston and Smith 1966, 1967, Andronikashvili et al 1969, Fuhrmans and Heiden 1974).

It is a rather difficult task to form a proper theory for all type II superconductors at all temperatures. In the case of pure material this may be achieved by solving the Bogoliubov equations (Caroli et al 1964, Bardeen et al 1969). In the case of material with a finite mean free path, Eilenberger (1967) has derived a set of transport-like integro-differential equations determining single-particle Green's functions integrated with respect to the excitation

energy. This may provide the right answer over all temperature ranges by a rather complicated process of solving the equations by numerical methods. A clear diagram has been given by Essmann (1974), which summarizes the work of many authors and the range of validity of the solutions.

Superconductivity is a quantum phenomenon shown on a macroscopic scale, of which the Meissner effect gave the first clue. Landau (1941,1947) first mentioned and London (1950) first showed that in a superconducting ring the magnetic flux maintained in the loop by the supercurrent should be quantized. This quantum effect was observed independently by Deaver and Fairbank (1961), and Doll and Näbauer (1961).

Finally, one must mention the quantum effects at a weak super-conducting junction first predicted by Josephson (1962), and amply proved by experiment.

1.2 The London and Pippard equations

Before the discovery of the Meissner effect, Becker et al (1933) generalized the electrodynamic properties of a perfect conductor in a form in which there is a finite skin depth for current flow. By means of the equation

$$\frac{m}{ne^2}\,\mathrm{curl}\,\dot{\underline{J}} + \dot{\underline{H}} = 0, \qquad 1.2.1$$

we can derive the following equations

$$\lambda^2\nabla^2\dot{\underline{H}} = \dot{\underline{H}},$$

$$\lambda^2\nabla^2\dot{\underline{J}} = \dot{\underline{J}},$$

and

$$\lambda^2\nabla^2\underline{E} = \underline{E}, \qquad 1.2.2$$

where $\lambda^2 = m/4\pi ne^2$ is a parameter having the dimension of length. Equation 1.2.2 predicts that the external field falls off exponentially inside a zero-resistivity material to a constant field in a length of λ. This is obviously in contradiction

with the Meissner effect, and H and F London showed that the Meissner effect could be incorporated into the Becker theory by replacing equation 1.2.1. with

$$\frac{m}{n_s e^2} \operatorname{curl} \underline{J}_s + \underline{H} = 0, \qquad 1.2.3$$

from which they derived the famous equations which bear their name:

$$\lambda_L^2 \nabla^2 \underline{H} = \underline{H},$$

$$\lambda_L^2 \nabla^2 \underline{J} = \underline{J},$$

and

$$\lambda_L^2 \nabla^2 \underline{A} = \underline{A}, \qquad 1.2.4$$

where $\underline{H} = \nabla \times \underline{A}$, and where $\lambda_L = (m/4\pi n_s e^2)^{\frac{1}{2}}$ is called the London penetration depth. Equation 1.2.3 introduces a vector potential $\underline{A}$ for the field $\underline{H}$,

$$\underline{H} = \operatorname{curl} \underline{A}, \qquad 1.2.4a$$

and satisfies

$$\underline{J}_s = -(m/n_s e^2)\underline{A}. \qquad 1.2.4b$$

In the static case, with $\underline{E} = 0$, one needs an additional restriction on $\underline{A}$ to ensure no charge build up, $\operatorname{div} \underline{J}_s = 0$, and so

$$\operatorname{div} \underline{A} = 0, \qquad 1.2.4c$$

with the boundary condition $A_{\perp} = 0$. We define the canonical momentum $\underline{P}_s$ of the superconducting electron as

$$\underline{P}_s = m\underline{v}_s + e\underline{A}, \qquad 1.2.4d$$

on rewriting equation 1.2.3 as

$$\text{curl } \underline{P}_s = 0,$$

and

$$\text{div } \underline{P}_s = 0.$$

The basic idea of the London theory is that the supercurrent in the superconductor is always determined by the local magnetic field. The London penetration depth λ_L depends only on electron mass, electron charge, and number density of the superelectrons, but the experimental results indicated that the penetration depth λ may be greatly modified by the addition of small amounts of impurity. Since neither the mass nor the number of superelectrons n_s is changed significantly by the impurity, the London theory as it stands is not able to account for these observed variations. Experimentally it has been found that rapid variation of λ with mean free path l begins at the point where λ and l become comparable in a manner similar to the situation in normal metals and the anomalous skin effect. In normal metals, the local relation

$$\underline{J}(0) = \sigma \underline{E}, \qquad 1.2.5$$

as long as l is short, and the electric field may be treated as constant over a region comparable to l. We can write the non-local relation between $\underline{J}(0)$ and $\underline{E}$ as

$$\underline{J}(0) = \frac{3\sigma}{4\pi l} \int \frac{\underline{r} \cdot (\underline{r} \cdot \underline{E})\, e^{-r/l}}{r^4} d\tau_v \qquad 1.2.6$$

where $\underline{r}$ is the radius vector from a volume element $d\tau_v$ to the point at which $\underline{J}$ is to be evaluated. Pippard (1950, 1951) suggested that the behaviour of the skin depth of the normal metal is similar to the variation of the penetration depth, and that equation 1.2.6 suggested that the London equation should be

subjected to the same transformation as that which leads from equation 1.2.5 to equation 1.2.6. We rewrite the first London equation 1.2.3

$$\underline{J}_s(0) = -(1/\Lambda)\ \underline{A}(0), \qquad 1.2.7$$

as a non-local current-potential relation

$$\underline{J}(\underline{o}) = \frac{3\sigma}{4\pi l}\int \frac{\underline{r}\,\underline{r}\cdot\underline{A}(\underline{r}')}{r^4} e^{-r/\xi}\, d\tau_v \qquad 1.2.8$$

and ξ depends upon the mean free path l as follows,

$$\frac{1}{\xi(l)} = \frac{1}{\xi_o} + \frac{1}{l} \qquad 1.2.9$$

where ξ_o is a constant for the metal. The mean free path is given by $l = \tau v_F$, where τ is the transport collision time for electrons with impurities in the normal state and v_F is the Fermi velocity. Here Pippard found empirically that

$$\xi_o = a(\hbar v_F/kT_c)$$

with $a = 0.15$, while the BCS theory gives the same relation with $a = 0.18$ which fitted Pippard's experiments with $\xi = 1.2 \times 10^{-4}$ cm.

The Pippard theory also gives the idea of the influence of a field on the superconducting electrons felt over a distance instead of acting at a point as in the London local theory. He called this distance the coherence length, which is the shortest distance in which a significant change of electronic structure in the superconductor could occur.

1.3 Ginzburg-Landau theory

The Ginzburg-Landau theory introduced an order parameter ψ which is small in the temperature region near T_c. The theory gives the free energy of a homogeneous superconductor in terms of ψ as

$$F_s = \underbrace{F_n + \alpha|\psi|^2 + \frac{\beta}{2}|\psi|^4 + \ldots}_{A} + \underbrace{\frac{1}{2m^*}\left|\left(\frac{\hbar}{i}\nabla - e^*\underline{A}\right)\psi\right|^2}_{B} +$$

$$+ \underbrace{\frac{1}{8\pi}\left[H(r) - H_a\right]^2}_{C} \qquad 1.3.1$$

where $e^* = 2e$ and $m^* = 2m$ are the effective charge and mass of the superconducting electron although we would now know this corresponds to values for a Cooper pair. The first part A in Equation 1.3.1 is the free energy density of the superconducting phase in zero field, which depends on the density of superconducting electrons, and which can be expanded as a power series in ψ:

$$F_{so} = F_{no} + \lambda\psi + \alpha|\psi|^2 + \gamma\psi^3 + \frac{\beta}{2}|\psi|^4 + \ldots \qquad 1.3.1a$$

where λ, α, γ and β etc, are functions of P and T. In equation 1.3.1a, λ must be zero to permit F_{so} to have a minimum at $\psi = 0$. The ψ^3 term does not appear, and the higher terms have been omitted. This limits the valid region of equation 1.3.1 to that close to T_c. The second part B represents the increase in free energy coming from the spatial variation in the order parameter, and prevents rapid variation in the superconducting electron density, because such variations are not physically possible. The third term C is the contribution due to the magnetic field. Minimizing the free

energy with respect to ψ^*, and $\underline{A}$ with the boundary condition $m_o(\frac{\hbar}{i}\underline{\nabla}-e^*\underline{A})\psi=0$ at the surface, we get

$$\alpha\psi + \beta|\psi|^2 \psi + \frac{1}{2m^*}\left(\frac{\hbar}{i}\underline{\nabla} - e^*\underline{A}\right)^2 \psi = 0 \qquad 1.3.2$$

and

$$J = \frac{1}{4\pi}\underline{\nabla}\times\underline{H} = \frac{e^*\hbar}{2m^*i}\left[\psi^*\underline{\nabla}\psi - \psi\underline{\nabla}\psi^*\right] - \frac{e^{*2}}{m^*}|\psi|^2\underline{A} \qquad 1.3.3$$

For a specimen which shows the perfect Meissner behaviour,

$$\alpha + \beta|\psi|^2 = 0$$

and

$$|\psi|^2 = -\frac{\alpha}{\beta} > 0.$$

As $T \to T_c$ and $|\psi|^2 \to 0$, we have

$$F_{no} - F_{so} = \frac{\alpha^2}{2\beta} = \frac{H_c^2}{8\pi},$$

and

$$H_c^2 = 4\pi\alpha^2/\beta. \qquad 1.3.4$$

The London penetration depth λ_L is then given by

$$\frac{1}{\lambda_L^2} = -\frac{4\pi e^{*2}}{m^*}\frac{\alpha}{\beta} = 4\pi N_s e^{*2}/m^*.$$

From

$$\frac{-\hbar^2}{2m^*}\nabla^2\psi + \alpha\psi = 0$$

we define the temperature-dependent coherence length as

$$\xi^2(T) = \frac{\hbar^2}{2m|\alpha|}. \qquad 1.3.5$$

The Ginzburg-Landau parameter κ is defined as

$$\kappa = \frac{\lambda}{\xi} = \frac{m^*}{\hbar e^*} \left(\beta/2\pi\right)^{\frac{1}{2}} = \frac{1}{\sqrt{2}} \frac{e^*}{\hbar} H_c \lambda_L^2 \qquad 1.3.6$$

Equation (1.3.2) and equation (1.3.3) can be written in other dimensionless forms,

$$\left(\frac{i\nabla'}{\kappa} + \underline{A}'\right)^2 \psi' = \psi' - \psi' \left|\psi'\right|^2 \qquad 1.3.2a$$

and $$-\nabla'^2 A' = \left|\psi'\right|^2 \underline{A}' + \frac{i}{2\kappa} \left(\psi'^* \underline{\nabla}' \psi' - \psi' \underline{\nabla}' \psi'^*\right), \qquad 1.3.3a$$

where $r' = r/\lambda$, $\underline{A}' = \underline{A}/\sqrt{2}\, H_c \lambda$, and $\psi' = \psi / \left|\psi_\infty\right|$.

1.4 Surface energy

Using the London equation it can be shown that the critical field for an infinite plate in a magnetic field parallel to its plane is

$$H_{cp} = H_c \left[1 - (2\lambda/d) \tanh(d/2\lambda)\right]^{-\frac{1}{2}} \qquad 1.4.1$$

where d is the thickness of the plate. In the case of $d \gg \lambda$, then $H_{cp} = H_c$ and in the opposite extreme where $\lambda \gg d$ we have

$$H_{cp}^* = 2\sqrt{3}(\lambda/d) H_c \qquad 1.4.2$$

Equation 1.4.2 shows that the critical transition field of a thin plate is higher than that of a thick one, which means that the free energy per unit volume of a thin specimen is lower than that of a thick one. It thus appears to be energetically favourable for a sample to split itself into super-

conducting domains separated by infinitesimal normal domains whose energy is negligible compared to the total energy. However, London has pointed out that this does not happen because the superconductor possesses a positive surface energy in order to maintain the Meissner state in a magnetic field, $H < H_c$. This positive energy of flux expulsion is the result of the kinetic energy of the superelectron pairs, which can be expressed as $\xi H_c^2/8\pi$ in terms of the condensation energy of the transition per unit area in zero field. Also, since the magnetic field penetrates the sample to a distance λ, we have an energy contribution due to this, and therefore the energy of the interface between the superconducting and the normal phases is just the sum of these two contributions,

$$\sigma_{ns} = \frac{1}{8\pi} (\xi H_c^2 - \lambda H_a^2). \qquad 1.4.3$$

One can also calculate the surface energy by using the Ginsburg-Landau equation

$$\sigma_{ns} = \int_{-\infty}^{-\infty} (F_{sH} - F_{nH} - MH_c)\, dx$$

$$= \int_{-\infty}^{0} [\alpha|\psi|^2 + \tfrac{1}{2}\beta|\psi|^4 + \frac{1}{8\pi}(B-H_c)^2 - (\frac{1}{2m^*}|(\frac{\hbar}{i}\nabla - e^*\underline{A}\ \psi|^2)] \qquad 1.4.4$$

where $x = 0$ is the boundary between the superconducting and normal regions. Equation 1.4.4 can not be integrated in closed form, but a solution by a numerical method gives the following results (De Gennes 1966)

$$\sigma_{ns} = 0 \quad \text{for } \kappa = \frac{1}{\sqrt{2}}$$

$$\sigma_{ns} \approx 1.89\ \xi(H_c^2/8\pi) \quad \text{positive for } \kappa << 1 \quad (\lambda << \xi)$$

$$\sigma_{ns} \approx -1.104\ \lambda(H_c^2/8\pi) \quad \text{negative for } \kappa >> 1 \quad (\lambda >> \xi)$$

In a type I superconductor σ_{ns} remains positive up to H_c, and in a type II super-conductor σ_{ns} remains positive up to H_{c1}, the lower critical field, at which point it becomes zero and then has a negative value up to H_{c2}.

From the surface energy difference, we can classify superconductors into two groups. Those which have positive surface energy are called type I, and those which have negative surface energy are called type II. Most type II superconductors are alloys except for the elements niobium, vanadium, and tantalum. This is because alloying gives rise to impurity scattering of electrons, i.e., $\kappa = \lambda/\xi \gg \frac{1}{\sqrt{2}}$, type II.

Fig 1 gives schematically the nature of the n-s interface in an applied field for (a) Type I, and (b) Type II superconductors. In (a) $\kappa \ll \frac{1}{\sqrt{2}}$ and $\xi \gg \lambda$; in (b) $\kappa \gg \frac{1}{\sqrt{2}}$ and $\xi \ll \lambda$. If $\kappa = \frac{1}{\sqrt{2}}$, we have $H_{c1} = H_c = H_{c2}$ i.e. the boundary between the two types.

1.5 Magnetic behaviour of the superconductor

The magnetic behaviour of a material can be described by equation

$$\underline{B} = \underline{H}_a + 4\pi\underline{M} \qquad 1.5.1$$

where $\underline{H}_a$ is the external applied magnetic field, $\underline{B}$ is the magnetic induction inside the material and $\underline{M}$ is the magnetization. For a superconductor in the Meissner state, with a positive surface energy, $\underline{B} = 0$, and equation 1.5.1

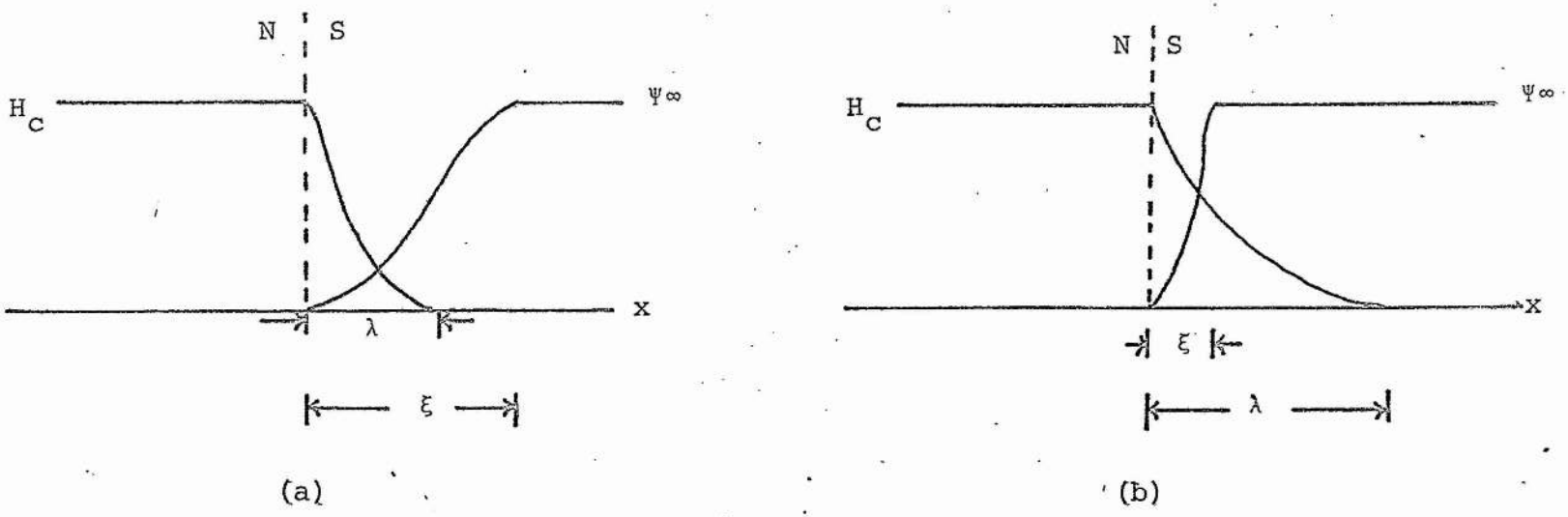

FIGURE 1 Schematical diagram of the n-s interface; (a) $\xi >> \lambda$, and (b) $\lambda >> \xi$

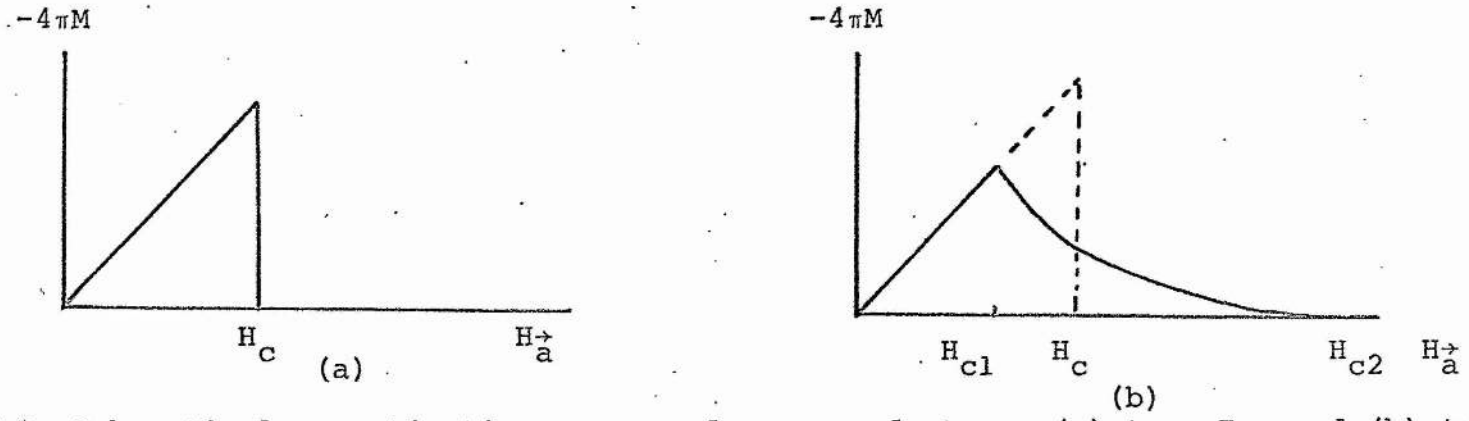

FIGURE 2 Schematical magnetization curves of superconductors; (a) type I , and (b) type II

becomes

$$\underline{H}_a = -4\pi\underline{M}, \qquad 1.5.2$$

and the specimen shows an ideal diamagnetic magnetization curve. The energy corresponding to the applied field is

$$-\int_0^{H_a} \underline{M}\cdot d\underline{H} = \int_0^{H_o} \frac{\underline{H}_a}{4\pi}\cdot d\underline{H} = H_c^2/8\pi \qquad 1.5.3$$

For a type I superconductor at $H = H_c$, the right hand side becomes $H_c^2/8\pi$, which is the condensation energy of the superconducting-normal transition, when $H > H_c$, $M_n = 0$ and the whole specimen becomes normal. The magnetization curve of an ideal type I superconductor with zero demagnetization factor is sketched in Figure 2(a).

In a type II superconductor, when the applied magnetic field $H_a = H_{c1} < H_c$, the surface energy becomes zero. With further increase of H_a the field starts to penetrate into the specimen, giving a lower free energy state. In this state, $\underline{B}$ is no longer zero, and we have

$$4\pi\underline{M} = \underline{H}_a - \underline{B} \qquad 1.5.4$$

The energy of the system is

$$\int_0^{H_a>H_{c1}} \underline{M}\cdot d\underline{H} = \int_0^{H_a>H_{c1}} \frac{\underline{H}_a-\underline{B}}{4\pi}\cdot d\underline{H} < \int_0^{H_a} \frac{\underline{H}_a}{4\pi}\cdot d\underline{H}. \quad (\because B>0) \qquad 1.5.5$$

When the external field reaches H_c, the energy of the system is

$$\int_0^{H_c} \frac{\underline{H}_a-\underline{B}}{4\pi}\cdot d\underline{H} < \frac{H_c^2}{8\pi} \qquad 1.5.6$$

The superconductor does not become normal until the external magnetic field reaches the upper critical field H_{c2}, where

$$\int_0^{H_{c2}} \frac{\underline{H}_a - \underline{B}}{4\pi} \cdot d\underline{H} = \frac{H_c^2}{8\pi} = F_{so} - F_{no}. \qquad 1.5.7$$

Superconductivity can exist in a thin surface layer of the specimen up to a much higher field, (Saint James and de Gennes 1964), $H_{c3} \approx 1.7\ H_{c2}$, a value which depends on the shape of the specimen. For convenient reference, we sketch the magnetization curve of a type II superconductor in figure 2(b).

1.6 Thermodynamic properties

The difference in heat capacity between the superconducting and normal phases can be derived from the "magnetic Gibb's function"

$$G_m = E - TS + PV - \underline{H}\underline{M}V, \qquad 1.6.1$$

or in differential form,

$$d\,G_m = VdP - SdT - V\underline{M}.d\underline{H}. \qquad 1.6.2$$

Since at $H = H_c$ the two phases are in equilibrium at every point on the surface, dG_m must be the same for each phase:-

$$(V_n - V_s)\,dP - (S_n - S_s)\,dT - (V_{n}\underline{M}_{n} - V_{s}\underline{M}_{s}).d\underline{H}_c = 0,$$

where $M_n = 0$ and H_c is a function of two independent variables P and T.

We can express the differences as

$$S_n - S_s = - (V_s H_c/4\pi) . \left(\frac{\partial H_c}{\partial T}\right)_P \qquad 1.6.3$$

$$V_n - V_s = (V_s H_c/4\pi) . \left(\frac{\partial H_c}{\partial P}\right)_T \qquad 1.6.4$$

and

$$\Delta C = C_s - C_n = T\frac{\partial}{\partial T} (S_s - S_n) = \frac{TV}{4\pi}\left[\left(\frac{\partial H_c}{\partial T}\right)^2 + H_c \frac{\partial^2 H_c}{\partial T^2} \right] \qquad 1.6.5$$

The latent heat of the transition per unit volume is

$$L = T\Delta S = - \frac{TH_c V}{4\pi} \left(\frac{\partial H_c}{\partial T}\right)_P \qquad 1.6.6$$

Since $\partial H_c/\partial T$ is always ≤ 0, the entropy of the superconducting phase is always less than that of the normal phase, and there is no change of entropy at T_c although there is a discontinuity in the specific heat at this temperature. The latent heat associated with the transition is zero in zero magnetic field, and the transition is consequently one of second order at T_c although it becomes one of first order below T_c in the presence of a magnetic field.

The existence of the latent heat of transition in a magnetic field implies a magneto-caloric effect which we shall discuss in chapter V. The specific heat of a metal has been generally interpreted as the sum of independent lattice and electronic terms.

$$C_n = C_{en} + C_{ln}$$
$$= \gamma T + \beta T^3 .$$

In the superconducting state, since the lattice contribution remains unchanged (Wilkinson et al 1955), we can write

$$C_s = C_{es} + \beta T^3 . \qquad 1.6.7$$

The specific heat jump at T_c, mentioned above, is predicted by the BCS theory to be $C_{es} = 2.43\ C_{en}$ in zero field.

The thermal conductivity (Olsen & Rosenberg 1953), of superconductors is a very complicated phenomenon, owing on the one hand to its being a non-equilibrium process, and on the other hand to the multiplicity of factors which contribute to it. Thermal energy in a normal metal is transported both by electrons and phonons. In a superconductor we can write

$$\kappa_s = \kappa_{es} + \kappa_{ps} \qquad 1.6.8$$

In the electronic component we have the contributions from the collisions between electrons and impurities (κ_{ed}), electron-phonon collisions (κ_{ep}) and electron-electron collisions (κ_{ee}). The lattice conductivity κ_p is determined by the interactions between phonon-electron, phonon-phonon and phonon scattering by the lattice impurities, crystal defects, and the boundary,

$$\kappa_s = \left(\frac{1}{\kappa_{ed}} + \frac{1}{\kappa_{ep}} + \frac{1}{\kappa_{ee}}\right)^{-1} + \left(\frac{1}{\kappa_{pe}} + \frac{1}{\kappa_{pp}} + \frac{1}{\kappa_{pd}}\right)^{-1}$$

The different mechanisms have varying dependences on temperature, impurities, sample size, etc, thus the thermal conductivity of particular superconductors can depend upon different mechanisms.

1.7 Pinning mechanisms in the mixed state

The hysteresis properties of the irreversible type II superconductor and the existence of the flux lattice in the mixed state raises many interesting problems; flux flow, dissipation, critical current, etc. It

is generally believed (e.g. Narlikar and Dew-Hughes 1964) that inhomogeneities in a specimen are able to distort flux lattices, and also to create higher field densities at places where the inhomogeneities occur. Bean (1972) and Kim et al (1962, 1963, 1963a) have introduced the concept of the "critical state", in which they extended the filamentary model (Mendelssohn, 1935) and assumed that the flux density in any part of the superconductor has to reach its critical value before it can diffuse into other parts. Anderson (1962) showed that the pinning of flux lines would produce a metastable flux gradient and hence a local critical current $J_c(B)$, and also suggested that a Lorentz-type force $\underline{B}$ x curl $\underline{B}$ tended to even out the flux density. The balance between these two forces under isothermal condition gives the following critical state equation

$$\underline{F}_{PV} + (\underline{J}_c \times \underline{B}) = 0, \qquad 1.7.1$$

where F_{PV} is pinning force per unit volume and J_c the critical current density. For this reason, type II superconductors, apart from the ability to carry a surface current can also carry a much bigger body current, which is dependent on the degree of "dirtyness" or in other words the irreversibility of the superconductor.

The critical current in a superconductor is usually defined as that required to produce an observable voltage (about 1 μV) as the current is steadily increased. This voltage is associated with the motion of the flux lines between pinning sites caused by the Lorentz force, provided by the transport current, overcoming the pinning forces.

The pinning forces due to different pinning sources add up to a total pinning force density F_{PV}, expressed as

$$\sum_i F_{pi} = F_{PV}$$

If all of these pinning forces F_{Pi} are constant, then we can equate this to the driving force. In the case of the Lorentz force, we have

$$\underline{J}_c \times \underline{B} = \underline{F}_{PV} = \text{const.}, \qquad 1.7.3$$

and

$$J_c \propto B^{-1}. \qquad 1.7.3a$$

A generalized expression of equation 1.7.3a derived from experimental results is

$$J_c = \text{const. } B^{-\gamma} \qquad 1.7.4$$

where γ is an experimentally determined constant.

Theoretical investigations of pinning mechanisms in general are based on the so-called "micromagnetic Ginzburg-Landau equations" derived by different authors (Labusch 1968, Kammerer 1969 and Kronmuller and Seeger 1969), but it is difficult to compare theory with experiment because there is no theory at present which can be applied to practical materials.

1.8 Transport properties

Under the condition of a non-isothermal flux flow state, in addition to the flux flow there is also a heat flow. In the mixed state the thermal 'force' of a temperature gradient can also bring the flux lattice into motion, and the motion of a fluxon across the superconductor is associated with the transport of entropy. Since within a flux line the entropy is larger than that of the superconducting phase, $S_n > S_s$ and $\kappa_n > \kappa_s$ (Bardeen et al 1959), the entropy currents must flow in such a way that they (1) supply entropy to the leading edge of the normal region to increase the entropy density there from S_s to S_n, and (2) carry away entropy from the trailing edge of the normal region to reduce the entropy there from S_n to S_s. The temperature distribution associated with these entropy currents

must be such that the leading edge of the moving fluxon is cooler than the trailing edge.

The condition for the fluxon lattice to be stationary under a non-isothermal condition in the presence of a transport current, becomes

$$\underline{\phi}_o \times \underline{J} + S_\phi \underline{\nabla} T - \underline{F}_{PV} = 0 \qquad 1.8.1$$

where $\underline{\phi}_o \times \underline{J}$ is the driving force per unit length on one quantised flux line or fluxon, and $S_\phi \underline{\nabla} T$ is the thermal 'force' where S_ϕ is the entropy difference between the superconducting and normal phases per unit length of a fluxon.

The transverse (Ettinghausen effect) and the longitudinal (Peltier effect) temperature gradients associated with the motion of fluxons under the presence of the transport current, and the transverse (Nernst effect) and the longitudinal (Seebeck effect) electric field associated with the motion of fluxons due to the thermal force are all determined by equation 1.8.1. Most of these effects are large, about three orders of magnitude larger than the corresponding effects in the normal state. The power dissipation associated with the motion of the fluxon is

$$Q = Q_{el} + Q_{th}, \qquad 1.8.2$$

which is the sum of the electrical power dissipation and the thermal dissipation, and which we shall give in more detail in chapter VII.

1.9 The purpose of the thesis

The original work of this thesis was to examine the possibility of making a refrigerator using the motion of quantized flux lines of a type II superconductor to transfer heat between the lower and the higher temperature reservoirs. Flux lines formed at one end of the specimen are swept to the other and carry entropy with them. It was found that it was not possible to move the flux lines by bodily moving a uniform magnetic field although the field distribution in the specimen was not uniform; this will be discussed in Chapter VIII.

In order to drive the flux lines we used a non-uniform field instead of the uniform field. The motion of the non-uniform field was accompanied by the transition of the metal from the superconducting state into the mixed state. After the passage of the field the metal reverted from the mixed state to the superconducting state, and consequently the corresponding absorption or release of the latent heat of magnetization or demagnetization produced cooling or heating which will depend on the entropy state of the specimen. There was also heating due to the dissipation accompanying flux flow. The experimental results of this on different specimens raised some interesting aspects of the dissipation mechanisms of a type II superconductor.

Dissipative mechanisms in a type II superconductor have been widely studied, but the detailed understanding of it is still far from satisfactory. Most experiments on the mixed state of a type II superconductor have been performed with a transport current and results were interpreted in terms of motion of flux lines. It seemed worthwhile to approach the problem with an experiment in which flux flow is mechanically induced. The idea of mechanically sweeping a field over a superconductor is a particularly useful tool with which to measure pinning forces in a specimen. Therefore we have built an apparatus to do this, and different kinds of forces were observed

which will be described in Chapter VI.

Pinning forces in a specimen are closely related to the hysteresis properties as well as the flux density in the specimen. Therefore we have used the magnetization curve measurement to determine the magnetic properties of a superconductor. In doing this for a finite specimen, we have to take the demagnetization and the surface effects into account and these have been done as will be described in Chapter IV. From the pinning force and the magnetization measurements we have derived the critical current density in different specimens. The dependence of pinning forces and magnetic properties on the temperature and on the surface treatment of specimens has also been studied.

The dissipation associated with flux flow in a type II superconductor is a thermo-magnetic effect. Therefore measurement of the specific heat in the mixed state was affected by the rate of the flux change of the specimen. In order to investigate whether the mixed state specific heat can be calculated from a simple 'two-fluid' type phenomenological equation, we have measured the heating effect from the magneto-caloric effect, and from that we have demonstrated that it was possible to correct for the heating due to flux flow in the specific heat measurement. The specific heat and the magneto-caloric effect measurements will be described in Chapter V.

The temperature variation associated with the flux flow in terms of pinning and viscous dissipation will be described in Chapter VII.

CHAPTER II

Apparatus and Experimental Detail

CHAPTER II Apparatus and Experimental Detail

2.1 Introduction

The thermodynamic and magnetic properties of superconductors are sensitive to the physical and chemical imperfections of the crystal. The critical fields H_{c1}, H_{c2} and H_c, the Ginzburg-Landau parameter κ, and the specific heats C_s and C_m vary from sample to sample of the same material. It is necessary to measure these parameters for each sample.

The critical fields of a specimen were determined by measuring the dependence of the resistivity or magnetization of the material on the external magnetic field. Measurement of the magnetization was chosen to determine the critical field not only because this method is simple and fast but also because it can provide the hysteresis curve of the sample from which one can determine the amount of flux trapping, and the magnetic induction inside the specimen.

Some magnetization measurements were made on a specimen which was thermally isolated, so that eddy-current heating during flux movement could be studied.

The heat capacity of a long Nb cylinder was measured, with the cylinder in different magnetic states, by supplying heat pulses to it and measuring the accompanying temperature rises.

The pinning forces of different specimens were determined by measuring, under isothermal conditions, the mechanical forces on the specimens produced by the passage over them of a magnetic field from a moving magnet.

During the movement of flux lines or flux bundles through a specimen there is both the transport of heat in the direction of flux motion as well as the generation of eddy current heating. Measurement of temperature

changes due to these two causes was made in nearly adiabatic conditions.

Measurements were made in the temperature range 1.4 K to 10.0 K. The basic cryostat consisted of a silvered Monax glass helium dewar of internal diameter 8.5 cm and of length 87 cm. Visual observations of the experiment could be made through unsilvered strips running vertically the length of the dewar. Temperatures from 1.4 - 4.2 K were obtained using a mercury manometer read with a cathetometer to measure the vapour pressure to an accuracy of 0.02 torr, as well as with carbon resistance thermometers calibrated from helium vapour pressure data. Since many of the measurements were made in the presence of a magnetic field the carbon resistance thermometers were calibrated in the magnetic fields that we used. The magneto-resistance was found to be small although we did correct for it. Temperatures above 4.2 K were obtained by isolating the sample in a vacuum can immersed in liquid helium and heating the sample to the desired temperature. Temperature measurements were made using carbon resistance thermometers calibrated from a germanium thermometer previously calibrated in the range from 1.5 K to 77.5 K. (Cryo-Cal). The carbon thermometers were Speer 220Ω and Allen-Bradley 100Ω and 10Ω chosen for their sensitivity for the particular application. Resistance measurements were made using a two wire Oxford Instruments A.C. resistance bridge which dissipated less than 10^{-9}W. Temperature changes of 10μK could be detected. The resistance of the germanium thermometer was measured by passing a constant current through it and measuring the potential drop on a Pye universal precision potentiometer in a standard four terminal configuration. The polarity was periodically reversed to enable corrections to be made for thermal emf's.

An epoxy, Araldite AT1, was frequently used as a construction material

for the low temperature apparatus. It comes as a powder which is melted and cured in an oven to give a rigid material which can be easily machined and glued. The epoxy was found to withstand thermal cycling after it had been cured at 120 C for 16 hours. This was a cure at a slightly lower temperature than that recommended by the manufacturer and probably left the epoxy slightly flexible. The epoxy could be glued to itself with room temperature curing Epibond 121 using hardener 951. Thin wires and even a piece of Niobium 1mm thick and 4mm wide were successfully sealed into the epoxy to give a superfluid tight joint.

2.2 Isothermal Magnetization Measurements

The magnetization curves were obtained by mounting a cylindrical specimen in one coil of an astatic pair and integrating the output voltage as the applied magnetic field varied. The voltage representing the magnetization was plotted against the applied magnetic field on an X-Y recorder.

The magnetic field was produced by a superconducting solenoid (Olafsson 1971) with a bore of 45 mm and a length of 150mm wound with Niomax-S 25/40 wire (56%Nb: 44% Ti). Calculation gave the central field to be 450 Oe/A. An experimental check on this value was made by measuring the critical field of a pure lead cylinder in the temperature range 1.5K-4.2K. This gave a result of 446 Oe/A and this was the value used subsequently. The current for the solenoid was supplied by a British Oxygen Cryoproducts power supply fitted with a linear sweep facility. The actual current supplied to the magnet was measured by the voltage drop across an 0.01Ω standard resistor (accuracy 0.1%) in series with the solenoid. The maximum field

of the magnet was 10 K Oe.

The pick-up coils were wound on a former which also held the specimen. The formers were made from cylinders of Teflon, Araldite or Tufnol with an axial hole at the lower end to accept the specimen which was held in place by a threaded plug.

The coils, 70mm apart, were wound from 40 s.w.g enamelled copper wire into sections of the former with reduced diameter. The number of turns was chosen to give a suitable signal at the appropriate sweep rate of the field and of the critical field of the specimen. Typical critical data for the Nb specimen were ∿1000 turns on the pickup coil, a sweep rate of 4460 Oe/min and a critical field of ∿3KOe.

The coils were wound as nearly as possible the same, the two pairs of leads were twisted together. A 5KΩ potential divider was used to balance the coils in the absence of a specimen. The balance could also be checked during a run by driving the specimen normal when the magnetization also disappears to within the accuracy required. The experiment is shown in block form in Figure 2.1.

Thermal contact was made to the specimen by drilling a number of holes through the former around the specimen to allow the liquid helium to circulate freely.

Great care was necessary in ensuring that all the low level leads were adequately screened and that rapid flux changes in the specimen were avoided. The high frequency components of the signal were distorted by the Keithley Millimicro voltmeter, which had a narrow bandwidth, and so these did not integrate to zero. This effect could be seen from time-dependent offsets on the magnetization curves.

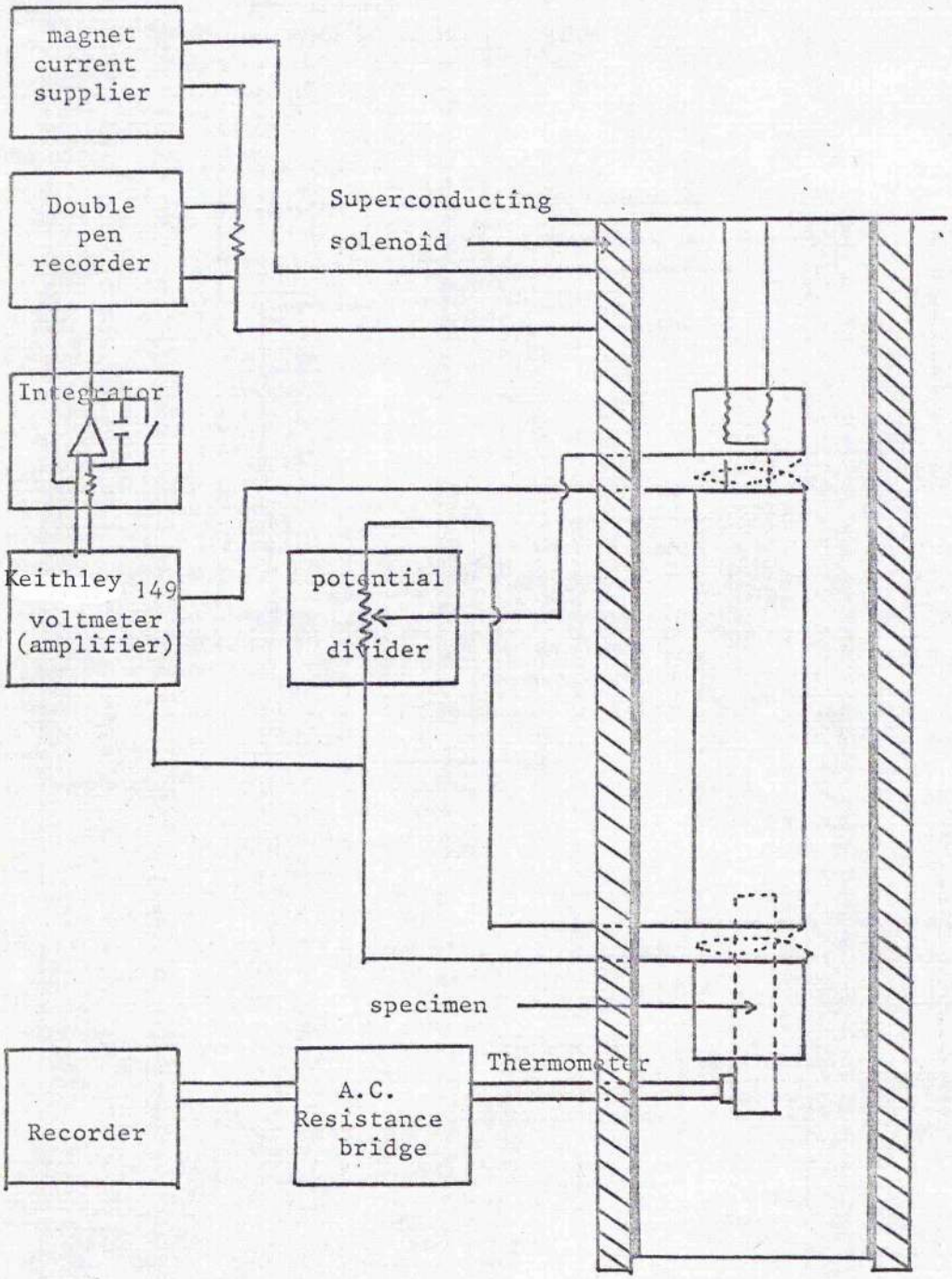

FIGURE 2.1 Apparatus for Magnetization Measurement

2.3 Specific Heat at constant applied field

A long cylindrical Nb specimen was hung by cotton threads at the centre of a high vacuum can which fitted inside the solenoid described in section 2.2. Around one end of the specimen a heater of Eureka wire of 10.9Ω was wound non-inductively. The heater had two current leads and two potential leads which were made of superconducting wire to reduce the heat leak which was mainly by thermal conduction. The other end of the specimen carried the thermometer, a 100Ω Allen Bradley resistor. To measure the state of magnetization of the specimen, a pair of astatic coils were mounted with the specimen at the centre of one of the coils but not in thermal contact with it. The coils were wound on a $\frac{3}{4}$" i.d. Tufnol tube.

On supplying a small amount of heat to the specimen, its temperature rose with a time constant of a few seconds to a new steady value. The specific heat measurements were made by driving the heater with a square pulse generator (pulse width 5-10 seconds, pulse height 0-200 mV, pulse separation 30-60 seconds) and recording the temperature variations. The pulse sizes were chosen so that $0.012 < \frac{\Delta T}{T} < 0.03$. This allowed measurement of ΔT to be made to $\pm$ 2% without subjecting the specimen to rapid changes of its magnetic state.

A schematic diagram of the apparatus is shown in Figure 2.2.

The following procedure was taken to ensure a known magnetic history for the specimen. The specimen was cooled to the desired starting temperature by having 0.5 torr of helium exchange gas. This was then removed by pumping for between 10 and 20 hours. The thermal isolation of the specimen was checked by supplying a pulse of heat and observing the time required to return to its original temperature. When an acceptably long cooling time was obtained the helium bath temperature was reduced to as low a value as

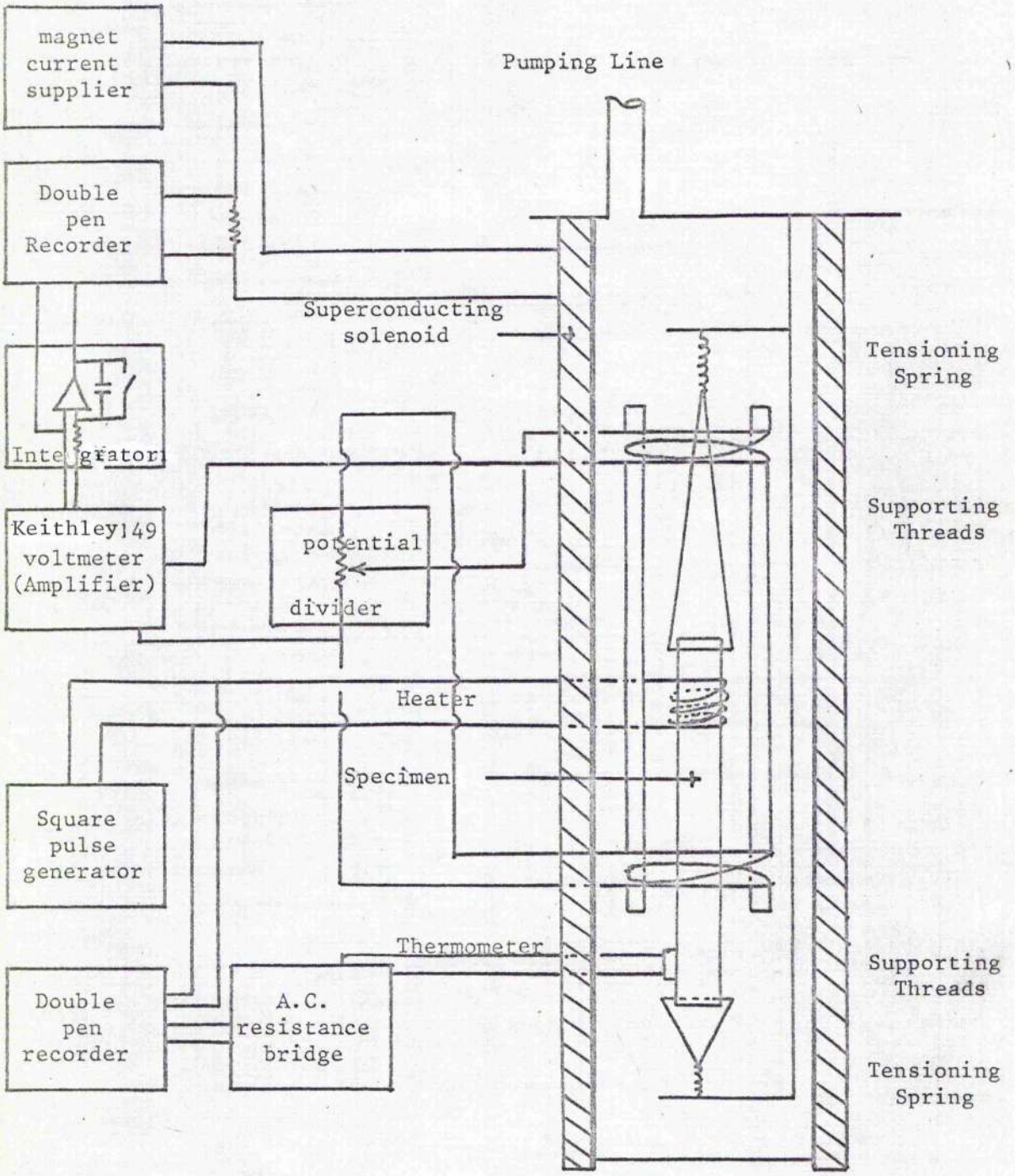

FIGURE 2.2 Apparatus for the specific heat measurement

possible. This appeared to improve the thermal isolation, presumably by decreasing the residual gas pressure. The magnetic field, of such a value as to leave the specimen in the Meissner state, was then applied. Heat pulses were then supplied and the magnetization and temperature changes were recorded.

The specific heat was taken to be

$$C(T) = C\left(\frac{T_{i+1} + T_i}{2}\right) = \frac{1}{n}\left(\frac{\Delta Q}{T_{i+1} - T_i}\right) \text{ (per mole)}.$$

This apparatus was also suited to making adiabatic magnetization measurements. The same procedure was followed as for the specific heat measurements except that no heat was supplied and the magnetic field was continuously increased at a constant rate while the state of magnetisation and temperature were again recorded.

2.4 The pinning force measurement

The apparatus for the pinning force measurement is shown diagramatically in Figure 2.3, and in Plates 2.1, 2.2. It consisted mainly of a pair of magnets mounted in a rotating cage and a specimen holder which was free to rotate against the restoring force of a spiral spring. The superconducting magnets which were encapsulated in Araldite were located in the brass rotating cage. This cage we connected rigidly to the rotating shaft.

The pair of superconducting solenoids, one above and one below the specimen, each consisted of 1036 turns of ZrNb superconducting wire of diameter 0.35mm wound on soft iron formers of length 26mm and diameter 8mm. The iron formers had end pieces 1mm thick and 22mm diameter. These

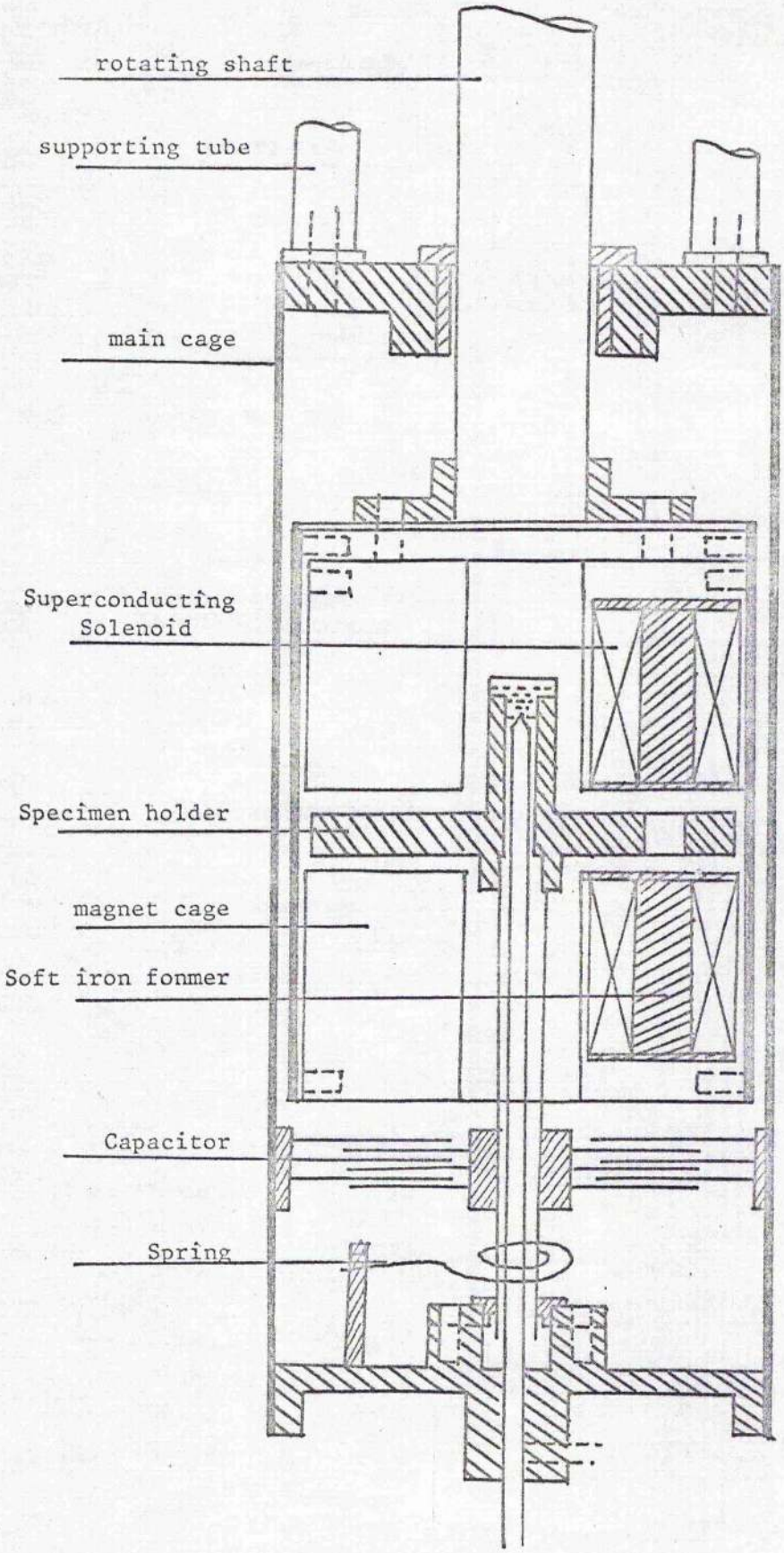

FIGURE 2.3 Apparatus for the pinning force measurement

PLATE 2.1

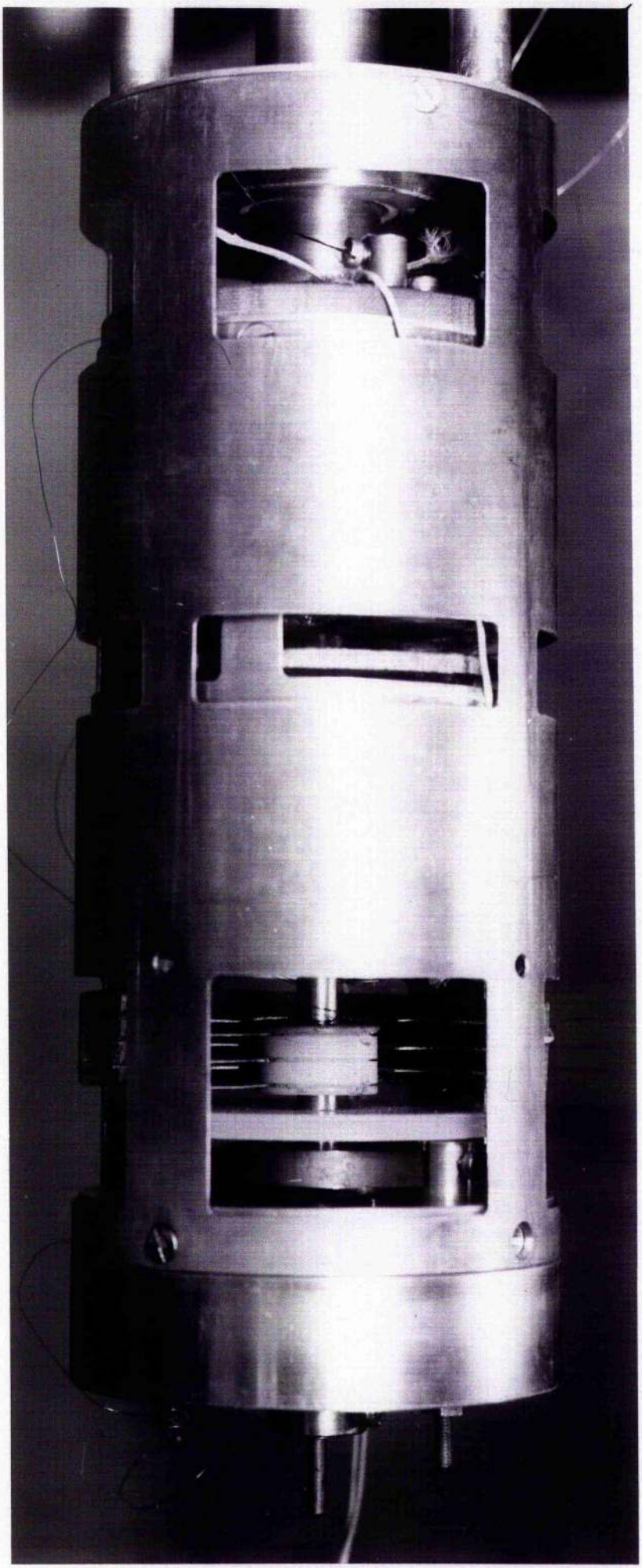

PLATE 2.2

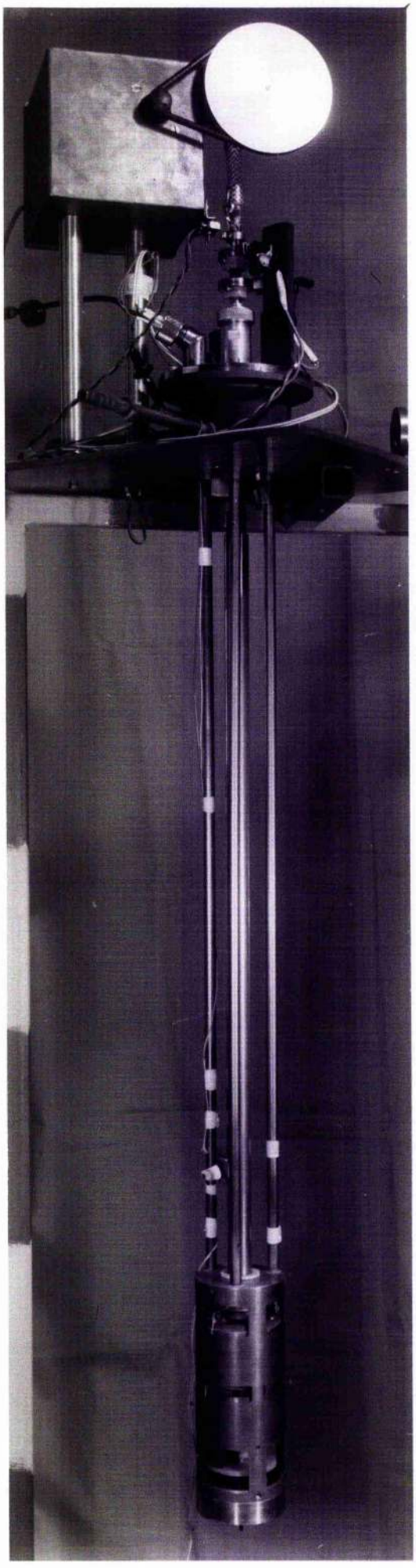

dimensions were chosen so as to give the maximum "G factor" (Montgomery 1964) in a solenoid of that overall size. The soft iron case was used to saturate the field in the bore area in order to achieve a working field of 3 K Oe without exceeding a current of 15A. The solenoids were mounted so as to leave a gap of 10mm between them with their axes parallel to and 22mm from that of the drive shaft. In the mid-plane between the two solenoids the field could be represented by

$$H(r) = H_o \exp(-0.0033\ r^2)$$

where r is the distance from the axis in mm.

The field/current coefficient of the magnet is not linear owing to the presence of the soft iron core; it rises rapidly in the low current region and then becomes linear with a value of $2290 Oe/_A$ above 3 amperes.

A circular Araldite specimen holder was placed between the two magnets. The circular holder had a hollow extended centre to accept the Teflon pivot so as to bring its centre of gravity below the bearing point. A $\frac{1}{8}$" silver steel rod with conical point on its upper end supported the specimen holder. A $\frac{1}{4}$" O.D. thin wall stainless steel tube was attached to the specimen holder and located in a teflon bush at the bottom of the main cage to keep the specimen holder central. A capacitor made of six pieces of half-annular brass plates was used to record the rotation of the specimen. The three moving plates of the capacitor were attached to a Teflon annulus which was fixed to the stainless steel tube while the other three stationery plates were fixed to the wall of the main cage. Two clock springs were mounted so as to spiral in opposite directions in order to minimize resultant transverse forces when the holder turned. The main cage was suspended by three $\frac{1}{4}$" stainless steel tubes from the top plate of the cryostat.

The mechanism for rotation of the magnet system is shown in Plate 2.2. The rotating shaft was a combination of a 20mm stainless steel tube from the top of the magnet cage to just below the top plate of the cryostat, and a 6.3mm stainless steel tube through the top plate with a vacuum sealing assembly. It was very important to have very low friction at the seal or else the shaft snatched at low speeds. A satisfactory seal was obtained using conventional 'knife-edge' seals with a lower than recommended loading and compensating for this by reducing the tolerances on shaft alignment and eccentricity. The shaft was located by Fafoir 5E 3K ball bearings and the seals were George Angus MIS 06. This choice of components allowed a small overall diameter for their housing. Initially some 'snatching' was experienced using ordinary vacuum greases and oils because their film strength was insufficient. Good seal lubrication was achieved with 'Trojan' o-ring lubricant supplied by Cities Oil Co. Ltd.

The rotating drive was from a small AC/DC electric motor (Singer, CAT NAB 2) supplied from a variac transformer and speed reduction was obtained through a combination of 2" radius aluminium pulley and a G & K Osborne "m" type gear box with ratio of 60:1. This gave uniform rotation speeds of any value between 0.7 and 7r.p.m. The direction of rotation could be reversed by reversing the current leads to the armature. The reversing system worked satisfactorily except for an increase in electrical noise due to sparking at the brushes. This noise was sufficiently reduced by mounting the motor in an iron box, although a better solution might have been to make the brushes moveable so that they could be advanced towards the approaching pole.

The current leads from the solenoids were brought up inside the drive shaft and out of the cryostat through glass seals. A pair of copper rings

with nylon insulating bushes were mounted onto the shaft and two carbon brushes provided the current connection. Provided that the copper slip rings and carbon brushes were kept clean the contact resistance was less than 0.3Ω during shaft rotation. A small screw was mounted on the top of the shaft surface to operate a microswitch once each revolution, and this was connected to one of the pens on the chart recorder.

In the isothermal experiments, the flat annular specimen was glued with GE varnish to the top surface of the specimen holder. In the case of a cylindrical specimen mounting was done by placing it in a $\frac{1}{4}$" I.D. Araldite tube wound outside with 20 turns of 42.s.w.g. copper wire, as shown in Plate 3.1(a). This Araldite tube was then inserted into a $\frac{3}{8}$" hole drilled in the specimen holder. The distance from the centre of the specimen to the centre of the cage was equal to the distance between the centres of the magnet and that of the cage.

During a run, the magnet cage was set in rotation with zero field and no rotation of the specimen holder was observed. When the field was increased step by step the specimen holder started to rotate against the restoring force.The rotation of the specimen holder was recorded through the off-balance voltage of the Marconi Universal bridge TF 2700, which was used to measure the capacitance change of the capacitor. The angle of rotation was also observed visually by reading the scale on the outside face of the specimen holder through the cathetometer from outside the cryostat. The force was determined by calibrating the restoring force of the clock springs at both room and nitrogen temperatures. The constant as determined showed no difference and it was taken to be the same below 4.2 K.

2.5 The dissipation associated with flux flow

The temperature variation of the specimen due to flux flow was investigated with two apparatuses in two different ways:

(a) We have measured the temperature variation of a specimen, relating to the pinning forces, by putting the specimen inside a sealed container, as described in the previous section. Because of the small separation of the two solenoids between which the sealed container had to fit, there was considerable restriction on the size of the container. In the case of a small cylindrical specimen this, together with a thermometer was sealed in a Tufnol cylindrical container with diameter 12mm and height 6mm and glued together with stycast 2850 GT, as shown in plate 3.1(a). Thermal contact to the helium bath was substantial since the leads of the thermometer were copper wire. The leads to the thermometer were carefully thermally anchored to the specimen before reaching the thermometer. In the case of a specimen in the shape of a "Bitter pancake", one end of the annulus was extended with a'tongue', as shown in Plate 3.1(c).

The specimen was encapsulated by making the specimen holder with two pieces of Araldite disc as shown in plate 3.1(b). Each disc was machined to give an annular groove, 12mm in width and 1.5mm in depth. The middle of the groove was co-axial with the centre of the magnet bore. The specimen was placed in this capsule without touching it anywhere except at the tongue, which extended through the edge of the groove to the helium bath. A thermometer was attached to the other end of the specimen. The joint between the tongue and the Araldite was sealed with Epibond 121 and hardener 951. This joint appeared to be superfluid-tight even after thermal cycling. The air inside the container was expected to condense at the liquid helium temperature to give a good thermal vacuum.

The temperature and the rotation (pinning force) were recorded simultaneously by a double pen recorder during every field passage. Another double pen recorder was used to record the velocity of the field rotation and the total field sweeping through the pick-up coil.

(b) We have also measured the temperature variation, due to flux flow, on a "Bitter Pancake" specimen placed in a vacuum can, as in Plate 2.3. Here the specimen was mounted so that only one end made thermal contact to the helium bath via a copper post. Both ends of the specimen had thermometers and the end opposite the thermal ground also carried a heater. The moving flux was generated by rotating two horseshoe magnets, one above and one below the specimen, with unlike poles opposite so that a region of high magnetic field could be swept from one end of the specimen to the other.

It was decided to mount the magnets inside the vacuum can along with the specimen. This allowed the apparatus to be set up with only a small clearance between the magnet poles and the specimen, a necessary requirement for achieving a useful field of 460 Oe, but also enabled there to be space around the specimen for mounting the thermometers, heaters and pick-up coils.

The magnets were driven inside the vacuum can without introducing any heat leak and without introducing any gas leak which could degrade the high vacuum. In order to do this, we used a magnetic coupling through the thin stainless steel top of the vacuum can.

The rotating mechanism was similar to that described in the previous section except that the aluminium shaft was a solid rod and the main drive shaft was a 6.3mm stainless steel tube. The magnet system inside the can contained a pair of horseshoe magnets which provided the experimental field.

PLATE 2.3

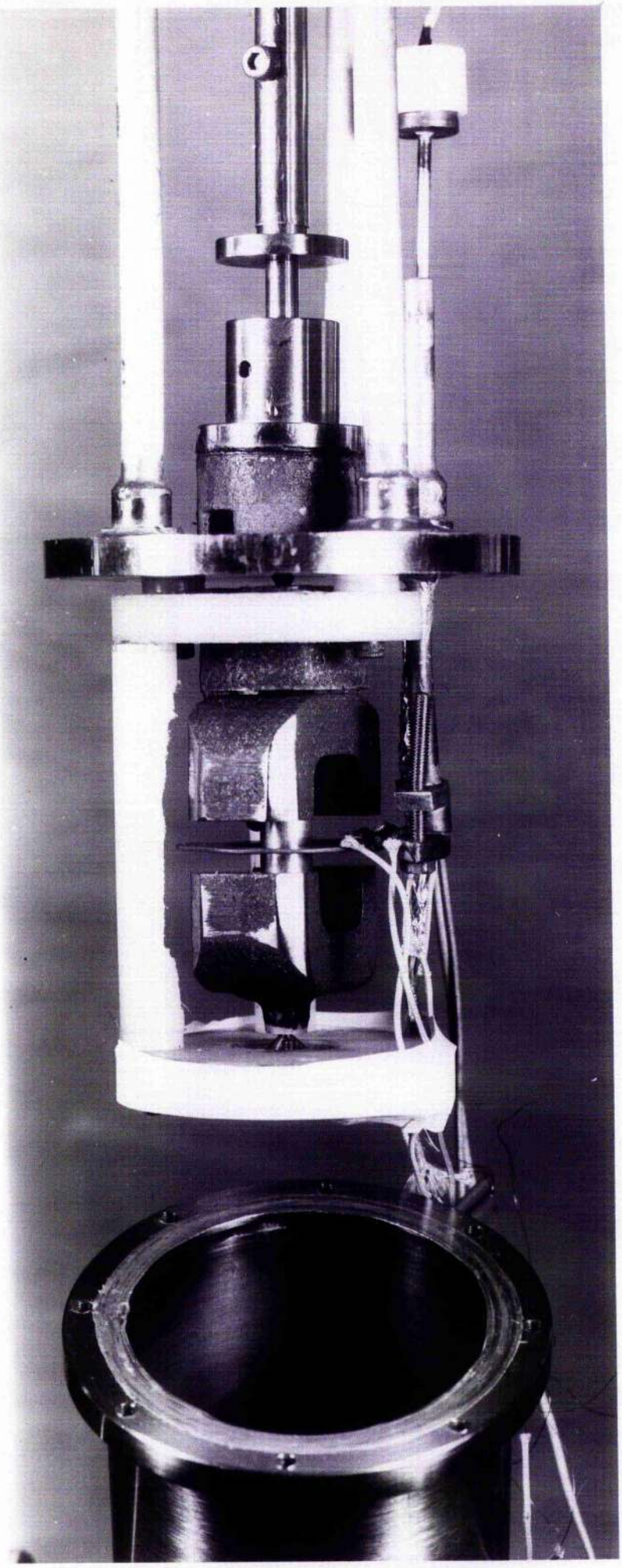

These were mounted on the same shaft as the drive magnet. The top and bottom bearings of this assembly were steel needles resting in Teflon bushes. The magnetic coupling between the drive magnets was just sufficient to lift the assembly against the needle so it also acted as a thrust bearing. The loading on this bearing could be altered by adjusting the lift and could be made quite small. This arrangement could be run at quite high speeds although this was not required for the experiments. The apparatus is shown diagramatically in Figure 2.4.

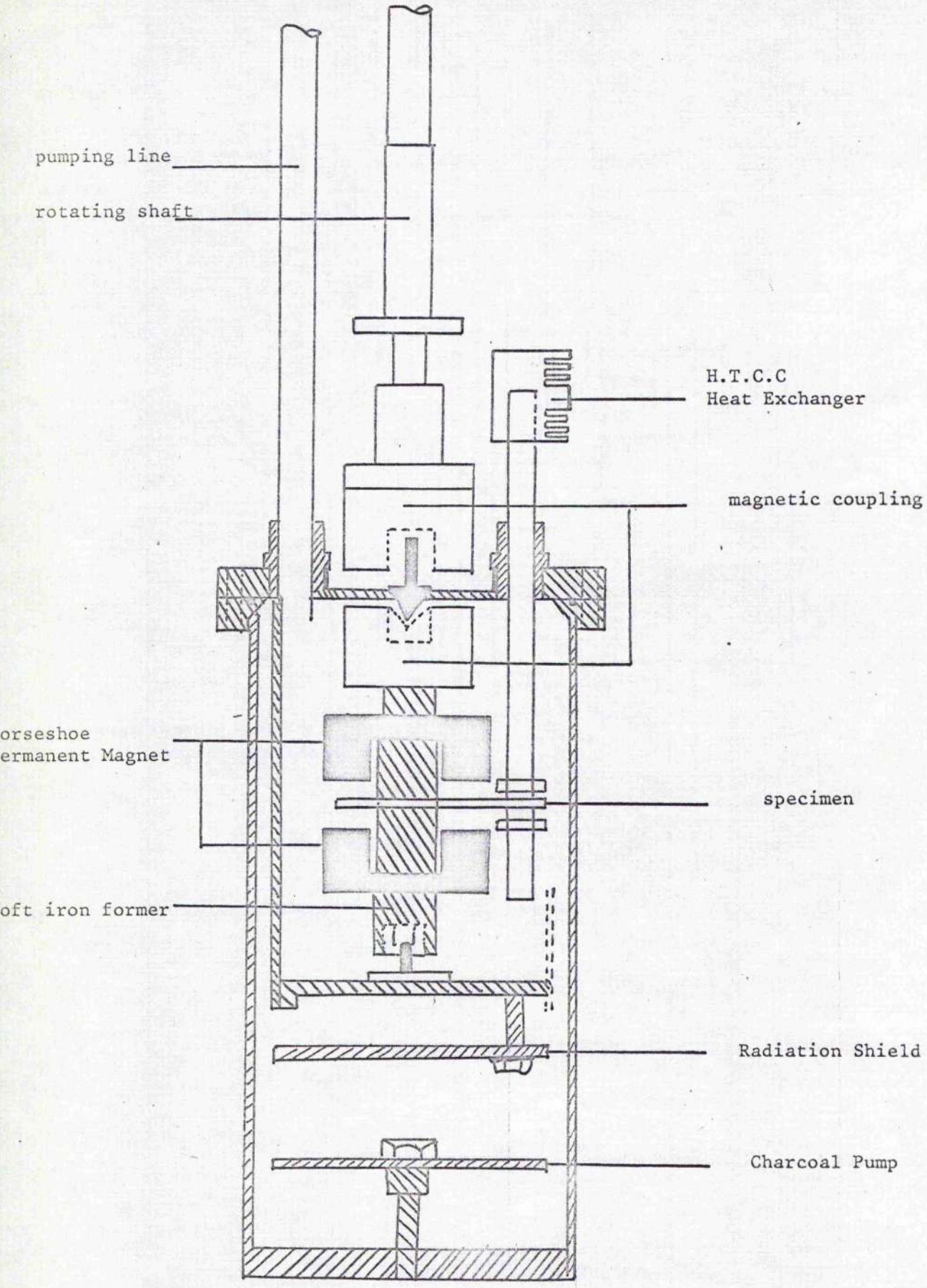

FIGURE 2.4 Apparatus for the dissipation experiment

CHAPTER III

Specimens

CHAPTER III Specimens

3.1 Introduction

Two groups of specimens have been used in this thesis. One group is composed of cylinders and flat specimens of niobium of different grades of purity, described in Table 3.1, and the other is composed of lead-indium alloys, described later.

Niobium serves as a base metal in the fabrication of many high field or high current superconducting materials; e.g. $NbSn_3$, NbTi, and $Nb_3Sn_xGa_y$. Therefore, it is particularly useful if we can understand the pinning mechanism in this substance. Niobium is a type II superconductor with a transition temperature $T_c \approx 9K$ and upper critical field $H_{c2} \approx 3$ K Oe at 4.22 K, and a wide range of $H_{c2}-H_{c1} \approx 1$ K Oe at 4.22 K in the mixed state. These properties made it very convenient for our experiments.

The $Pb_x In_y$ alloys were used to investigate the magnetic flux motion in the intermediate state or the mixed state, by varying the percentage of indium in the alloy. The melting points of pure lead ($326^{\circ}C$) and pure indium ($155^{\circ}C$) are low enough to make it easy to prepare specimens in the Laboratory with simple apparatus.

3.2 Niobium Specimens

A niobium rod, 99.9% purity, length 70 mm and diameter 6.35 mm was obtained from Koch-Light. Both ends of the rod were machined to a smooth surface and the length was reduced to 60 mm. This specimen was used for the magnetization, specific heat and magneto-caloric measurements before any pieces were cut from it.

TABLE 3.1

Specimens	Dimensions	Purity (%)	Demagnetization factor
Nb rod	60mm long x 6.35mm dia	99.9	≈ 0
Nb I	3mm long	99.9	0.443 ± 0.002
Nb II	3mm long	99.9	0.443 ± 0.002
Nb III	Annular shape, 1mm thick inner radius 17.5mm, annular width 7mm	99.5	large
Nb IIIa	Nb III with 15° gap, "Bitter pancake" shape	99.5	large
Nb IV	Segment 34° wide cut from Nb IIIa	99.5	large
Nb V	1.2mm long	99.9	0.725
Nb Va	1.2mm long	99.9	0.725
Nb VI	8mm long	99.9	0.206
Nb VIa	21.3mm long	99.9	≈ 0.09

Note: All specimens except NbIII, NbIIIa and NbIV were cut from the same Nb rod, and were all 6.35mm in diameter.

Two short cylindrical specimens, Nb I and Nb II were then cut from the rod for the measurements of the pinning force. Various mechanical polishing, oxidizing and chemical polishing treatments have been employed to modify the surface of these two specimens in order to investigate the variation of the pinning forces with surface treatment.

Four specimens, Nb V, Nb Va, Nb VI, and Nb VIa were used for the demagnetization experiments described in Chapter 4.

A 7 mm wide, 1 mm thick annular shaped niobium specimens NbIII, NbIIIa, and NbIV, which were also from material supplied by Koch-Light, were also used in the pinning force experiments. The NbIIIa specimen was associated with flux flow described in Chapter 7. NbIV was used to study pinning forces which are described in Chapter VI.

3.3 $Pb_x In_y$ alloys

Four different alloys, where x and y indicate the weight %, $Pb_{98}In_2$, $Pb_{96}In_4$, $Pb_{93}In_7$ and $Pb_{90}In_{10}$, were prepared from 6-9's purity Pb shot and 5-9's purity In ingots supplied by Koch-Light. They were melted together and cast into 60 mm long, 7 mm diameter glass tubes with no prolonged annealing. From each cast rod a specimen 3 mm long and 6.35 mm diameter cylinder was cut.

A 1 mm thick $Pb_{90}In_{10}$ annular specimen of inner diameter 17.5 mm and outer diameter 30 mm with a 20° gap was prepared by rolling and machining from a disc cast as described above. This was used for dissipation studies.

A photograph of some of the specimens and their method of mounting is shown in Plate III.1. The scale is full size.

Nb I and Nb II

Isothermal mounting

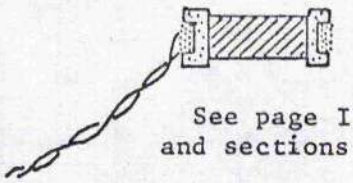

See page II-9
and sections 6.4.1 and 6.4.2.

Thermally isolated mounting

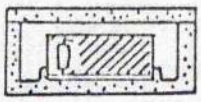

See page II-10
and section 7.3.3.

(twice actual size)

(a)

Nb III a

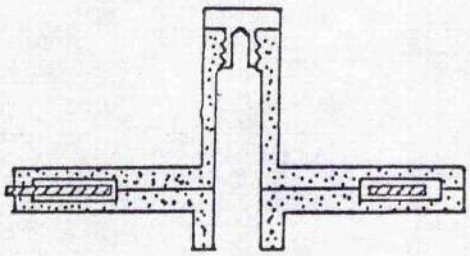

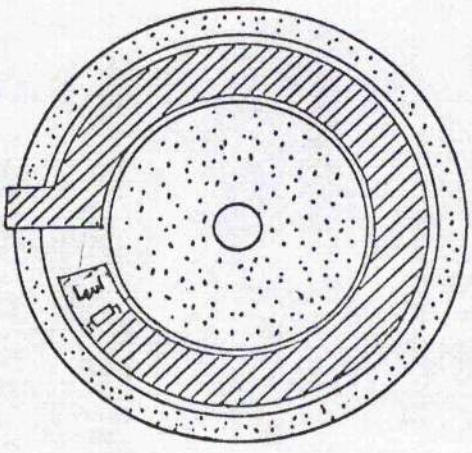

See page II-10
and section 7.3.3.

(b)

Pb_{90} In_{10}

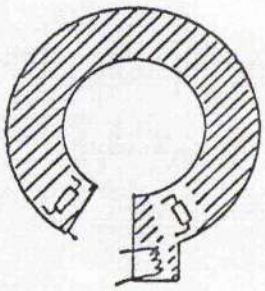

See page II-10
and section 7.3.2.

(c)

thermometer

heater

sample

Araldite

Fig 3.1

3.4 Other Specimens

A 3mm long 6.35mm diameter 6-9's pure Pb specimen, prepared in a similar manner as described above, was used to determine the demagnetization factor of the pure metal with the same geometry. It was also used to determine the field strength of the home-made soft-iron-cored superconducting magnets used in the pinning force experiments.

An annular specimen of Pb_{60} Tl_{40} was prepared in the same way as the Pb_{90} In_{10} annulus, and was also used in dissipation studies.

Care was also taken to avoid breathing the indium and thallium vapours which are toxic, and also to avoid handling the metals directly.

3.5 Surface Treatments

3.5.1 Mechanical Polishing

All the specimens used were first polished down to the finest grade of emery paper and were measured in this condition.

3.5.2 Oxidizing

The NbII and NbI specimens were heated in an oven with atmospheric pressure of air for two minutes at 400°C. This allowed a layer of niobium oxide to form on the surface of the specimen which we and others (De Sorbo 1963) found gave results which indicated a reduction in the number of surface defects.

3.5.3 Chemical Polishing

The NbI and NbII specimens, after oxidizing were immersed in a bath containing a 40% aqueous solution of HF plus 60% of fuming HNO_3 for five minutes. This solution is extremely dangerous and toxic and one must take

extreme care in handling it. The estimated rate of removal of metal in this process is about 0.2 mm in five minutes. After polishing, the specimen has a shiny silver appearance.

CHAPTER IV

MAGNETIZATION OF SUPERCONDUCTOR

CHAPTER IV Magnetization of Superconductor

4.1 Introduction

While the magnetic properties of a superconductor can in principle be determined from its magnetization curve, in practice these properties are shape-dependent and are also sensitive to the internal and surface microstructure of the specimen. The basic aspects of the Meissner phase of both type I and type II superconductors are the same, and therefore the magnetization curve of a type I superconductor can be treated as a particular case of the type II superconductor with zero region of the mixed state.

For a homogeneous, defect-free superconductor with zero demagnetization factor, the internal magnetization of the specimen is uniform. Abrikosov's analysis of the Ginzburg-Landau equations provide a remarkable description of the fundamental behaviour of this kind of superconductor. According to his model, the field begins to penetrate the specimen at a "lower critical field H_{c1}". When penetration is complete the specimen becomes wholly normal at an "upper critical field H_{c2}". Between H_{c1} and H_{c2} the magnetic flux distributes itself uniformly in the form of single quantized fluxons inside the specimen, and this forms what is known as the "mixed state". The fluxons can be treated as independent in lower field regions but show increasing interaction with each other as the external field increases. In the state of minimum free energy of the system, the fluxons form a two-dimensional lattice inside the specimen.

In practice, although many superconducting elements and some dilute

alloys approximate the ideal behaviour, real materials always exhibit some degree of magnetic irreversibility. Positive remanent magnetization in zero external field which is observed after driving the specimen normal magnetically and then removing the field, indicates that some of the magnetic fluxons remain trapped inside the superconductor. This flux trapping is due to the pinning sites in the specimen. It is generally believed (Livingston 1963) that inhomogeneties and the boundaries of the specimen can distort the flux configuration. Therefore, the internal flux distribution can not in general be treated as uniform. There are field gradients which contribute a driving force. Both the pinning forces and the driving forces are dependent on the size and the nature of the specimen, and so lead to hysteretic behaviour. The balance between these forces, and the size of the specimen all play a crucial role in the hysteresis properties.

In this chapter we shall describe the Abrikosov theory and briefly its extension by other authors, and compare them with our experimental results. We shall also consider the hysteresis properties in this chapter, and in chapter VI through the critical current model.

4.2 Theoretical considerations

4.2.1 The structure of a single vortex

A superconductor with negative surface energy in a magnetic field, i.e. $H_a > H_{c1}$, tends to split itself into normal and superconducting regions in the form of vortices. Each vortex carries one flux quantum, a fluxon (Träuble and Essmann 1968). The structure of an isolated vortex line is shown schematically in Fig 4.1. $\psi^*\psi$, which is identical

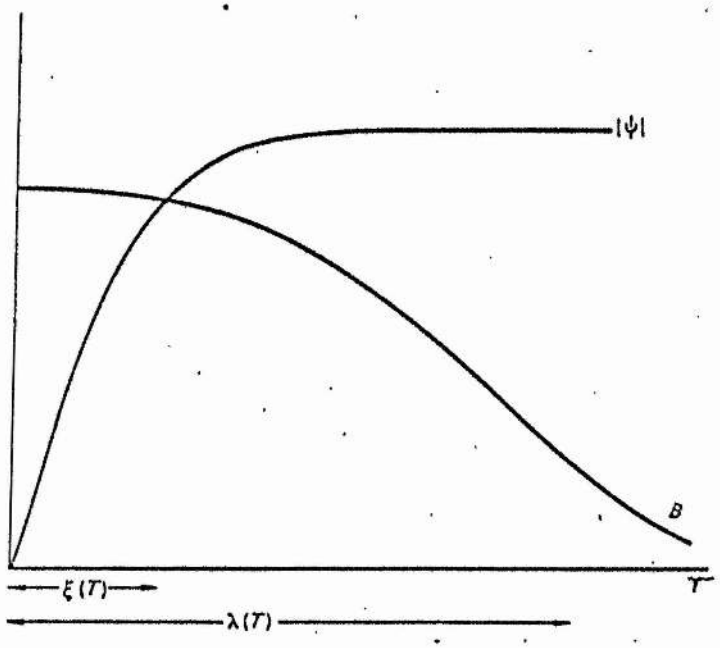

FIGURE 4.1 Structure of an isolated vortex line

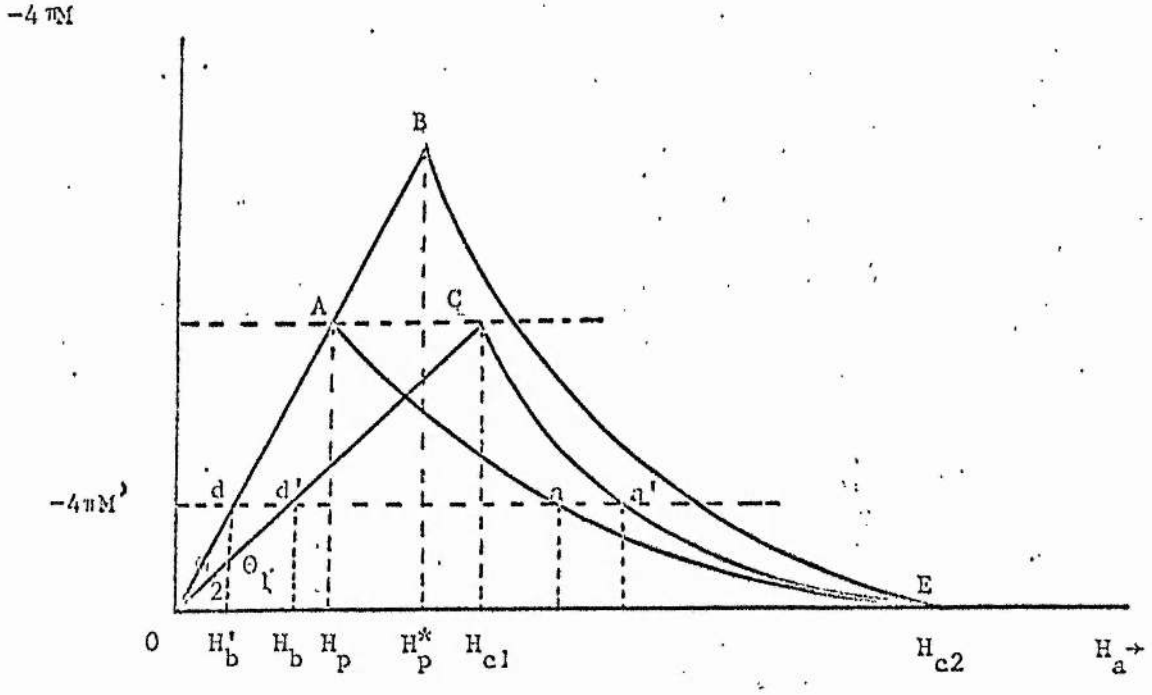

FIGURE 4.2 Illustrated magnetization curves for different type II superconductors.

with the number density of superconducting electrons, is depressed to zero in the centre of the vortex and reaches its full value at a radius nearly equal to the coherence length ξ. The field in the vortex attains its maximum in the centre of the vortex and diminishes exponentially and effectively vanishes at a radius of the order of the London penetration depth λ_L. The area of the vortex is $\pi\xi^2$, which is temperature-dependent. The angular momentum of the superelectron circulation in the vortex is constant. The surface energy of the vortex is negative, which is similar to that of the bulk surface energy.

4.2.2 The modified London model

In the Meissner state, the flux expulsion is complete (B=0), and $-4\pi M = H$. This state can be well described by the London equation. In the case of a specimen containing a single rectilinear vortex parallel to the $\hat{z}$ axis, the London equation can be modified to account for this flux and we have

$$\underline{H} + \lambda^2 \nabla^2 \underline{H} = \underline{\phi}_o \ \delta_2(\underline{r}) \qquad 4.2.1$$

where $\delta_2(\underline{r})$ is a two-dimensional delta function. With div $\underline{H}=0$, and using the Fourier transformation, we derive the following solution for Equation (4.2.1),

$$\underline{H}(\underline{r}) = \frac{\underline{\phi}_o}{2\pi\lambda^2} \ K_o \ (r/\lambda), \qquad 4.2.2$$

and

$$\underline{J}_s \ (\underline{r}) = \frac{\underline{\phi}_o}{2\pi\lambda^3} K_1 \ (r/\lambda), \qquad 4.2.3$$

where K_o and K_1 are the Hankel functions of imaginary argument of order zero and of order one. For $r/\lambda \ll 1$, K_o behaves as $\ln \lambda/r$, whereas for $r/\lambda \gg 1$,

K_o vanishes exponentially as $(\lambda/r)^{\frac{1}{2}} \exp(-r/\lambda)$. Then equation (4.2.2) becomes

$$\underline{H}(\underline{r}) = \frac{\underline{\phi}_o}{2\pi\lambda^2} \ln(r/\lambda) \qquad \xi < r << \lambda, \qquad 4.2.2a$$

and

$$\underline{H}(\underline{r}) = \frac{\underline{\phi}_o}{2\pi\lambda^2} \left(\frac{\pi\lambda}{2r}\right)^{\frac{1}{2}} \exp(-r/\lambda) \qquad r >> \lambda \qquad 4.2.2b$$

The energy per unit length of an isolated vortex line is

$$\varepsilon_1 = (8\pi)^{-1} \int d^2r\, \underline{H}(\underline{r}).\delta(r)\, \underline{\phi}_o$$

$$= (\phi_o/4\pi\lambda)^2 \ln(\lambda/\xi). \qquad 4.2.4$$

The Gibbs free energy per unit length of a vortex line is given by

$$G = \varepsilon_1 - \underline{\phi}_o \cdot \underline{H}/4\pi \qquad 4.2.5$$

Since, in thermodynamic equilibrium, the Gibbs free energy of the specimen must be a minimum, $\underline{\phi}_o$ and $\underline{H}_a$ must be parallel (straight vortex line). Furthermore, vortex lines cannot be in equilibrium inside the specimen unless $H_a > H_{c1}$, the initial penetration field, where

$$H_{c1} = 4\pi\varepsilon_1/\phi_o$$

$$= \frac{\phi_o}{4\pi\lambda^2} \ln(\lambda/\xi)$$

$$= \frac{\phi_o}{4\pi\lambda^2} \ln \kappa \qquad 4.2.5$$

Since $\phi_o = h/2e$ and

$$\kappa = \sqrt{2}\, H_c \frac{e^*}{\hbar} \lambda^2, \qquad 1.3.7$$

We can rewrite Equation (4.2.5) into

$$H_{c1}/H_c = \left(\frac{1}{\sqrt{2}}\kappa\right) \ln \kappa \qquad 4.2.5a$$

4.2.3 A system of vortices and lattice configurations

In the Gibbs free energy of a system with vortices we must account for the repulsive interaction U_{ij} between the vortices,

$$G \text{ (per unit cube)} = n\varepsilon_1 - \underline{B}\cdot\underline{H}/4\pi + \sum_{ij} U_{ij} \qquad 4.2.6$$

where $U_{ij} = \underline{\phi}_o \cdot \underline{H}_{ij}/4\pi$ and $\underline{H}_{ij} = \frac{\underline{\phi}_o}{2\pi\lambda^2} K_o(r_{ij}/\lambda_L)$, and n is the number of vortices per unit area.

The total free energy per unit volume of the system is

$$F = n\,\varepsilon_1 + (n\phi_o^2/16\pi^2\lambda^2) \sum_j{}' K_o\,(r_j/\lambda), \qquad 4.2.7$$

where the sum is over all vortices, excluding the one at the origin.

The arrangement of the flux lines in the specimen in a state of equilibrium with a minimum free energy is given by

$$\left(\frac{\partial G}{\partial B}\right)_{eq} = 0 .$$

With Equation 4.2.5 and the relation $r_j \propto B^{-\frac{1}{2}}$, we derive

$$\underline{H} - \underline{H}_{c1} = \left(\frac{\underline{\phi}_o}{8\pi\lambda^2}\right) \sum_j{}' \{2\,K_o\,(r_j/\lambda) + (r_j/\lambda)\,K_1\,(r_j/\lambda)\}. \qquad 4.2.8$$

The equilibrium Gibb's free energy is then

$$G = -\left(\frac{B\underline{\phi}_o}{32\pi^2\lambda^2}\right) \sum_j{}' (r_j/\lambda)\,K_1\,(r_j/\lambda). \qquad 4.2.9$$

We can neglect the energy contribution due to the interaction of vortices for separations $d > \lambda$, and only nearest neighbours become important. Equation (4.2.7) and equation (4.2.8) then reduce to

$$G = -(B\underline{\phi}_o/32\pi^2\lambda^2)\; z\;(\pi d/2\lambda)^{\frac{1}{2}} \exp(-d/\lambda), \qquad 4.2.7a$$

$$\underline{H} - \underline{H}_{c1} = (\underline{\phi}_o/8\pi\lambda^2)\; z\;(\pi d/2\lambda)^{\frac{1}{2}} \exp(-d/\lambda) \qquad 4.2.8a$$

where z is the number of nearest neighbours, the coordination number. If we now take the logarithm of Equation (4.2.8a) and rearrange, we get

$$\frac{d}{\lambda} = \tfrac{1}{2} \ln \left(\frac{\pi d}{2\lambda}\right) + \ln\left\{\frac{\phi_o z}{8\pi\lambda^2 (H-H_{c1})}\right\} \qquad 4.2.10$$

which is valid for any lattice in the region $H-H_{c1} << H_{c1}$. Furthermore, a combination of Equation (4.2.7a) and Equation (4.2.8a) gives

$$G = -\underline{B}(\underline{H}-\underline{H}_{c1})/4\pi, \qquad 4.2.11$$

so that the lattice structure affects the Gibbs free energy only through the constitutive relation $B_e(H)$. Using the relations

$$\underline{B} = n\underline{\phi}_o = \underline{\phi}_o / d^2 \qquad z = 4 \text{ (square lattice)}$$

$$\underline{B} = n\underline{\phi}_o = 2\underline{\phi}_o/\sqrt{3}d^2 \qquad z = 6 \text{ (triangular lattice)}$$

we can calculate the difference of Gibbs free energy between these two lattice structures,

$$G_{sq} - G_{tri} = \frac{\underline{\phi}_o(\underline{H}-\underline{H}_{c1})}{4\pi\lambda^2} \qquad \left[\frac{\frac{1}{3}(2\sqrt{3}-3)}{\{\ln\phi_o/4\pi\lambda^2(H-H_{c1})\}^2}\right]$$

$$> 0,$$

neglecting terms of order $(H-H_{c1})\{\ln(\phi_o/\lambda^2(H-H_{c1})\}^{-1}$. The triangular lattice is thus shown to be more stable than the square lattice. (Fetter, 1966).

4.2.4 Magnetization curve

The magnetic induction first appears when H_a exceeds H_{c1}, and it increases as the density of the fluxons increases. For a triangular lattice, we have

$$\underline{B} = {}^{2\phi_o}/_{\sqrt{3}\, d^2}$$

where
$$d = \lambda \ln\left[\frac{3\phi_o}{4\pi^2\lambda^2(H-H_{c1})}\right] + \frac{\lambda}{2}\ln\left[\frac{\pi}{2}\ln\left\{\frac{3\phi_o}{4\pi\lambda^2(H-H_{c1})}\right\}\right]$$

The magnetization curve is

$$4\pi\underline{M}(H) = \underline{B}-\underline{H} .$$

From these equations it can be shown that the magnetization curve has a vertical tangent just above H_{c1} (Marcus, 1964). This implies a first order transition but it can in fact be either first or second order, depending upon the magnitude of ${}^{\lambda}/_{\xi}$.

In the region $H_{c1} << H << H_{c2}$, exact results are known only for $\lambda >> \xi$, in which case, the electromagnetic regions of two adjacent vortices overlap, but their cores remains well separated. Equation (4.2.7) can then be integrated over a smoothed vortex density n, and we obtain

$$\underline{H}-\underline{H}_{c1} = \underline{B}-({}^{\phi_o}/_{8\pi\lambda^2})\ \{\ln[4\pi(H-H_{c1})\lambda^2/_{\phi_o}] + 2 - 2\gamma\},$$

where $\gamma = 0.5772 \ldots$ is Euler's constant (Fetter 1966). The magnetization

$$-4\pi\underline{M} \approx -\underline{B} + \underline{H} = \frac{\phi_o}{8\pi\lambda^2}\ \ln\ {}^{\phi_o}/_{4\pi\xi^2(H-H_{c1})} . \qquad 4.2.12$$

In the region $H_{c2}-H<<H_{c2}$, the order parameter is small (Maki, 1964). Therefore we can neglect higher order terms in Equation (1.3.2a). Equation (1.3.2a) becomes

$$\left(\frac{i\nabla'}{\kappa} + \underline{A}'\right)^2\ \psi' = \psi' . \qquad 4.2.13$$

The general approximate solution for Equation (4.2.13) is

$$\psi' = \sum_{-\infty}^{\infty} C_n e^{iKny'} e^{-\frac{\kappa^2}{2}(x' - kn/\kappa^2)^2}, \qquad 4.2.14$$

where $C_n = C_{n+N}$ is constant and ψ' is periodic in the x'-y' plane. The period in the y'-direction is $2\pi/k$ and in x'-direction is $2k/\kappa^2$. The upper critical field H_{c2} is determined by putting $n = 0$, and $k = 0$. If we substitute Equation (4.2.14) into Equation (1.3.3a), we obtain

$$H' = dA'/dx' = H_a - |\psi'|^2/2\kappa, \qquad 4.2.15$$

in which all quantities are dimensionless. With equation (4.2.15) and Equation (1.3.2a), we derive a necessary restriction on any solution of Equation (4.2.14):

$$\frac{\kappa - H'}{\kappa} |\psi'|^2 + (1/2\kappa^2 - 1) |\psi'|^4 = 0 \qquad 4.2.16$$

From Equation (4.2.16) and Equation (4.2.15), we derive

$$4\pi M = B - H = -\frac{H_{c2} - H}{(2\kappa^2 - 1)\beta_A}, \qquad 4.2.17$$

in conventional units, and

$$4\pi \frac{dM}{dH} = 1/\beta_A (2\kappa^2 - 1), \qquad 4.2.18$$

where $\beta_A = \langle|\psi|^4\rangle / |\langle\psi^2\rangle|^2$. For a triangular lattice, the calculation of Kleiner et al (1964) gives $\beta_A = 1.16$, and we have

$$4\pi M = B - H = -\frac{H_{c2} - H}{1.16(2\kappa^2 - 1)} \qquad 4.2.17a$$

4.2.5 Extension of Abrikosov's theory and the characteristic lengths

The original Abrikosov theory was restricted in validity to temperatures $T_c - T \ll T_c$, where the order parameter is small, and where it and the field are slowing varying in space. An extension of the Ginzburg-Landau-Abrikosov theory for real type II superconductors must take account of following factors:

(a) For those temperatures lower than T_c, and where the order parameter is no longer small, we need to take account of the higher order terms in Equation (1.3.1a), e.g. $|\Psi|^6$.

(b) As the field increases, the vortices get close together and the field is no longer slowing varying in space and the order parameter is also depressed.

(c) The superconducting parameters in a perfectly homogeneous superconductor are dependent simply on the composition, temperature, and the uniform state of strain of the specimen. In a real material, these parameters become inhomogeneous because of the long range stress field due to the crystal imperfection, e.g., a change of the mean values of λ, ξ, κ by the reduction of the electron mean free path.

Different approaches have been made by different authors. We shall not give their work in detail but simply review their results. Gor'kov reformulated the BCS microscopic theory in the form of Green's functions and showed that near the transition temperature at zero-field $T_c(o)$, the resulting equation for the spatially varying energy gap $\Delta(r)$ is essentially the same as the Ginzburg-Landau equation for $\Psi(r)$. This provided the link between ξ and λ and the physical characteristics of the

metal, such as the Fermi velocity and the density of states. We have

$$\xi_o = 0.18\ {}^{hv_F}/_{k\ T_c}, \qquad 4.2.19$$

and

$$\lambda_L(o) = \frac{3}{2}\ \mu_o\ e^2\ v_F^2\ N(o)\ . \qquad 4.2.19a$$

The dependence of λ, ξ, and κ on the mean free path l in the normal state has been given by Gor'kov (1959) and Caroli et al (1963). Gor'kov has derived the following results:

In the clean limit (subscript p):

$$\xi_p = 0.74\ \ \xi_o\ \left(\frac{T_c}{T_c - T}\right)^{\frac{1}{2}}, \qquad 4.2.20$$

$$\lambda_p = \frac{1}{\sqrt{2}}\ \lambda_L(o)\ \left(\frac{T_c}{T_c - T}\right)^{\frac{1}{2}}, \qquad 4.2.20a$$

and

$$\kappa_p = 0.96\ {}^{\lambda_L(o)}/_{\xi_o} = {}^{\lambda_p}/_{\xi_p} \qquad 4.2.20b$$

In the dirty limit (alloys with an impurity parameter $\alpha = 0.88\ {}^{\xi_o}/_{l} < 2$, and subscript d):

$$\xi_d = 0.85\ (\xi_o l)^{\frac{1}{2}}\ \left(\frac{T_c}{T_c - T}\right)^{\frac{1}{2}}, \qquad 4.2.20c$$

$$\lambda_d = 0.615\ \lambda_L(o)\ \left(\frac{\xi_o}{l}\right)^{\frac{1}{2}} \left(\frac{T_c}{T_c - T}\right)^{\frac{1}{2}}, \qquad 4.2.20d$$

and

$$\kappa_d = 0.725\ \lambda_L(o)\ /_l \qquad 4.2.20e$$

Also

$$\kappa = \kappa_o + 7.5 \times 10^{-3}\ \gamma^{\frac{1}{2}}\ \rho_n$$

where κ is expressed in terms of the coefficient of the electronic specific heat γ and the electrical resistivity in the normal state ρ_n.

The application of the microscopic theory to the mixed state was first attempted by Maki (1964) and de Gennes (1964). Maki extended the theory to all temperatures below T_c through some temperature-dependent parameters κ_1, κ_2, and κ_3, which are defined as

$$\kappa_1(T) = H_{c2}(T)/\sqrt{2}\, H_c(T), \qquad 4.2.22$$

$$\left(\frac{dM}{dH}\right)_{H_{c2}} = 1/4\pi\beta(2\kappa_2^2-1), \qquad 4.2.23$$

and

$$H_{c1}(T) = H_c(T)\, f(\kappa_3(T)), \qquad 4.2.24$$

where $f(\kappa_3(T))$ has a rather complicated form depending on the value of κ. Where $\kappa \gg 1$, $f(\kappa_3(T)) = \frac{\ln \kappa_3(T)}{\sqrt{2}\,\kappa_3(T)}$. The values of κ_1, κ_2 and κ_3 approach the same value at T_c where they equal the Ginzburg-Landau parameter κ.

The most extensive calculation of the temperature dependence of κ_1, κ_2 for materials of arbitrary purity is given by Eilenberger (1967), who calculated the free energy density up to fourth order in the order parameter Ψ, and who predicted that the variation of κ_1 and κ_2 would depend strongly on $1/\xi_o$ and also on the rates of s- and p- scattering by the impurities. For fields much below H_{c2}, Brandt et al (1967), developed another extension of the Abrikosov theory for pure superconductors. Instead of using a power series expansion of the order parameter, they used the periodicity of the flux line lattice in the centre of mass coordinates, and derived

$$\kappa_1 = \kappa\left\{1+0.41\,(1-\frac{T}{T_c})\right\} \qquad 4.2.25$$

and

$$\kappa_2 = \kappa\left\{1+(1.37-0.14\,\kappa^{-2})(1-\frac{T}{T_c})\right\}. \qquad 4.2.25a$$

Wada and Tamura (1973) have proved theoretically that the periodic structure of the flux lines lattice extended over the whole temperature region. In the case of a dirty type II superconductor, Kramer et al (1974) used the Gor'kov theory to calculate numerically the self-consistent structure and free energy of isolated vortices and of the vortex lattice using a circular cell approximation.

4.2.6 Demagnetization effect on the magnetization curve

The magnetization M of any homogeneous, isotropic specimen can be related to the local field $\underline{H}$ and the external field $\underline{H}_a$ by

$$4\pi\underline{M} = \underline{B} - \underline{H},$$

and

$$\begin{aligned}\underline{H} &= \underline{H}_a - 4\pi N\underline{M} \\ &= \underline{H}_a - N(\underline{B} - \underline{H}),\end{aligned} \qquad 4.2.26$$

where the purely geometric factor N is called the demagnetization factor. The demagnetization factor of a cylindrical specimen can be calculated using the Nagaoka formula (Grover 1946) for the inductance,

$$K = \frac{2\beta}{\pi}\left(\ln\frac{4}{\beta} - \tfrac{1}{2}\right) + \frac{\beta^2}{8}\left(\ln\frac{4}{\beta} + \frac{1}{8}\right) - \frac{\beta^4}{64}\left(\ln\frac{4}{\beta} - \frac{2}{3}\right) + \frac{5}{1024}\beta^6\left(\ln\frac{4}{\beta} - \frac{109}{120}\right) + \ldots , \qquad 4.2.27$$

and

$$N = 1 - K,$$

where $\beta = {}^{b}/_{2a}$, a being the radius and b the length of the cylindrical specimen.

For an ideal type I superconductor with demagnetization factor N, the transition from the superconducting state to the normal state takes place not by a single jump but continuously over a field interval from (1-N) H_c to H_c. The superconductor is said to be in an intermediate state in the region $(1-N)H_c < H_a < H_c$. This field penetration has been investigated by Olafsson and Allen (1972). For non-ideal type I superconductors, Habermeier (1974) has studied the magnetization change due to domain wall pinning.

For an ideal type II superconductor with demagnetization factor N, Abrikosov has shown that the intermediate state is not realized if the transition is a second order one. The distribution of the magnetization inside the specimen is macroscopically uniform, with $\underline{M} \parallel \underline{H}_a$, $\underline{B} \parallel \underline{H}_a$, and $\underline{H} \parallel \underline{H}_a$. In this case we have what is called a mixed state in the field interval $H_p = H_{c1}(1-N) < H_a < H_{c2}$ as sketched in Figure 4.2 In figure 4.2 the curve OCE represents the ideal case with N=0 and with $\theta_1 = 45^\circ$. The curve OAE represents a real type II superconductor where $N > 0$ and $\theta_2 > 45^\circ$. We thus have $\frac{\tan \Theta 2}{\tan \Theta_1} = \frac{H_p}{H_{c1}}$. Since we are interested in finding the curve CE from the observed curve AE and from the ratio of tangents, we can assume following (Kulik 1966) that for any given value of the ordinate $-4\pi M'$, the distance dd' is equal to the distance a a'.

For a non-ideal type II superconductor with demagnetization factor N, the penetration field H_p^* can not be related to H_{c1} directly because of the pinning effect of the specimen surface. In the interval $H_p^* < H_a < H_{c2}$, there are regions with non-uniform flux density in certain parts of the specimen (Harrison et al (1973), Rollins et al (1974)). An extra amount of free energy ΔF = ABE is required in addition to the condensation energy in order to

magnetize the specimen. This energy ΔF corresponds to the pinning effect of the specimen. Therefore we can derive the pinning force from the observed magnetization curve, which we shall discuss in Chapter 6.

4.3 Experimental results and discussion

4.3.1 Introduction

The magnetization curves of the specimens pure Nb, pure Pb, $Pb_{98}\ In_2$, $Pb_{96}\ In_4$, $Pb_{93}\ In_7$, $Pb_{90}\ In_{10}$ and $Pb_{60}\ Tl_{40}$ have been measured in a longitudinal magnetic field parallel to the cylindrical axis. The value of H^*_{c1} of each specimen was determined from the full cycle hysteresis curve of the specimen, by determining the initial slope of the curve in low field where the specimen is in the Meissner state and by extending this line to intersect the curve at H^*_{c1}, as shown in Figure 4.13a. On completion of a full cycle where H_a is again zero we reach the point 'R''. We increase H_a again in the original sense to some value H'_a, less than H^*_{c1} and then again reduce this to zero, so that we reach R' as shown in Figure 4.13a. We noted that the slope $R'H'_a$ was the same as the original initial slope O H^*_{c1}. We found that this was a general feature for all specimens where H'_a was not greater than H^*_{c1}. In particular, if $H_a = H^*_{c1}$ the remanence is zero, which thus enables us to determine H^*_{c1} with some accuracy. This is made clear in Figure 4.13 which shows the curves for chemically polished NbI at various temperatures.

If we cycle the external field above H^*_{c1} and remove it, the magnetization curve always intercepts the y-axis below the origin, and we have used this intercept $4\pi M$ to determine the remanent field, B_R, corresponding to a particular external field. When the cycling field H_a reaches

a maximum anywhere between H_R and H_{c2}, as in Figure 4.13a, the value of the intercept on the y-axis is always the same, and this gives us the maximum remanent field $B_{R\ max\ b}$ of the specimen at the temperature of measurement.

In order to compare the pinning force measurements (Chapter 6) with those derived from the magnetization curves by using the Irie-Yamafuji model, it is necessary to determine the values of $B_{R\ max}$ and $H_{R\ max}$ in the bulk metal as distinct from the surface contribution. The method which we used to eliminate the surface contribution in the magnetization was based on the following assumptions; (1) the critical state concept holds, and (2) if there is no surface contribution then the magnetization and demagnetization curves are a single straight line so long as $H_a < H_R$. Therefore, the surface contribution M_s can be determined as the difference in y-value between points A and B in Figure 4.3. Knowing M_s, which we now call CD, we can determine the maximum bulk remanence $B_{R\ max}$(OD) from the observation of $B_{R\ max\ b}$(OC) via $B_{R\ max} = B_{R\ max\ b} - M_s$, as also shown in Figure 4.3. If we now construct a line through D parallel to CA to intersect the line FB at E, we get the projection G on the x-axis which gives $OG = H_R^*{}_{max}$ which is the field which must be applied in order to obtain $B_{R\ max}$. The experimental results based on the above assumptions and derived from the magnetization curves of (a) the chemically polished cylindrical NbII specimen, and (b) after its cylindrical surface was roughened with a file, are shown in Figure 4.4. This shows the difference in surface contribution due to roughening as $\Delta B_{R\ max} = M_{s1} - M_{s2}$. We consider that this shows that our procedure is basically satisfactory.

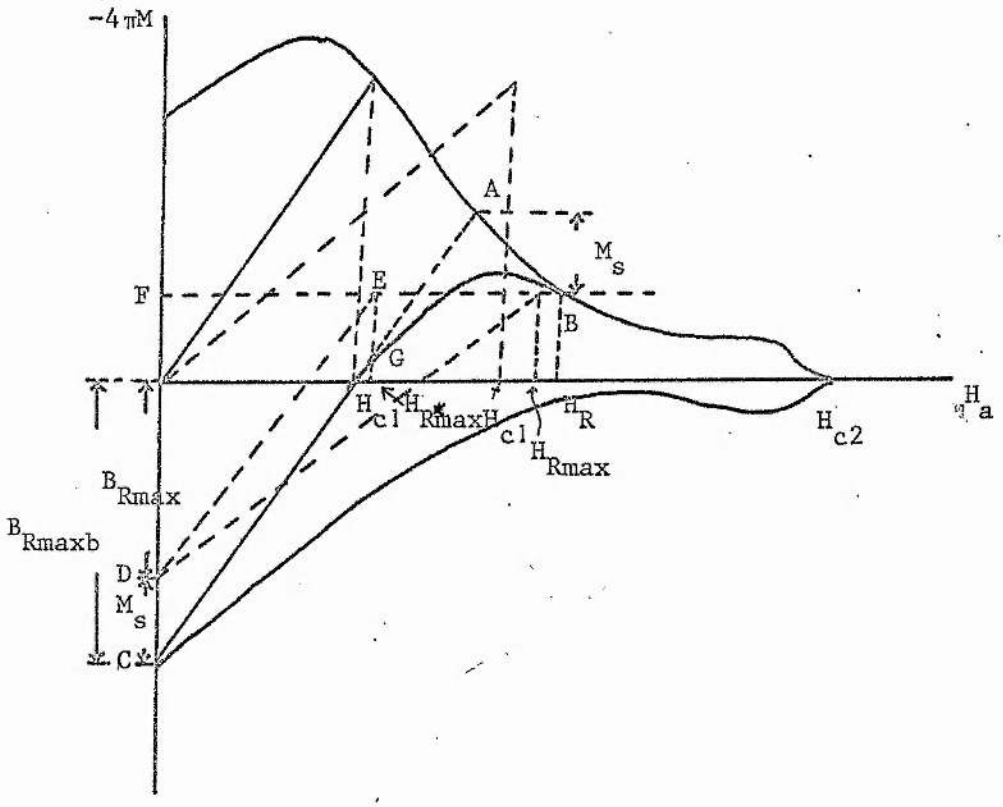

FIGURE 4.3 The magnetization curve for the chemically polished NbI Specimen at 1.48 K

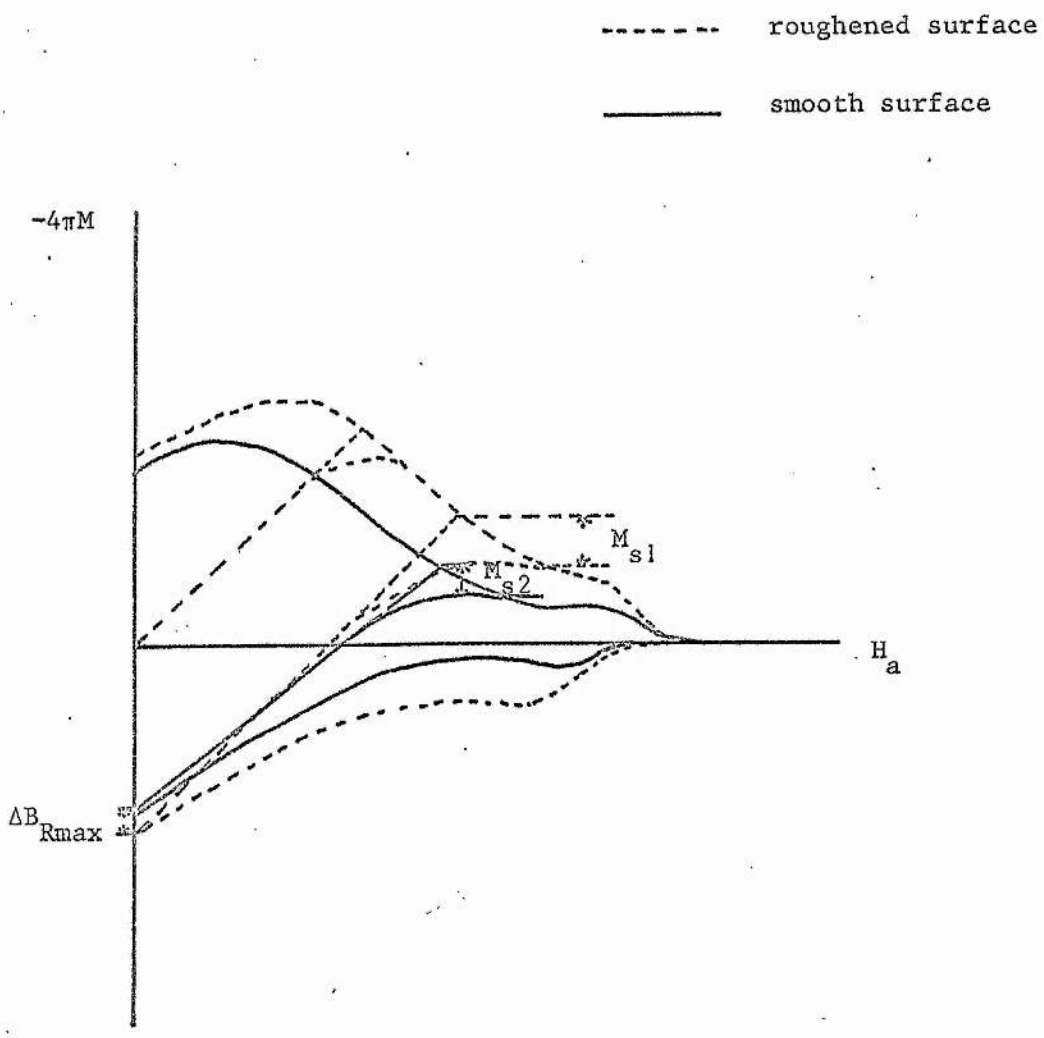

FIGURE 4.4 Magnetization curves of the NbII specimen at 4.22 K with chemically polished surface and roughened cylindrical surface

Because of the shape of our specimen, it was necessary to take into account the demagnetization effect in the derivation of the values of B, $H_{R\ max}$, etc. Instead of trying to solve Laplaces' equation for the field distribution, which has difficulty in taking account of surface pinning, we have applied the idea we described in 4.2.5 of an ideal-superconductor to a non-ideal type II superconductor and found that it was possible to take account of the demagnetization effect as shown in Figure 4.5. In (a) we show the magnetization curve of NbV as the solid lines, and the corresponding curve obtained by placing NbV and NbVa on top of one another shown as the dotted lines. Thus we have NbV like a single coin with demagnetization factor 0.725 and NbVa with NbV as two coins together with demagnetization factor 0.584.

In (b) we show similar results for NbVI (6 mm long, solid lines) and NbVI on top of Nb VIa (29.3 mm long, dotted lines) with demagnetization factors 0.206 and 0.084, respectively.

The magnetization value of a specimen is given by $-4\pi M = \alpha H_a$, where $\alpha = V/(1-N)$, V being the volume and N the demagnetization factor. For our geometry of two specimens, separately and then piled together, we have

$$\frac{\alpha_1}{\alpha_2} = \frac{-4\pi M_1}{-4\pi M_2} = \frac{(H^*_{c1})_1}{(H^*_{c1})_2} ,$$

where $H^*_{c1} = H_{c1}(1-N)$. In Figure 4.5(b) if we take the scale of $-4\pi M_2$ and replot $-4\pi M_1$ into $-4\pi M_1 \frac{\alpha_1}{\alpha_2}$, we have points A and B of curve (NbVI) raising to A' and B', respectively. The shifting of the point A' to A'' is due to the demagnetization effect which is determined by the shifting of the slope EO to B'O at the same value of $-4\pi M$, and in consequence A'A'' = CC'. Thus we can see that this procedure has provided us with a

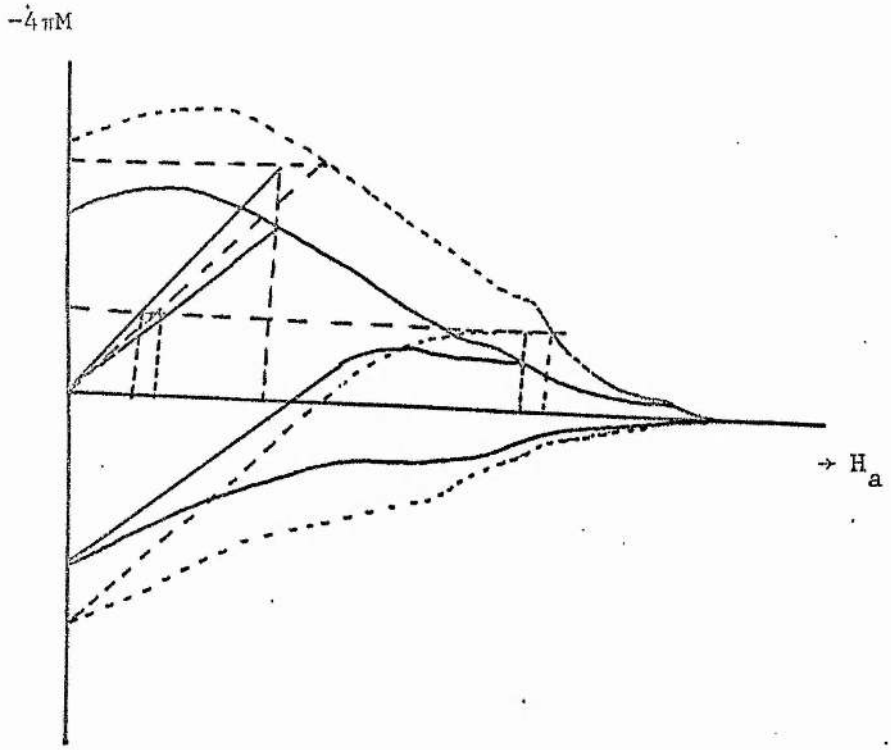

FIGURE 4.5(a) Magnetization curves of NbV (solid line) and NbV + NbVa (dotted line) specimens at 4.22 K.

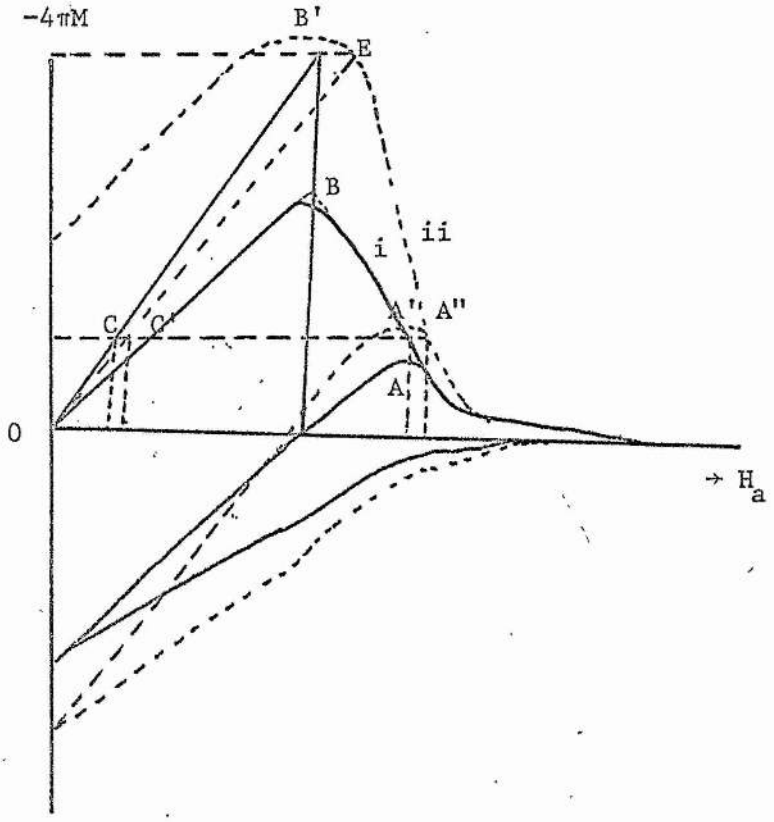

FIGURE 4.5 (b) Magnetization curves of Nb VI (solid line) and Nb VI + Nb VIa (dotted line) specimens at 4.22 K.

simple method of taking account of the demagnetization effect in the measurement of the magnetization of a non-ideal type II superconductor.

We can find the value of H_{c2} from Figures 4.14(a) and (b) by extrapolating the final steep part of the magnetization curve to cut the H-axis where M=0, the intercept of the extrapolation being H_{c2}. In (b), the NbII specimen was mechanically polished, the tail for $H > H_{c2}$ representing surface superconductivity. In (a), the specimen was oxidised (solid curve) and then chemically polished (dotted curve), and in both cases the tail for $H > H_{c2}$ can be seen to be very small indeed. In none of the Pb-In specimens did we see any surface superconductivity 'tail'.

The values of H_c for Pb-In alloys were found by using

$$< + 4\pi \underline{M}_e > \approx \tfrac{1}{2} < 4\pi \underline{M}_+ + 4\pi \underline{M}_- >, \qquad 6.3.5c$$

to derive their reversible magnetization curves, and using $\int_0^{H_{c2}} M dH = \frac{H_c^2}{8\pi}$. For the niobium rod specimen, the value of H_c was found from the specific heat measurements via Rutger's formula which will be described in Chapter 5.

4.3 Pb-In alloys

(a) Pb

The magnetization curves of a pure lead specimen with dimensions of 6.35 mm diameter and 3 mm long, have been measured at different temperatures as shown in Figures 4.6(a) and (b). In (a) ΔW is due to the 'wall' energy of the specimen (Habermeier 1974), where the wall is the interface between a normal and a superconducting region. The critical field H_c of this specimen at different temperatures can be well represented by the parabolic

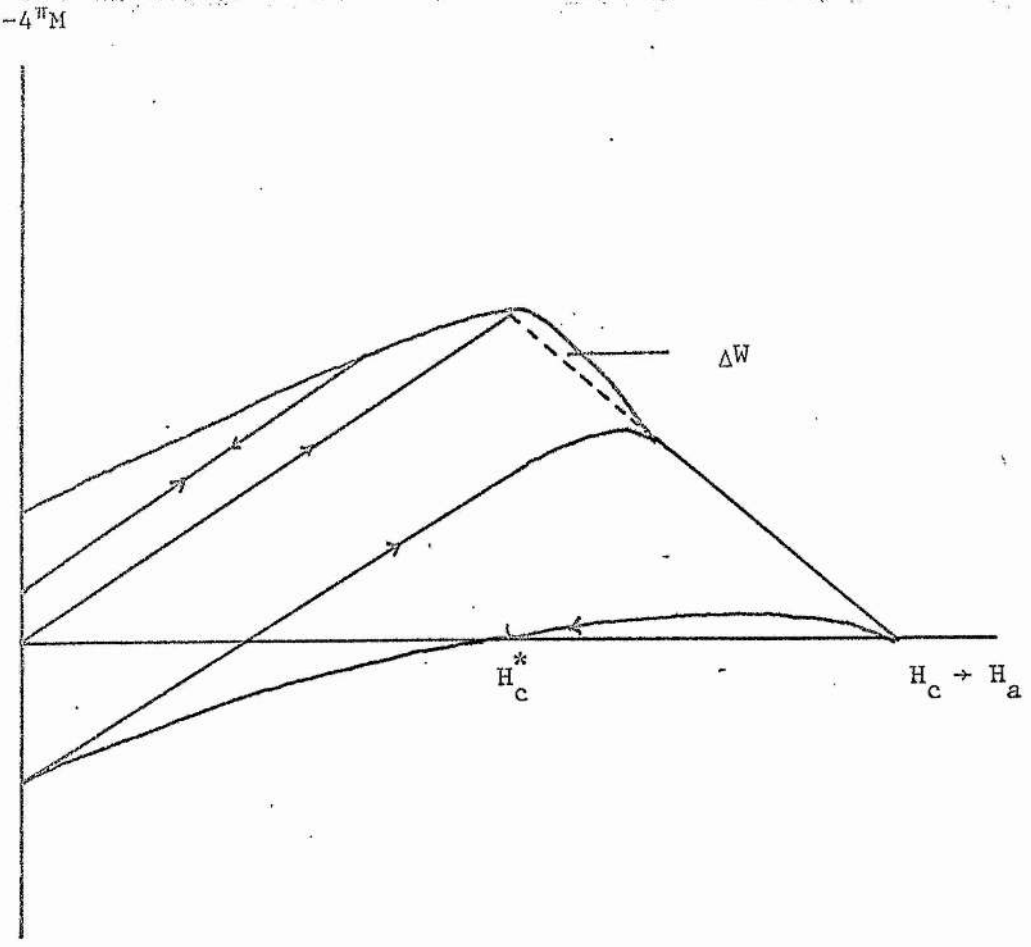

FIGURE 4.6(a) Magnetization curve of Pb at 3.25 K

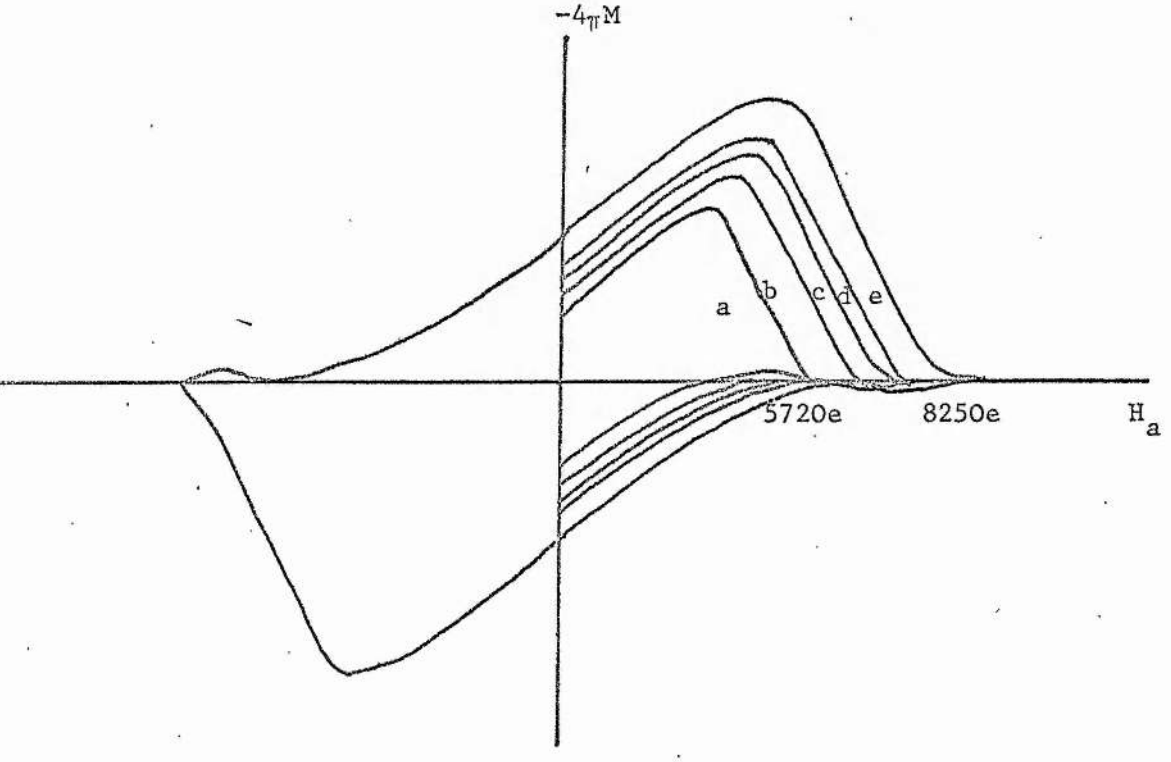

FIGURE 4.6 (b) Magnetization curves of Pb at different temperatures; (a) 4.22 K, (b) 3.07 K, (c) 2.90 K, (d) 2.45 K, and (e) 1.58 K.

relation of Equation (1.1.1) as plotted in Figure 4.7(a)

The main purpose of this measurement was to determine the demagnetization factor of a specimen of this shape. From this and from the alloy $Pb_{98}In_2$, we obtain $N = 0.443 \pm 0.002$, which is in agreement with the value calculated from Equation (4.2.27).

(b) The $Pb_{98}In_2$ alloy

The critical field curve of this alloy as function of temperature is shown in Figure 4.7(a) along with the curve for pure Pb. The magnetization curve at 4.22 K is shown in Figure 4.7(b), which suggests that it is a type I superconductor. This result is different from that of Livingston (1963), who found type II behaviour for $Pb_{97.92}In_{2.08}$, for which we can offer no explanation.

(c) $Pb_{96}In_4$, $Pb_{93}In_7$, and $Pb_{90}In_{10}$ alloys

The magnetization curves of these alloys have been measured from 1.4 K to 4.22 K. The magnetization curves of $Pb_{96}In_4$ and $Pb_{93}In_7$ at 4.22 K are shown in Figures 4.8 and 4.9, respectively, as solid lines. The values of H^*_{c1}, H_{c1}, H_c, H_{c2}, $B_{R\,max}$, B_{Rmax}/H_{Rmax}, $4\pi(\frac{\partial M}{\partial H})_{H_{c2}}$, κ_1 κ_2, $f(\kappa_3)$, and T_c for all of these alloys are given in Table 4.1. Their characteristic lengths κ, λ_p, $\lambda_L(0)$, ξ_o, ξ_p and v_F (Fermi velocity) at 4.22 K are calculated from Equations (4.2.19), (4.2.19a), (4.2.20), (4.2.20a) and (4.2.20b), and are given in Table 4.2.

The reversible magnetization curves of these specimens derived from Equation (6.3.3) are shown in dotted lines in Figures 4.8 and 4.9. The basic assumption of these derivation is that the surface current

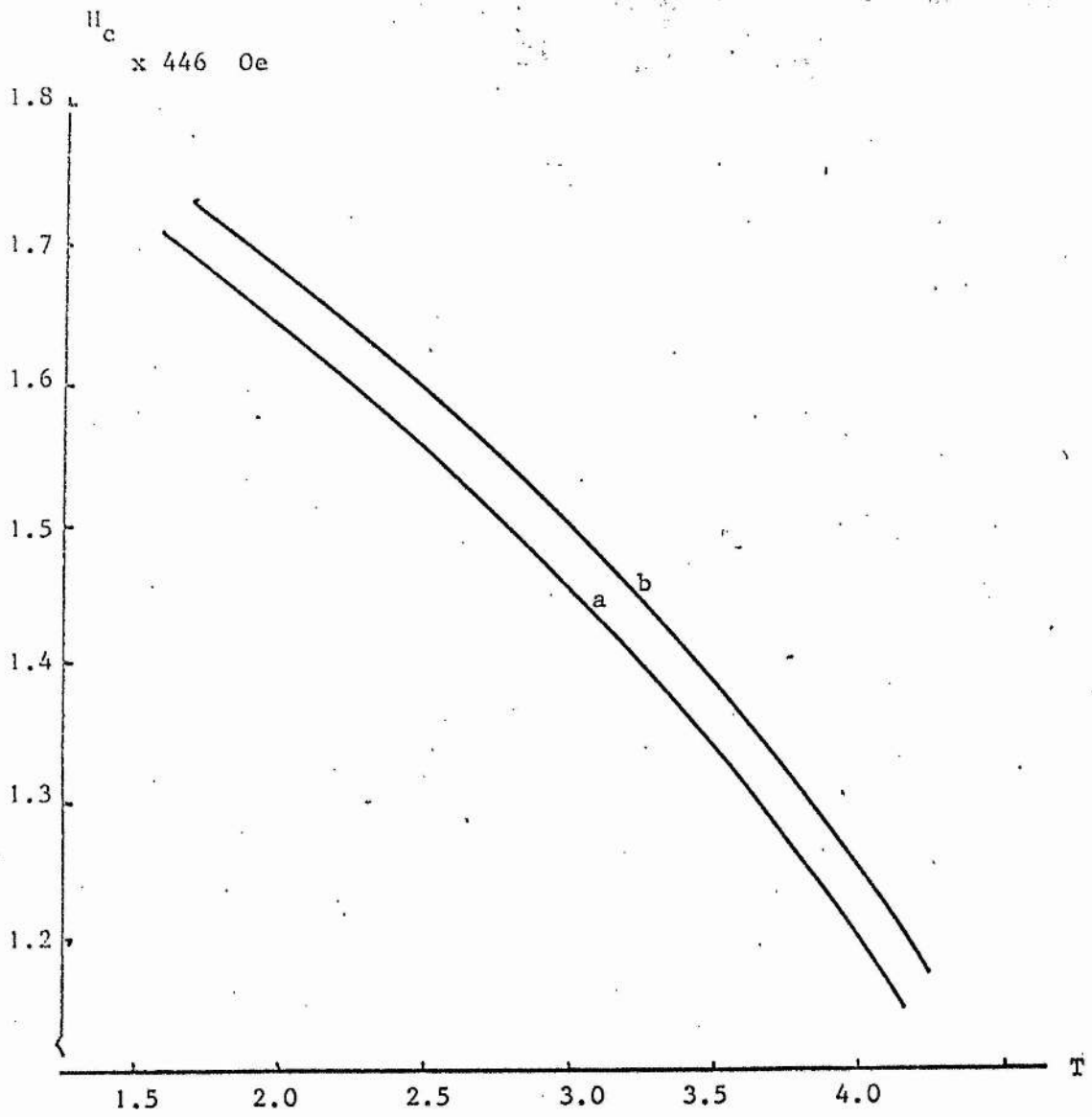

FIGURE 4.7 (a) The H_c vs T curves; (a) Pb and (b) Pb_{98} In_2

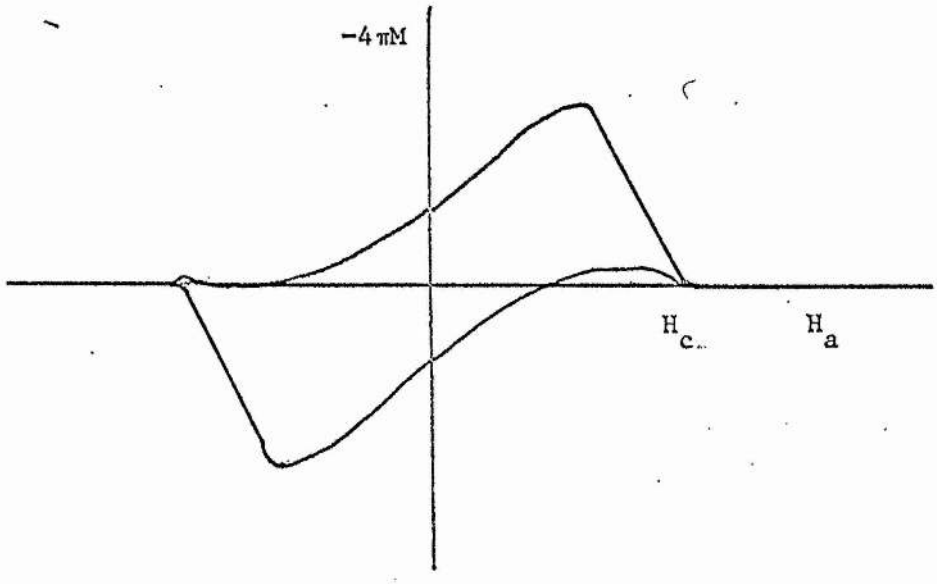

FIGURE 4.7(b) Magnetization curve of Pb_{98} In_2 at 4.22 K

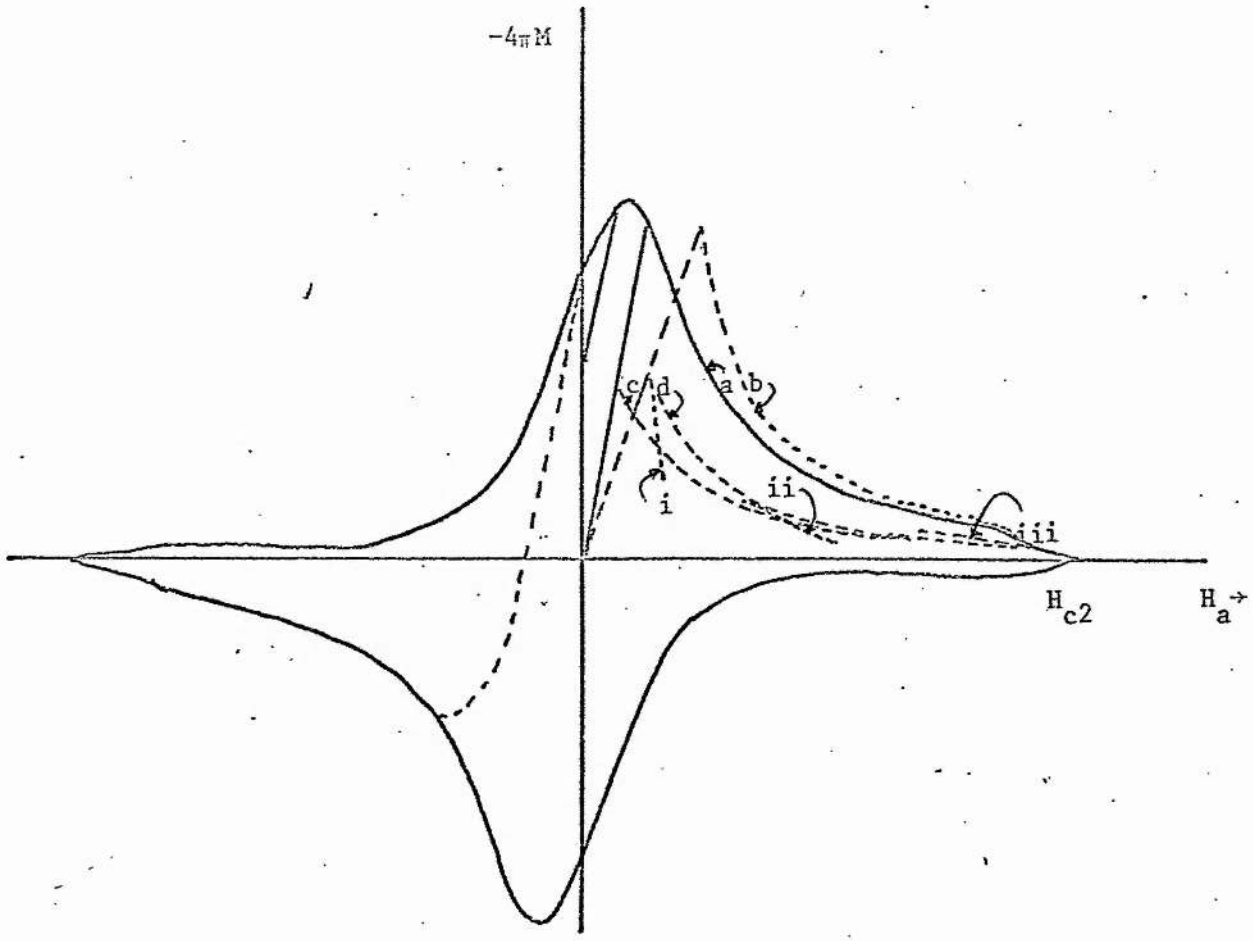

FIGURE 4.8 Magnetization curves of Pb_{96} In_4 at 4.22 K; (a) experimental curve; (b) curve (a) with N=0, (c) reversible curve for N=0.443, and (d) reversible curve for N=0

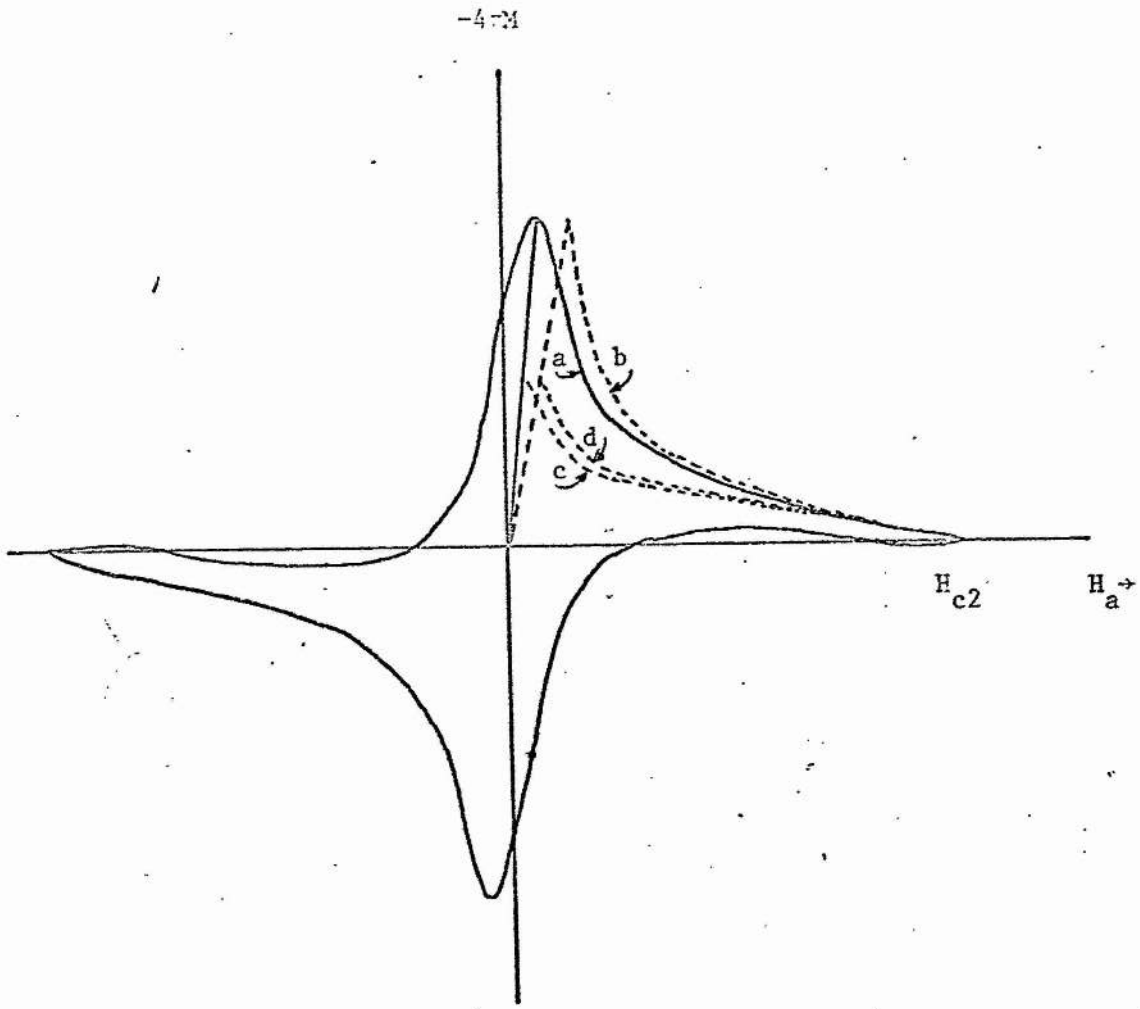

FIGURE 4.9 Magnetization curves of Pb_{93} In_7 at 4.22 K; (a) experimental curve, (b) curve (a) with N=0, (c) reversible curve for N=0.443, and (d) reversible curve for N=0.

TABLE 4.1

$Pb_{96}In_4$ alloy

T	$(1-N)H_{c1}$	H_{c1}	H_c	H_{c2}	B_{Rmax}	H_{Rmax}	$\frac{B_{Rmax}}{H_{Rmax}}$	$4\pi(\frac{\partial M}{\partial H})_{H_{c2}}$	κ_1	κ_2	$f(\kappa_3)$
4.22	295	529	567	2360	430	629	0.698	0.045	2.94	3.15	0.77
Rev.	148	265									0.47
3.72	328	589	659	2780	499	714	0.6965	0.043	2.98	3.24	0.89
3.00	377	677	771	3300	555	796	0.697	0.041	3.04	3.31	0.88
2.18	432	776	869	3750	617	885	0.698	0.0384	3.07	3.42	0.893
1.52	473	850	926	4100	682	977	0.698	0.035	3.13	3.58	0.918
									2.72	2.72	

T_c = 6.5K

γ= 0.68

$Pb_{93}In_7$ alloy

4.22	206	373	542	2635	321	466	0.689	0.0359	3.44	3.53	0.69
3.75	270	485	625	3078	340	494	0.688	0.0356	3.48	3.56	0.78

γ= 0.78

$Pb_{90}In_{10}$ alloy

4.22	178	320	532	3345	342	502	0.681	0.0211	4.44	4.58	0.602
Rev.	89	160									
3.80	223	400	596	3820	376	552	0.681	0.0204	4.55	4.65	0.671
3.63	249	449	624	4068	422	610	0.682	0.0200	4.61	4.70	0.719
3.12	269	483	701	4570	456	669	0.681	0.0189	4.63	4.83	0.689
2.18	299	536	813	5400	493	723	0.681	0.0184	4.69	4.89	0.66
1.85	307	552	843	5853	524	769	0.682	0.0175	4.77	5.01	0.655
1.40	320	574	876	6040	601	881	0.682	0.0156	4.92	5.30	0.655
									4.10	4.11	

T_c = 6.4K

γ= 0.85

$Pb_{60}Tl_{40}$ alloy

422K		320	550	2650							

T_c = 5.8K

TABLE 4.2

at 4.22K	$Pb_{96}In_4$	$Pb_{93}In_7$	$Pb_{90}In_{10}$
T_c	6.5K	6.5K	6.4K
κ_p	2.94	3.44	4.44
H_c	567Oe	542Oe	532Oe
λ_p	1.098×10^{-5}cm	1.215×10^{-5}cm	1.393×10^{-5}cm
$\lambda_L(o)$	0.918×10^{-5}cm	1.018×10^{-5}cm	1.149×10^{-5}cm
ξ_o	0.299×10^{-5}cm	0.283×10^{-5}cm	0.249×10^{-5}cm
ξ_p	0.373×10^{-5}cm	0.353×10^{-5}cm	0.314×10^{-5}cm
v_F	1.413×10^{7}cm/sec	1.337×10^{7}cm/sec	1.152×10^{7}cm/se

contribution to the magnetization is small, as will be seen when we come to describe the pinning force measurements in Chapter 6.

The magnetization curve calculated by Equation (4.2.10) in the region $H-H_{c1} \ll H_{c1}$, by Equation (4.2.1a) in the region $H_{c1} \ll H_a < H_{c2}$ and by Equation (4.2.17) in the region near H_{c2}, for $Pb_{96}In_4$ at 4.22 K is shown as three dotted lines i, ii, and iii, respectively, in Figure 4.8. The calculation in the region near H_{c1} shows an extremely steep slope, and in the region $H_{c1} \ll H \ll H_{c2}$, the calculated magnetization decreases faster than that determined from the experimental observations. As expected, there is good agreement between theory and experiment in the region near H_{c2}, since κ_2 in Equation (4.2.17) is itself determined from the experimental curve.

The temperature dependence of the upper critical field H_{c2} has been derived by different authors as follows:

(i) In the Gorter-Casimir theory, $\lambda = \lambda(0)(1-t^4)^{-\frac{1}{2}}$ and $H_c = H_o(1-t^2)$ and from Equation (4.2.22), we (Tinkham 1963) derive

$$H_{c2} = \frac{4\pi H_o^2 \lambda^2(o)}{\phi_o} \cdot \frac{(1-t^2)}{(1+t^2)} \, . \qquad 4.3.1$$

(ii) Bardeen (1954) and Ginzburg (1956) both derive the same temperature dependence of H_{c2} as

$$H_{c2}(t) = 2\sqrt{2}\,\kappa_1(T)\, H_c(o)\, [(1-t^2)/(1+t^2)] \, . \qquad 4.3.2$$

(iii) Gor'kov (1960) has derived

$$H_{c2}(t) = \kappa_1(T)\, H_{c2}(o)\, (1.77 - 2.20\, t^2 + 0.5t^4 - 0.09t^6) \, , \qquad 4.3.3$$

The determination of the H_{c2} from experiment is compared with the above

three theories for $Pb_{96}In_4$ and $Pb_{90}In_{10}$ in Figures 4.10(a) and (b). The agreement between theory and experiment is by no means good. Although we chose H_{c2} rather arbitrarily by extrapolation of the magnetization curve near H_{c2}, the degree of arbitrariness is at most $\pm$ 2% compared with the scatter of $\pm$ 10% between experiment and theory and between the theories themselves.

The values of κ_1, κ_2 and κ for $Pb_{96}In_4$ and $Pb_{90}In_{10}$ are plotted in Figures 4.11(a) and (b). They differ from the theoretical value of Equations (4.2.25) and (4.2.25a) by factors as great as 2 or 3. Discrepancies as large as this indicate theoretical shortcomings of the periodic structure model (Brandt et al 1967) rather than experimental errors.

4.3.3 $Pb_{60}Tl_{40}$ alloy

The values of H_{c1}, H_c, and H_{c2} of $Pb_{60}Tl_{40}$ at 4.22 K were measured for the cast cylinder, before it was rolled to its final circular shape; and are also given in Table 4.1.

4.3.4 Niobium specimens

(a) Nb (rod)

The phase diagram of the Nb(rod) is shown in Figure 4.12. The values of H_{c1} and H_{c2} were determined from the specific heat measurements and the adiabatic magnetization curves. Below 4.22 K, the value of H_{c1} and H_{c2} determined from the isothermal magnetization curves of this specimen agree with those determined from specific heat measurements. The comparison of the results for H_{c2} with the three theories are also shown in Figure 4.12. The Ginzburg-Landau parameter κ, determined in the limit of the transition

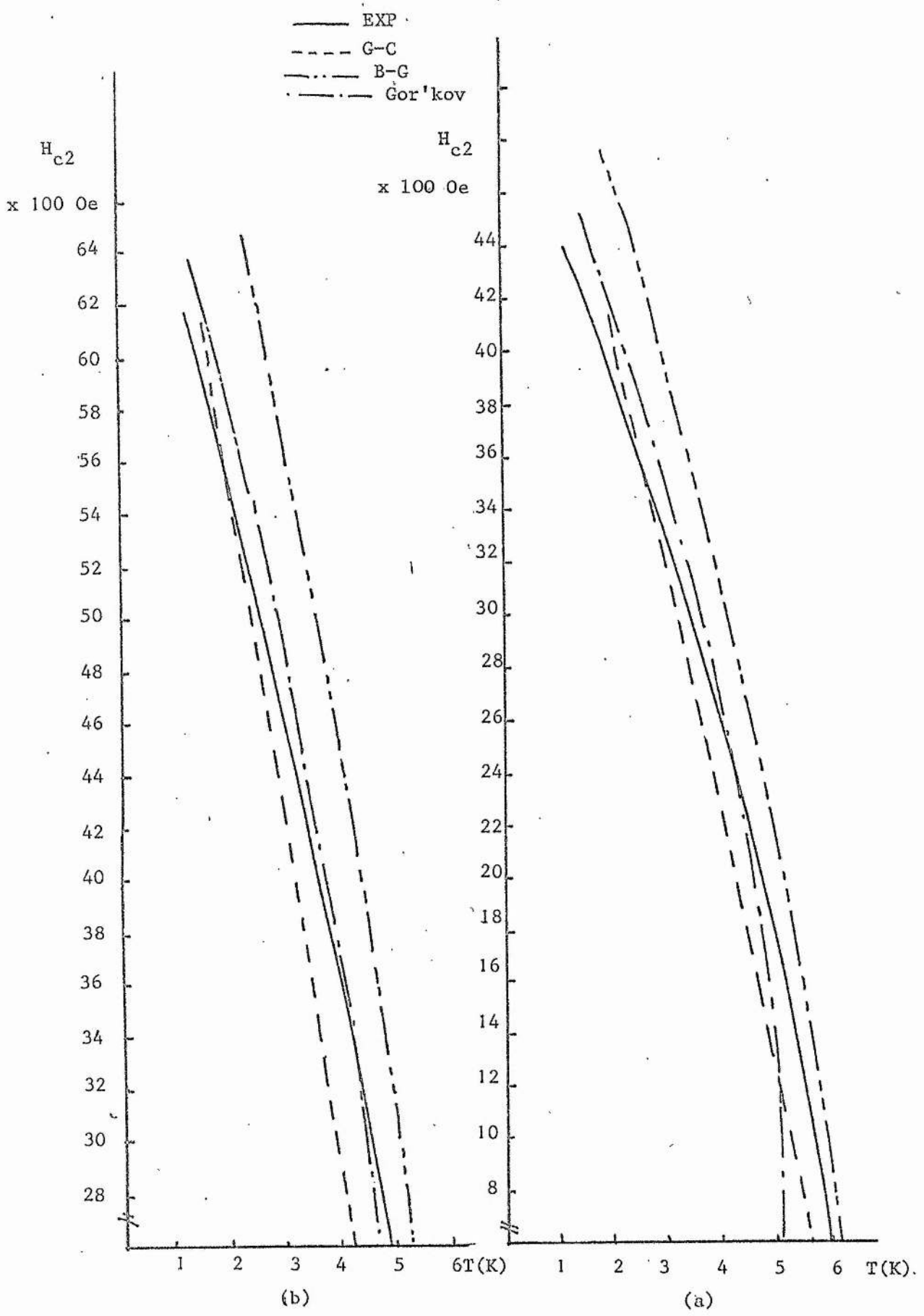

FIGURE 4.10 Theoretical and Experimental H_{c2} vs T curves for (a) $Pb_{96}In_4$, and (b) $Pb_{90}In_{10}$ specimens.

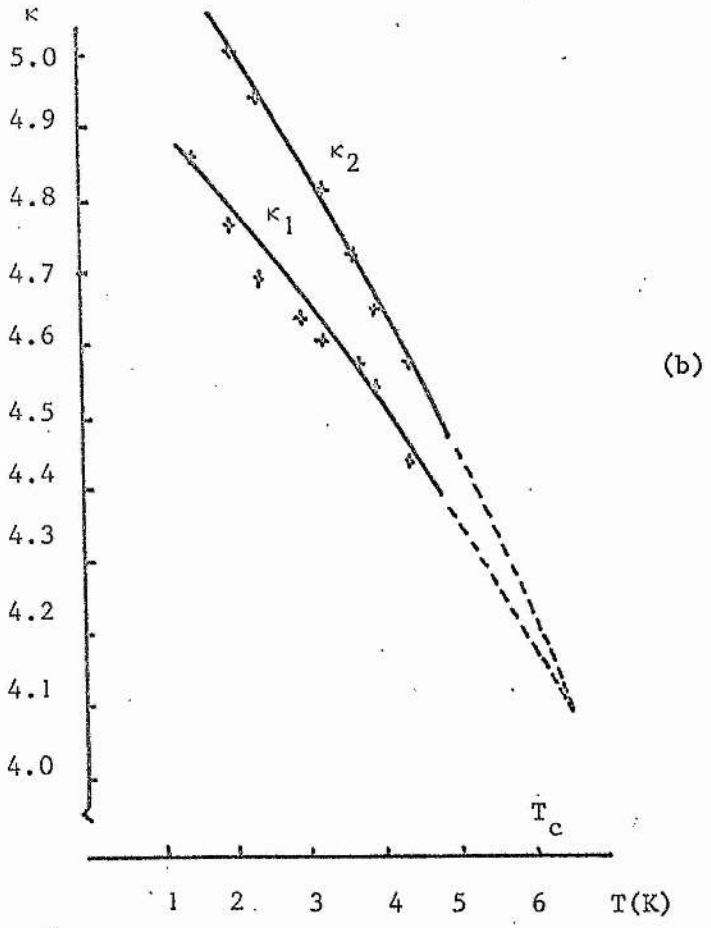

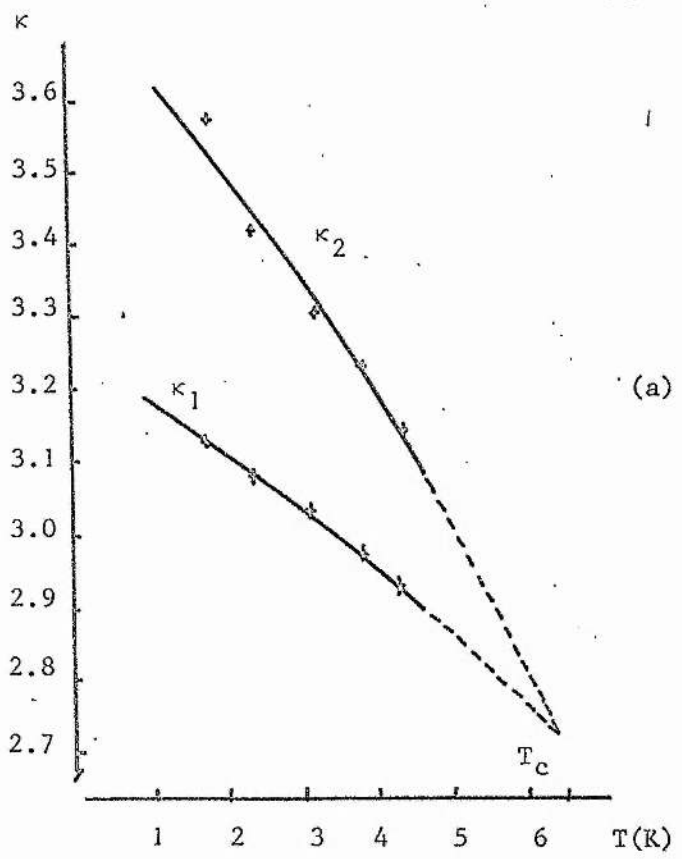

FIGURE 4.11 The values of κ_1 and κ_2 as functions of temperature for; (a) $Pb_{96}In_4$, and (b) $Pb_{90}In_{10}$.

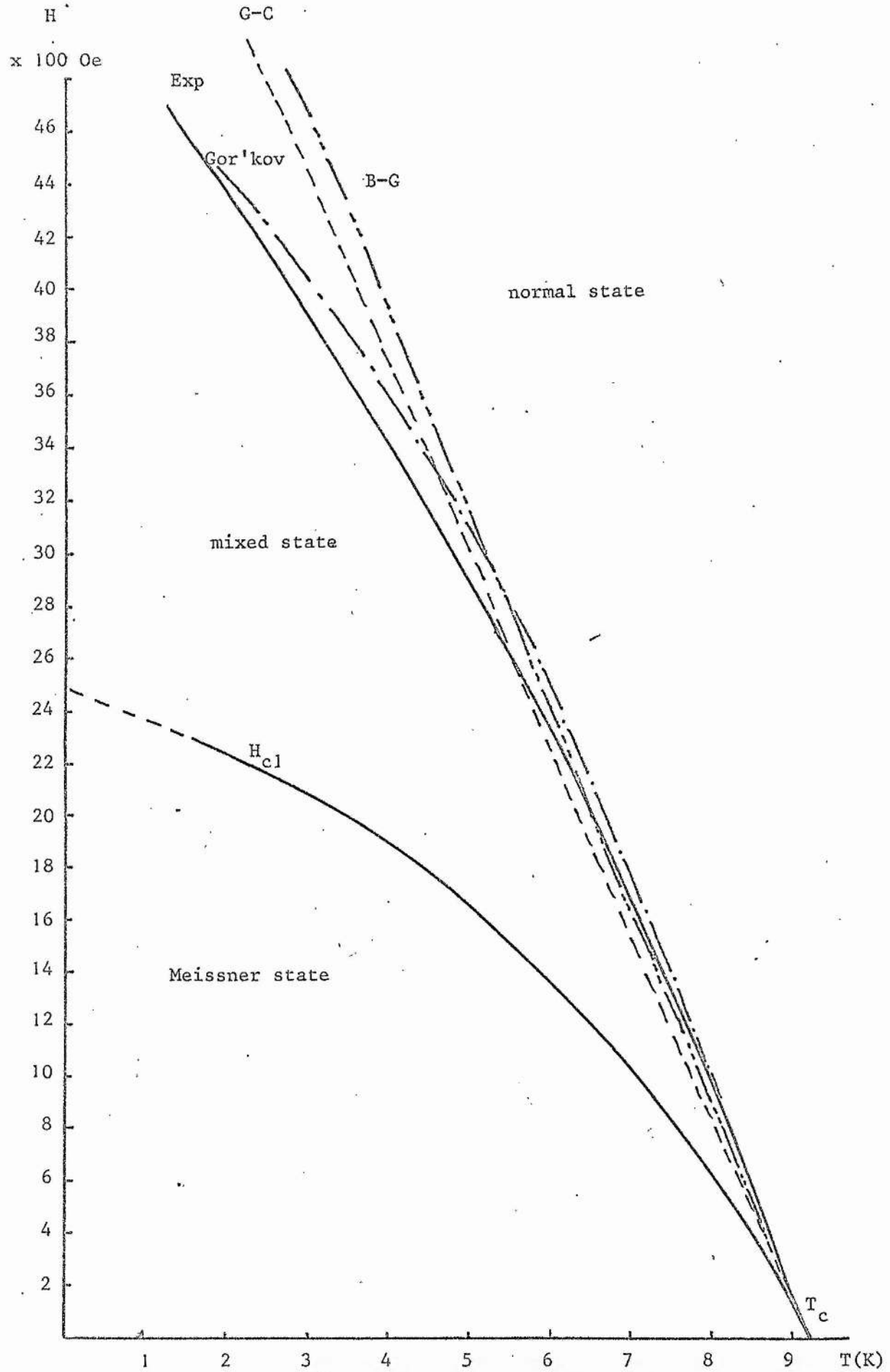

Figure 4.12 Phase diagram of Nb(rod) specimen

temperature, T_c=9.28 K , is equal to 1.29 . Some of the values of the $\kappa_1(T)$ and $\kappa_2(T)$ were calculated and are given in Table 5.2.

From the Gor'kov-Goodman equation

$$\kappa = \kappa_o + 7.53 \times 10^3 \gamma^{\frac{1}{2}} \rho_n \ , \qquad 4.2.21$$

putting in γ = 7.5 mJ mole^{-1} K^{-2} from the specific heat measurement (Chapter 5), and putting in κ_o = 0.78 from the measurement of Finnemore et al (1966), we obtain $\rho_n = 2.61 \times 10^{-8}$ Ω-cm. This value has the same order but is slightly smaller than that of the experimental results of De Sorbo (1969). The characteristic lengths κ, λ_p, $\lambda_L(o)$, ξ_o, ξ_p, and v_F were calculated via Equations (4.2.19), (4.2.19a), (4.2.20), (4.2.20a) and (4.2.20b), and are as follows

$$\kappa_1 = 1.42 \qquad \text{at } 4.22 \text{ K} ,$$

$$\lambda_p = 4.45 \times 10^{-6} \text{ cm},$$

$$\lambda_L(o) = 4.66 \times 10^{-6} \text{ cm},$$

$$\xi_p = 3.13 \times 10^{-6} \text{ cm},$$

$$\xi_o = 3.13 \times 10^{-6} \text{ cm}$$

and

$$v_F = 2.11 \times 10^7 \text{ cm/sec} .$$

By our method of defining H_{c1}, we find that it is greater than H_c for this specimen. Although we have found no report of this sort of behaviour of an irreversible type II superconductor in the literature, we believe that it is quite possible if the speciment has a large number of surface pinning sites.

(b) NbI and NbII

The magnetization curves of NbI and NbII were measured under three surface conditions, (a) after mechanical polishing, (b) after subsequent oxidation, and (c) after final chemical polishing. The values of H_{c1}^{*}, H_c, H_{c2}, $B_{R\,max}$, $H_{R\,max}$, $B_{Rmax}/H_{R\,max}$ and κ_1 of these two specimens at different temperatures and different surface conditions are given in Table 4.3. The magnetization curve at 4.22 K for NbI after chemical polishing is shown in Figure 4.13(a), while in Figure 4.13(b) we show the whole family of curves at different temperatures for the same specimen in the same condition. The purpose of (b) is to show the linear dependence of H_R on temperature. In Figure 4.14(b) we show the magnetization curves of NbII after mechanical polishing, at 4.22 K, and in Figure 4.14(a), the magnetization curves of NbII after (i) oxidation and (ii) chemical polishing, at 4.22 K. Note that the ordinate scales of (a) and (b) are different. The B vs H relation derived from the three curves of (a) and (b) are plotted in Figure 4.15.

From Table 4.3, we see that the values of H_{c2} of NbI and NbII are different from that of Nb(rod); both NbI and NbII were cut from Nb (rod), which indicates that the composition of Nb(rod) is not homogeneous. The value of H_{c2} of each specimen at a particular temperature does not change with different surface finish, only the values of H_{c1}^{*} decrease as the specimen surface becomes more smooth. Figure 4.14(b) shows a clear magnetization tail due to the surface superconductivity; this disappears after the specimen has been oxidized or chemically polished. The value of H_{c3} is about 1.6 H_{c2}, as shown in Figure 4.14(b).

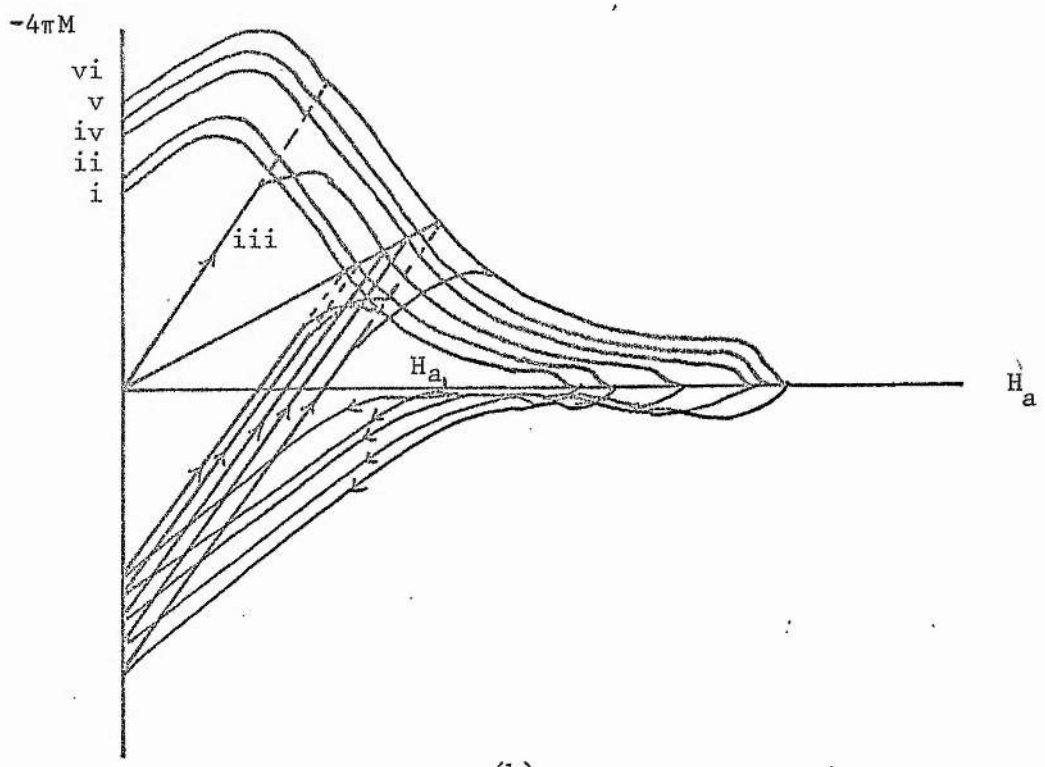

(b)

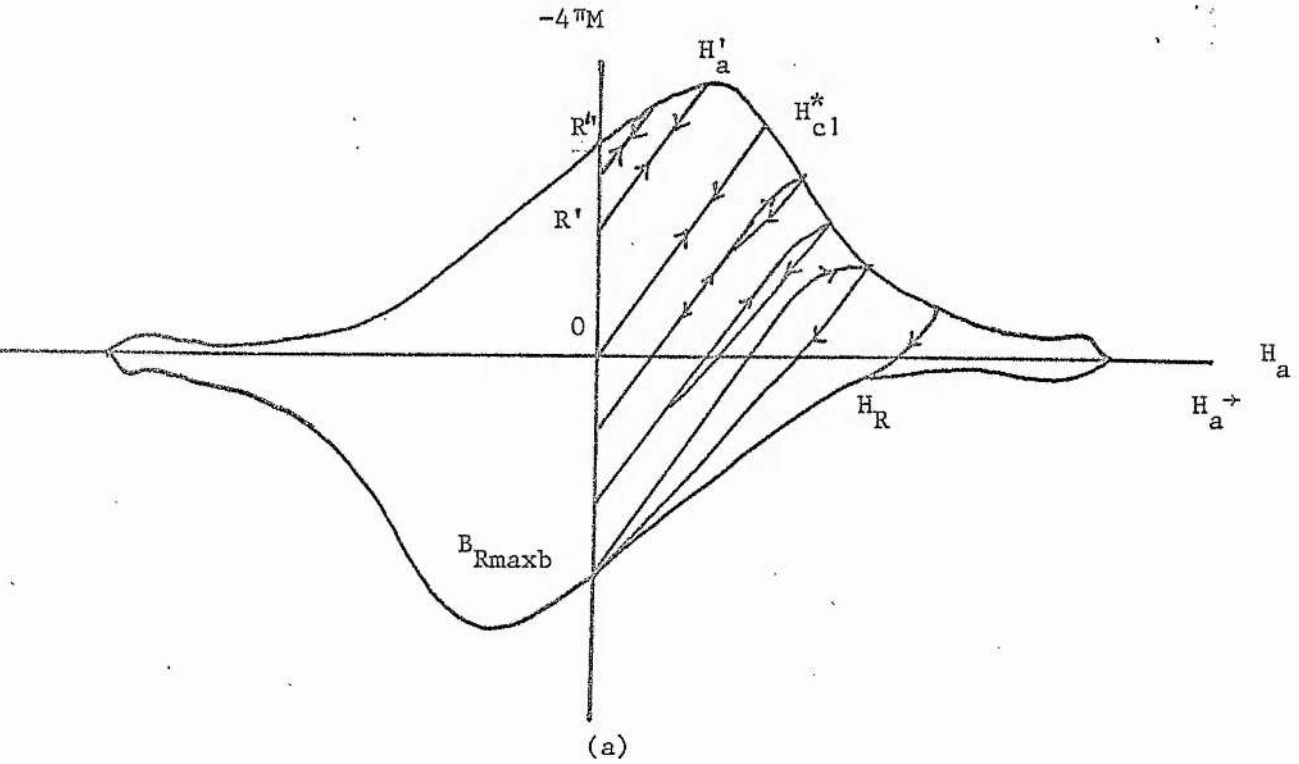

(a)

FIGURE 4.13 The magnetization curves of chemically polished NbI specimen at different temperatures; (a) 4.22 K, and (b); 4.22 K (i), 3.75 K (ii), 2.99 K (iii), 2.06 K (iv), 1.71K(v), and 1.48 K (vi).

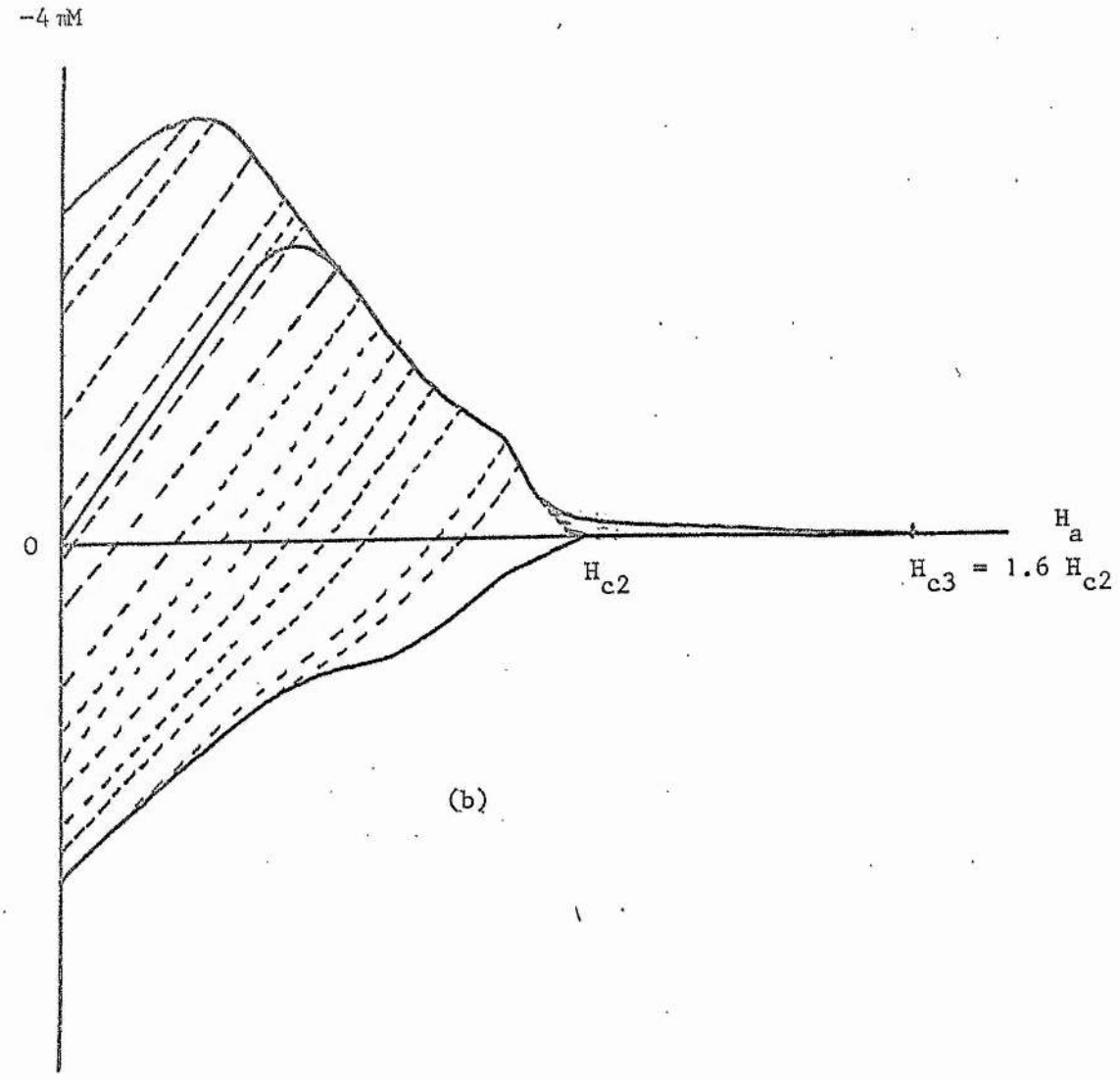

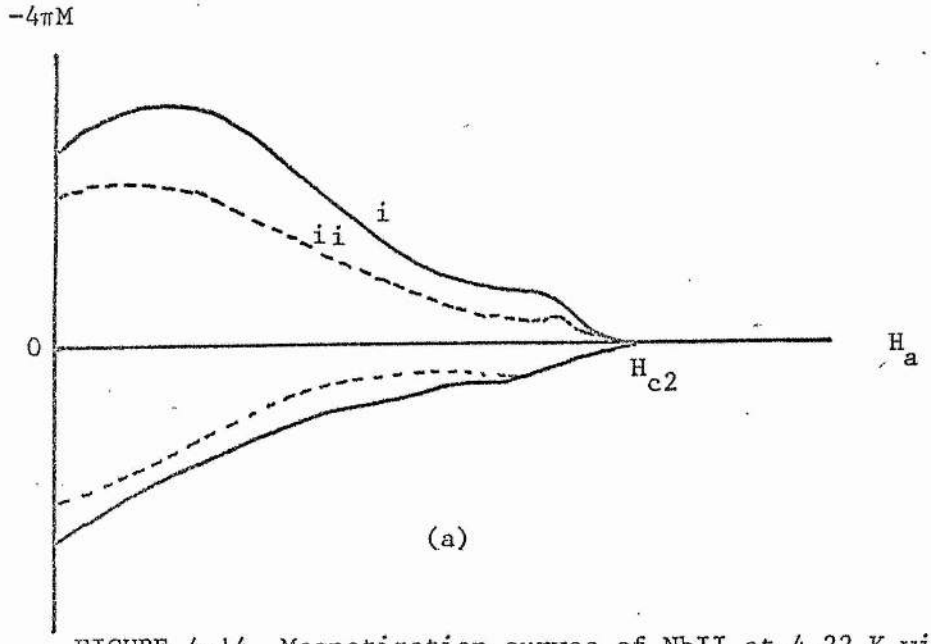

FIGURE 4.14 Magnetization curves of NbII at 4.22 K with different surface conditions; (a) (i) oxidized, (ii) chemically polished, and (b) mechanically polished.

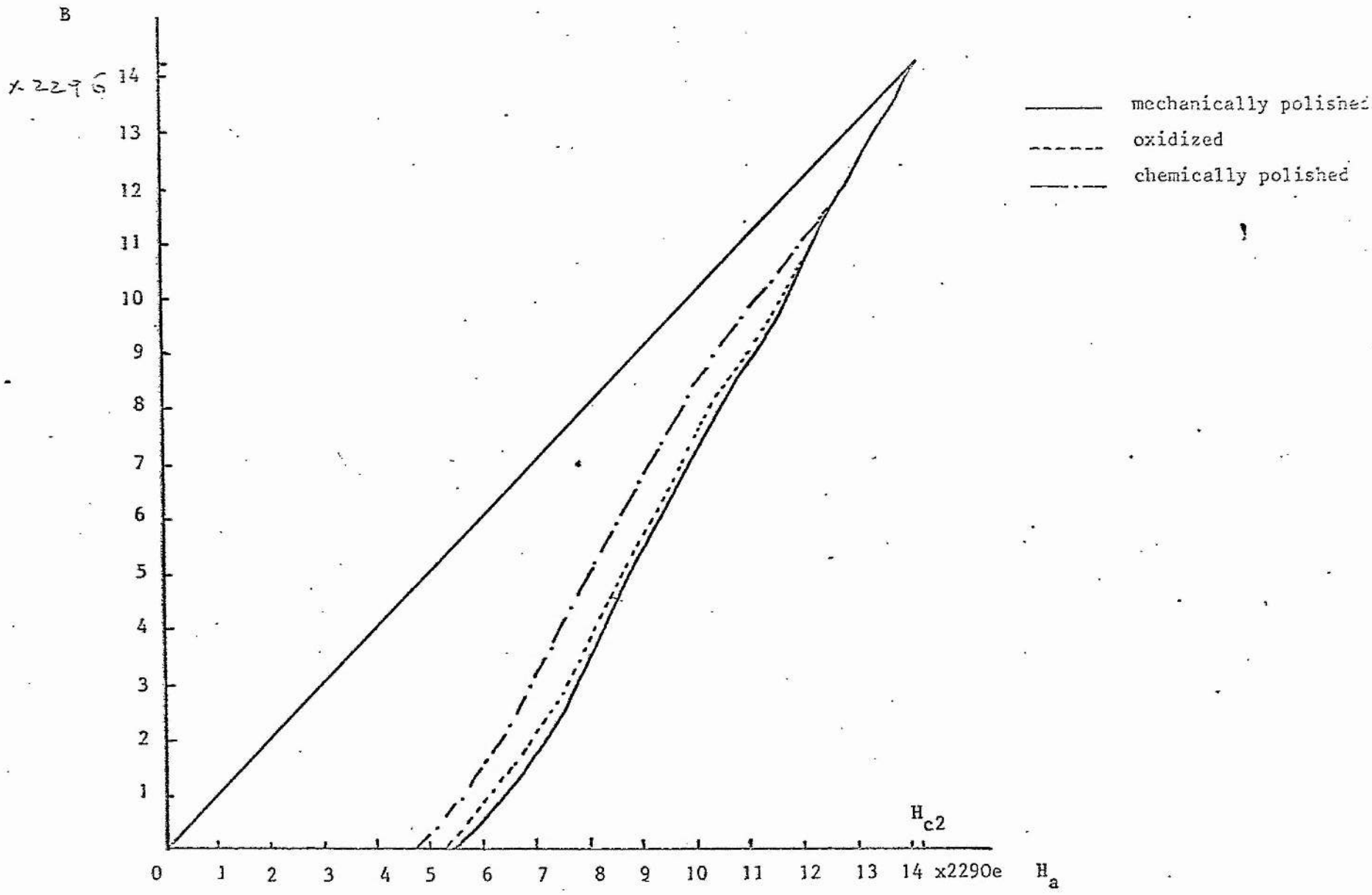

FIGURE 4.15 B vs H curves of NbII with three different surface conditions

TABLE 4.3

Specimen	T	H_{c1}^{*}	H_c	H_{c2}	κ_1	B_{Rmax}	H_{Rmax}	B_{Rmax}/H_{Rmax}	
NbI	4.22	1466	1621	3120	1.36				
mechanically polished									
NbI									
chemically polished									
	4.22	1022	1621	3120	1.36	1306	1901	0.687	
	3.75	1048	1710	3346	1.38	1425	2077	0.686	
	2.99	1161	1831	3723	1.437	1570	2282	0.688	
	2.06	1268	1943	4176	1.519	1746	2543	0.687	
	1.71	1314	1974	4305	1.542	1860	2710	0.686	
	1.48	1355	1992	4412	1.566	1900	2765	0.687	
									$\gamma = 0.7$
NbII									
mechanically polished									
	4.22	1534	1621	3256	1.42	1909	2811	0.679	
	3.27	1642	1774	3635	1.449	2102	3096	0.679	$\gamma = 0.8$
NbII									
oxidized									
	4.22	1494	1621	3256	1.42	1832	2668	0.689	
	3.05	1694	1823	3880	1.506	2286	3229	0.687	
	1.90		1958	4416	1.595	2615	3915	0.686	$\gamma = 0.8$
NbII									
chemically polished									
	4.22	1181	1621	3256	1.24	1575	2272	0.695	
	3.58	1307	1740	3501	1.423	1700	2453	0.694	
	2.46	1492	1900	4059	1.511	1920	2770	0.695	$\gamma = 0.7$
	2.07	1650	1942	4282	1.560	2001	2882	0.695	
	1.62	1797	1982	4550	1.634	2089	3012	0.695	

From Tables 4.1 and 4.3, we can see that the ratio of B_{Rmax}/H_{Rmax} is independent of temperature. The temperature dependence of B_{Rmax} and H_{Rmax} can be well represented to an accuracy of $\pm$ 2% by the following equations

$$B_{R\ max}(t) = B_{R\ max}(o)\ \ (1 - at), \qquad 4.2.31$$

and

$$H_{R\ max}(t) = H_{R\ max}(o)\ \ (1 - at), \qquad 4.2.31a$$

where $t = T/T_c$ is the reduced temperature, and a is a constant which varies from specimen to specimen. We have

$$B_{R\ max}(t) = 2240\ (1 - 0.917\ t)$$

and

$$H_{R\ max}(t) = 3260\ (1 - 0.917\ t),$$ for Nb I when chemically polished,

$$B_{R\ max}(t) = 3209\ (1 - 0.89\ t)$$

and

$$H_{R\ max}(t) = 4925\ (1 - 0.89\ t),$$ for Nb II mechanically polished,

$$B_{R\ max}(t) = 3228\ (1 - 0.951\ t)$$

and

$$H_{R\ max}(t) = 4613\ (1 - 0.951\ t)$$ for Nb II oxidized,

and

$$B_{R\ max}(t) = 2406\ (1 - 0.96\ t)$$

$$H_{R\ max}(t) = 3369\ (1 - 0.96\ t)$$ for Nb II chemically polished. The constant a is equal to 0.714, 0.599 and 0.804 for $Pb_{96}In_4$, $Pb_{93}In_7$, and $Pb_{90}In_{10}$, respectively.

CHAPTER V

SPECIFIC HEAT, ENTROPY AND MAGNETO-CALORIC EFFECT OF A NIOBIUM SPECIMEN

CHAPTER V Specific heat, Entropy and Magneto-caloric effect of a Niobium specimen

5.1 Introduction

In this chapter we have investigated the specific heat, the magneto-caloric effect and other thermal properties of the cylindrical Nb(rod) specimen. Since the demagnetization factor of the specimen is small, about 0.009, we will ignore the factor in this particular specimen.

In principle, measurement of the specific heats of different states of a type II superconductor can be used in the following kinds of analysis:

(a) From the behaviour of the specific heat at the transition from the Meissner state to the mixed state, and from the mixed state to the normal state, we can verify the order of the phase transition.

(b) We can determine the energy gap via the specific heat relation given in the BCS theory.

(c) From the specific heat jump at the transition from the superconducting to the normal state in zero field, we can estimate the thermodynamic critical field H_c of a type II superconductor, free from hysteresis.

(d) From the specific heat we can calculate the free energy of a particular state.

Therefore, the specific heat measurements provide a way to check theoretical calculations, e.g., those theories presented in the previous chapters, in which the free energy plays a central role.

The magnetization curve of a type II superconductor in the mixed state shows that the flux density in the specimen depends on the value of the

external field. From Equation 1.6.3, we can see that the isothermal change of entropy with field will result in change of temperature with adiabatic change in field. This effect was predicted and observed by Mendelssohn and Moore (1935), and is known as the magneto-caloric effect.

By measuring the temperature variations which accompany flux density changes during adiabatic magnetization, we can study the entropy change and the dissipation in the specimen.

Many experimental investigations of the specific heat of niobium in different states have been carried out (Ferreira et al 1969). The specific heat of the normal state can be expressed by

$$C_n = \gamma T + \text{const } (T/\theta_D)^3. \qquad 5.1.1$$

In the superconducting state, the specific heat in the low temperature limit follows the exponential relation $C_{es} \propto e^{-bT_c/T}$, where b is a constant, and it follows the T^3 relation quite well in the higher temperature region. In the case of the specific heat of Nb in the mixed state, Rosenblum and Cardona (1964) have suggested adding a linear term to the T^3 specific heat of the pure super-conducting state, corresponding to the increasing normal fraction in the specimen. However the variation of the specific heat with temperature in the mixed state is still not quite clear because the nature of the free energy is not exactly known.

5.2 Theoretical consideration of the specific heat, entropy and the magneto-caloric effect

5.2.1 The specific heat and the entropy of the superconducing state

The specific heat of a superconductor can be written in the general form

$$C_s = C_{es} + \beta T^3. \qquad 1.6.7$$

The superconducting electronic specific heat C_{es} at low temperatures ($T < T_c/10$) can be well represented by an energy-gap type of expression

$$C_{es}/\gamma T_c = a(H) \exp\left[-b(H)T_c(H)/T\right], \qquad 5.2.1$$

where a and b are field-dependent constants. From Equation 1.6.5

$$C_s - C_n = \frac{VT}{4\pi}\left[\left(\frac{\partial H_c}{\partial T}\right)^2 + H_c \frac{\partial^2 H_c}{\partial T^2}\right],$$

and

$$H_c = H_o\left(1 - \frac{T^2}{T_c^2}\right),$$

we derive, letting V = 1

$$C_n - C_s = \frac{H_o^2}{2\pi T_c}\left[\frac{T}{T_c} - 3\left(\frac{T}{T_c}\right)^3\right]. \qquad 5.2.2a$$

The first term of Equation 5.2.2a can be identified with the specific heat in the normal state, with

$$\gamma = \frac{H_o^2}{2\pi T_c^2}. \qquad 5.2.2$$

The second term must represent the superconducting electron specific heat;

$$C_{es} = \frac{H_o^2}{2\pi T_c}\left[3\left(\frac{T}{T_c}\right)^3\right]. \qquad 5.2.3a$$

As the lattice specific heat is proportional to T^3 and remains unchanged for the normal and superconducting state, we have,

$$C_s \propto T^3, \qquad 5.2.3.$$

at the higher temperatures and in zero field.

The entropy of the superconducting state is given by

$$S_s(H,T) = S_n(T_c) - \int_T^{T_c} \frac{C_s(H,T)}{T} \, dT, \qquad 5.2.4$$

while the free energy of the superconducting state at constant field and constant pressure is given by

$$G_s(H,T) = G_m(T_c) + \int_T^{T_c} S_s(H,T) \, dT \, . \qquad 5.2.5$$

5.2.2 The transition at H_{c1} and H_{c2}

Consider the phase transition line $H = H_{tr}(T)$ in the H,T plane, separating the thermodynamic phases which we label a and b. From the 'magnetic Gibbs function' Equation 1.6.2, we have

$$dG_m = -SdT - MdH, \qquad 5.2.6$$

at constant pressure. For a transition at constant T and constant field $H = H_{tr}(T)$, we derive

$$-\frac{dH_{tr}}{dT} = \frac{S_b - S_a}{M_b - M_a} \qquad 5.2.7$$

Since

$$S_b - S_a = {}^{L}/_{T}, \qquad 5.2.8$$

we have

$$L = -T\,(M_b - M_a)\,\frac{dH_{tr}}{dT} \, . \qquad 5.2.9$$

In the case of transition from the Meissner state to the mixed state, if it is a first order transition then we have a discontinuity ΔM in the magnetization curve as shown in Figure 5.1a, and the latent heat is equal to

$$L = -T\Delta M\,\frac{dH_{c1}}{dT} \qquad 5.2.10$$

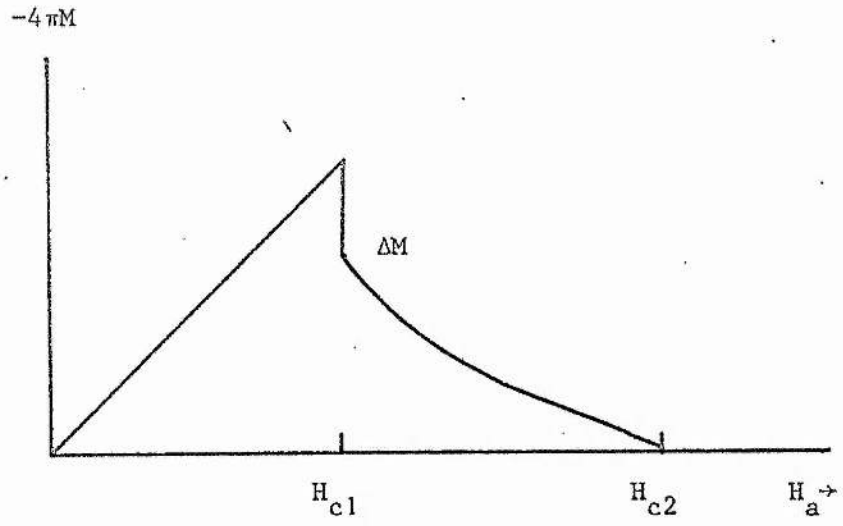

FIGURE 5.1a A schematic magnetization curve of a type II superconductor with a first order phase transition at H_{c1}.

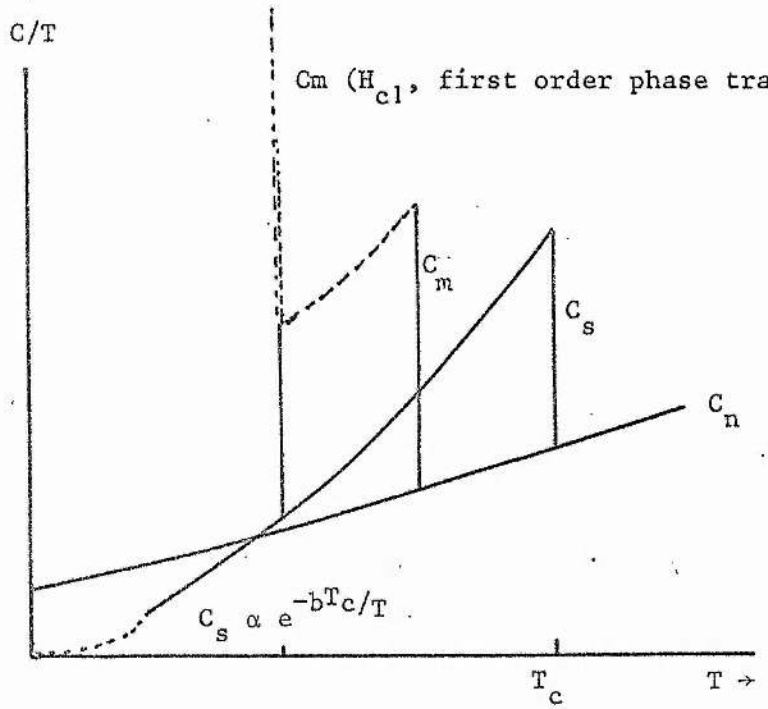

FIGURE 5.1b A schematic diagram showing possible forms of C/T vs T of a type II superconductor.

Since

$$\frac{dG_m}{dT} \neq \frac{dG_s}{dT} , \qquad 5.2.11$$

the entropy changes discontinuously by ΔS, where

$$\Delta S = S_m - S_s = -\Delta B \frac{dH_{c1}}{dT} . \qquad 5.2.12$$

In a second order phase transition without latent heat, then the two phases have the same entropy $S_a = S_b$, and the magnetization curve is continuous at the transition point. However, the specific heat does change discontinuously, and this discontinuity has been related to the magnetization curve by Goodman (1962) through a purely thermodynamic analysis

$$C_a - C_b = \frac{T}{4\pi} \left(\frac{dH_{tr}}{dT}\right)^2 \left\{\left(\frac{dB_a}{dH}\right)_T - \left(\frac{dB_b}{dH}\right)_T\right\} . \qquad 5.2.13$$

We can apply this equation to the second order phase transition from the mixed state to the normal state and from the Meissner state to the mixed state, if we know the values of $(dB/dH)_T$.

In the case of the second order phase transition from the mixed state to the normal state at $H_{tr}(T) = H_{c2}(T)$, we have

$$C_m (H_{c2},T) = C_n(H_{c2},T) + \frac{T}{4\pi} \left(\frac{dH_{c2}}{dT}\right)^2 [(2\kappa_2^2 - 1)\ 1.16]^{-1} \qquad 5.2.14$$

At low temperatures, the jump in the specific heat is therefore proportional to T^3, if $dH_{c2}/dT \propto T$ and if $\kappa_2 > 1/\sqrt{2}$.

5.2.3 In the mixed state

In principle, the specific heat of a specimen in the mixed state can be obtained from the mixed state free energy. Unfortunately, as we have shown in chapter IV, different approximations have to be made for the derivation of the free energy due to the fact that the interaction energy

between the vortices is not quite clear. Therefore, instead of doing it in this way, we will use a phenomenological approach to calculate the mixed state specific heat C_m.

We will assume that the entropy of those parts occupied by the flux lines are the same as that of the normal state, and that the remainder has the same entropy as has the pure superconducting state. We have, following van Vijfeijken (1968),

$$S_m(H,T) = (1 - A)\, S_s(T) + A\, S_n(T) \qquad 5.2.15$$

per unit volume, where A is the volume fraction occupied by the flux lines. We now replace the volume fraction A by the easily measurable quantity B/H_{c2}, and rewrite equation 5.2.15 as

$$S_m(H,T) = \left(1 - \frac{B(H,T)}{H_{c2}(T)}\right) S_s(T) + \frac{B(H,T)}{H_{c2}(T)}\, S_n(T). \qquad 5.2.16$$

We can now derive C_m from Equation 5.2.16,

$$C_m(H,T) = \left(1 - \frac{B(H,T)}{H_{c2}(T)}\right) T \frac{dS_s}{dT} + \frac{B(H,T)}{H_{c2}(T)} T \frac{dS_n}{dT} +$$

$$+ (S_n - S_s)\, T \left(\frac{\partial (B/H_{c2})}{\partial T}\right)_H . \qquad 5.2.17$$

With equation 1.6.3, and $S_n = \gamma T + \frac{1}{3}\beta T^3$, we have

$$C_m(H,T) = \gamma T + \beta T^3 + \frac{T}{4\pi}\left(\frac{dH_c}{dT}\right)^2 + H_c\left(\frac{d^2H_c}{dT^2}\right)\left(1 - \frac{B(H,T)}{H_c(T)}\right) +$$

$$+ \left(-\frac{T}{4\pi} H_c \frac{dH_c}{dT}\right)\left(\frac{\partial}{\partial T}\frac{B(H,T)}{H_{c2}(T)}\right)_H . \qquad 5.2.18$$

Substituting Equation 1.1 and its second derivative

$$\frac{d^2H_c}{dT^2} = -\frac{2H_c(0)}{T_c^2}, \qquad 5.2.19$$

in Equation 5.2.18, we have

$$C_m(H,T) = \gamma T + \beta T^3 + \frac{H^2_c(0)}{2\pi T_c^2}\left(\frac{3T^3}{T_c^2} - T\right)\left(1 - \frac{B(H,T)}{H_{c2}(T)}\right) +$$

$$+ \frac{H^2_c(0)}{2\pi T_c^2}\left(T^2 - \frac{T^4}{T_c^2}\right)\left(\frac{\partial (B(H,T)/H_{c2}(T))}{\partial T}\right)_H, \qquad 5.2.20$$

in which the parameters are all experimentally measurable.

A schematic diagram showing all the possible forms of C/T vs T is given in Figure 5.1b.

5.2.4 The magneto-caloric effects:

The reversible magnetization of a superconductor under adiabatic conditions implies an isentropic process; this results in

$$T\left(\frac{\partial S}{\partial H}\right)_T = -C\left(\frac{\partial T}{\partial H}\right)_S, \qquad 5.2.21$$

where $\left(\frac{\partial S}{\partial H}\right)_T$ is positive. Since the entropy of the superconducting state in the absence of a magnetic field is smaller than that of the normal state, as shown in Figure 5.2, we can produce cooling by adiabatic magnetization as along curve (a).

If the process is not completely reversible there will be an entropy production associated with this irreversibility, $\Delta_{ir}S$. In this process,

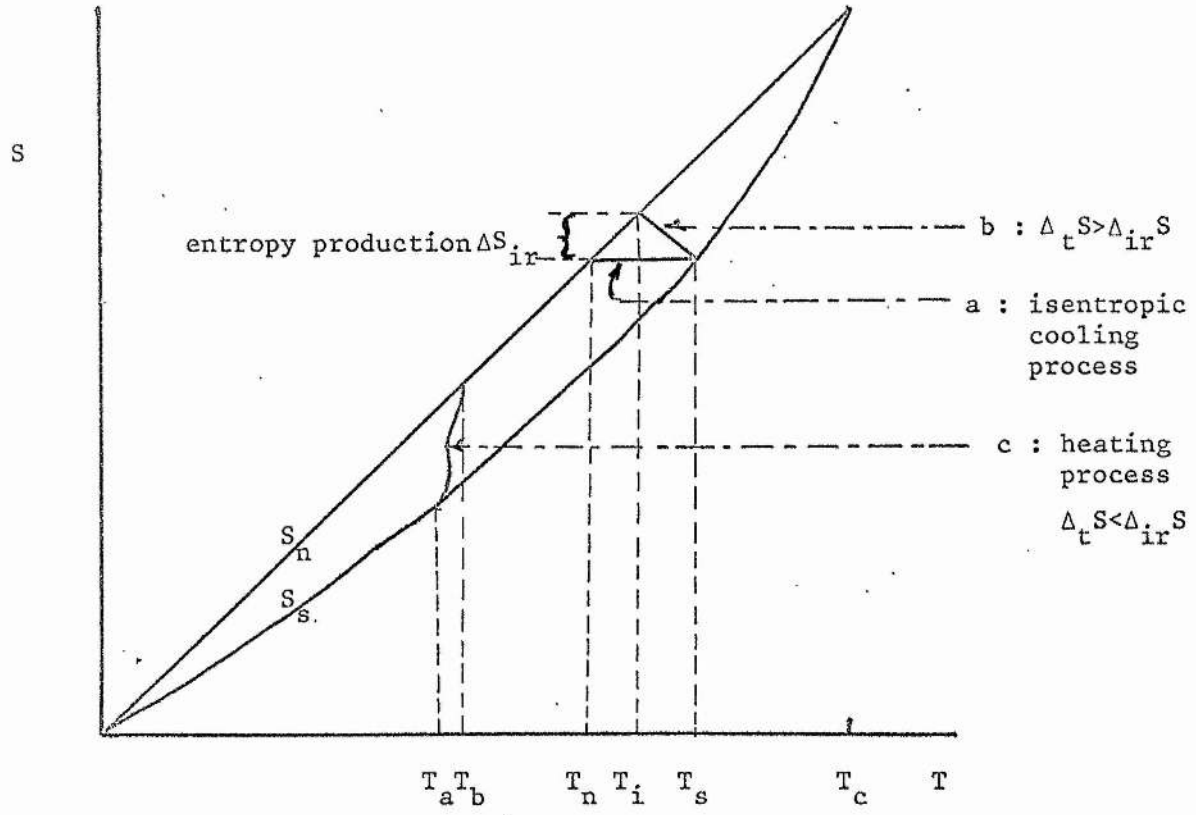

FIGURE 5.2 A schematic diagram to demonstrate the heating and the cooling processes.

If $\Delta_t S$ is the reversible isothermal change of entropy due to magnetization , we can see that this magneto-caloric effect results in either a cooling or a heating depending on the relative magnitudes of $\Delta_t S$ and $\Delta_{ir} S$. Schematic curves (b) and (c) in Figure 5.2 demonstrate the cooling and the heating processes for $\Delta_t S > \Delta_{ir} S$ and $\Delta_t S < \Delta_{ir} S$, respectively.

Entropy production associated with the hysteresis properties will be investigated in Chapter 7.

5.3 Experimental results

5.3.1 Specific Heat, Entropy and the Gibbs Free Energy

The specific heat measurements have been made by applying the magnetic field after cooling the specimen to the desired temperature; then supplying heat to the specimen and from the increase of temperature and the amount of heat supplied determining the specific heat.

Figure 5.3 shows some of the actual graphs, the signals of the pick-up coil voltage, the temperature variations of the specimen, and the heat pulses. From the pick-up signals, we can determine the magnetic state of the specimen and so calculate the magnetic induction inside the specimen.

Figure 5.4 shows the experimentally measured specific heat of the specimen in different states, plotted as C/T vs T.

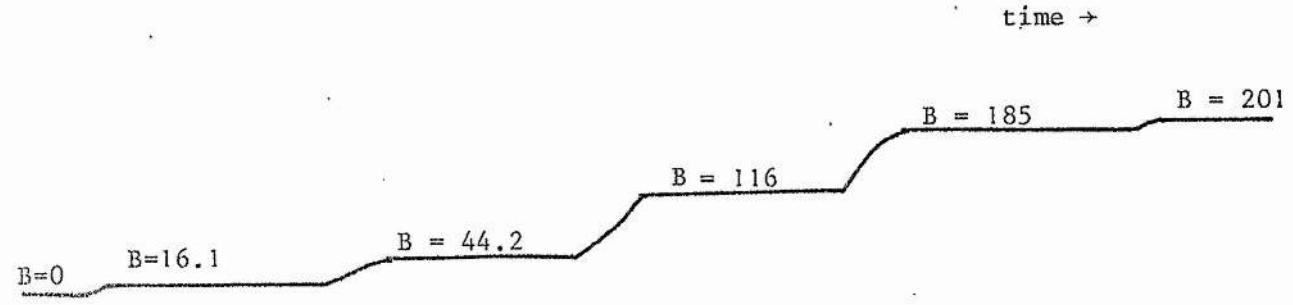

pick-up coil signal

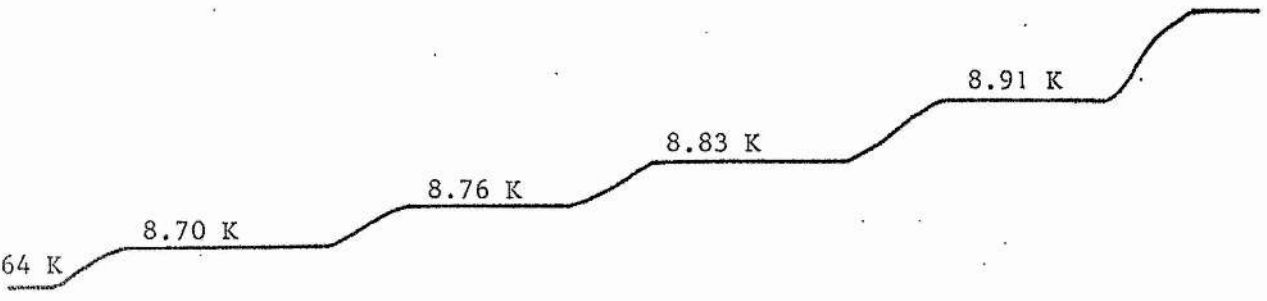

Temperature variation

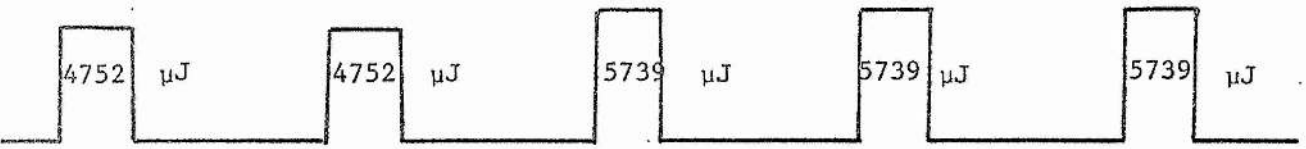

Heat pulses

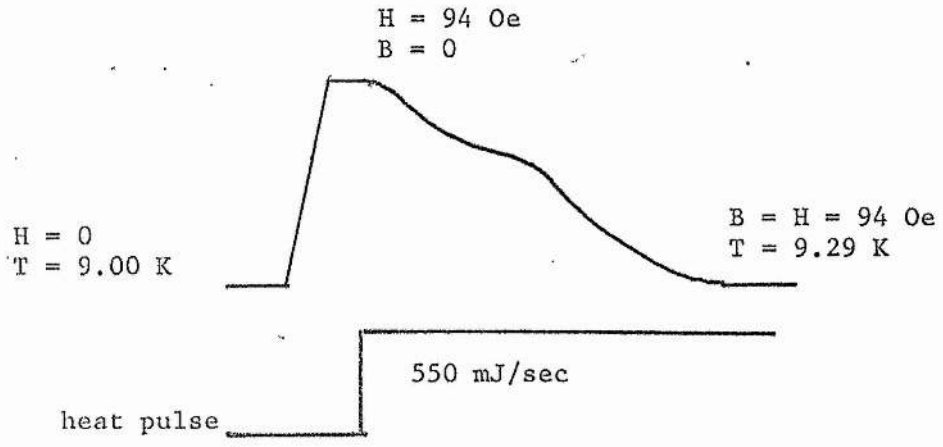

FIGURE 5.3 Experimental recorded signals during the specific heat measurements.

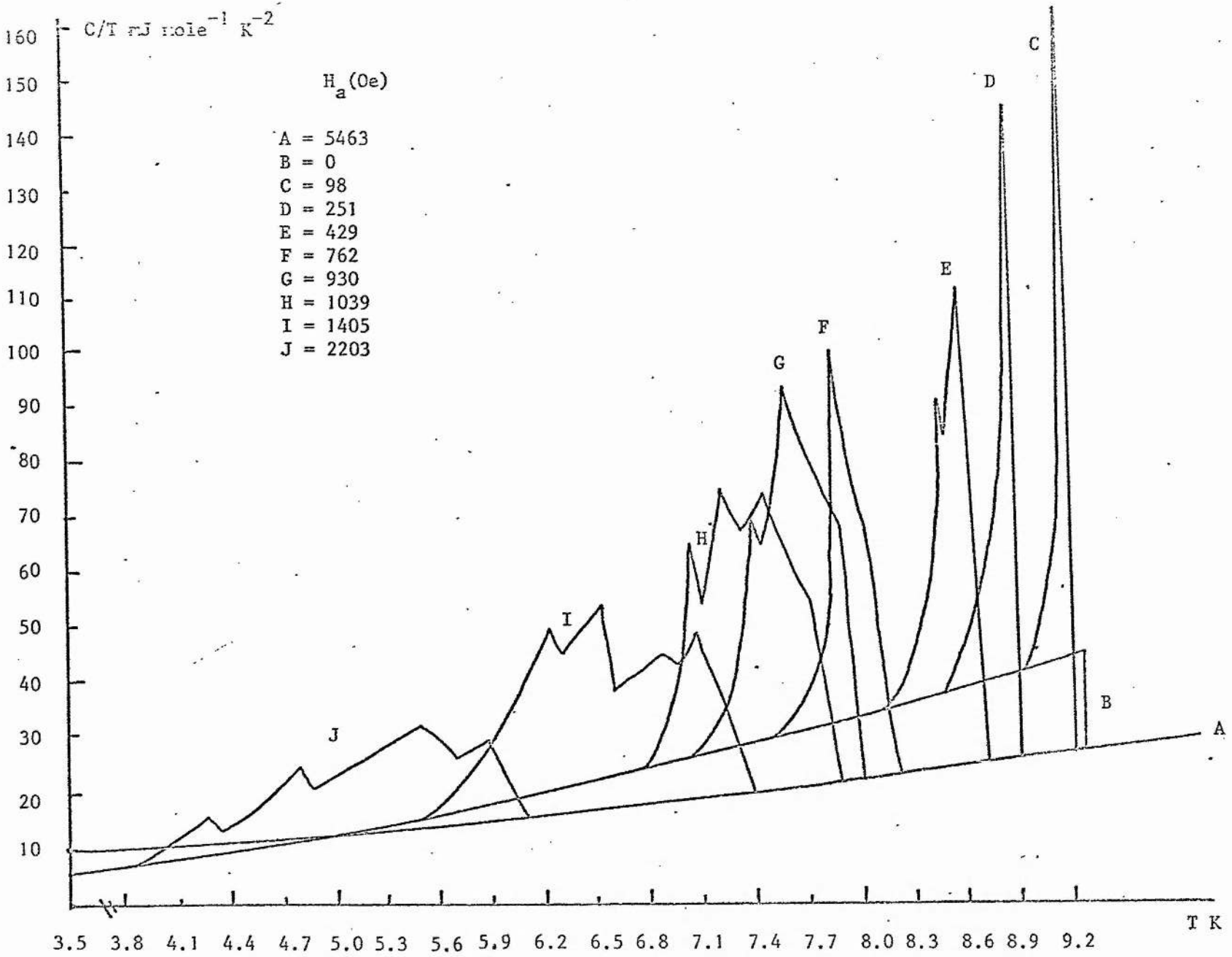

FIGURE 5.4 Experimental results of the specific heat measurements at constant fields, plotted as C/T vs T for Nb (rod).

The specific heat of the normal state C_n was measured in a field H_a = 5463 Oe. The result can be represented (Ferreira da Silva et al 1966) by

$$C_n = \gamma T + 1944 \times 10^3 (T/\Theta_D)^3,$$

with the electronic specific heat coefficient $\gamma = 7.85 \pm 0.05$ mJ mole^{-1}K^{-2} (which is very close to the value 7.72 of Equation 5.2.2) and with the Debye temperature $\Theta_D = 209 \pm 1$ K. The molar volume of Nb is 10.8 cm^3.

The specific heat of the superconducting state measured in zero field, in the temperature range from 3.5 K to 7.5 K, can be fitted to Equation 5.2.3 with $C_s = \beta_1 T^3$ mJ mole^{-1} K^{-4}, where $\beta_1 = 0.50 \pm 0.02$.

At the transition from the superconducting state to the normal state, the specific heat drops by $\Delta C = C_s - C_n = 157.76$ mJ mole^{-1}K^{-1} at T_c=9.28 K. We have used this value to calculate the thermodynamic critical field H_c of the specimen, through the Rutger's relation Equation 1.6.5 and $H_c(0)$ = 2044 Oe. The slope, $(dH_c/dT)_{T_c}$, at the transition point is equal to -445 Oe K^{-1}. The ratio $\gamma T_c^2/H_c^2$ (0) is equal to 0.151 which is very close to 0.159, as predicted by the Gorter-Casimir two-fluid model.

The values of the specific heat in the mixed state differ from each other quite irregularly in different fields at different temperatures, for example, measurements at fields 98 Oe, 251 Oe, 429 Oe, 762 Oe, 930 Oe, 1037 Oe, 1405 Oe and 2230 Oe are plotted as C_m/T vs T as shown in Figure 5.4.

The specific heats of the specimen at the above fields calculated from the variation of the magnetic induction in the specimen via Equation 5.2.20 are shown in Figure 5.5. Two sets of data, at 762 Oe and 1405 Oe, of the magnetic induction variations and the measured and calculated specific heats are given in Table 5.1.

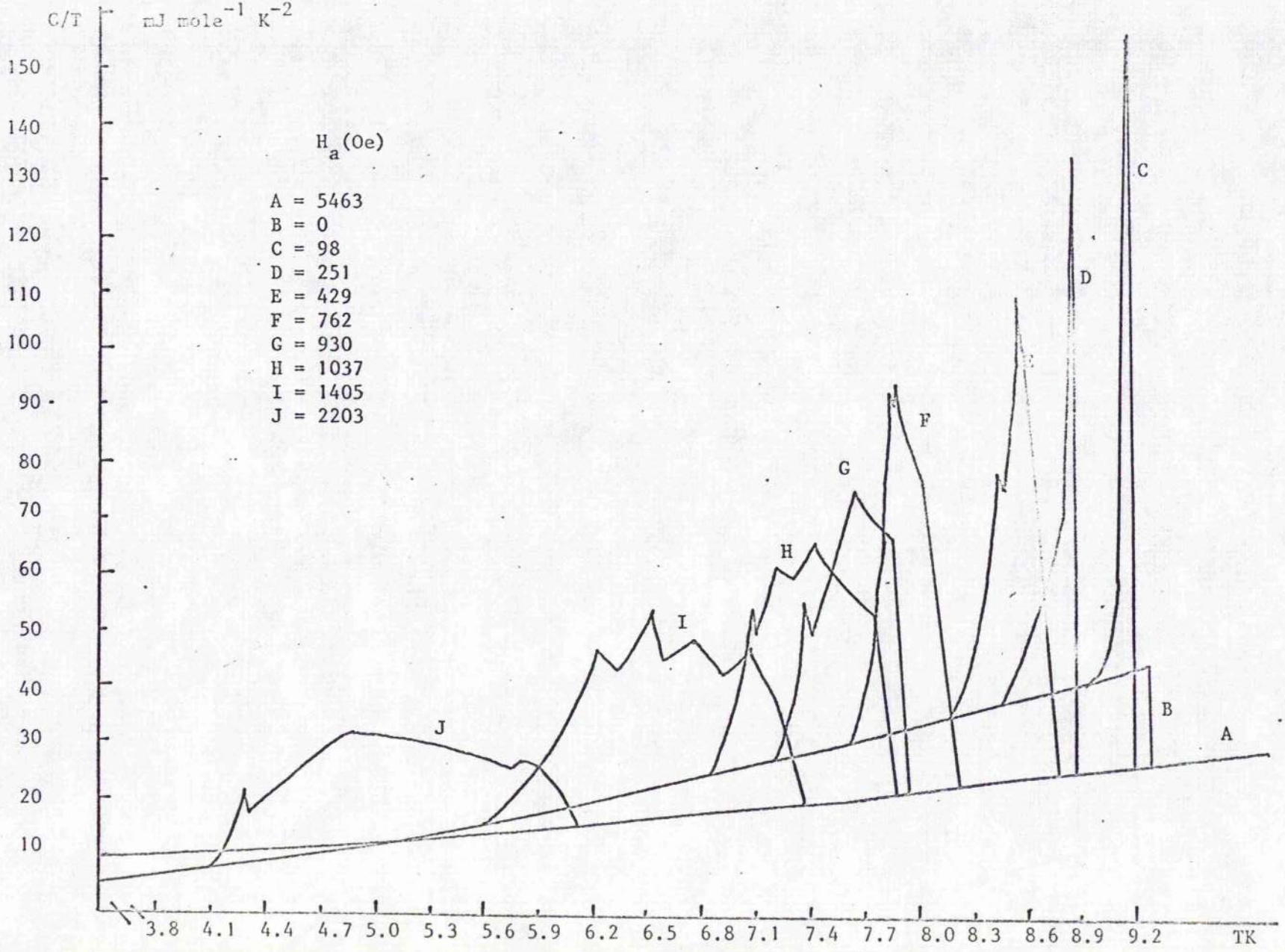

FIGURE 5.5 Specific heat at constant field calculated from the magnetic induction measurement, plotted as C/T vs T for Nb (rod)

TABLE 5.1

Field	Magnetic Induction	C_m/T (mea.)	Temp	C_m/T(calc)
762 Oe	79	58.23	7.805	62.48
	215	99.93	7.858	94.74
	373.2	79.84	7.908	95.39
	509.8	72.67	7.965	79.80
	646.4	69.50	8.03	77.76
	754	43.42	8.12	61.82
	762	24.5	8.253	-
1405 Oe	9	22.79	5.755	20.66
	27	23.57	5.808	21.8
	55.8	27.20	5.87	23.86
	105.3	29.94	5.949	27.08
	177.4	33.48	6.028	32.90
	258.4	40.18	6.103	35.96
	339.4	42.55	6.175	37.96
	443	49.13	6.24	46.96
	564	45.60	6.31	45.05
	683	48.06	6.393	45.91
	783	47.43	6.478	44.5
	913	53.9	6.553	54.5
	1016	38.08	6.63	45.6
	1084	42.34	6.803	48.90
	1165	44.64	6.885	44.96
	1233	41.73	6.978	43.5
	1319	46.05	7.068	47.85
	1376	30.78	7.175	40.78
	1395	22.44	7.31	30.2
	1405	20.5	7.395	-

Figure 5.6 shows the flux density and the upper critical field H_{c2} vs temperature of the specimen, from which the transition temperatures are determined from the specific heat curves.

The entropy of the normal state is found from

$$S_n = \int_0^T (C_n(T)/T)\, dT$$

$$= \gamma T + \frac{1}{3}\beta T^3 = 7.85T + \frac{1}{3}\,\frac{1944 \times 10^3}{209^3}\, T^3 \quad (\text{mJ mole}^{-1}\text{K}^{-1}).$$

The entropy of the superconducting state is found from

$$S_s(H,T) = S_n(T_c) - \int_T^{T_c} (C_s(H,T)/T)\, dT \qquad 5.2.4$$

The last term of Equation 5.2.4 is calculated by numerical integration of the specific heat curve in Figure 5.4.

The entropies of the mixed state in different fields have been derived in two ways:

(a) Using

$$S_m(H,T) = S_n(T_c) - \int_T^{T_c} (C_m(H,T)/T)\, dT \qquad 5.3.1$$

and calculating the last term by numerical integration of the specific heat curves of Figure 5.4. The results are plotted with the solid lines in Figure 5.7.

(b) Using

$$S_m(H,T) = \left(1 - \frac{B(H,T)}{H_{c2}(H,T)}\right) S_s(T) + \frac{B(H,T)}{H_{c2}(H,T)}\, S_n(T), \qquad 5.2.16$$

the results are plotted as dotted lines in Figure 5.7.

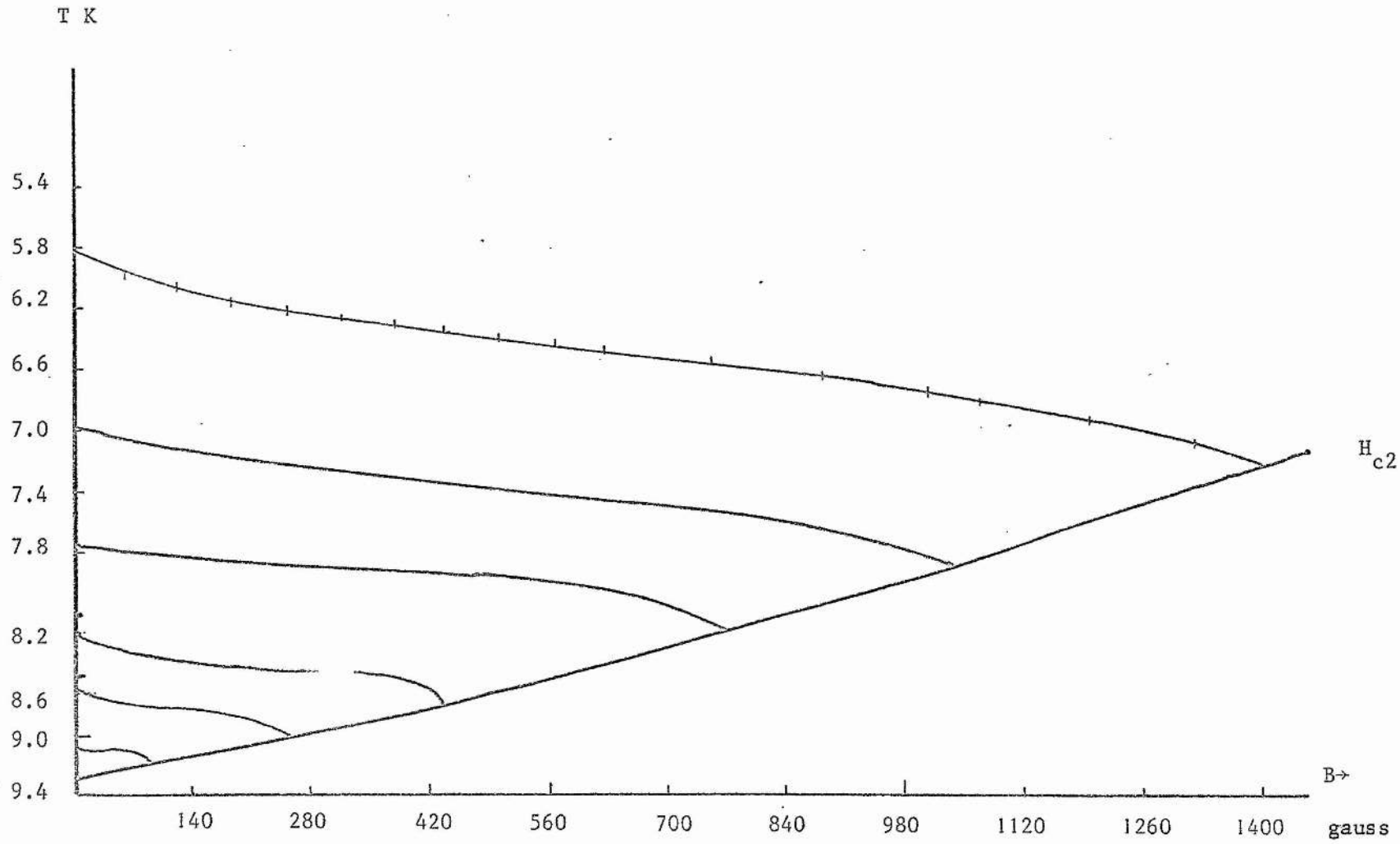

FIGURE 5.6 Flux density and the upper critical field H_{c2} vs T of Nb (rod)

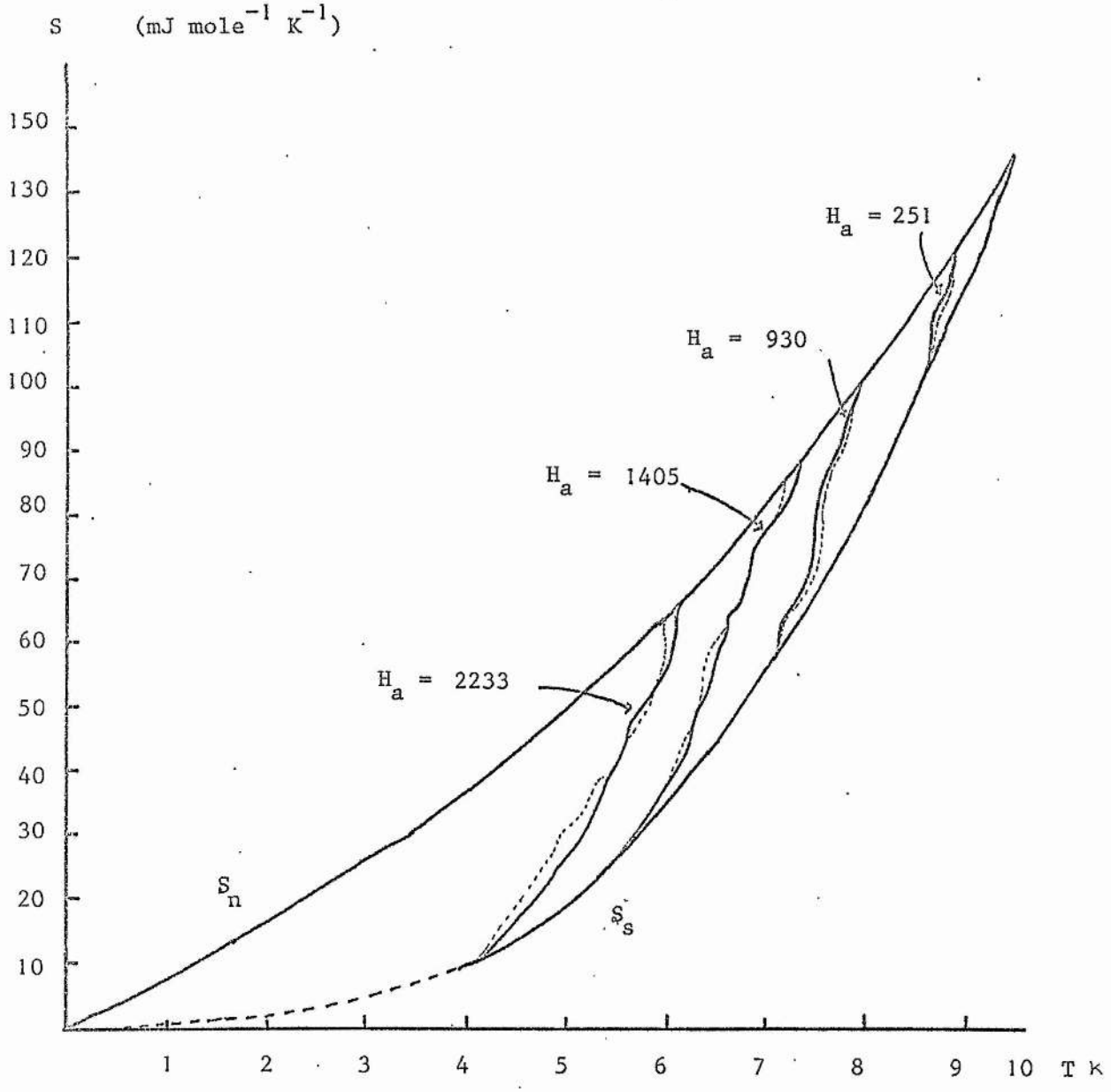

FIGURE 5.7 The entropy of the Nb rod specimen in different applied fields.

The Gibbs free energy of the specimen can be calculated by

$$-G_n = \int_0^T S_n(T)\, dT = \tfrac{1}{2}\gamma T^2 + \frac{\beta T^4}{12} \quad ,$$

for the normal state, and

$$G_s(H,T) = G_n(T_c) + \int_T^{T_c} S_s(H,T)\, dT$$

for the pure superconducting state. The Gibb's free energy of the mixed state is given by

$$G_{mH} = F_{mH} - BH/4\pi$$

and

$$G_{mH} = G_n(T_c) + \int_T^{T_c} S_m(H,T)\, dT.$$

We have not calculated the Gibb's free energy but we have plotted the amount of heat supplied to the specimen in the mixed state vs the magnetic induction variation inside the specimen in Figure 5.8.

5.3.2 The magneto-caloric effect

The measurement of the magneto-caloric effect has been done under nearly adiabatic conditions, temperature variation of the specimen being recorded while the field swept at a constant time rate. There were no heat or electric currents applied externally during the measurements. After each sweep of the field, heat was supplied to drive the specimen above its transition temperature in zero field, thus excluding the trapping of flux.

The measurement was first done with a Nb disc of diameter 25 mm and thickness 1 mm. The temperature variation of the specimen as function of the sweeping field is plotted in Figure 5.9. The field sweeping rate was

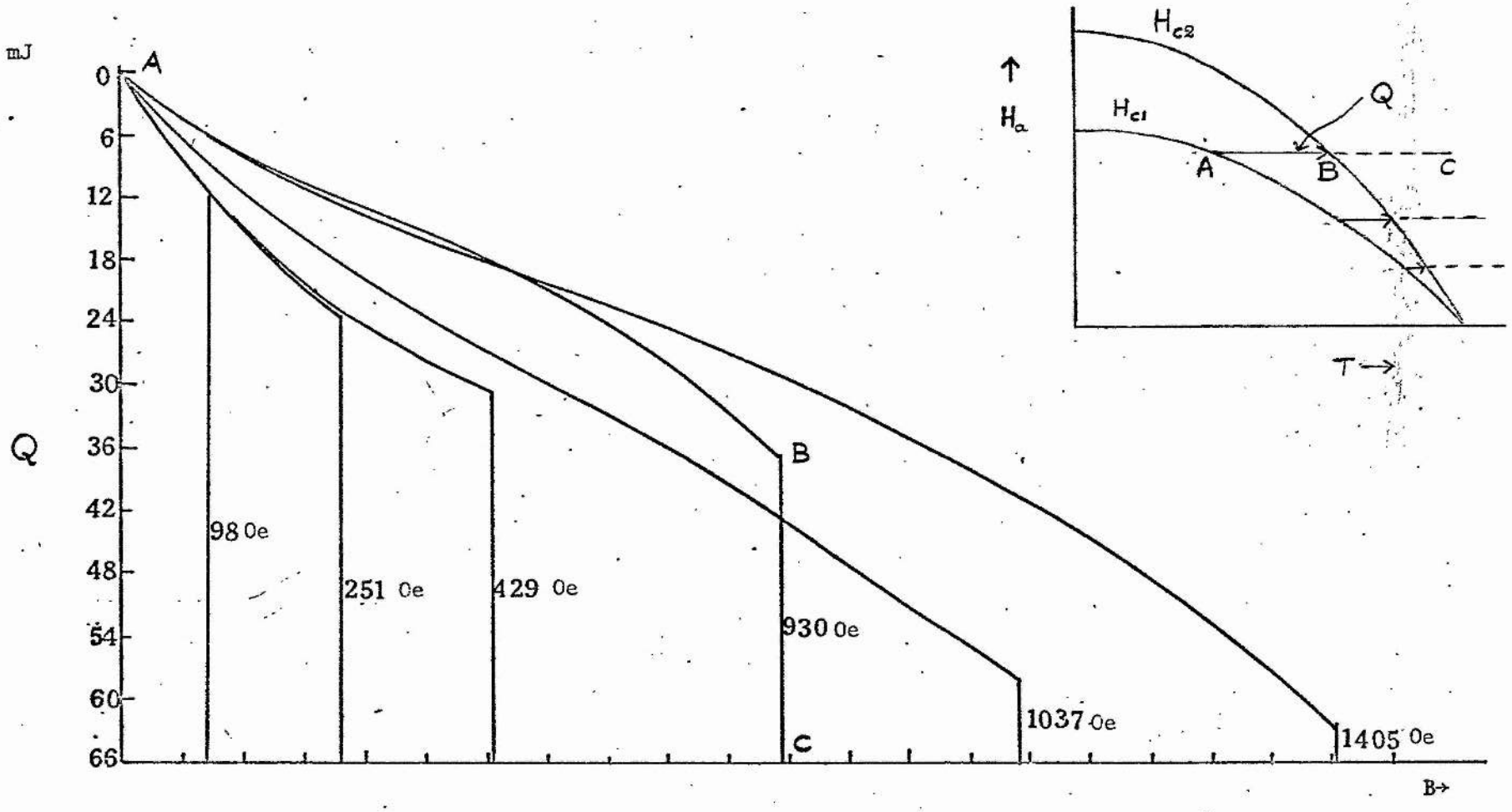

FIGURE 5.8 Heat supplied vs the magnetic induction variation inside the Nb(rod) specimen at constant H_a.

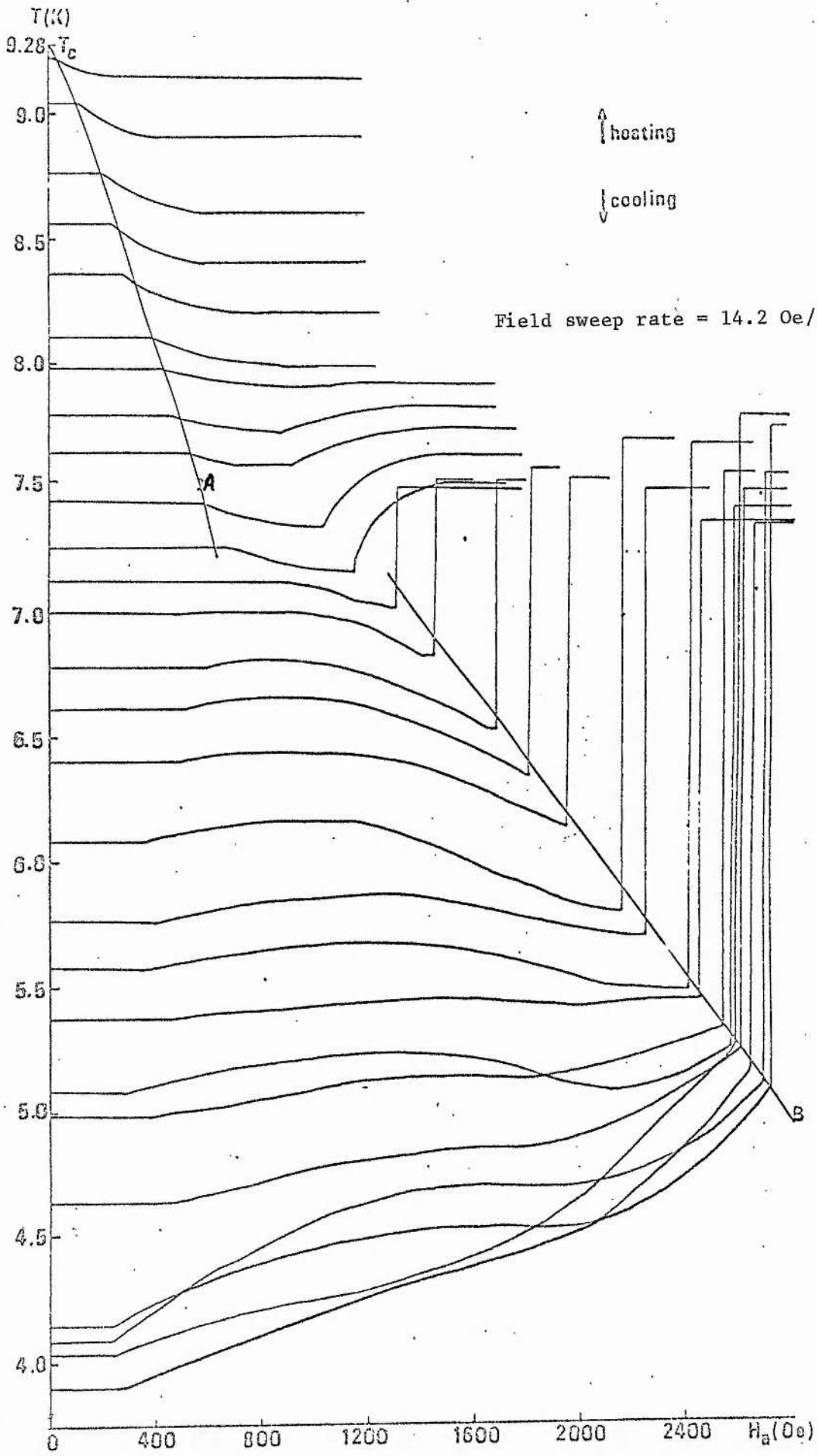

Fig 5.9 Magnetocaloric effect in Nb

14.2 Oe/sec.

In order to obtain a better understanding of the magneto-caloric effect, we must know how the magnetic induction changes in the specimen. We had the magnetic induction data as well as the specific heat data for the niobium rod specimen, and we therefore did the magneto-caloric measurements on this specimen as well.

Figure 5.10 shows some of the recorded curves of temperature variation in the rod while the field was swept through the entire superconducting region at the rate of 37.2 Oe/sec. The adiabatic magnetization curves of the specimen recorded during the magneto-caloric measurements are shown in Figure 5.11, while the net temperature variations at two different sweep rates, 37.2 Oe/sec and 15.0 Oe/sec, as functions of the initial temperatures of the specimen are plotted in curves (a) and (b) respectively in Figure 5.12. Curve (c) in the Figure represents the maximum magneto-caloric effect, as determined from specific heat measurements, on the basis of no dissipation.

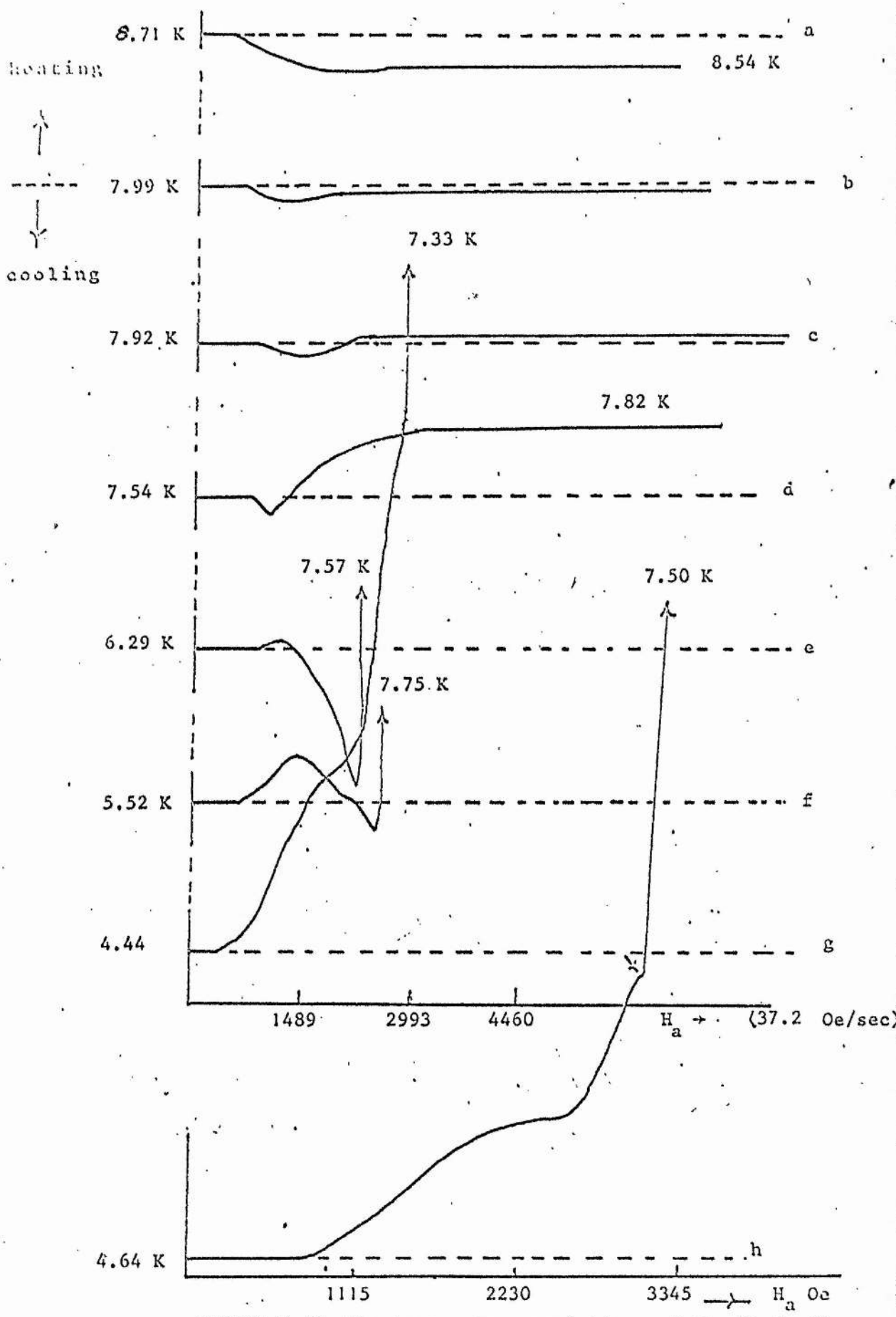

FIGURE 5.10 The temperature variations of the Nb (rod)

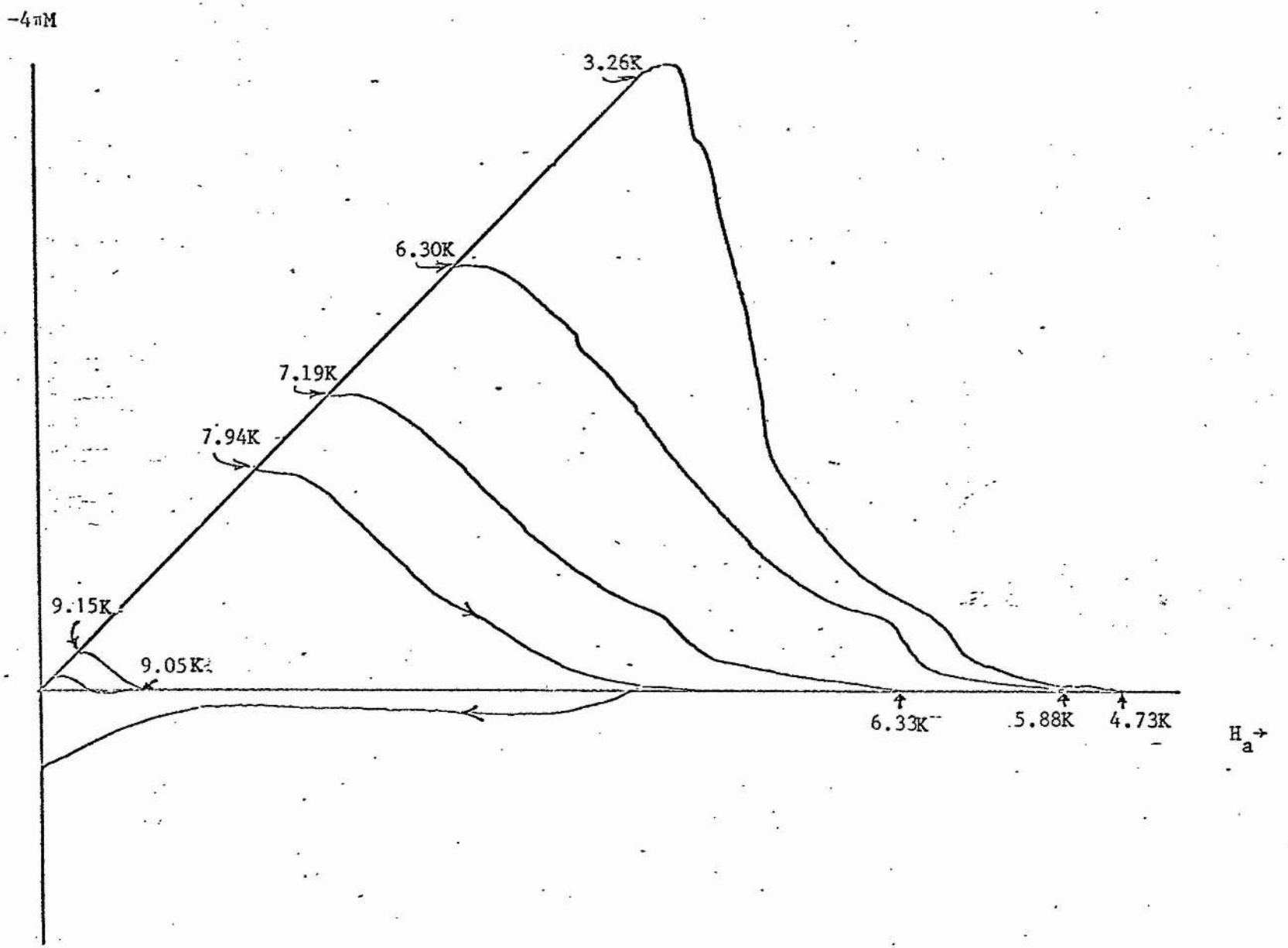

FIGURE 5.11 The magnetization of a niobium rod from different starting temperatures. The starting temperatures are given on the Meissner curve while the final temperatures at H_{C2} are given along the abscissa.

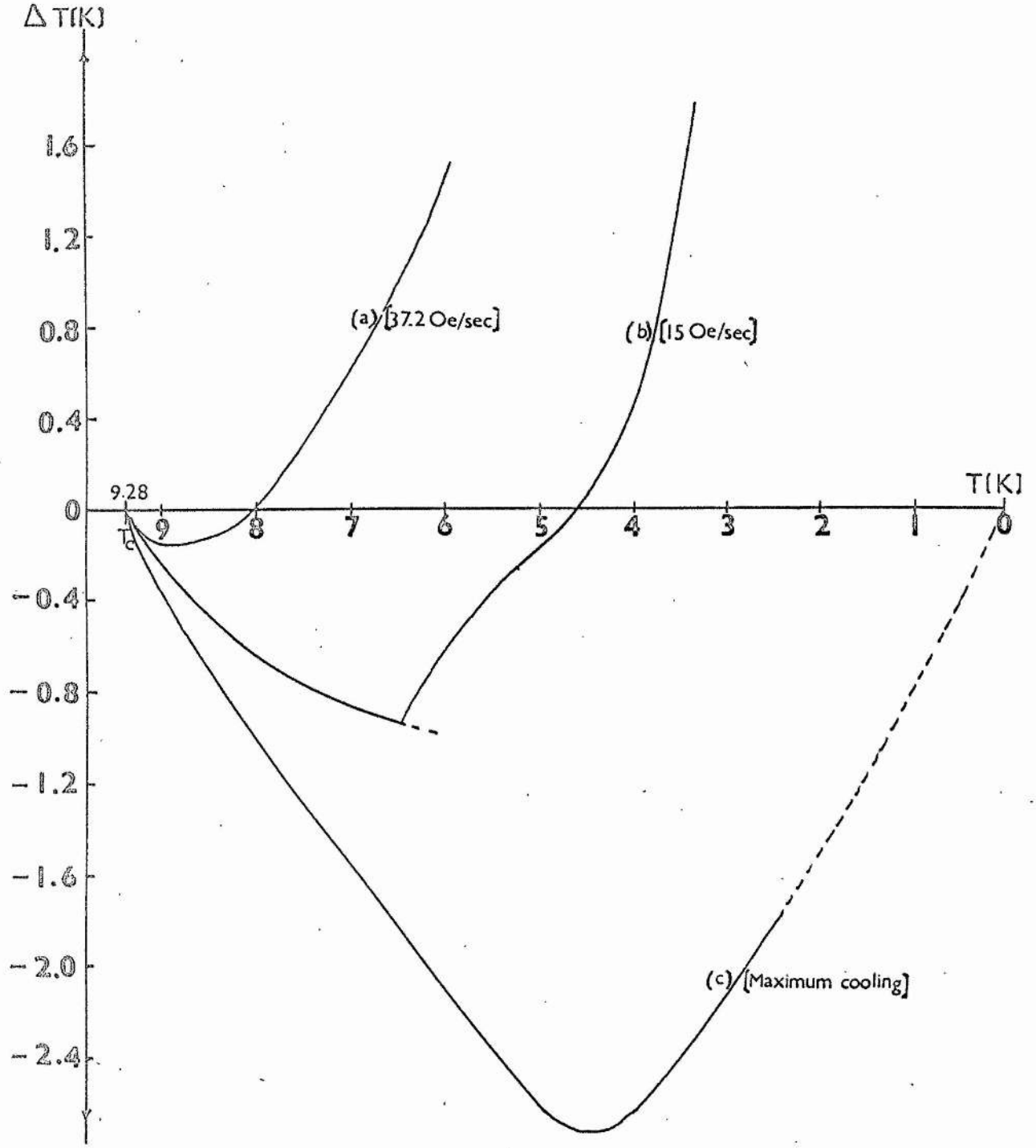

Fig 5.12 The temperature change of the Nb rod in an adiabatic magnetization vs initial temperature

5.4 Discussion

5.4.1 The magneto-caloric effect

From the magneto-caloric effect in a completely reversible specimen, one would expect cooling all the way through the magnetisation from the superconducting to the normal state according to Equation 5.2.21. This maximum cooling, which is calculated from the measured specific heat data, as shown in curve (c) of Figure 5.12, depends on the entropy difference between the normal and superconducting states. In general, a superconductor always possesses some degree of irreversibility which damps the flux motion and dissipates energy in the form of Joule heating. This heating effect depends on the velocity of the flux flow, and the flux flow velocity is determined by the gradient of the field distribution. The magnitude of the field gradient is related to the density of pinning sites and thus the latter determines the degree of irreversibility in the specimen. A pinning site in a superconductor constitutes a kind of potential well which is favourable for the trapping of flux lines. It is imagined that a pinning site can trap more than one flux line. Since each line trapped will decrease the well depth, the energy of release of a trapped line will be governed by the number already trapped. It will also be governed by a Boltzmann factor, with the result that at lower temperatures release of a flux line becomes more difficult, it will have a higher velocity on release and will consequently generate more heat.

Our experimental results can be understood qualitatively from the above argument. At the higher temperatures, there is no detectable change in temperature as the field is varied through the Meissner state, of which the approximate locus of H_{c1} is the curve A in Figure 5.9. For some reason that we do not know, the temperature of the specimen starts to change in a field well below H^{*}_{c1} at lower temperatures.

Near the transition temperature, the specimen is less irreversible because the fluxoid escape probability is higher, and the specimen shows a continuous cooling. As the starting temperature drops, the escape probability also drops and heating starts to appear. In the middle temperature region, there was cooling between initial and final heating, which appears as a small dip in curve (d) and larger dips in (e) and (f) of Figure 5.10. This sequence of heating - cooling - heating is also difficult to understand, but it seems to be general since it was observed in a different specimen, as recorded in Figure 5.9. It might arise from the fact that an intermediate density of flux lines will give a lattice which hinders flux motion, while if there are few flux lines they can move freely and if the flux density is great enough the lattice is swamped and flux freedom of motion is again greater. This is similar to the force F_s vs H_a experiment, which is discussed in Chapter VI.

The great temperature rise in Figures 5.9 and 5.10 we have associated with the large change in magnetization which occurs near the upper critical field H_{c2}. The $H_{c2}(T)$ dependence is shown as the curve B in Figure 5.9.

5.4.2 The specific heat measurements

We have a finite differential permeability $(\frac{\partial B}{\partial H})_T$ greater than unity in the mixed state and a permeability equal to unity in the normal state. Therefore Equation 5.2.13 predicts that C_m is always greater than C_n. As we described in Figure 5.1, if one measures the specific heat at constant field as a function of temperature, one expects discontinuities at both H_{c1} and H_{c2}. Specific heat values as measured from the heat supplied and as calculated from the magnetization via Equation 5.2.20 differ from each

other for reasons to be discussed later, but both showed jumps at H_{c1} which were much smaller than expected. Particularly at lower temperatures, for example at 3.26 K Figure 5.11 curve (a) for the specimen appeared to show that the transition from the Meissner state to the mixed state was very much like a first order transition although we did not observe any discontinuity in the measured specific heat at H=2230 Oe as we expected. This is possibly due to the specimen having quite a long thermal equilibrium time constant ($\sim$5 seconds) which was comparable to the duration of the heat pulse. Some part of it may also be due to the small but finite demagnetization effect of the specimen which reduces the sharpness of the first order transition.

The specific heat also changes discontinuously at H_{c2}; the drops being larger and steeper in low fields and high temperatures than in high fields and low temperatures. The magnitudes of these drops at H_{c2} calculated using Equation 5.2.14 and with $\beta = 1.16$ (which assumes a triangular lattice) and the corresponding values of the Ginzburg-Landau parameters $\kappa_1(T)$ and $\kappa_2(T)$ are given in Table 5.2.

The reason for the high specific heat of the specimen before the transition is that it needs a certain amount of energy (heat) to fill the energy gap $2\,\varepsilon(0)$. The energy gap of the specimen at $T = 0^{\circ}K$, is calculated from the Anderson (1959) relation

$$\frac{2\varepsilon(0)}{k_B T_c} = \frac{4}{\sqrt{3}}\,\pi\left(\frac{H_c^2(0)}{8\pi\gamma T_c^2}\right)^{\frac{1}{2}} = 3.63,$$

The mixed state specific heat C_{mT} data as determined from thermal measurements,

$$C_{mT} = \frac{1}{n}\frac{dQ}{dT} = \frac{1}{n}\frac{V^2}{R}\frac{t}{\Delta T},$$

where t is the length of the heat pulse.

TABLE 5.2

T	H_{c2}	$(\frac{dH_{c2}}{dT})_{H_{c2}}$ Oe/deg	$4\pi(\frac{dM}{dH})_{H_{c2}}$	κ_1	κ_2	$\frac{Cn - Cm}{T}$ mJ/mole K^2
9.2		820	0.2960		1.43	188 .58
9.0	230	752	0.1990	1.30	1.63	112.53
8.5			0.1211		2.1	
8	980	693	0.0920	1.32	2.28	44.182
7.85			0.0852		2.36	
7.2			0.0673		2.63	
7	1645	653	0.0635	1.325	2.70	27.07
6.6			0.0569		2.84	
6.3			0.0532		2.93	
6	2250		0.0506	1.34	3.00	17.79
5	2835		0.0429	1.38	3.25	13.99
4	3380		0.0374	1.436	3.47	11.31
3	3900		0.0335	1.506	3.66	8.78

are in reasonable agreement with the mixed state specific heat C_{mB} data as determined from induction measurements via Equation 5.2.20. The difference between C_{mT} and C_{mB} is due to irreversible heating in the specimen. During the measurements, apart from the externally supplied heat, there is heat generated in the specimen due to the flux flow inside it. The sum total of the quantities of heat are

$$\Delta Q_i = \Delta Q + \Delta Q_{ir} + \Delta Q_r ,$$

where ΔQ_{ir} contains all of the dissipation heat due to flux flow, flux jumping etc., and ΔQ_r is the heat absorbed in the transition between the superconducting and normal states at temperature T ($0 < T < T_c$). Dissipation in a superconductor depends on the flux flow velocity, and therefore results can depend on the rate of supplying heat during the measurements. Here, we encounter the well-known difficulty that we wish to keep down the applied heat in order to minimize the ΔT but in so doing we increase the error in the specific heat itself.

The specific heat C_{mT} is greater or smaller than C_{mB} depending on whether $\Delta Q_{ir} + \Delta Q_r$ is negative or positive. The value of $\Delta Q_{ir} + \Delta Q_r$ can be determined from the magneto-caloric measurements as in Figure 5.12. From Figure 5.12 at the flux flow rate of 15 Oe/sec, we would expect that C_{mT} would be smaller than C_{mB} below $\sim 5.3^{\circ}K$ and greater above this temperature.

Table 5.3 gives the specific heat data of the specimen in a field of 2230 Oe, C_{mT}/T, C_{mB}/T, T, ΔT, where the latter is the temperature rise of the specimen after each heat pulse supplied. It also contains the rate of

TABLE 5.3

$C_{mT/T}$	$C_{mB/T}$	T	ΔT	ΔT_i	ΔQ_i	B Oe/sec
11.06	14.02	4.097	0.059	0.0120	0.715	5.21
12.39	17.02	4.152	0.052	0.0141	0.999	5.23
13.15	22.31	4.20	0.045	0.0185	1.731	7.82
11.90	17.46	4.271	0.097	0.0292	2.179	10.42
13.79	19.95	4.361	0.082	0.0253	2.203	10.42
14.24	21.38	4.441	0.078	0.0260	2.473	10.42
16.81	22.78	4.513	0.065	0.0170	1.751	9.16
17.61	24.59	4.589	0.087	0.0247	2.787	13.05
19.81	27.08	4.670	0.076	0.0204	2.580	13.05
22.82	29.23	4.740	0.065	0.0143	1.975	11.68
23.99	29.47	4.804	0.061	0.0113	1.606	10.42
20.28	29.32	4.882	0.096	0.0296	4.237	15.68
22.58	28.55	4.973	0.085	0.0178	2.524	6.53
24.15	32.13	5.053	0.076	0.0188	3.065	12.95
23.75	31.54	5.130	0.077	0.0190	3.077	11.68
26.1	28.03	5.203	0.07	0.0048	0.703	7.8
27.75	30.97	5.27	0.065	0.0067	1.103	7.8
28.28	29.7	5.333	0.063	0.0030	0.477	5.26
31.57	29.6	5.513	0.17	-0.0113	-1.846	18.3
29.76	28.24	5.608	0.195	-0.0105	-1.662	6.4
26.24	26.2	5.711	0.117	0	0	3.9

increase of the flux density inside the specimen, as well as ΔQ_i and $\Delta T_i \cdot \Delta Q_i$ is given by

$$\Delta Q_i = [\, C_{mB} - C_{mT} \,] \Delta T \ .$$

The first order approximation of the temperature increment corresponding to ΔQ_i is

$$\Delta T_i = {}^{\Delta Q_i}/_{C_{mB}} \ .$$

The heat generated due to dissipation is $\Delta Q_{ir} = \Delta Q_i - \Delta Q_r - \Delta Q$ and the temperature rise corresponding to ΔQ_{ir} is

$$\Delta T \cong \Delta T_r + \Delta T_i ,$$

where ΔT_r is the cooling effect as shown in Figure 5.12.

Unfortunately, we have not measured the magneto-caloric effect with all the field sweep rates given in Table 5.3, but comparing ΔT_i with ΔT_r as derived from Figure 5.12, the agreement is reasonably good.

What has been written above shows the difficulty of measuring specific heat in a Type II superconductor in the mixed region where we are concered with irreversible effects. Since the flux line density depends on temperature the rate of entry and motion of flux lines depends on the rate of heating, and their motion itself generates heat in a manner and of magnitude which is difficult to estimate. This will be discussed further in Chapter VII.

CHAPTER VI

Pinning Forces in Nb and Pb-In Specimens

CHAPTER VI. Pinning forces in Nb and Pb-In Specimens

6.1 Introduction

The pinning mechanism in a type II superconductor in the mixed state can be studied experimentally by the following methods:

(a) D.C. resistance measurement to determine the critical current density J_c. We determine when the flux starts to flow from the voltage change between two points on the specimen, and hence find the pinning force from Equation 1.7.1. When a current is passed through a specimen it will exist first as a surface current. At some point or points on the surface the magnetic field may rise to such a value that vortices will be nucleated and move into the specimen. The result of this is that part of the initial surface current becomes distributed within the specimen, as a bulk current, and can interact with the vortices there. Whether or not they continue to move depends upon the absence or presence of the pinning. Continuous motion of the vortices causes dissipation and a voltage drop along the direction of the current.

(b) Magnetization measurement. This is based on the critical state concept that vortices which have been nucleated at the surface have to reach a certain spatial gradient to overcome the pinning forces before they can penetrate further into the specimen. Different experimental techniques have been developed to measure the field profile in the specimen; e.g. the tube magnetization measurements by Kim et al (1963), direct measurements of the internal field by moving a microprobe in a slot by Coffey (1967) and Weber and Riegler (1973) and d.c. magnetization measurements (e.g. Fietz and Webb, 1969).

(c) By mechanical means, as mentioned in Chapter I.1. A gradient in the flux distribution can be created in the specimen by moving the external field source. When this gradient reaches a certain value its Lorentz force can overcome the pinning forces and the flux will start to flow in the specimen. By measuring the resulting force on the specimen the pinning forces in the specimen can be determined.

The theory of pinning is complicated, since the effects of the pinning sites are not independent of each other, but are coupled by the elasticity of the vortex configuration. The theory of dislocations in crystal lattices (e.g. Nabarro, 1967) and the concept of elasticity of the magnetic flux have been modified and applied by introducing the flux lattice spacing instead of the atomic spacing and by expressing the forces on the vortices in terms of the line tension and compressibility of the flux field through an elastic constant C_{ij}. This can be expressed as

$$\sigma_i = C_{ij}\, \varepsilon_j \qquad 6.1.1$$

where σ_i and ε_j are the stresses and the strains, respectively. An isotropic superconductor is assumed and Voigt's notation is used.

Labush (1967, 1969) has calculated these constants for a reversible, hexagonal lattice type II superconductor, while Seeger and Kronmuller (1968) and Campbell (1974) have used a statistical summation method to cover the effects of different pinning sites on the elastic constants. However, there is still no appropriate theory which can connect the experimental results of the pinning forces to the array of the local pinning sites.

We have no intention of reviewing these accounts in detail, but simply summarize some basic pinning mechanisms and some phenomenological theories

which can be used to analyse our experimental results.

Theoretical considerations

6.2 The nature of the pinning forces

The pinning force is defined as a maximum value of flux density gradient that a pinning site can sustain, and is given by

$$\underline{F}_p(\underline{B}) = \underline{B} \times \text{curl } \underline{H}(\underline{r}) \quad . \qquad 6.2.1$$

A flux line in a flux gradient will experience a Lorentz-type driving force due to the mutual interaction between the flux lines. The force tends to move the flux down the gradient. Therefore, the larger the gradient, the bigger the pinning force that is needed to stablize the flux lattice. In a stable flux configuration, the flux gradients are also stable, and the forces acting on every superconducting electron are constant and the magnetic pressure acting on the flux lines or flux bundles are balanced out. Any distortion in the configuration of the flux lines needs the application of a force. This can be done by changing the external applied field or by introducing a transport electric current.

The pinning sites act as potential barriers in a superconductor (Anderson, 1962), and the height of the barriers depends on the nature of the pinning sites.

The experimental results of Träuble and Essmann (1966, 1968) and Livingston (1963) showed that the pinning sites include dislocation lines, small dislocation loops, point dislocation precipitates with superconducting parameters different from those of the matrix, conducting and non-conducting impurities, and absorbed gases. The effects due to these defects can be

separated into 'long range' and 'short range' perturbations, which depend on the range of the interaction between the pinned fluxons and the flux lattice. The 'short range' perturbations refer to those whose interaction distance is smaller than the coherence length. This kind of localized interaction is not important, since the superconducting properties are unlikely to change appreciably over this distance. In a 'long range' perturbation, the pinning can interact with several vortices so that the regular flux lattice become disturbed.

Träuble and Essmann (1966) have confirmed the existence of flux lattice defects, which were predicted by Labush (1967, 1969). They also introduced a simple notation to describe the various defect configurations observed. The simplest vacancy, formed by removing one vortex, is denoted by (-1), whereas the split vacancy or 'dumbbell' configuration, formed by removing two adjacent vortices and replacing one at a point midway between the two empty sites, is denoted by $(^{-2}/_{+1})$. In addition to these single vacancies, there are di-vacancies of types (-2), $(^{-3}/_{+1})$, $(^{-6}/_{+4})$ and tri-vacancies of type $(^{-6}/_{+3})$, etc.

Although the interaction range of the point defects, (-1), and $(^{-2}/_{+1})$ due to vacancies or interstitial vortices obeys an exponential law, because the size of the defects is less than the vortex spacing d and because the defects interact directly only with nearest flux lines, such defects do not give any significant pinning effect.

If each pinning site pins one flux line, the total pinning force per unit volume is

$$f_p(B) \cdot n$$

where $f_p(B)$ is the pinning force per unit pinned length and n is the number

of pinning centres per unit volume. The critical current of this is given by

$$J_c = f_p(B) \cdot {}^{n}/_{B} \quad , \qquad 6.2.2$$

or $$J_c \propto B^{-1}.$$

A line defect, (-2), $({}^{-3}/_{+1})$ and $({}^{-6}/_{4})$, which has one dimension greater than d due to dislocations of the vortex lattice, results in an interaction field which decreases according to a '1/d law'. This kind of defect in an Nb specimen has been calculated by Hill et al (1969). They used the London expression for the total energy of a system of flux lines:

$$U_T = n\varepsilon_1 + \left(\frac{\Phi}{4\pi\lambda}\right)^2 \sum_{i=1}^{n} \sum_{\substack{j=1 \\ i \neq j}}^{n} K_o({}^{r_{ij}}/_{\lambda}) \qquad 6.2.3$$

with λ = 462 Å and ξ = 357 Å, to determine the stability of various defect configurations. Their computer-aided calculations showed that the line defects should be 'squeezed out' of the flux lattice at high fields unless they are stabilized by strong pinning centres. An average expression of the pinning effect of the line defects has been given by Campbell et al (1968). They calculated the flux line spacing

$$d = 1.07 \left({}^{\Phi_o}/_{B}\right)^{\frac{1}{2}} \quad ,$$

for a reversible triangular lattice, and assumed that the number of vortices per unit length of line pinning was inversely proportional to the vortex density and equal to $0.93 \left({}^{B}/_{\Phi_o}\right)^{\frac{1}{2}}$. They give the resulting critical current as

$$J_c = 0.93\, f(B) \cdot {}^{n}/_{(B\,\Phi_o)^{\frac{1}{2}}},$$

$$\text{or} \quad J_c \propto f(B)/B^{\frac{1}{2}} \quad . \qquad 6.2.4$$

Applying the above argument to the boundary, we derive

$$J_c = 0.93\, S_{V\perp}\, f(B)/(\Phi.B)^{\frac{1}{2}} \quad , \qquad 6.2.5$$

where $S_{V\perp}$ is the total phase boundary per unit volume perpendicular to the driving force.

Anderson (1962) has treated the pinning mechanism as though the flux lines were trapped in a potential well, of depth Δg, caused by variation in free energy between the matrix and the defects. A force $F_p = \Delta g/l$ must be exerted to move the flux lines out of or into the traps, where l is a characteristic distance which depends on the nature of the interaction.

The pinning force due to a superconducting second phase material depends on the interaction between the flux lines and the second phase material. The second phase material is surrounded by a Meissner screening current. The interaction between this screening current and the flux lattice is a long range one, since the current decays exponentially with a characteristic length greater than the flux line spacing. The flux line affected by this second phase material will tend to slip away from it, and interact with the rest of the flux lattice resulting in a resistive (pinning) force which impedes the flux motion. Campbell et al (1968) have calculated this type of pinning and have shown that the critical current can be expressed as

$$J_c = \frac{S_v \Delta M}{\lambda} \left(\frac{\phi_0}{B}\right)^{\frac{1}{2}}, \qquad 6.2.6$$

where S_{vv} is the surface area per unit volume perpendicular to the Lorentz

force and ΔM is the difference in equilibrium magnetization across the boundary. From the free energy change of the specimen,

$$\Delta g = V\int_{H_{ext}}^{H'_{c2}} M'dH - V\int_{H_{ext}}^{H'''_{c2}} M'' dH , \qquad 6.2.7$$

where V is the volume of the superconducting second phase material and the primes refer to the properties of the two materials. Dew-Hughes (1971) has derived

$$J_c = \frac{VB^{\frac{1}{2}}}{4.64\Phi_o^{\frac{3}{4}}}\left[\left(\frac{H'_{c2}-H}{\kappa'_1}\right)^2 - \left(\frac{H''_{c2}-H}{\kappa''_1}\right)^2\right]. \qquad 6.2.8$$

Livingston (1966) has observed that the pinning is stronger the greater the magnetization difference between the matrix and the second phase material in his experiments with tin precipitate in a Pb-In matrix.

In the case of normally conducting second phase material, we have a situation similar to that of the field penetrating from a finite permeability material into a superconductor. The flux lines tend to persist in these pinning sites, and act as magnetic dipoles with field decreasing into the superconductor exponentially (London penetration law). The second phase material is screened by a superconducting current. The field inside the pinning sites must be quantized, as given by,

$$\bar{\Phi} = \oint \underline{A} \cdot dl = n\,\bar{\Phi}_o = \bar{\Phi}_{ext} + \bar{\Phi}_{s.c} , \qquad 6.2.9$$

where $\bar{\Phi}_{ext}$ represents the flux lines due to the external field and $\bar{\Phi}_{s.c}$ the flux lines due to the screening current. The energy of the matrix is lowered by

$$\Delta g = \frac{VH_c^2}{8\pi} + \frac{H_c^2}{8\pi} A\Delta , \qquad 6.2.10$$

where V is the volume of the second phase material, Δ is the boundary energy parameter and A is the surface area of the second phase material.

Anderson (1962) and Friedel et al (1963) calculated the pinning force when the dimension of the second phase was within a range of order of magnitude ξ, and obtained

$$F_p = \frac{H_c^2 V}{8\pi\xi} \quad . \qquad 6.2.11$$

For a field inside the second phase material less than H_c we have to rewrite Equation 6.2.10 as

$$\Delta g = V\int_{H}^{H_{c2}} H(B)dB/_{8\pi} + \Delta A\int_{H}^{H_{c2}} H(B)dB/_{8\pi} \qquad 6.2.10a$$

Love (1970) has derived the critical current from the above arguments and has obtained

$$J_c \propto (\frac{B}{\Phi_0})^{\frac{1}{2}} \qquad 6.2.12$$

The experimental result of Bibby (Dew-Hughes 1971) has shown that there is little difference between a conducting and an insulating second phase material, which might be due to the different permeability of the material. In this case the pinning force is again proportional to the surface area and the geometry of the second phase material.

In the case of high permeability ferromagnetic second phase material, the pinning force appears to be no greater than for an equivalent distribution of any non-superconducting material (Alden and Livingston 1966, Campbell et al 1968).

The pinning force of the second phase material depends on the energy barrier at the boundary (Gifkins et al 1968) between the second phase and the matrix plus the repulsive force from the matrix flux configurations. In order to derive the pinning force of a system, different assumptions have to be made in considering the interaction of an individiaul flux line with the pinning centres and the presence of other flux lines. The most difficult part of the work lies in the modification to the total flux configuration due to different functional dependence on B of the pinning forces and the random occurrence of pinning sites. The distorted flux configuration is particularly important in high fields with dense flux lines, since the flux lines are not rigid; a rigid flux line would be more difficult to pin since it would not deform locally to minimize its energy.

6.3 Summary of some phenomenological approaches

6.3.1 Bean-London model and its extension

Bean (1964) and London (1963) introduced the field-dependent penetration depth concept to the critical state, that is, when a current or a field is changed in a specimen, a shielding current is induced. Up to a maximum current density J_c, the field within the specimen decreases linearly with distance as a consequence of Ampere's Law. In regions where J_c is reached the current density remains unchanged, and flux penetrates deeper into the material, where more shielding currents are induced. The magnetization of the specimen is given by

$$\underline{B} = \int \underline{H}\, dV / \int dV, \qquad 6.3.1.$$

and

$$4\pi \underline{M} = \underline{B} - \underline{H}.$$

Therefore the magnetization depends on the size of the specimen. In this model, the critical current is independent of B, and we have

$$J_c = \text{const}, \qquad 6.3.2.$$

and

$$F_p \propto B.$$

This model gives a good account of the hysteresis in high κ superconductors which have a very large number density of defects which is uniform throughout the material.

Fietz and Webb (1969) have used this critical state to deduce the critical current density $J_c(H_a)$ from the magnetization curve. They ignored any surface effect by assuming that its contribution to the magnetization was small.

For a long cylindrical specimen, they took a Taylor series expansion of the critical current $J_c(r)$ about the point r=R, and thus

$$J_{\pm}(r) = J_{\pm}(R) + J'_{\pm}(R)(r-R) + J''_{\pm}(R)(r-R)^2/_{2!} + \ldots \qquad 6.3.3$$

where $\pm$ signs refer to sweeping the field up and down, and by integrating Equation (6.3.3) to obtain the induction B,

$$B_{\pm}(r) = B_o + k\,[\,J_{\pm}(R)(r-R) + J'_{\pm}(R)(r-R)^2/_{2!} + \ldots .\,] \quad ,$$

where k is a conventional factor equal to $\frac{4\pi}{10}$ if B is in gauss and J is in $^{A}/_{cm^2}$. The magnetization of the specimen is

$$4\pi\overline{M}_{\pm} = 4\pi M_e + 2k\left(\frac{J_{\pm}R}{3!} - \frac{J'_{\pm}R^2}{4!} + \frac{J''_{\pm}R^3}{5!} + \ldots .\right), \qquad 6.3.4.$$

where $4\pi M_e$ is the magnetization of the reversible state of the specimens. The difference between $\overline{M}_+$ and $\overline{M}_-$ is

$$4\pi(\overline{M}_+ - \overline{M}_-) = \frac{4kJ_+R}{3!} + \frac{4kJ_+''R^3}{5!} + \ldots \quad , \qquad 6.3.5$$

and the sum of $\overline{M}_+$ and $\overline{M}_-$ is

$$4\pi(\overline{M}_+ + \overline{M}_-) = 2(4\pi M_e) - \frac{kJ_+'R^2}{3!} \cdot \qquad 6.3.5a$$

Note that

$$\partial^n J_+ / \partial r^n = (-1)^n \, \partial^n J_- / \partial r^n \quad \text{at } r=R.$$

To first order approximation of Equation (6.3.5) and (6.3.5a), we have

$$4\pi\,[\overline{M}_+(H_a) - \overline{M}_-(H_a)] \approx \frac{2}{3} k R J_c(H_a), \qquad 6.3.5b$$

and

$$4\pi\,[\overline{M}_+(H_a) + \overline{M}_-(H_a)] \approx 2(4\pi M_e) \quad , \qquad 6.3.5.c$$

from which $J_c(B)$ and $4\pi M_e$ can be calculated.

6.3.2 Silcox-Rollins model

Silcox and Rollins (1963, 1964) have developed the Abrikosov theory to incorporate the effects of pinning due to defects, and have predicted size-dependent hysteresis in the magnetization of the specimen. They have assumed that there are uniformly distributed pinning points with equal pinning strength f_p throughout the specimen, with the pinning force given

by

$$\sum_i F(r_i) = \rho f_p \quad , \qquad 6.3.6$$

where ρ is the pinning site density. By taking the energy arising from this force into the Gibb free energy of the specimen, we have

$$\Delta g = n \varepsilon_1 + f(n) - {}^{n\Phi_o H}/_{4\pi} \quad , \qquad 6.3.7$$

where $n\varepsilon_1$ represents the energy increase due to the fluxoids, and $f(n)$ is identified with the increase in energy due to the interaction between the fluxoids and the pinning sites. For a one dimensional variation of the fluxoid density, they have derived

$$B_x^2 = B_o^2 - \frac{4}{3} n \rho H_{c1} \Phi_o \frac{H_{c2}}{(H_{c2}-H_{c1})} x, \qquad 6.3.8 .$$

where B_o and B_x are the magnetic induction at the origin and at x, respectively. The pinning force per unit volume is

$$\Phi_o \frac{dB}{dx} = \mp F_p \quad , \qquad 6.3.9$$

$$J_c \propto B^{-1}$$

and

$$F_p = \text{constant}. \qquad 6.3.10$$

This model can be applied to low κ superconductors, with relatively few pinning sites and where a fluxoid may be thought of as jumping from one pinning site to the next so that all the pinning sites are used. Kim et al (1963a) have found an empirical relation for their critical current measurements similar to that above,

$$J_c = \frac{\alpha}{b_o + B} \qquad 6.3.10a$$

where α and b_o are empirical constants.

6.3.3 Irie - Yamafugi's model

Irie and Yamafugi (1967) have made the assumption that

$$J_c = \alpha B^{\gamma-1} , \qquad 6.3.11$$

where α describes the intensity of the interaction between the pinning sites and fluxoids, and γ is a constant dependent on the density and the distribution of the pinning sites and which can have any value.

For an infinite slab of thickness 2d with X axis perpendicular both to the slab surface and the field, from Equation 6.3.11, we derive

$$B(x)^{2-\gamma} = B_o^{2-\gamma} - (2-\gamma)\alpha x/2, \qquad 6.3.12$$

where x is the depth of the field penetration and B_o is the field just inside the specimen,

$$B_o = H_a - \Delta H$$

where $\Delta H = 4\pi M_e + \delta H$, and δH is the field drop resulting from the surface sheath current. It will be assumed that ΔH is negligible.

The magnetization of a long cylindrical specimen with radius R is

$$-4\pi\bar{M} = \frac{1}{\pi R^2} \int_0^R [H_a - B(r, H_a)]\, 2\pi r dr. \qquad 6.3.13$$

On increasing the field H_a up to the penetration field value H_p, we have

$$B^{2-\gamma}(r, H_a) = H_a^{2-\gamma} - \frac{2-\gamma}{2} \alpha (R-r). \quad 0 \leqslant r \leqslant R \qquad 6.3.14$$

The penetration radius r_p is found from $B(r, H_a) = 0$, and we have

$$r_p = R - \frac{2}{(2-\gamma)\alpha} H_a^{2-\gamma} . \qquad 6.3.15$$

From the condition $r_p = 0$, we obtain the penetration field

$$H_p = \left(\frac{2-\gamma}{2} \alpha R\right)^{\frac{1}{(2-\gamma)}} . \qquad 6.3.16$$

The magnetization of the specimen is

$$-4\pi\bar{M} = H_a \left[1 - \frac{4}{\alpha R^2 (3-\gamma)} + \left(R - \frac{2}{\alpha(5-2\gamma)} H_a^{2-\gamma}\right) H_a^{2-\gamma}\right]. \qquad 6.3.17$$

At the maximum point of the magnetization curve following from the condition $d(-4\pi\bar{M})/dH=0$, we have

$$H_{max} = \left(\frac{\alpha R}{4}\right)^{\frac{1}{(2-\gamma)}} \left[(3-\gamma)\left(1-\sqrt{\frac{1-\gamma}{3-\gamma}}\right)\right]^{\frac{1}{(2-\gamma)}} , \qquad 6.3.18$$

and

$$-4\pi\bar{M}_{max} = H_{max} \frac{2-\gamma}{5-2\gamma} \left(1 + \sqrt{\frac{1-\gamma}{3-\gamma}}\right). \qquad 6.3.19$$

Equation 6.3.19 shows that the ratio $\left(\frac{-4\pi\bar{M}_{max}}{H_{max}}\right)$ depends only on γ. For the penetration field H_p the magnetization derived from Equation 6.3.16 is

$$-4\pi\bar{M}_p = \frac{1}{5-2\gamma} H_p , \qquad 6.3.20$$

In the region $H_p \leqslant H_a \leqslant H_{c2}$, we have

$$-4\pi\overline{M} = H_a + \frac{8}{\alpha^2 R^2 (3-\gamma)(5-2\gamma)} \left[H_a^{5-2\gamma} - \left(H_a^{2-\gamma} - \frac{2-\gamma}{2} \alpha R\right)^{\frac{5-2\gamma}{2-\gamma}} \right] - \frac{4}{\alpha R(3-\gamma)} H_a^{3-\gamma}$$

6.3.21

In a field which decreases from H_{c2} to zero, $0 \leqslant H < H_{c2}$, Equation 6.3.14 becomes

$$B^{2-\gamma}(r,H_a) = H_a^{2-\gamma} + \frac{2-\gamma}{2} \alpha (R-r), \qquad 6.3.14a$$

and the magnetization derived from Equation 6.3.13 is

$$-4\pi\overline{M} = \frac{8}{\alpha^2 R^2 (3-\gamma)(5-2\gamma)} \left[\left(H_a^{2-\gamma} + \frac{2-\gamma}{2} \alpha R\right)^{\frac{5-2\gamma}{2-\gamma}} - H_a^{5-2\gamma} \right] - \frac{4}{\alpha R(3-\gamma)} H_a^{3-\gamma} - H_a$$

6.3.22

The remanent magnetization is obtained by letting $H_a = 0$, and we obtain

$$4\pi\overline{M}(0) = H_p \frac{2(2-\gamma)^2}{(3-\gamma)(5-2\gamma)} = B_{Rmax} . \qquad 6.3.23$$

From Equation 6.3.14a, we derive

$$H_{Rmax}^{2-\gamma} = (2-\gamma) \alpha R, \qquad 6.3.24$$

where H_{Rmax} is the external field needed for the field to reach the centre of the specimen. Furthermore, all the pinning sites are occupied at $H_a = H_{Rmax}$. With Equation 6.3.16, we have

$$\frac{H_p}{H_{Rmax}} = 2^{\frac{1}{2-\gamma}} . \qquad 6.3.25$$

Rewriting Equation 6.3.23 in terms of H_{Rmax},

$$B_{Rmax} = H_{Rmax} \frac{2(2-\gamma)^2}{(3-\gamma)(5-2\gamma)} 2^{\frac{1}{2-\gamma}} \qquad 6.3.26$$

The above considerations only take into account the irreversible part of the magnetization and also ignore the surface contribution. If the surface role is big then one has to modify $\underline{J}$ into $\underline{J} + \underline{J}_s$ in Equation 6.3.11, and the problem becomes much more complicated.

The Irie-Yamafugi model contains no more physical understanding of the pinning mechanism than other models, but since the dependence of J_c on B is different for different pinning mechanisms this model includes some of the others, e.g. Bean-London, $\gamma=0$; the Silcox-Rollins, $\gamma=1$; and the Yasukochi et al model (1964), $\gamma=0.5$.

6.3.4 Fields higher than H_{Rmax}

The model described in Section 6.3.3 can be used to determine the maximum critical current density J_c, the pinning force density F_p, in the region $H_p < H_a \leq H_{Rmax}$. Above H_{Rmax}, the observed value of J_c decreased and approached zero as the field approached H_{c2}. In this region different relations between F_p, J_c and B have been proposed. Goedemoed et al (1967) assumed

$$F_p \propto (H_{c2} - B) \qquad 6.3.27$$

in order to interpret their experimental results on niobium wires, and found the coefficient of proportionality to be proportional to $(1-t^4)$. Campbell et al (1968) found

$$J_c \propto B^{\frac{1}{2}}(H_{c2} - B) \qquad 6.3.28$$

for their Pb-Bi experimental results. Equation 6.3.28 is similar to the derivations of Alden and Livingston (1966), Coffey (1968). Fietz and Webb (1969) and Hampshire and Taylor (1972) have shown that

$$J_c \propto H_{c2}{}^{m} h^{n} (1-h) \qquad 6.3.29$$

covers their results over the range $0.3 < h < 1$, where $h = {}^{H_a}/_{H_{c2}}$, and constants m and n depend upon the pinning mechanisms.

6.4 Experimental Results

6.4.1 Introduction

The pinning forces were measured by the direct measurement of the force exerted on the superconducting specimen when a non-uniform magnetic field was swept past it. The apparatus was described in Chapter II. A set of rotation (force) signals of the specimen holder is shown in Figure 6.1., in which is shown the force on the specimen as a function of time for different values of the sweeping field. The temperature was 4.22 K and the specimen was the mechanically polished NbI. The force depends in a complex way on the magnitude and non-uniformity of the sweeping field in the neighbourhood of the specimen and on the magnetic state of the specimen.

Let us first refer to Figure 6.2. Our specimen is not completely reversible, that is, it will not show an ideal Meissner effect. The applied field $H_{amax} < H^{*}_{c1}$; where H_{amax} refers to the maximum value of the applied field. Down the left hand side of the Figure we have in elevation four positions of the magnet with respect to the specimen, with the field lines being vertical. On the right hand side we have the corresponding plan views which show that the magnets are rotating clockwise about the centre O while the specimen is at the end of a torsion arm also centred on O and whose length is such that the axis of the magnet tracks over the centre of the specimen. The torque measuring system, described in Chapter II is such that the torque angle can be large, say 20^{o} (15g) or more.

In (a) the 'virgin' specimen is on the 'edge' of the field and no torque is measured. In (b) the specimen experiences repulsion from the field. In (c) the specimen again experiences repulsion, but as we can see from (d) the departure from pure Meissner is evident in the trapped

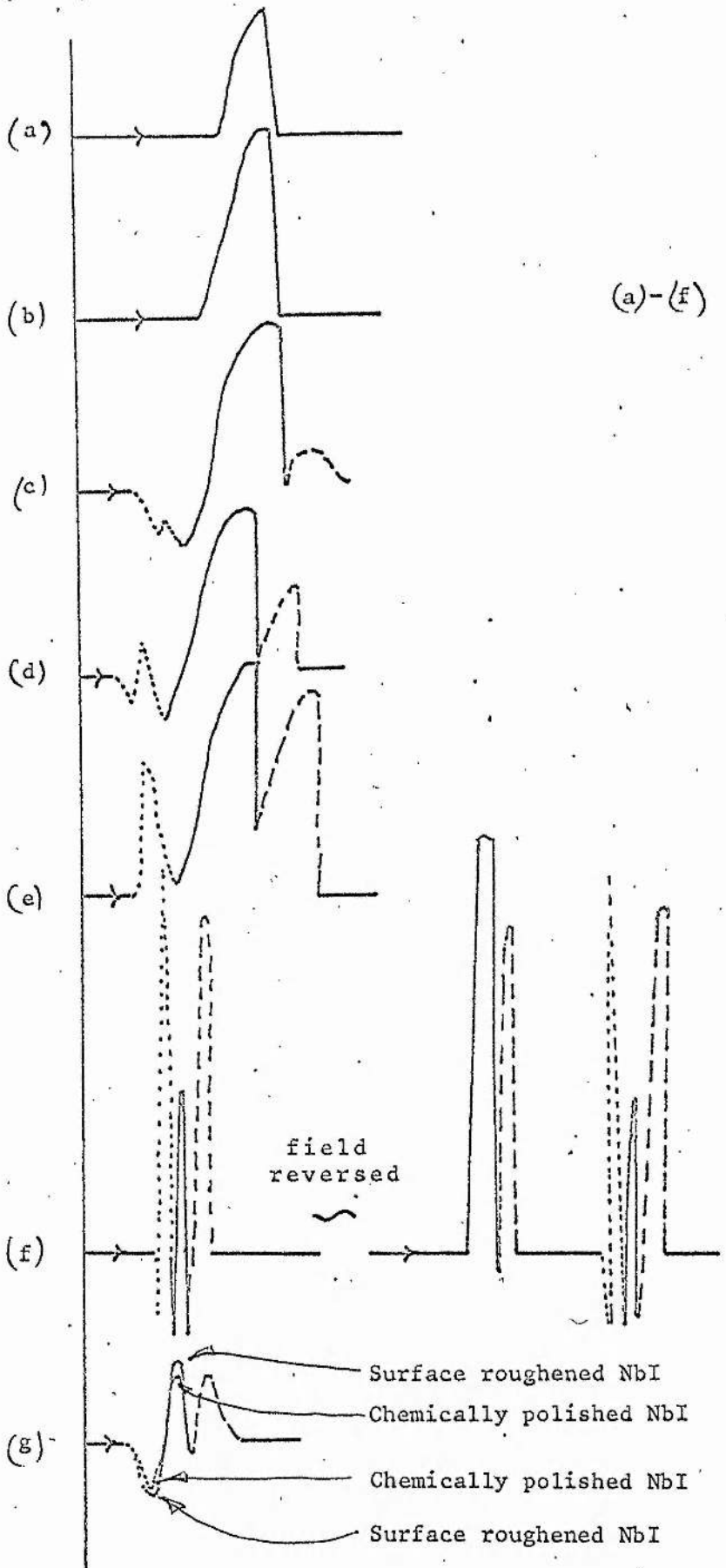

FIGURE 6.1 Experimental recorded rotation signals of the specimen
The ordinate is 'position', and the abscissa is 'time'.

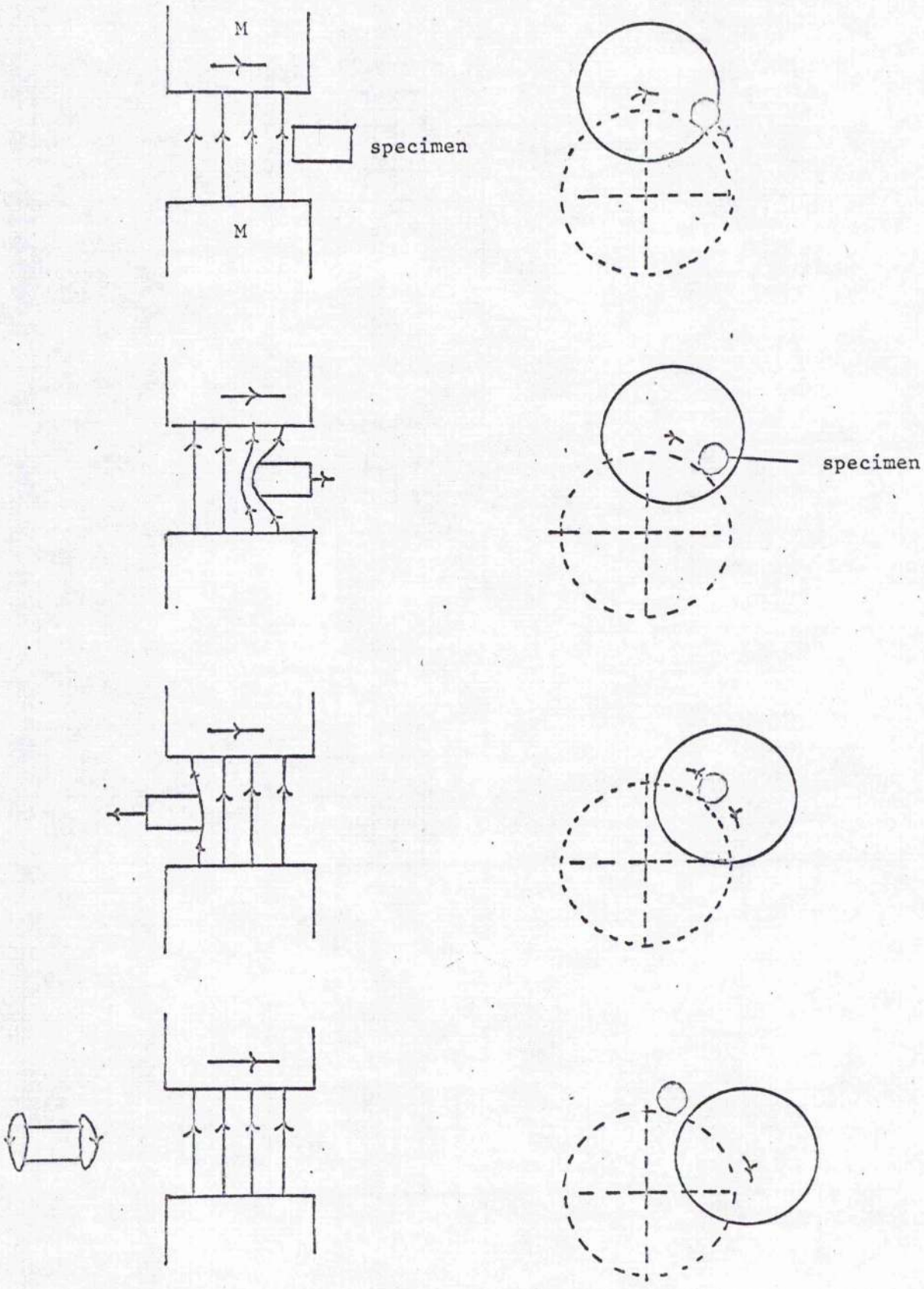

FIGURE 6.2 Schematic diagram of the positions of the magnet and the specimen; corresponds to curves (a) and (b) of Figure 6.1

flux mainly on the surface. In Figure 6.1, (a) and (b) refer to Figure 6.2 with two different values of H_{amax}. It must be realized that with the large torque angle available to the specimen the method of measurement yields only the maximum force, which we are calling F_s.

The force F_s was greatest if the specimen had no magnetic flux trapped within it prior to sweeping the magnetic field through it. During the first passage some magnetic flux lines were trapped and all subsequent passages yielded a smaller but reproducible value of F_s for the same field. Once magnetic flux had been trapped by a previous passage, then as the magnet approached the specimen on the next passage there was an initial attractive force F_A which was manifested by the specimen holder rotating towards the approaching field, as shown in the dotted line in Figure 6.1 (c), (d) and (e). When the magnetic field was reversed between passages this attractive force became a very large repulsive force as shown in Figure 6.1 (f), confirming that this was just the interaction between the applied field and the residual magnetic moment of the specimen resulting from the previous passage.

At fields higher than H^*_{c1}, in which it is expected that the specimen goes into the mixed state, another repulsive force appeared after F_A and F_s, which is the coupling force between the pinned flux lines and the magnet. This force will be referred to as the bulk pinning force F_p. The signals rising from this force are shown in Figure 6.1 (c), (d), (e), (f), (g) as dashed curves. The relative positions of the specimen to the magnet corresponding to curves (c) to (e) in Figure 6.1 are shown in Figure 6.3, together with a schematic representation of the magnetic fields in elevation and plan, following the description of Figure 6.2.

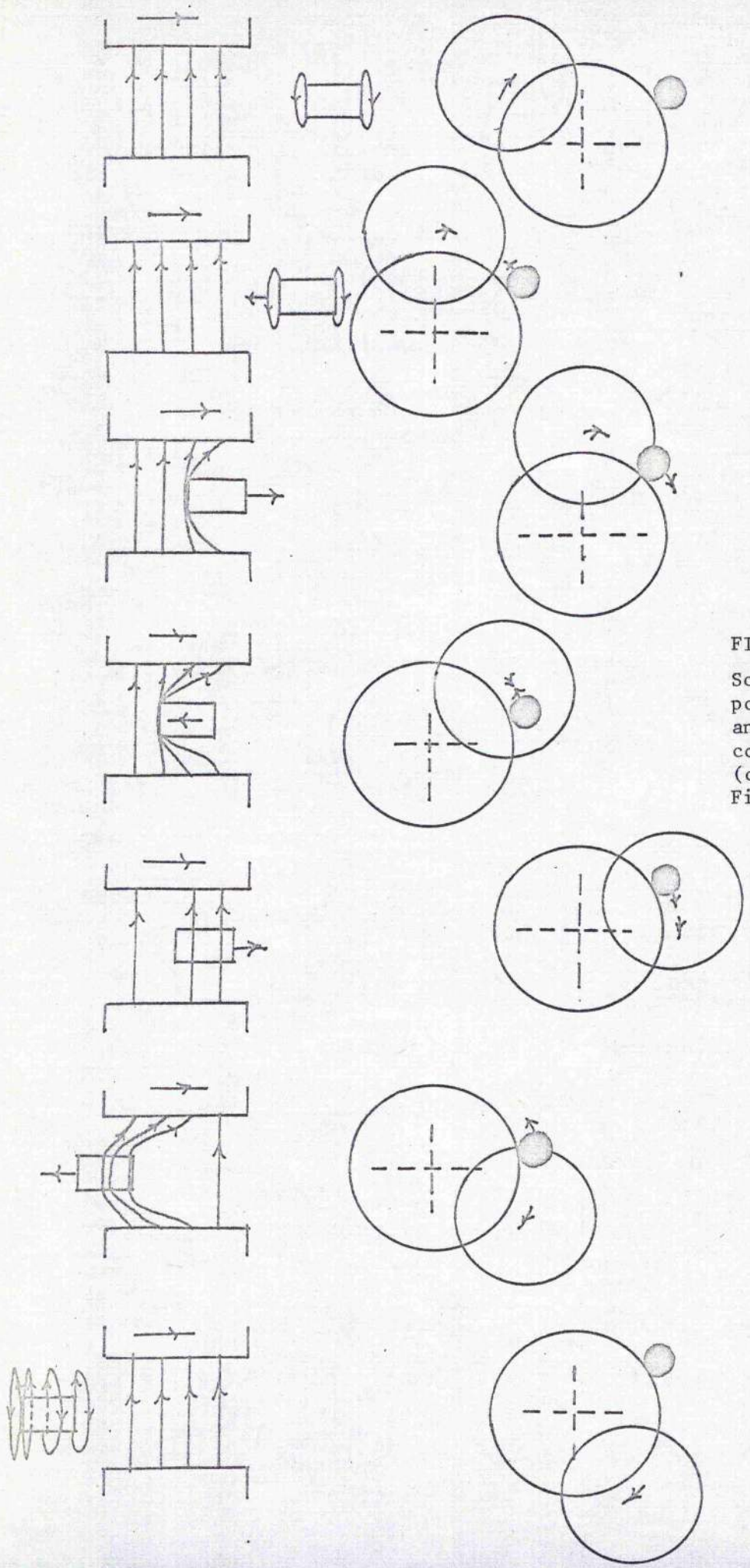

FIGURE 6.3

Schematic diagram of the positions of the magnet and the specimen corresponding to curves (c), (d), and (e) of Figure 6.1.

The three forces F_A, F_s and F_p each reach their maximum value at different values of the applied field. The forces were constant at their maximum values for applied fields, $H_{Rmax} < H_{amax} < H_{c2}$.

We have interpreted the F_s as that due to the Meissner effect and the surface pinning effects which resist the penetration of the flux lines into the specimen, the F_p force as that due to the pinning effect of the bulk, and the F_A force as that due to the interaction between the external field and the remanent field inside the specimen.

The forces under isothermal conditions were not changed in any particular way by sweeping the field at different speeds. Figure 6.4 shows a set of rotation signals for specimen NbI at 4.22 K, recorded at the same magnetic field but with different sweeping speeds.

Hereinafter, we shall consider the forces F_s, F_p and F_A, separately but will concentrate on F_p.

6.4.2 Pinning forces in Nb specimens

(a) Nb I

The F_p and F_s forces measured on the mechanically polished NbI at 4.22 K, 3.73 K, 3.12 K, 2.58 K and 1.78 K are plotted in Figures 6.5 and 6.6, rspectively. The y-axis of Figures 6.5 and 6.6, and other graphs in this chapter is H_{amax}, the maximum value of the Gaussian profile of the applied field, and the x-axis is the total force acting on the whole specimen.

The F_s force at 4.22 K, 2.95 K and 2.44 K and the F_p force at 4.22 K, 2.95 K, 3.44 K, 2.09 K and 1.76 K on the chemically polished NbI are shown in Figures 6.7 and 6.8, respectively. In Figure 6.7, the dotted line of curve 4.22 K is the F_{sp} measurement which is the curve of F_s when the sweep

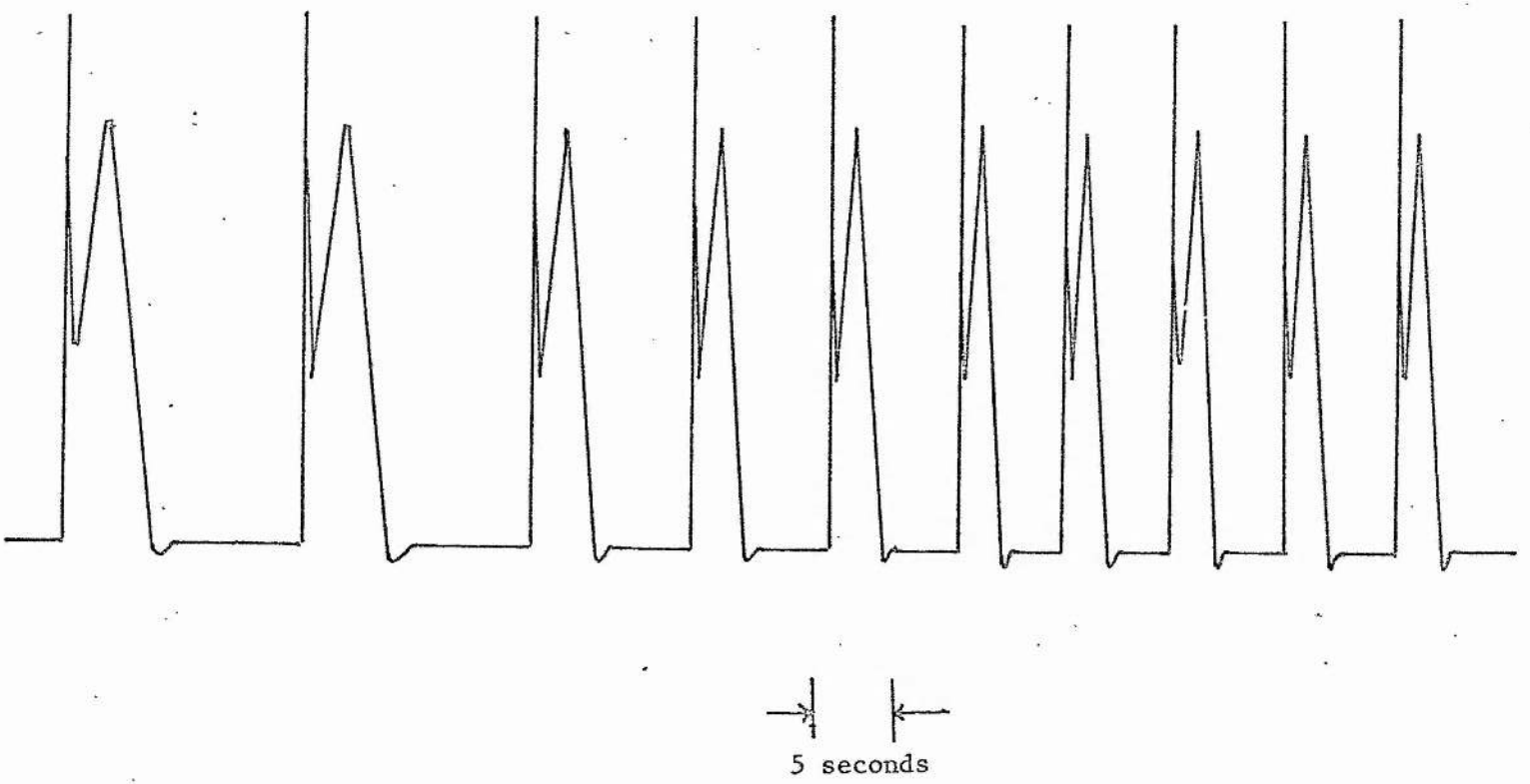

FIGURE 6.4 Signals of rotations of the specimen at different sweeping speeds with a constant H_{a-max}.

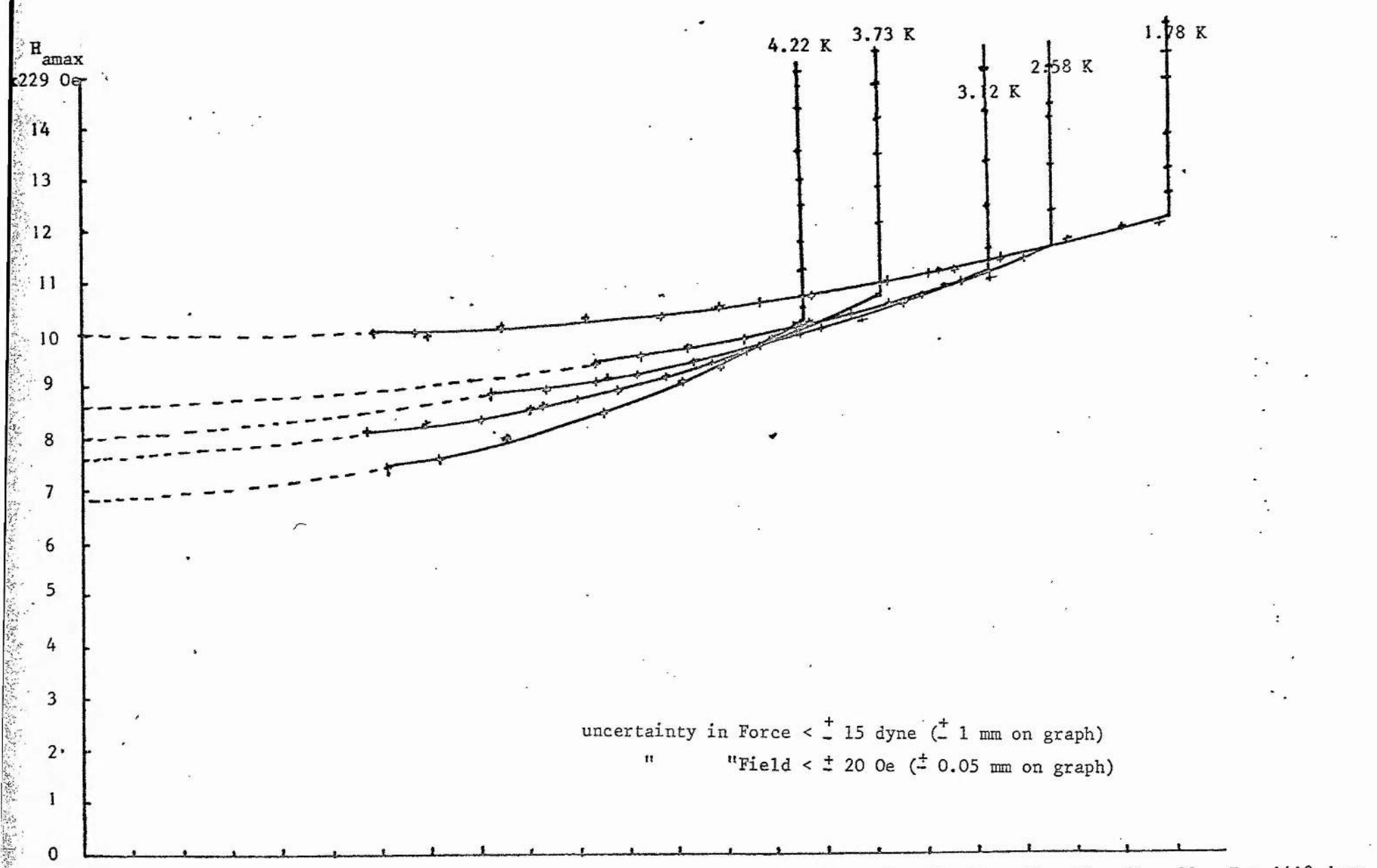

FIGURE 6.5 F_p vs H_{amax} of mechanically polished NbI at different temperatures

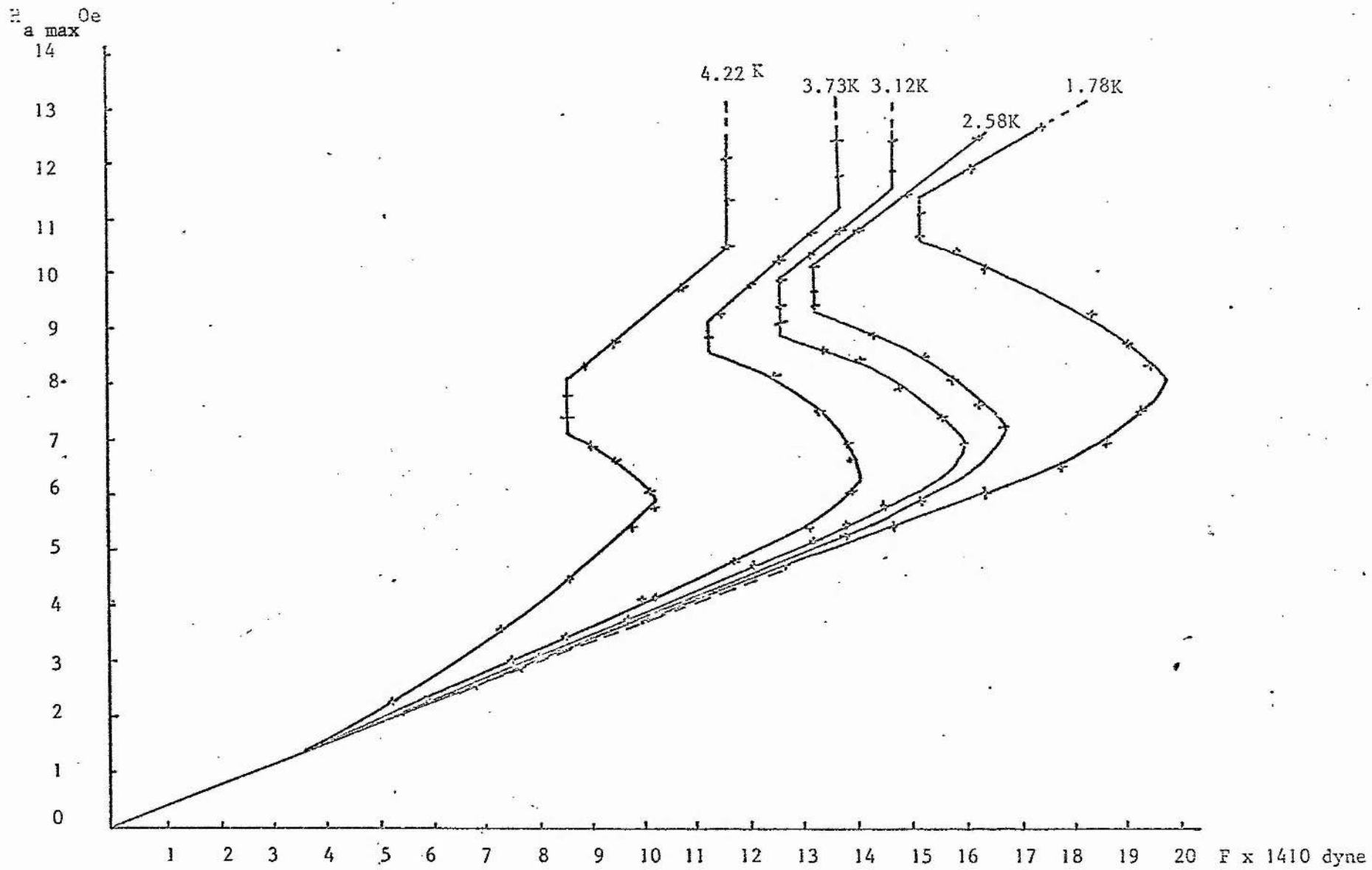

FIGURE 6.6 F_s vs $H_{a\ max}$ of mechanically polished NbI at different temperatures

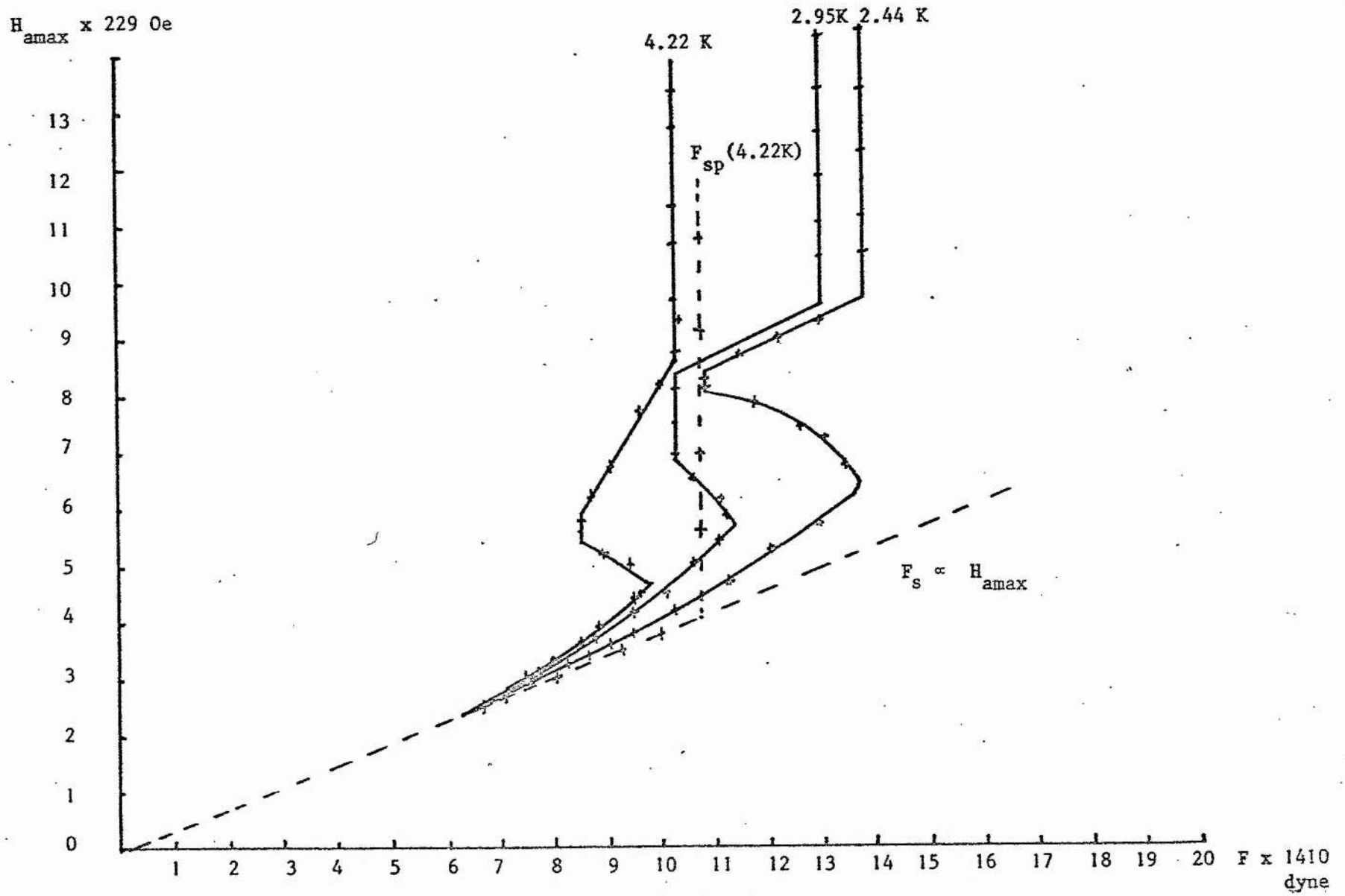

FIGURE 6.7 F_s vs H_{amax} of chemically polished NbI at different temperatures

The extension of the dashed line from the origin past the abscissa value of 10.5 is described at the bottom of page VI-20. Error bars similar to Figure 6.5.

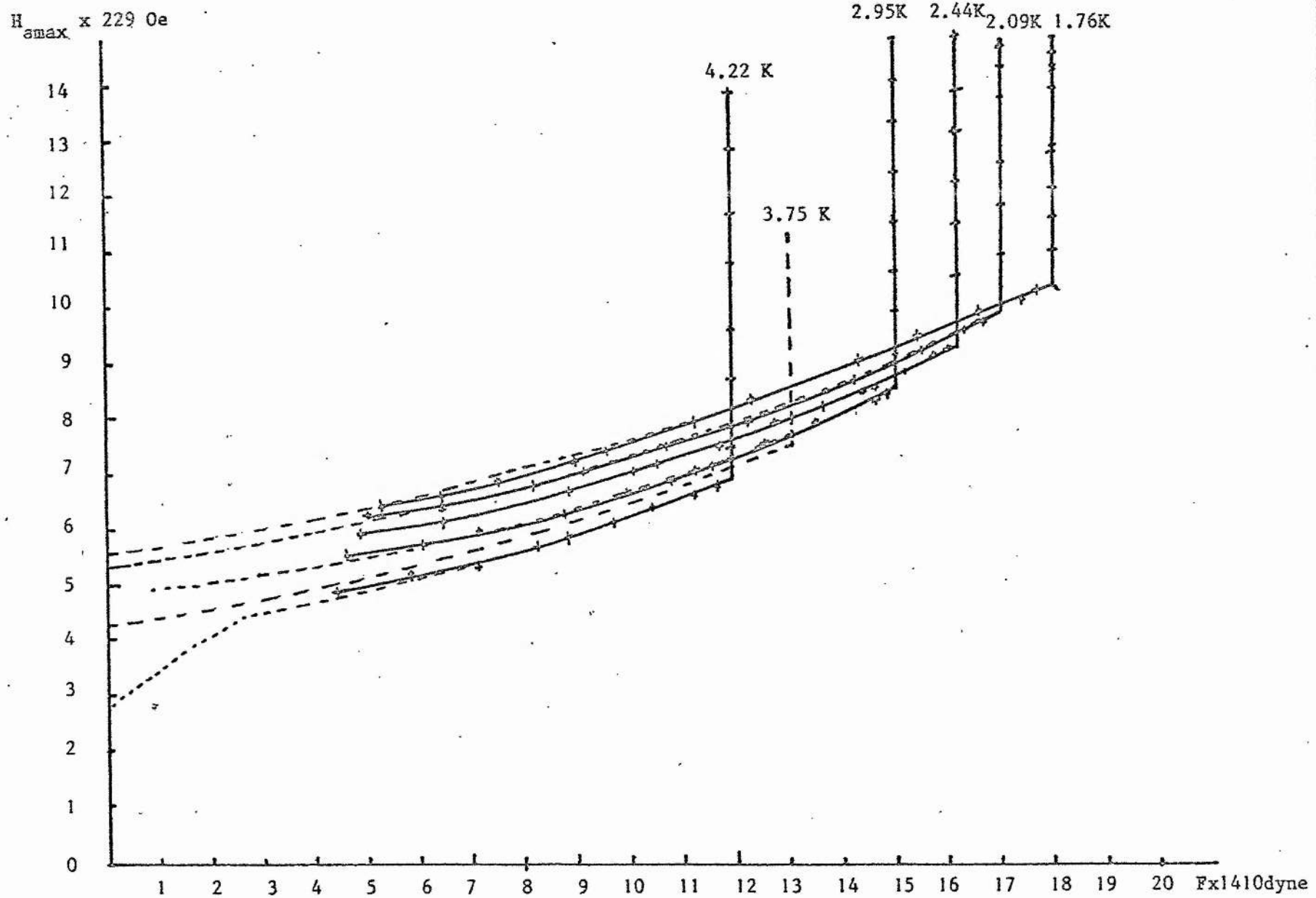

FIGURE 6.8 F_p vs H_{amax} of chemically polished NbI at different temperatures

Error bars similar to Figure 6.5.

field makes its first passage over the specimen.

(b) NbII specimen

The F_s and F_p forces on the Nb II specimen were measured at various temperatures after it had been treated in three different ways, mechanically polished, oxidized, and chemically polished. The results for F_s and F_p of the specimen at 4.22 K are plotted in Figure 6.9.

(c) Nb III Specimen

The force measurements on this annular shaped specimen, Nb III, were much more complicated because the dimensions of the specimen were larger than the field region. While the field swept round the annulus at a steady rate, the annulus moved intermittently as it was affected by flux pinning and flux release as well as continuous superconducting - mixed state transitions as the field swept along the specimen. Although it was not possible to relate a particular specimen rotation to a particular source, nevertheless the same maximum angle of rotation was recorded during each passage of the same applied field. Curve (a) in Figure 6.10 shows forces corresponding to these maximum rotations at different values of H_{amax}.

(d) Nb IV Specimen

The force measurement on the short annular segment Nb IV specimen showed similar rotation signals to the Nb I and the Nb II specimens. The F_p, F_s and F_A forces vs H_{amax} have been plotted in curves (b), (c) and (d), respectively, in Figure 6.10. The temperature was 4.22 K.

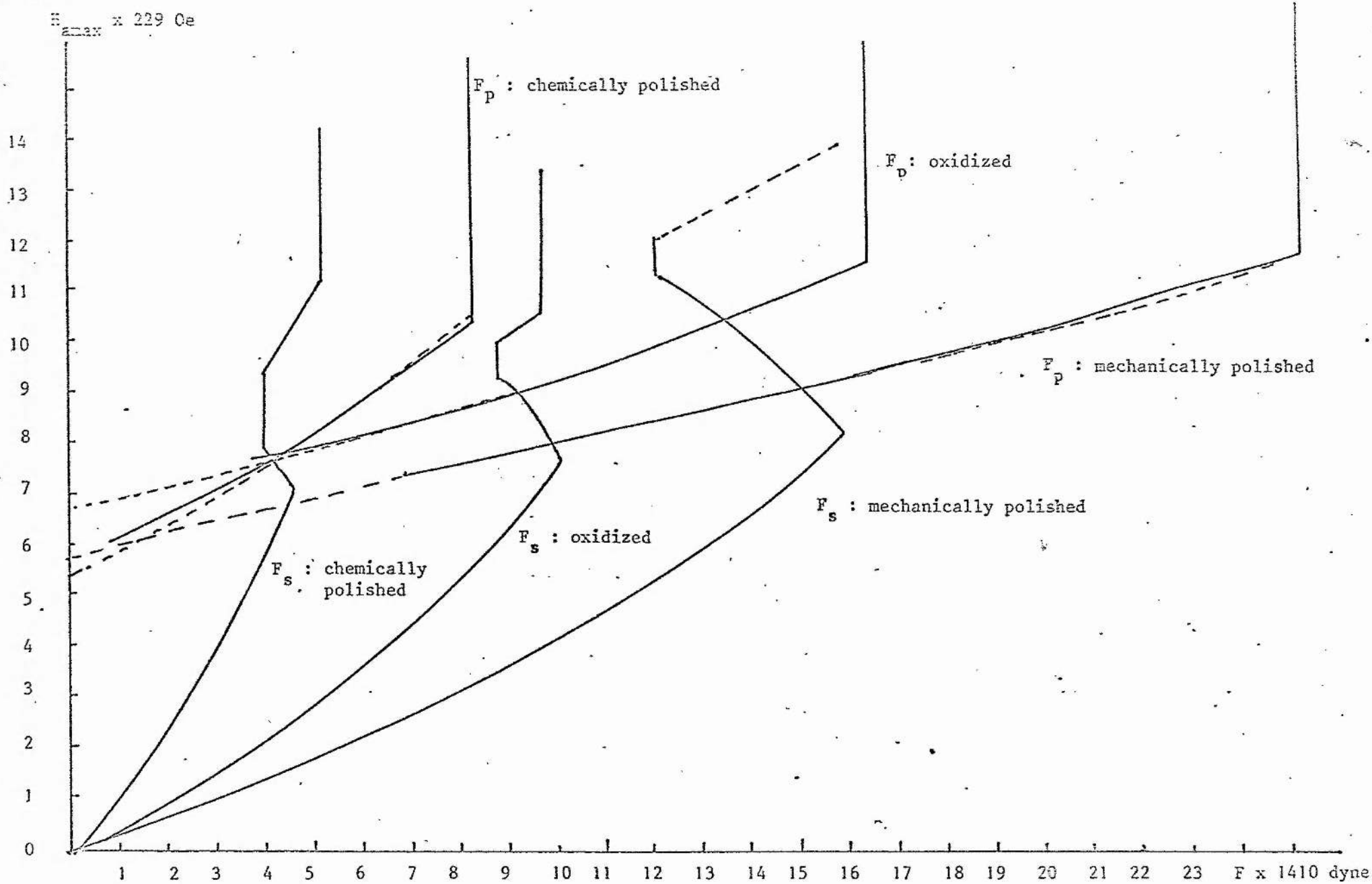

FIGURE 6.9 $F_{p,s}$ vs H_{amax} of NbII with different surface polishing at 4.22 K

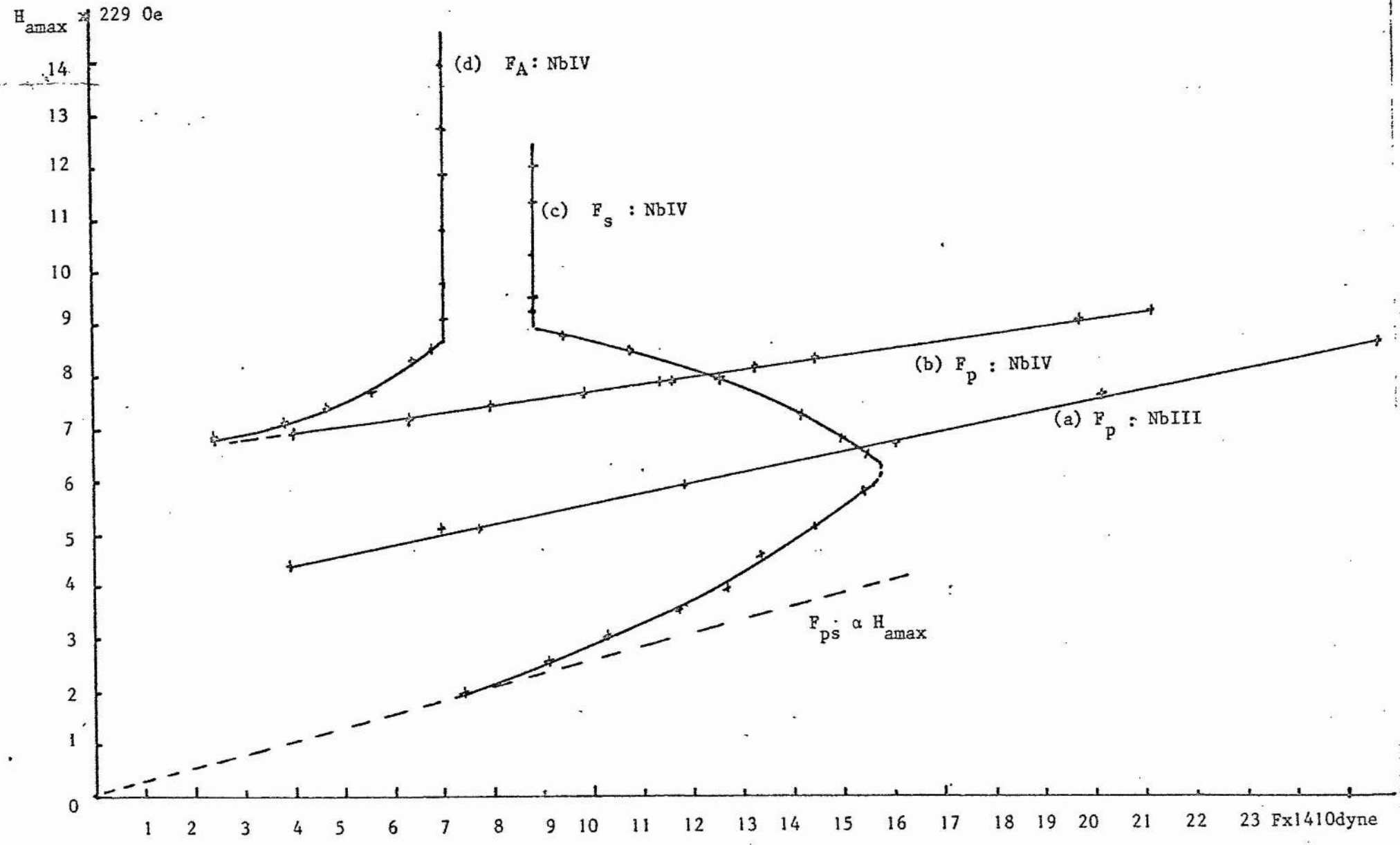

FIGURE 6.10 The pinning forces; F_p of NbIII and F_p, F_s, and F_A of NbIV vs H_{amax} at 4.22 K

Error bars similar to Figure 6.5.

6.4.3 Pinning forces in Pb-In Alloys

The angles of the rotation in the measurements on $Pb_{90}In_{10}$ and $Pb_{93}In_{7}$ specimens were much smaller than those in the Nb specimens, as we might expect. The F_p force curves of the specimens $Pb_{90}In_{10}$ and $Pb_{93}In_{7}$ at 4.22 K and 2.19 K are plotted in Figure 6.11. The magnitude of F_s was too small to be measured accurately in our apparatus, as is evident in the right top corner insert in Figure 6.11, which is the combined F_s and F_p signal from the $Pb_{93}In_{7}$ alloy at maximum sensitivity.

6.5 Discussion

6.5.1 Pinning forces and the magnetization curve

The pinning force measurements on the two Niobium specimens as seen in Figures 6.5, 6.6, 6.7, 6.8 and 6.9, have shown that both F_p and F_s pinning forces for the mechanically polished specimens were greater than those for the oxidized specimens, and both were greater than those for the chemically polished specimens. The magnetization curves of the two specimens; e.g. Nb II shown in Figure 4.14, with different surface polishing, have shown that the magnetic induction B of the specimen in a particular field was increased after oxidizing and again after chemical polishing,

B_{H_a} (mechanically polished) $<$ B_{H_a} (oxidized) $<$ B_{H_a} (chemically polished). Although we were not able to analyse in microscopic detail the surface after any particular treatment, it is still possible to conclude that the oxidizing and chemical polishing processes have reduced

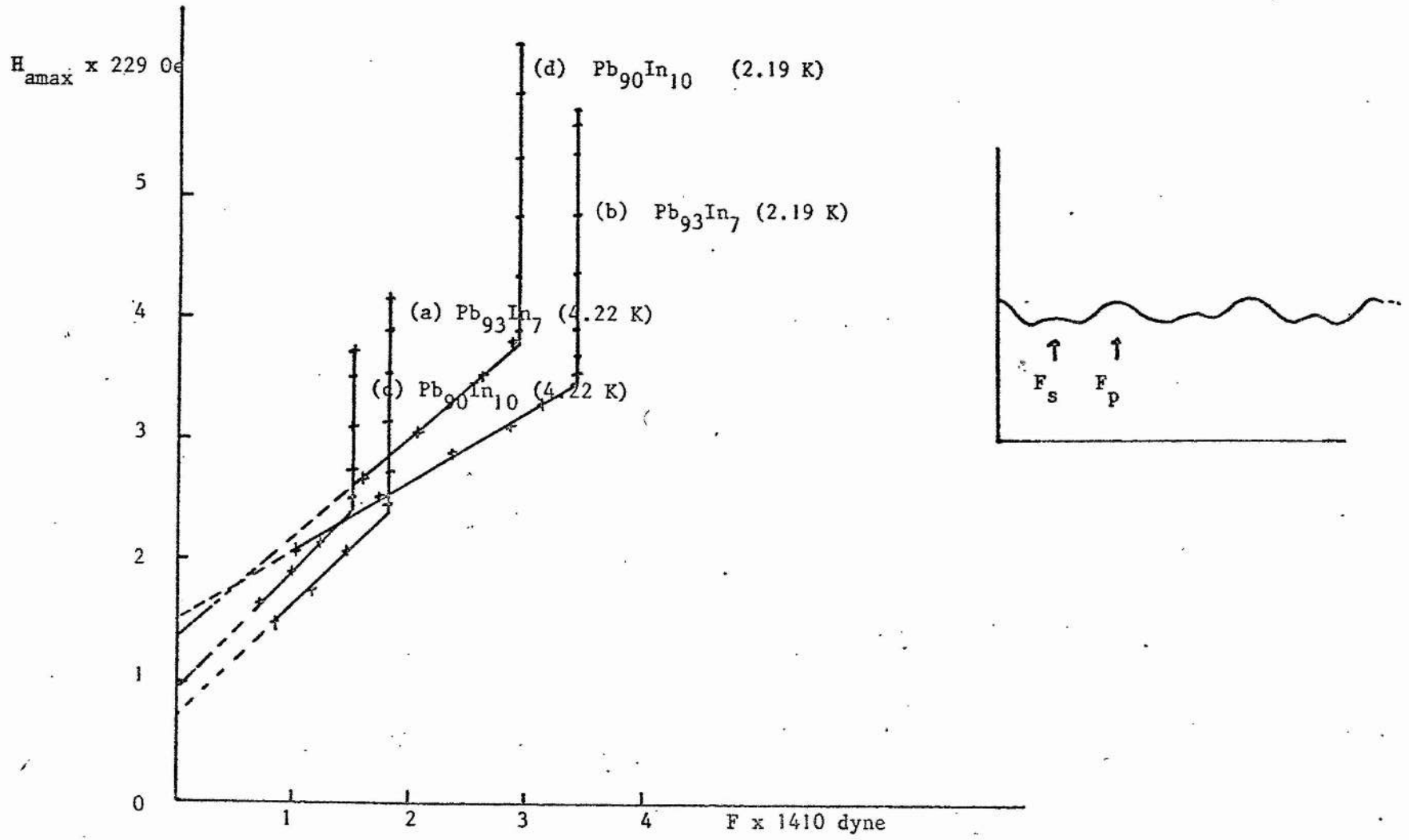

FIGURE 6.11 F_p vs H_{amax} of $Pb_{93}In_7$ and $Pb_{90}In_{10}$ at different temperatures
Error bars similar to Figure 6.5.

the number of surface defects. Therefore the surface pinning force F_s was smaller, and the bulk pinning force F_p was also reduced due to the decrease in the pinning sites on the top and bottom surfaces of the cylinder normal to the field.

In order to check whether it is correct to interpret the force measurements in terms of F_s and F_p, we measured the force and the magnetization curve of the chemically polished specimen Nb II after its cylindrical surface (excluding the top and the bottom surfaces) was roughened with a file. The change in the magnetization curve is shown in Figure 4.4. The signals arising from the torque changes during field passage are shown in Figure 6.1 (g). The change in the F_s signal is about 1.5° which corresponds to 3550 dynes but there was no change in the F_p signals.

Another reason for this F_p and F_s interpretation is that the F_p forces appeared only when H_{amax} exceeded H_{c1}^* and reached a maximum at $H_{amax} = H_{Rmax}$.

(a) F_A Forces

The "attractive" interaction between the specimen and the applied field were observed only when the field approached a specimen which had been previously magnetized. This indicates that this attraction was caused by the interaction between the remanent field in the specimen and the sweeping field. The interaction is attractive because of the interaction of the sweeping field and the 'residual field' of the flux lines trapped near the surface as sketched in Figure 6.12a. The interaction becomes a repulsive one if the applied field has opposite direction to the trapped field. We have plotted the attractive force between the

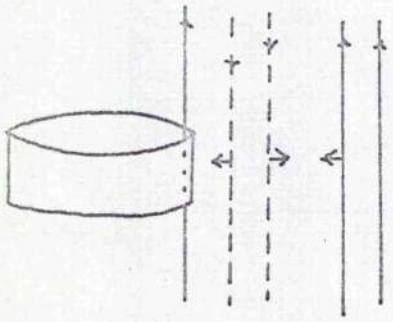

(a) Attractive interaction between the residual flux and the external field.

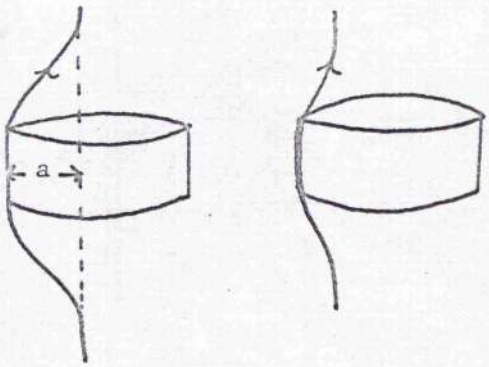

(b) Flux curvature a; the repulsive force.

(c) Plan view; penetration of flux lines into specimen

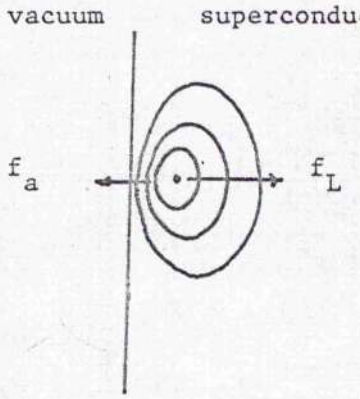

(d) Vortex current and Meissner current near the surface, f_a is the attractive force of the vortex to the surface and f_L is the repulsive force.

FIGURE 6.12

specimen and the applied field as a function of different values of applied field in Figure 6.13(a) and the repulsive force in Figure 6.13(b). The specimen was Nb I at 2.95 K with chemically polished surface. The repulsive force as shown in Figure 6.1 (f) is the sum of the F_A and the F_s forces. The F_s force is plotted in curve (c). Curve (b) is not quite equal to the sum of $(F_A + F_s)$. We do not know whether this was due to the very fast rotation which caused errors in the measurements or if it arose from some other cause.

(b) F_s Forces

The magnitude of the F_s forces due to field gradients created by an external field making its first passage over a pure Meissner state, F_{sp}, was different from that over a specimen with remanent field. We have measured only a few values of F_{sp} at different applied fields because it was awkward with the experimental set up to bring the specimen back to a pure Meissner state. The results of F_{sp} on the chemically polished Nb I specimen at 4.22 K are shown in the dotted lines in Figure 6.7, and indicate that

$$F_{sp} \propto H_{amax}, \qquad 6.5.1.$$

where the coefficient of proportionality must depend on the surface condition of the specimen. In the lower field region, the remanence in the specimen was small, and therefore the difference between F_{sp} and F_s was negligible, and therefore the coefficient can be determined. F_{sp} determined from the Equation 6.4.1 for different specimens are plotted in Figures 6.7, 6.9 and 6.10 with dotted lines. A schematic diagram of this kind of interaction is shown in Figure 6.2 (b). As the applied field becomes larger the curvature

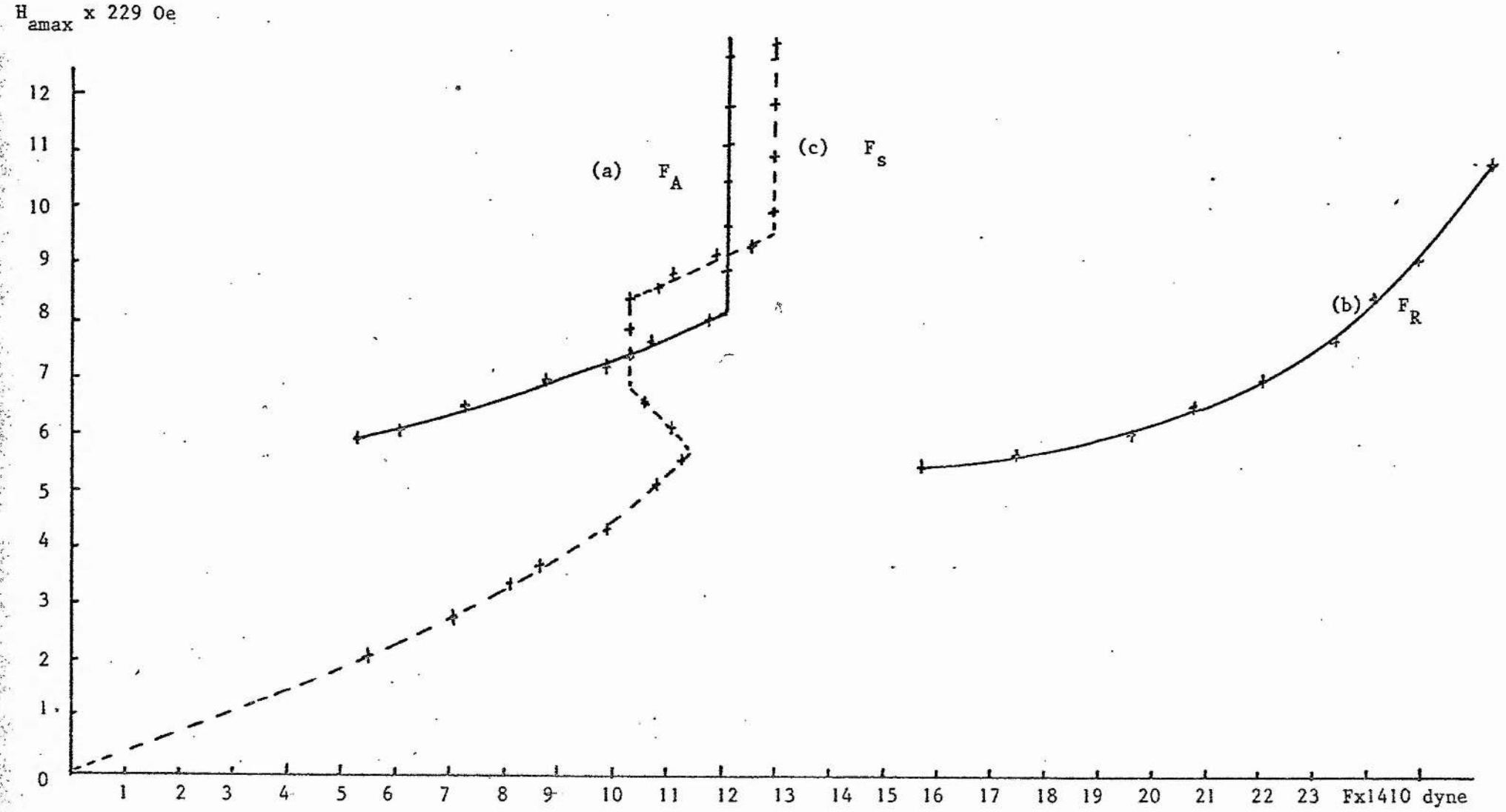

FIGURE 6.13 The F_A, F_s and F_R, vs H_{amax} of chemically polished NbI at 2.95 K

Error bars similar to Figure 6.5

of the flux in Figure 6.12 (b) will increase and reach a maximum value just before the field exceeds H^*_{c1}. A sketch of the probable mode of field penetration into a specimen is given in Figure 6.12 (c) (Lerski, 1973).

The repulsive force F_s between the applied field and a specimen with some remanent field was much more complicated than F_{sp}, as shown in Figures 6.5, 6.7, and 6.9. There are two types of force; attrative and repulsive acting on the surface during the penetration as shown in Figure 6.12 (d) (Bean and Livingston 1969, Shmidt and Mkrtchyan 1974). For a single vortex trapped near the surface, the distribution of the vortex current is distorted by the surface of the superconductor, and the currents are denser on the side near the surface; consequently the superfluid velocity is larger on this side. Because of the difference of Bernoulli pressures on the two sides, the vortex is drawn to the surface. In other words, there is a Lorentz force exerted on the vortex by its image. The energy corresponding to this interaction for $x >> \xi$ and $\lambda >> \xi$ is

$$E(x) = \varepsilon_1 - \left(\Phi_o / 4\pi\lambda\right)^2 K_o\left(2x/\lambda\right), \qquad 6.5.2.$$

where $\varepsilon_1 = \left(\Phi_o / 4\pi\lambda\right)^2 \log\left(\lambda/\xi\right)$ is the energy per unit length of a single flux line far from the surface. For $x >> \xi$, $E(x)$ decreases to zero as $e^{-2x/\lambda}$.

The repulsive force is the Lorentz force f_L exerted by the Meissner current of the external field, and is directed toward the interior of the specimen. It is repulsive if the vortex and the external field have the same direction. The energy corresponding to this is

$$E_R(x) = \Phi_o H \, e^{-x/\lambda} / 4\pi \qquad 6.5.3.$$

The vortex tends to move away from the surface under the influence of f_L, and this lowers the surface energy by $E_R(x)$.

The sum of equations 6.5.2 and 6.5.3 is equal to the Gibbs free energy per unit area near the surface, giving

$$\Delta g(x) = E(x) + E_R(x)$$

$$= \varepsilon_1 - (\Phi_o/4\pi\lambda)^2 K_o(2x/\lambda) + \frac{\Phi_o H}{4\pi} e^{-x/\lambda} \quad , \qquad 6.5.4$$

which represents the barrier to the penetration of vortices. This is called the Bean-Livingston barrier. As the remanent field gets greater the barrier decreases and the F_s needed to cross the boundary is decreased. When the remanent field becomes still larger the interaction between vortices become appreciable and there is an extra contribution to the Gibb's free energy. Equation 6.5.4 then has an extra term, giving

$$\Delta g(x) = E(x) + E_R(x) + \sum_{ij} U_{ij},$$

where $U_{ij} = \Phi_o H_{ij}/4\pi$. This raises the barrier energy with a consequential increase in F_s. The latter reaches a maximum which remains constant when the maximum remanent field of the specimen is reached.

Our F_s measurements agree qualitatively with this model. The exact calculation of F_s is very difficult since one has to calculate the exact distribution of the remanent field and we have no knowledge of the microscopic structure of the specimen.

(c) The bulk pinning force F_p

On the Irie-Yamafuji model, the bulk pinning force is given by $F_p = \alpha B^\gamma$. The results of our measurements of F_p with the chemically polished Nb I and the mechanically polished, oxidized, and chemically polished Nb II

specimens are compared with the Irie-Yamafuji model in Figures 6.8 and 6.9. The dotted lines are calculated from the magnetization curve measurements and the full lines are from our experimental results. The values of F_p for the chemically polished Nb I specimen at various temperatures are

$$F_p = 55.5\ B^{0.79} \text{ dyne at } 4.22 \text{ K},$$
$$F_p = 58.9\ B^{0.79} \text{ dyne at } 3.75 \text{ K},$$
$$F_p = 61.7\ B^{0.79} \text{ dyne at } 2.95 \text{ K},$$
$$F_p = 63.9\ B^{0.79} \text{ dyne at } 2.06 \text{ K},$$

and

$$F_p = 64.1\ B^{0.79} \text{ dyne at } 1.71 \text{ K}.$$

The value of F_p for the mechanically polished Nb II is

$$F_p = 43.5\ B^{0.87} \text{ dyne at } 4.22 \text{ K},$$

for the oxidized Nb II is

$$F_p = 43.6\ B^{0.8} \text{ dyne at } 4.22 \text{ K},$$

and for the chemically polished Nb II is

$$F_p = 43.6\ B^{0.73} \text{ dyne at } 4.22 \text{ K}.$$

The values of γ in the above expressions were determined from the remanence field via Equation 6.3.26 as described in Chapter IV. The value of γ probably depends only on the density and distribution of the pinning sites. The values of the coefficient α, which varies with temperature, is determined by

$$\alpha = {}^{F_{pmax}}/_{B^{\gamma}_{H_{Rmax}}} \qquad 6.5.5$$

We have used the experimental maximum force F_{pmax} and the magnetic induction $B_{H_{Rmax}}$ of the specimen at H_{Rmax}. Although the surface force F_s, is not small in these specimens, the F_p force determined from Equation 6.5.5. with B derived from the magnetization curve agrees with the experimental measurements as shown in Figures 6.8 and 6.9. Surface effects only stop the flux from penetrating into the specimen but do not affect the flux lines inside the specimen, and the density of flux lines is still given by the magnetization.

6.5.2 Temperature dependence of the bulk pinning force F_p

The maximum bulk pinning force F_{pmax} in different specimens; mechanically polished and chemically polished Nb I and Nb II, oxidized Nb II , and Pb-In alloys, plotted as function of the reduced temperature T/T_c, are shown in Figure 6.14. The results can be well-represented by a remarkably simple equation

$$F_{pmax}(T) = F_{pmax}(o)\ (1-\frac{T}{T_c}), \qquad 6.5.6.$$

where $F_{pmax}(o)$ is the maximum bulk pinning force of the specimen at zero temperature. The magnitudes of $F_{pmax}(o)$ for different specimens were derived by extrapolating the curves in Figure 6.14 to intersect the y-axis, and are:

Specimen	$F_{pmax}(o)$ (dyne)	T_c(K)
Mechanically polished Nb I	38.4×10^3	9.28
Chemically polished Nb I	30.9×10^3	9.28
Mechanically polished Nb II	65.2×10^3	9.28
Oxidized Nb II	42.4×10^3	9.28
Chemically polished Nb II	20.8×10^3	9.28
$Pb_{93}\ In_7$	7.3×10^3	6.5
$Pb_{90}\ In_{10}$	6.1×10^3	6.4

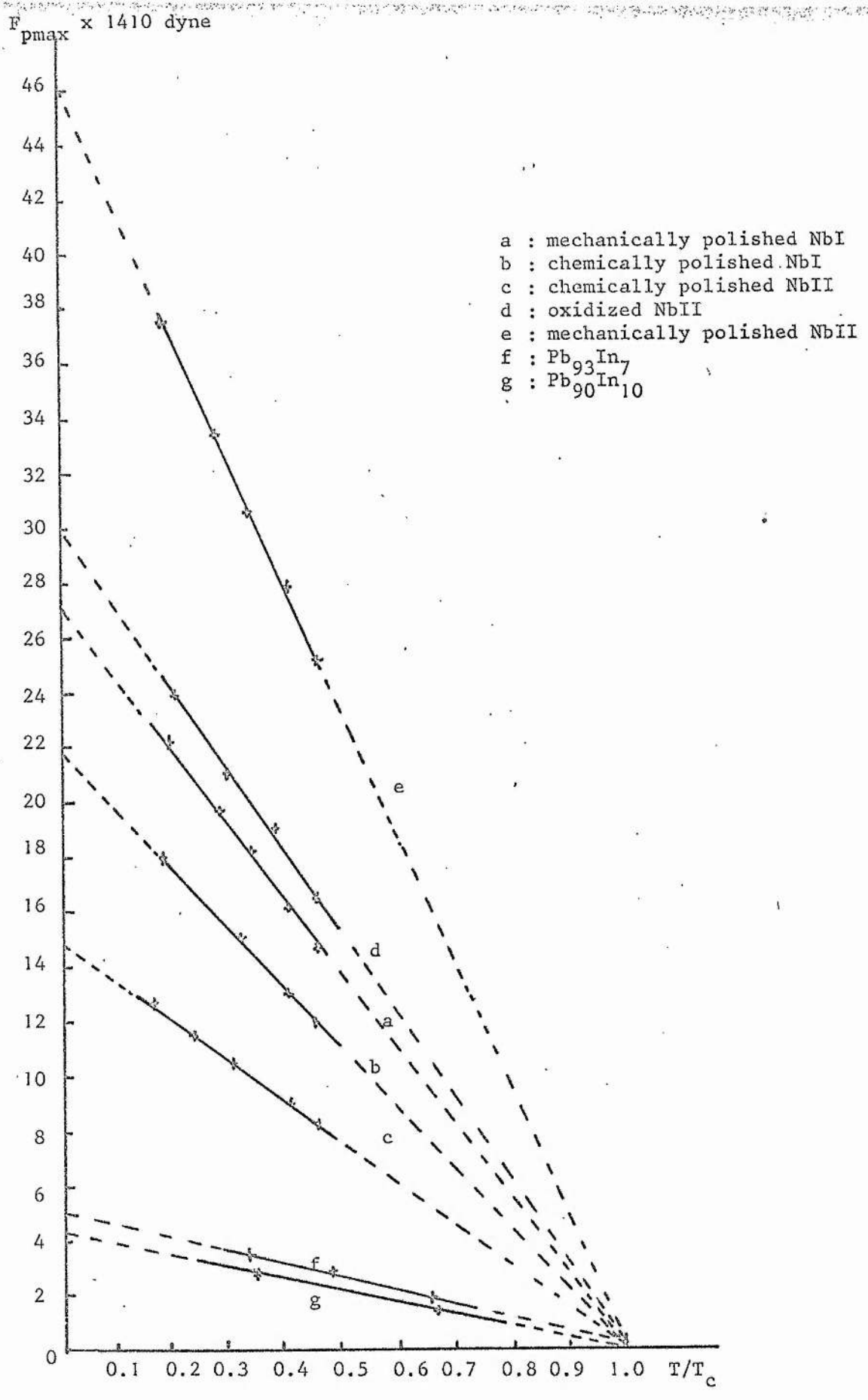

FIGURE 6.14 Temperature dependence of F_{pmax} of different specimens

The general expression for the pinning force per unit length, for all types of pinning mechanisms, is given by Kronmuller (1974) as

$$F_p(\text{unit length}) = \frac{H_c^2}{8\pi} \, l_{int} \, (\kappa, \lambda, N_{V,A}, \epsilon_i), \qquad 6.5.7.$$

where l_{int} corresponds to an effective interaction length which depends on the parameters of the material and on defect properties ϵ_i, and $N_{V,A}$ corresponds to the number of defects in a unit volume or area.

Neither Equation 6.5.7 nor Equation 6.3.29 agrees with our experimental results as shown in Equation 6.5.6, but Ekin and Clem (1975) have derived the magnetic coupling force

$$F_{m.c.} \propto (1-t), \text{ at } T \text{ near } T_c,$$

in their calculations for the superconducting d.c transformer, which is similar to Equation 6.5.6.

If we take Anderson's (1962) original concept of a pinning barrier which was that the flux lines were trapped in a potential well of depth Δg, the rate at which they can escape from the pinning barrier can be expressed in terms of an activation energy U,

$$R = R_o \exp (- U/kT), \qquad 6.5.8$$

where R_o is the natural frequency of vibration of the flux line and k is Boltzmann's constant. The activation energy U of a flux bundle may be written

$$U = \Delta g - V_p \, F1,$$

where V_p is the bundle volume, F is the gradient of the magnetic pressure which is equal to F_p of the pinning site at the critical point just before the release of the bundle, and l is some characteristic length relating the force to an energy. If the rate of escape of the flux from the potential well at $F = F_{pmax}$ is designated as R_c, Fietz and Webb (1966) have given

$$F_p = [\Delta g - k\, T \ln (R_o/R_c)]\, (lV_p)^{-1} \qquad 6.5.9$$

If we assume that R_c and l are independent of temperature, we have

$$F_p(o) = \Delta g (l\, V_p)^{-1} \qquad 6.5.10$$

at $T = 0$. Since $F_p(T_c) = 0$ and $(l\, V_p)^{-1} \neq 0$ at $T = T_c$, we have

$$\Delta g = k\, T_c \ln (R_o/R_c) \qquad 6.5.11$$

Rewriting Equation 6.5.9 as

$$F_p(T) = [\Delta g - k\, T_c \ln (R_o/R_c)\, \frac{T}{T_c}]\, (l\, V_p)^{-1}, \qquad 6.5.9a,$$

and substituting Equations 6.5.10 and 6.5.11 into Equation 6.5.9a, we obtain

$$F_p(T) = F_p(0)(1 - \frac{T}{T_c}) \qquad 6.5.12$$

This result is in agreement with our experimental observations. Our temperature dependence of F_p has not been reported before, to our knowledge, which may be because the F_{pmax} of a specimen determined from critical current measurements is somehow misleading due to F_{pmax} and J_c both being dependent on T and B.

6.5.3 The critical current J_c as predicted from the pinning force.

The calculated critical currents in the chemically polished Nb I, and mechanically polished, oxidized and chemically polished Nb II specimens at 4.22 K are plotted as functions of H_{amax} in Figure 6.15. The values of J_c below H_{Rmax} were calculated using Equation 6.3.11:

$$J_c = \alpha B^{\gamma-1}$$

and above H_{Rmax} were calculated using

$$J_c = F_p / B.$$

The values of J_c do not go to zero at H_{c2}, and therefore some kind of modification such as Equation 6.3.27 or Equation 6.3.28 is needed. It would be useful to compare these calculated critical current densities with direct critical current measurements, but in our apparatus the specimens were too small to produce an observable voltage difference.

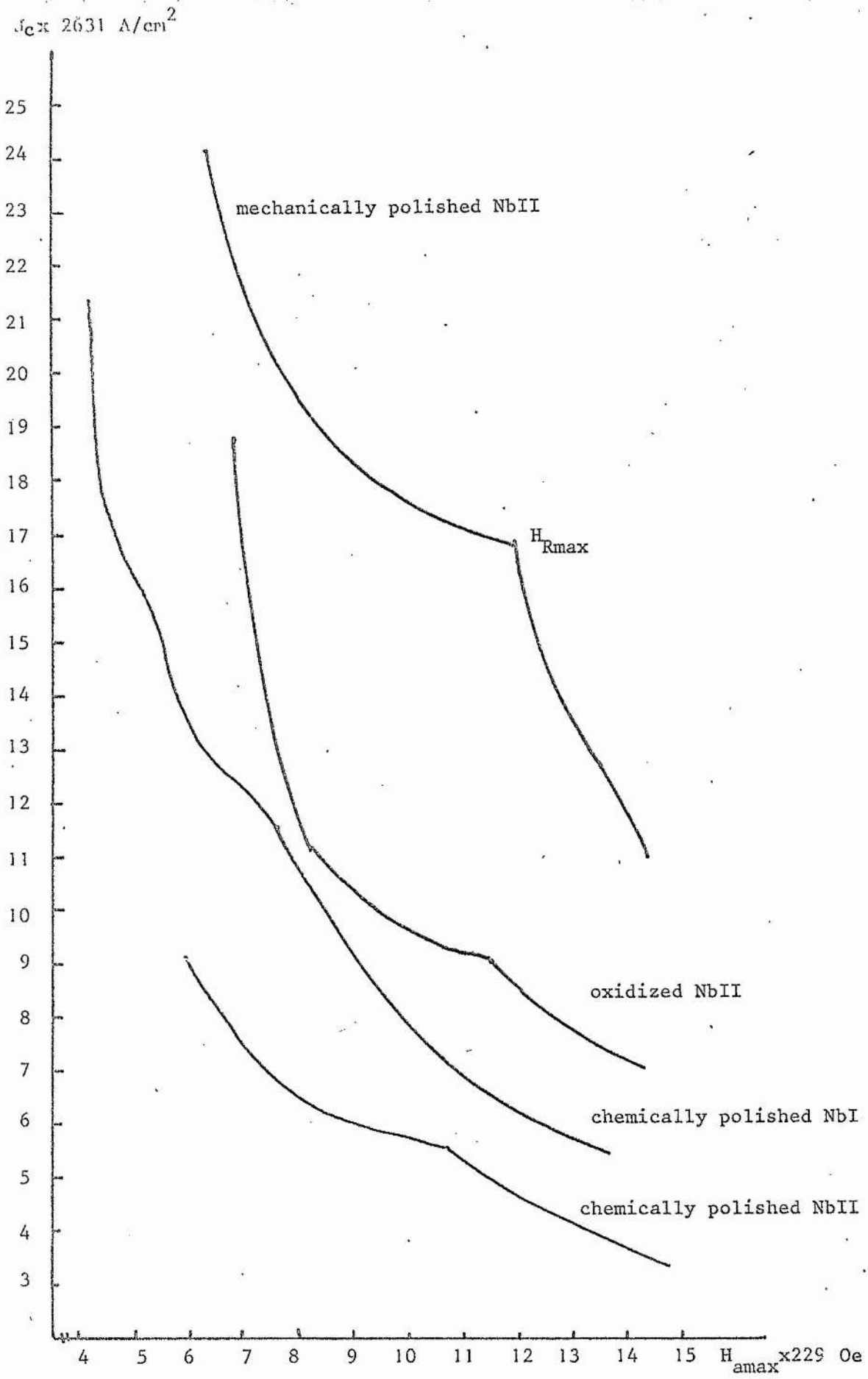

FIGURE 6.15 The predicted critical current density J_c vs H_{amax}

CHAPTER VII

MOTION OF THE FLUX LINES AND TRANSPORT PROPERTIES

CHAPTER VII

Motion of the Flux Lines and Transport Properties

7.1 Introduction

A normal domain in a superconductor cannot remain fixed in position in the presence of an electric current, i.e., transport current or induction current, and its motion as a result of a Lorentz-type force is expected to occur. This current-induced flux motion was noted by Shoenberg (1952) in a type I superconductor. Gorter (1957) proposed flux flow as a resistive mechanism. The first experimental evidence of flux flow in a hard type II superconductor was shown by Kim et al (1962, 1963). A stationary flux line distribution in a hard type II superconductor was interpreted in the previous chapter in terms of the critical state concept. The critical state of a superconductor can be distorted, not only by a sufficient transport current but also by flux gradient or by a thermal force. Resulting from these distortions, flux lines start to flow in a specimen if the force is sufficiently large. The motion of the flux lines generates an inductive-type electrical field as well as various dissipative and galvo-magnetic effects. The motion also carries entropy and gives rise to thermomagnetic effects, such as the Hall, Peltier, Ettinghausen and Nernst effects, which have been observed by Fiory and Serin (1966), Otter and Solomon (1966), and Lowell et al (1969). This enabled Kim et al to attribute the resistive state of a hard superconductor to the motion of flux lines. The resistive state model suggested that the specimen offers resistance to the flux flow. The resistance contribution arises from the pinning forces of the pinning sites, the viscous damping force, and the Magnus force (De Gennes and Matricon, 1964).

In this chapter, we will use as a basis this resistive state model to review all the possible forces involved, and compare it with our own experimental results, made on some irreversible type II superconductors under non-isothermal conditions.

7.2 Theoretical Conditions

7.2.1 Forces acting on the moving flux lines

The total forces associated with the flow of flux lines are:

$$\underline{f}_L - \underline{f}_M - \underline{f}_d - \underline{f}_p = 0 \quad \text{(isothermal)} \qquad 7.2.1$$

where f_L, f_M, f_d, and f_p are the Lorentz driving force, Magnus force, damping force, and pinning force, respectively. The Lorentz driving force f_L on a flux quantum ϕ_o can be written as

$$\underline{f}_L = \underline{J} \wedge \underline{\phi}_o.$$

The general form of the pinning force f_p was discussed in the previous Chapter VI, Section 6.5.1(c), and given as

$$\underline{F}_p = \alpha B^{\gamma}. \qquad 7.2.2$$

The Magnus force $\underline{f}_M$ was suggested by De Gennes and Matricon. It plays a role in the motion of vortex lines in a superconductor similar to the situation of the quantized vortex lines in superfluid helium. A rotating cylinder moving in a fluid, finds itself subjected to a pressure difference in the fluid in a direction perpendicular to the motion, which has the form

$$\underline{f}_m = x\, n_s\, e\, (v_\phi \wedge \underline{\phi}_o) \qquad 7.2.3$$

where x is a coefficient which gives the fraction of the Magnus force which

is acting and v_ϕ is the flow velocity. For most superconductors except those that are very pure, the magnitude of the Hall angle $(v_\phi \wedge \phi_o)$ is similar to that in the normal state, and x is much smaller than unity.

The damping force in the system can be described by a scalar damping factor (viscosity factor) η which contains all the dissipative processes, and is proportional to the flow velocity $\vec{v}_\phi$,

$$f_d = \eta v_\phi \qquad 7.2.4$$

The general form of equation 7.2.1 is

$$(J \wedge \phi_o) - x\, n_s\, e\, (\vec{v}_\phi \wedge \phi_o) - \eta v_\phi - \alpha B^\gamma = 0 \qquad 7.2.5$$

7.2.2 Dissipation under isothermal conditions

We consider a flat superconductor with its broad surface located in the x-y plane, and with the applied field $H_{c1} < H < H_{c2}$ perpendicular to the broad surface. Making a scalar product of v_ϕ on the both sides of Equation 7.2.5, and assuming x to be negligible,

$$-(J \wedge B) \cdot v_\phi = (F_p + F_d)\, v_\phi \qquad 7.2.6$$

The right hand side of Equation 7.2.6 gives the total power dissipated due to eddy current damping during the steady flux flow. Since it is a dissipative process, its magnitude is given by $J.E$, where

$$E = -\text{grad}\ V = -(v_\phi \wedge B) \qquad 7.2.7$$

and V is the voltage drop between two points on the specimen.

If we use the critical state concept, the Lorentz force is just balanced by the pinning force, and we use this to define the critical current density J_c of the specimen with induction B,

$$J_c = {}^{F_P}/_{B} \qquad 7.2.8$$

From Equation 7.2.6, we derive (Lowell 1970)

$$\frac{dV}{dx} = \phi_o B(J_x - J_c)/\eta \qquad 7.2.9$$

Here, we define the "flow resistivity" by

$$\rho_f = \frac{dE}{dJ_x} = \phi_o B/\eta \qquad 7.2.10$$

The original work of Kim et al (1963) gives the following empirical relation in the low temperature limit:

$$\rho_f/\rho_n = H/H_{c2}(o) \approx \xi^2/d^2, \qquad 7.2.11$$

where $\rho_n = (ne^2\tau/m)^{-1}$ is the resistivity in the normal state, and d is the interfluxline distance, and ρ_f/ρ_n is just the ratio of the superconducting to the normal area in the superconductor. A general expression of Equation 7.2.11 is

$$\rho_f/\rho_n = (H/H_{c2}(o))\ f(T/T_c). \qquad 7.2.12$$

where $f(T/T_c)$ is a slowly varying function of temperature. We can rewrite Equation 7.2.10 in the simple form

$$\eta = \phi_o H_{c2}(o)/\rho_n \qquad 7.2.13$$

which gives values slightly lower than experimenters have observed.

Clem (1968) has proposed a normal-core model which introduced an additional contribution to ρ_f from the irreversible entropy production which is associated with the temperature gradient in the vicinity of the core generated by the motion of the flux line. The rate of dissipation per unit length of normal core cylinder associated with the local temperature gradient is given by

$$Q = \eta_{th} v_\phi^2 = \int dx \int dy \; T_o \dot{S}$$
$$= \left[(\pi\xi^2 T (S_n - S_s)^2 / (k_n + k_s)\right]_{T=T_o} v_\phi^2 \quad , \qquad 7.2.14$$

where ξ is the radius of the core, and also

$$\eta(T)/\eta(o) = H_{c2}(T)/H_{c2}(o) + \eta_{th}(T)/\eta(o). \qquad 7.2.15$$

The contribution to ρ_f from the local temperature gradient is appreciable only in the impure superconductor and disappears in the pure limit.

There have been several phenomenological local theories based on the assumption that the normal electrons outside the core of the vortex can be neglected, and that the core can be treated as being fully normal resulting in dissipation due to the quasi-particle scattering by the lattice. Among these, Bardeen and Stephen (1965) have considered the force on a vortex line produced by a uniform transport current J_T. The electric field generated by the motion drives the current through the core, so the total flow is $J_T + J_o(r-v_\phi t)$, and where $J_o(r)$ is the circulation current of a stationary vortex. J_T represents the sum of the superfluid flow J_s and part of the normal flow J_n; part only because as a result of the Hall effect of the normal component in the region of the core, the motion of the vortex is at a Hall angle θ_H relative to the transport current. The component of the velocity in the direction of J_T is $(H/H_{c2})v_\phi$. This leads to a Hall field in the mixed state, which is the same as in the normal state for a field

equal to that in the core. Thus

$$\tan \Theta_H = \omega_c(H) = \eta/\pi\hbar m \ ,$$

where $\omega_c = e^B/m$ is the cyclotron frequency in the field H_{c2}, ηv_L is a viscous drag opposing the Lorentz force $J_T\phi_o$ on the vortex. Bardeen and Stephen derive

$$\eta = \phi_o H_{c2}(o)/\rho_n = \pi\hbar m\omega_c \ ,$$

which is the same as the Kim expression of Equation 7.2.13. In the pure limit $\omega_c(H_{c2})\tau >> 1$, they obtain

$$v_L = v_T \, H/H_{c2} \qquad 7.2.16$$

for the flow velocity.

Van Vijfeijken (1968) assumed a continuous chemical potential at the core, and also assumed that the transport current density J_T was uniform throughout the specimen, and calculated the electric field $\underline{E}$ to obtain

$$E_x = v_{Lx}B = J_T \rho_n \frac{2B}{h_v + H_{c2}}$$

$$E_y = v_{Lx}B = J_T R_H \frac{2B}{h_v + H_{c2}}$$

$$\rho_f = E_x/J_T = \rho_n \frac{2B}{h_v + H_{c2}} \qquad 7.2.16a$$

where h_v is the core induction and $R_H = -1/ne$ is the Hall constant of the normal state. The Hall angle was thus given by

$$\tan \Theta_H = e\tau h_v(H)/m = \omega_c(h_{core})\tau$$

These results are similar to those of Bardeen & Stephen. All of the above models are in agreement with the experimental results at low temperatures. The Hall angle increases with decreasing magnetic field H below H_{c2}, and becomes larger than the normal state Hall angle at H near H_{c2}.

A more fundamentally theoretical calculation has been given by Caroli and Maki (1967), and Maki (1969) in which they derived the flux flow resistivity in the dirty type II superconductor ($\kappa >> 1$) near H_{c2}:-

$$\rho_f/\rho_n = 1-\alpha^*(T)\left[1-H/H_{c2}(T)\right] \qquad 7.2.17$$

where $\alpha^* = {}^{H_{c2}}/_{\rho_n} \left(\frac{\partial \rho_f}{\partial H}\right)_{H_{c2}} = 4\kappa_1^2(0)/\left\{1.16\left[2\kappa_2^2(T)-1\right]+1\right\}$ 7.2.18

increases monotonically with temperature, with value $\alpha^*(o) = 1.7$ to $\alpha^*(T_c) = 5$ (Thompson 1970).

For the pure type II superconductor near H_{c2},

$$\alpha^* = \frac{m}{\alpha e N} \frac{H_{c2}}{\left\{1.16\left[2\kappa_2^2(T)-1\right]+1\right\}} \qquad 7.2.19$$

where m and N are the mass and the density of states of the electrons.

7.2.3 Dissipation under non-isothermal conditions

The motion of magnetic flux in a superconductor is associated with the transport of entropy. Under non-isothermal conditions, there is a temperature gradient built up in the specimen. If this temperature gradient maintains a constant value then there is a steady flux flow along the specimen. The total forces, including the thermal force due to the heat current acting on the vortex structure satisfies the following equation:

$$\underline{v}_\phi \wedge \underline{B} - S_\phi \text{ grad } T - x\, n_s e(\underline{v}_\phi \wedge \phi_o) - \eta \underline{v}_\phi - f_o = 0 \qquad 7.2.20$$

where S_ϕ is the transport entropy per unit length of flux line and other terms have the same definitions as before. This thermal force can be a driving force or a damping force depending upon the direction of the temperature gradient and on S_ϕ. Equation 7.2.20 is only valid for a specimen with a small temperature gradient. If the temperature gradient is too large, the flux lines at the hot end will move faster than at the cold end due to the damping drag being smaller at higher temperatures, and flux will move back towards the region of lower density.

The local rate of the increment of entropy per unit volume is given by using the Kelvin-Onsager relation of the thermodynamics of the irreversible processes (London 1950) as

$$\frac{dS}{dt} = - \underline{\nabla}(\underline{Q}/T) + \dot{S}_{th} + \dot{S}_{el}. \qquad 7.2.21$$

The first term on the right hand side represents the rate of increase of entropy arising from the flow of the entropy current, $\underline{Q}/T$ and

$$\underline{Q} = nT\, S_\phi\, \underline{v}_\phi \qquad 7.2.22$$

The other terms on the RHS of equation 7.2.21 represent the rate of irreversible entropy production and are proportional to the second power of the flux flow velocity. Therefore we have

$$S_{el} + S_{th} = (\eta + \eta_{th})v_\phi^2/T \qquad 7.2.23$$

Substituting Equations 7.2.13 and 7.2.14 into Equation 7.2.23, we obtain

$$S_{el} + S_{th} = \left\{ \phi_o H_{c2}(o)/\rho_n + \left[\frac{\pi\xi^2 T(S_n - S_s)^2}{k_n + k_s} \right] \right\}_{T_o} v_\phi^2/T \quad . \qquad 7.2.23a$$

When unit length of vortex is added to the specimen by increasing the average magnetic induction by δB, the entropy increase is

$$S_i = \frac{\phi_o \, \delta Q}{T \, \delta B} \qquad 7.2.24$$

where δQ is the heat increment required to maintain the temperature of the specimen constant. De Lange and Otter (1972) have derived the relation

$$S_i(T) = [\, \alpha\phi_o/2H_{c2}(T) \,] \; (S_n - S_s), \qquad 7.2.25$$

where α is a constant of the order unity.

We derive

$$S_i(T) = [\, \phi_o/H_{c2}(T) \,] \; . \; [\, S_n(T) - S_s(T) \,] \qquad 7.2.26$$

from equation 5.2.16, which agrees with the Stephen (1966) results.

In a specimen with a constant temperature gradient and flux flow velocity v_ϕ, the heat current of Equation 7.2.22

$$n \, T \, S_\phi \, v_\phi = -k\nabla T \qquad 7.2.27$$

where k is the thermal conductivity.

In a low magnetic field the vortices are well-separated and the transport entropy per flux line of unit length can be written as

$$S_\phi = -\frac{1}{4\pi}\frac{\partial H_{c1}}{\partial T}\ \phi_o \qquad 7.2.28$$

This relation is clearly not valid close to T_c where S_ϕ should approach zero. Instead we must use Equation 7.2.25 which implies that near T_c the interaction between fluxoids smears the field so that they are not distinct. The microscopic calculation of transport entropy for a dirty type II superconductor in a high field region has been calculated by Maki (1969),

$$S_\Phi(T) = \frac{1}{4eT}\ \frac{(H_{c2}-B)L_D(T)}{1.16\left\{2\kappa_2^2(T)-1\right\}+1} \qquad 7.2.29$$

where $L_D(T) = 1 + \bar{\rho}\ \psi^{(2)}(\frac{1}{2}+\bar{\rho})/\psi^{(1)}(\frac{1}{2}+\bar{\rho})$, with $\bar{\rho} = {eDH_{c2}}/{2\pi T}$ and $D = {lv}/{3}$ is the diffusion constant, ψ is the di-gamma function $\psi^{(2)} = {\Gamma'^{(2)}}/{\Gamma(2)}$, and $L_D \sim T^2$ at low temperature. Hu (1975) has modified Maki's analysis and made Equation 7.2.29 valid for all temperatures and fields. For pure superconductors, Maki (1969a) has derived

$$S_\phi(T) = \frac{1}{4eT}\ \frac{(H_{c2} - B)}{1.16\left\{2\kappa_2^2(T)-1\right\}+1}\ \ L_D(T) \qquad 7.2.29a$$

where $L_D(T)$ is a function of ${l}/{\xi}$. Equation 7.2.29 and Equation 7.2.29a are only qualitatively in agreement with experimental results (Fiory and Serin 1971).

Equation 7.2.20 has described all of the galvanomagnetic and thermomagnetic effects in a type II superconductor as first suggested by Volger (1966). The vortices in a type II superconductor moving with velocity $\vec{v}_\phi$ at a Hall angle θ_H give transverse and longitudinal voltages and temperature gradients in a plane specimen.

7.2.4 Summary

The total heat current associated with the motion of vortex lines in a type II superconductor can be derived by taking the scalar product of v_ϕ with equation 7.2.20, which gives the terms, taken in sequence and adding in brackets the ordinary thermal conduction, and putting in the appropriate signs,

$$0 + Q_{th} + 0 + Q_{el} + Q_p + (Q - k \nabla T) = 0 \qquad 7.2.30$$

The amount of heat absorbed by the vortices added to the specimen per unit time is

$$\dot{Q} = n T S_i v_\phi = \frac{n\phi_o}{H_{c2}(T)} T\{S_n(T) - S_s(T)\} \cdot v_\phi \quad . \qquad 7.2.31$$

The amount of heat generated due to the eddy current heating per unit time is

$$Q_{el} = J^2 \cdot \rho_f$$

$$= \eta \ v_\phi^2 \ ,$$

and from Equation 7.2.13 we have

$$Q_{el} = \phi_o H_{c2}(o)/\rho_n \cdot v_\phi^2 \ . \qquad 7.2.32$$

The heat contribution due to the local temperature gradient is

$$Q_{th} = \eta_{th} \ v_\phi^2$$

and from Equation 7.2.14 we have

$$Q_{th} = [\pi\xi^2 T(S_n - S_s)^2/(k_n + k_s)]_{T_o} \cdot v_\phi^2 \qquad 7.2.33$$

where ξ is the radius of the core. The values of $\pi\xi^2 = \phi_o/2H_{c2}(T)$ and $S_n = \gamma T$ are suggested by Bardeen and Stephen (1965).

The heat dissipated due to the pinning force is

$$Q_p = F_p \ v_\phi \ ,$$

and from Equation 7.2.2 we have

$$Q_p = \alpha B^{\gamma} v_{\phi}. \qquad 7.2.34$$

The heat current flow into or out of a specimen per unit time, to maintain a steady flux flow is given by

$$-k \nabla T = Q_{\text{in or out}}.$$

Rewrite equation 7.2.30 into the form

$$T n \frac{\phi_o}{H_{c2}(T)} \{S_n(T) - S_s(T)\} v_{\phi} - n \left[\left(\frac{\phi_o H_{c2}(0)}{\rho_n} + \frac{\phi_o T}{2H_{c2}(T)} \left\{ \frac{(S_n - S_s)^2}{k_n + k_s} \right\}_{T=T_o} \right] v_{\phi}^2 \right.$$

$$- \alpha B^{\gamma} v_{\phi} - k \nabla T = 0 \qquad 7.2.30a$$

The temperature gradient along the specimen is

$$\nabla T = \frac{1}{k} \left[\left(\frac{T n \phi_o \{S_n(T) - S_s(T)\}}{H_{c2}(T)} - \alpha B^{\gamma} \right) v_{\phi} - n \left[\frac{\phi_o H_{c2}(0)}{\rho_n} + \right. \right.$$

$$\left. \left. + \frac{\phi_o T \{S_n(T) - S_s(T)\}^2}{2H_{c2}(T) (k_s + k_n)} \right]_{T=T_o} \right] v_{\phi}^2 . \qquad 7.2.35$$

7.3 Experimental Results and Discussion

7.3.1 Introduction

The experimental results of the temperature variation due to the flux motion in $Pb_{90}In_{10}$, $Pb_{60}Tl_{40}$ alloys and in the Nb specimens are presented and discussed in this section. The measurements on the $Pb_{60}Tl_{40}$ and $Pb_{90}In_{10}$ annuli were carried out with the 'rotating permanent magnet apparatus' described in Chapter 2.5(b). As we mentioned before, this set-up was to examine the possibility of making a refrigerator using the motion of the quantized flux lines to transfer heat. The result of this will be discussed in 7.3.2.

After doing the above experiment, and in order to study the source of the observed dissipation we built a 'rotating superconducting solenoid system' as described in Chapter 2.5(a), to measure the temperature changes associated with the pinning and viscous dissipations. For experimental convenience and practical application reasons we used Nb as our material. We investigated the dissipation in different Nb specimens with different geometry. We are going to discuss the results obtained from the specimens NbI, NbII and NbIIIa in 7.3.3 because these broadly cover our results and our consequent problems.

7.3.2 $Pb_{60}Tl_{40}$ and $Pb_{90}In_{10}$ alloys

In an actual experiment with a specimen of one or other of these alloys, the temperature variation of the two ends of the specimen, T_F and T_H (where the subscripts F and H refer to the ends far from and near to the thermal ground respectively) rose when the magnet started to rotate. After the magnet had rotated several times both temperatures

varied periodically about a steady mean value and with a frequency twice that of the magnet rotation. The mean values of T_F and T_H are plotted in Figure 7.1a for $Pb_{60}Tl_{40}$ and in Figure 7.2a for $Pb_{90}In_{10}$. In figures 7.1 and 7.2, T_F and T_H were the temperatures while the magnet was rotating in the direction from T_F to T_H, while T_F^* and T_H^* were the temperatures while the magnet was rotating in the direction from T_H to T_F. In Figures 7.1(b) and (c) for $Pb_{60}In_{40}$ and in Figures 7.2(b) and (c) for $Pb_{90}In_{10}$ we have plotted the temperature differences $\Delta T = T_F - T_H$ and $\Delta T^* = T_F^* - T_H^*$, while the difference between ΔT and ΔT^* is plotted as a function of the linear velocity of the magnet passing over the specimens. Since the results on these two specimens were very similar, we are only going to discuss the results on $Pb_{60}In_{40}$ in detail.

We were not able to calculate the power generated in the specimen since we did not know the exact number of vortices involved, but we have measured the rate of heat $\dot{Q}$ which had to be supplied to the specimen in order to achieve the same steady temperature differences as in the dynamic experiments. This heat was supplied by a heater attached to the far end of the specimen, and is therefore half the value of the heat needed by a uniformly distributed source. The results are plotted in Figure 7.3 as a function of the linear velocity of the magnet passing over the specimen when adjusted to give the same temperature difference. The value of $\dot{Q}$ was in agreement with $\dot{Q} \propto T_o^2 \Delta T$, and where $T_o = \frac{T_F + T_H}{2}$, and where $k \propto T_o^2$.

The temperature gradient along the specimen due to flux flow is given by

$$\Delta T = \frac{1}{k} \left\{ \frac{T\, n\, \phi_o [\, S_n(T) - S_s(T)\,]}{H_{c2}(T)} \right\} v_\phi - F_p\, v_\phi + \\ - n \left\{ \frac{\phi_o H_{c2}(o)}{\rho_n} + \frac{\phi_o T [\, S_n(T) - S_s(T)\,]^2}{2 H_{c2}(T)\ (k_s + k_n)} \right\} v_\phi^2 \Bigg|_{T=T_o} \qquad 7.2.35$$

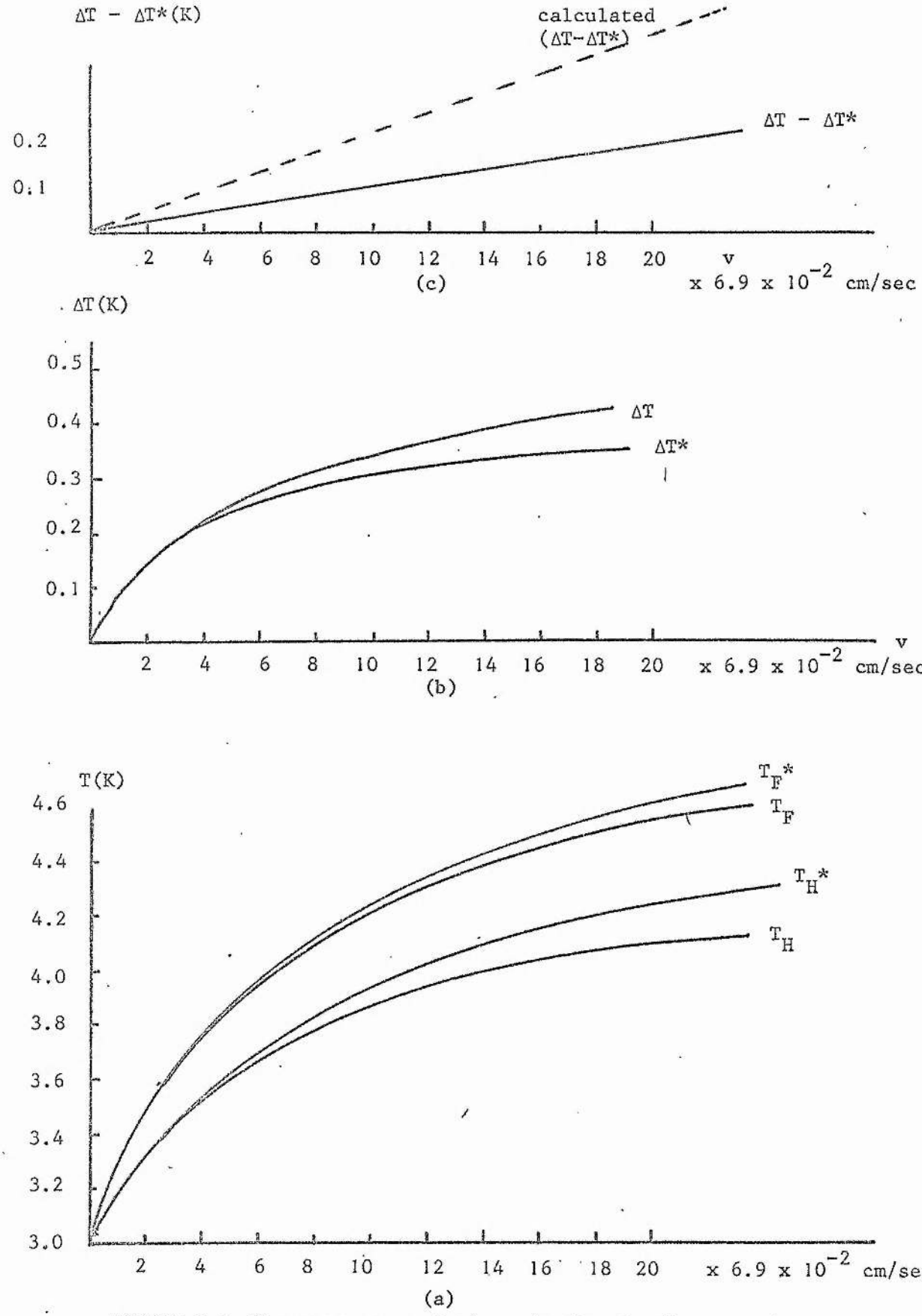

FIGURE 7.1 Temperature variations in the $Pb_{60}Tl_{40}$ specimen as function of the linear velocity of the magnet passing over the specimen.

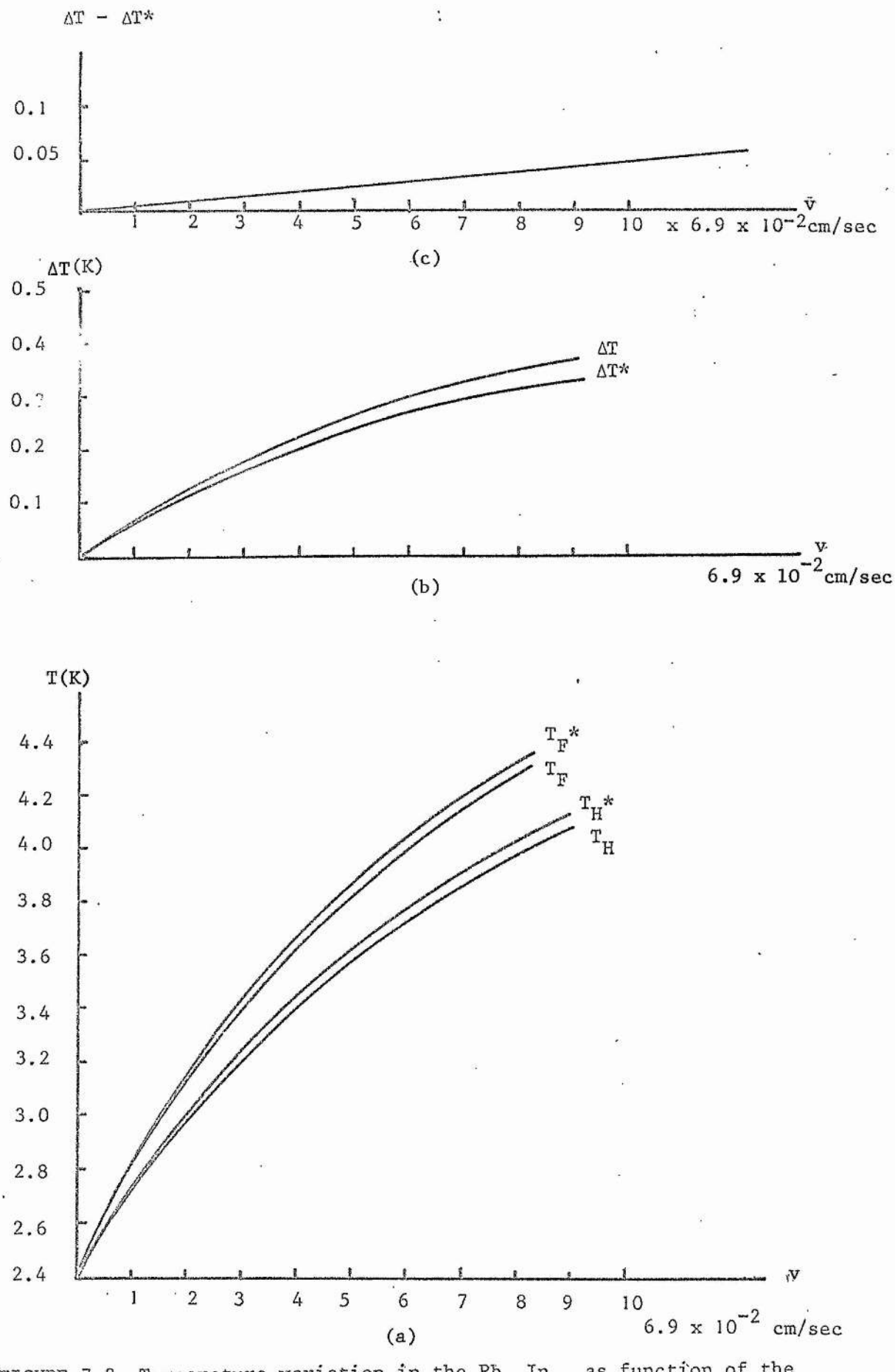

FIGURE 7.2 Temperature variation in the $Pb_{90}In_{10}$ as function of the linear velocity of the magnet passing over the specimen.

The first term of the equation gives the cooling power due to parts of the specimen making the transition from the superconducting state to the mixed state. This turns out to be about 5.8×10^{-6} erg per unit flux line at 3.0 K for $Pb_{60}Tl_{40}$, calculated from Equation 7.2.26 in the low field region. During the rotation of the magnet there was also heat released after the passage of the magnet due to the metal reverting from the mixed state to the superconducting state, and part of this was carried away by the motion of the flux lines and part of it was absorbed locally. The latter reduces the cooling power which depends on the thermal conductivity both of the vortex core and of the material of the specimen in the superconducting state. If the transition from the mixed state to the Meissner state takes place when $\dot{Q} = 0$, then if the thermal relaxation time is long compared with the transit time of the core, there is no heat transport associated with flux flow, but if the relaxation time is short there will be maximum cooling power.

The heat generation, which accompanies flux flow due to viscous dissipation is given by the third term of Equation 7.2.35, which is of order 2×10^{-11} erg per unit velocity per unit flux line. The fourth term of equation 7.2.35 gives the contribution from the irreversible entropy production due to the temperature gradient in the vortex core and is of order 10^{-19} erg per unit velocity squared per unit flux line at 3K. These two sources of dissipation are relatively small compared with the cooling power, and therefore our heating power must come from the pinning dissipation. Using the experiment results on the pinning force, in Chapter VI,

$$F_p(T) = F_p(0)\ (1-t)$$

and ignoring the third and fourth terms of Equation 7.2.35, we have

$$\dot{Q} = \left\{ F_p(o)\ (1-t) - \frac{T\ n\ \phi_o [S_n(T) - S_s(T)]}{H_{c2}(T)} \right\} v_\phi \qquad 7.3.1$$

The experimental results of $\dot{Q}$ given in Figure 7.3 can be fitted by Equation 7.3.1, with

$$\dot{Q} = [\,2312\ (1-t) - 446\ t^2\,]\ v_\phi . \qquad 7.3.1a$$

Equation 7.3.1a gives $F_p(o) = 2.3 \times 10^3$ dyne, which is the right order of magnitude for the specimen, and gives the temperature-dependent cooling power. To give this cooling power in the specimen, that is $Pb_{60}Tl_{40}$, 1mm thick, at 3K, we need the total number of flux lines per unit velocity to be $n = 446\ t^2/(5.8 \times 10^{-6} \times 0.1)$. This prediction of the value of n is reasonable for a value of the external field $H_a = 460$ Oe, at B = 200 G, where we get $n = 7 \times 10^8$. The calculated cooling term $\Delta T - \Delta T^*$ is also plotted in Figure 7.1c which was larger than the experimental value of $\Delta T - \Delta T^*$. In these experiments it was very difficult to maintain the same bath temperature for both clockwise and anticlockwise runs. This is the most likely reason for the factor of two difference between calculated and observed temperature difference in Figure 7.1c.

Even for a specimen which has $F_p = 2.3 \times 10^3$ dyne, which was lower than $F_p(o)$ for all of the specimens described in Chapter VI, the dissipation was already sufficient to destroy any cooling effect. Although it might be possible to reduce this pinning dissipation by annealing the specimen, this can only be done to a limited extent. The cooling term becomes smaller at lower temperatures as the entropy difference becomes smaller, and it would seem that this kind of refrigerator would have very little practical application.

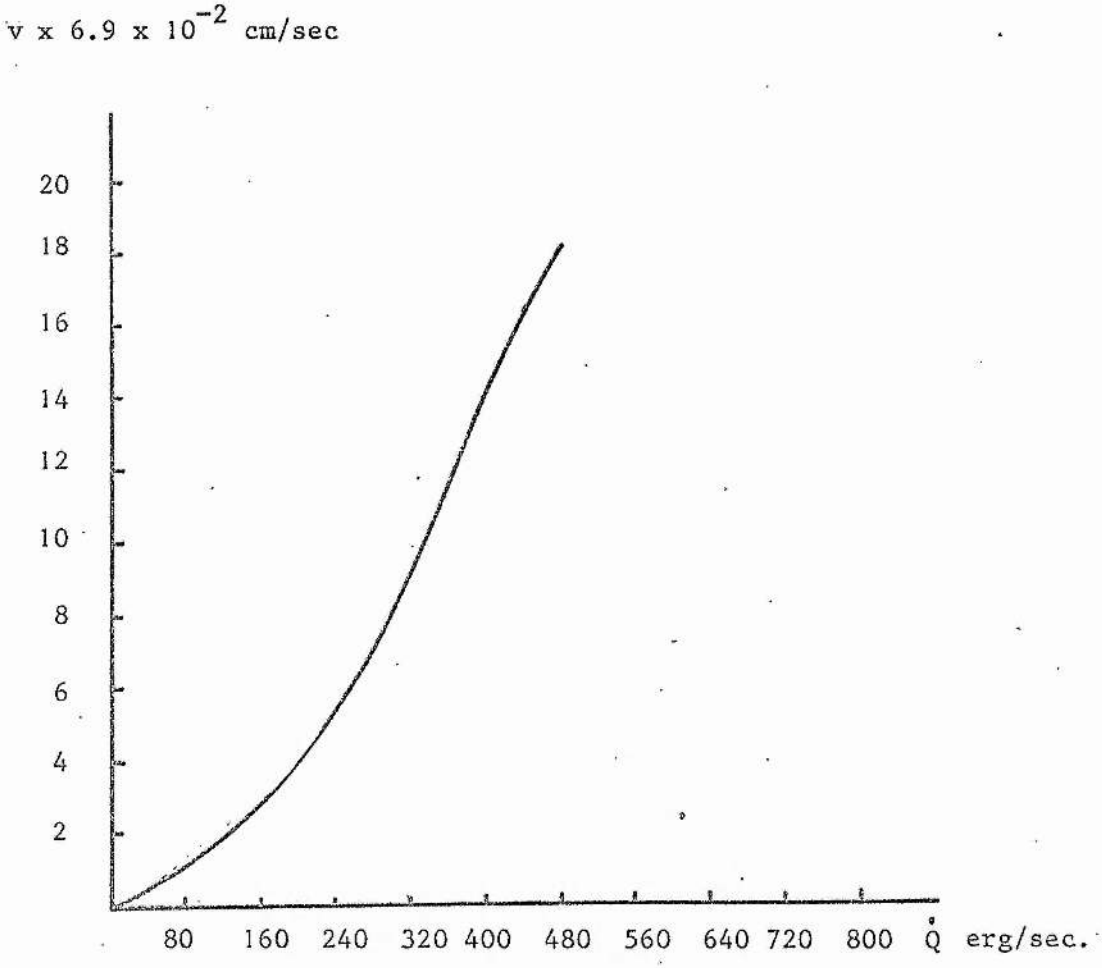

FIGURE 7.3 Power dissipated in the $Pb_{60}Tl_{40}$ specimen as a function of the linear velocity of the magnet passing over the specimen.

7.3.3 Nb Specimens

(a) NbI and NbII

In Figure 7.4 we show a typical set of experimental recorder traces of the pinning force and the accompanying temperature variation while a magnetic field of constant space profile is swept over the specimen at different sweep speeds. The specimen was the oxidized NbII at 4.22 K, and the swept field H_{amax} was 2440 Oe. Figure 7.4 shows that the temperature of the specimen remained unchanged when the field was approaching it and while the attractive interaction force F_A was operating. This regime extends to point a. When the repulsive force F_s begins to operate, the specimen is forced to rotate in the same sense as the field motion, and when the rotation reaches a maximum, at point b, the flux lines start to penetrate the specimen and its temperature begins to rise. This rise is referred to as ΔT_s.

After b, there was continuous heating during the pinning force interaction F_p which was due to continuous field penetration into the specimen. A sharp temperature rise, ΔT_p, at point c coincided with the sudden release of the pinning force. The magnitudes of these temperature rises, ΔT_s and ΔT_p, both depended on the field sweep speed. In Figure 7.5, we have plotted the values of ΔT_s, ΔT_p and $(\Delta T_s + \Delta T_p)$ of Figure 7.4 as functions of the field sweep speed for NbII at 4.22 K with H_{amax} = 2440 Oe. In Figure 7.6 (a) and (b) we have plotted the maximum temperature rise of NbII and the chemically polished NbI under different values of H_{amax} at different field sweep speeds. In Figure 7.7 we have plotted 7.6(a) into ΔT vs B, where B is the magnetic induction of the specimen calculated from its magnetization curve Figure 4.15.

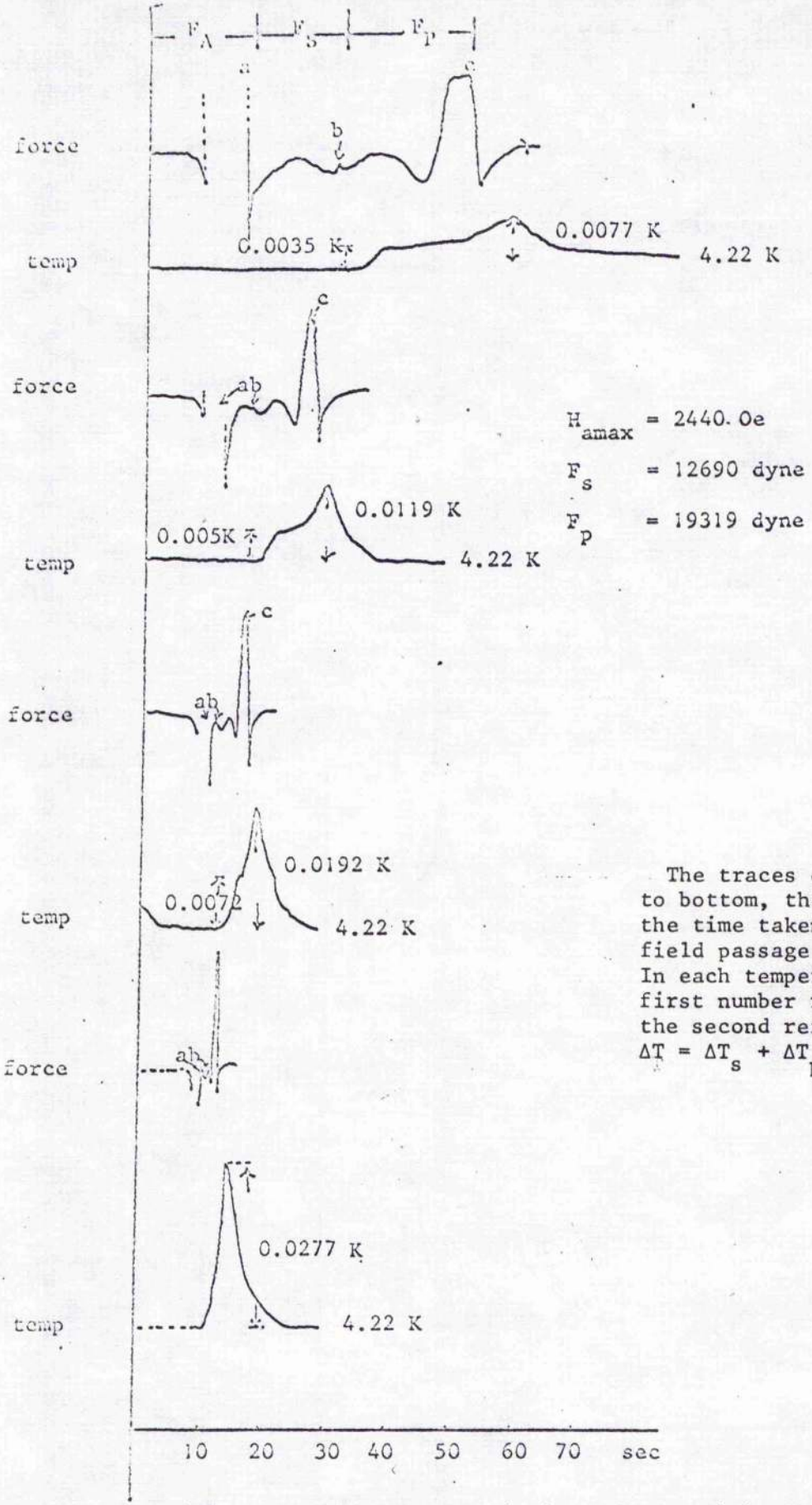

The traces describe, from top to bottom, the effect of decreasing the time taken for a complete field passage over the specimen. In each temperature graph, the first number refers to ΔT_s while the second refers to $\Delta T = \Delta T_s + \Delta T_p$.

FIGURE 7.4 The temperature variation of the oxidized NbII specimen associated with the pinning forces

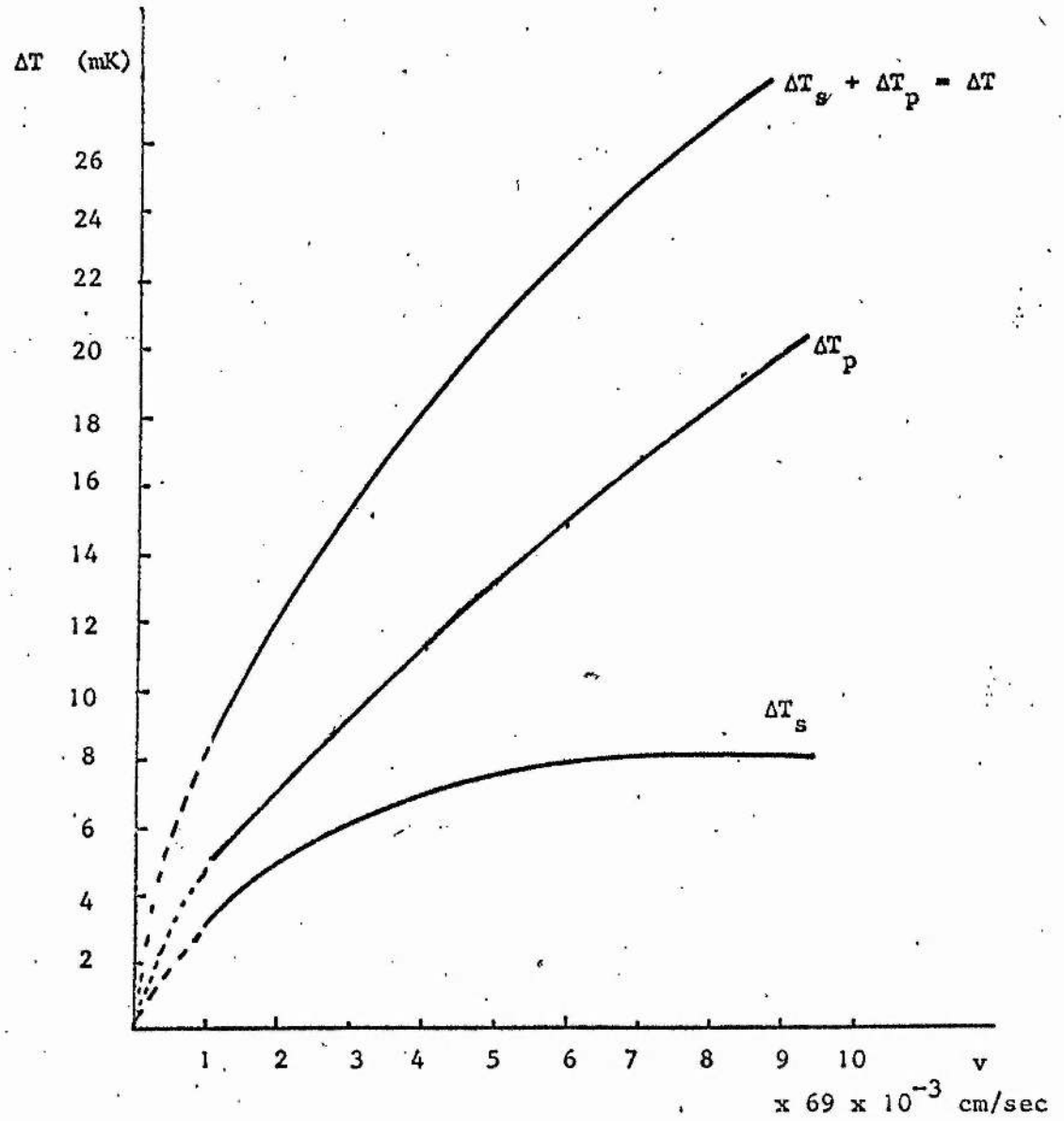

FIGURE 7.5 Temperature variations; ΔT_s, ΔT_p, and $(\Delta T_s + \Delta T_p)$ of the oxidized NbII during a constant field, H_{amax}=2440 Oe sweeping over it vs the field sweeping speed, at 4.22 K

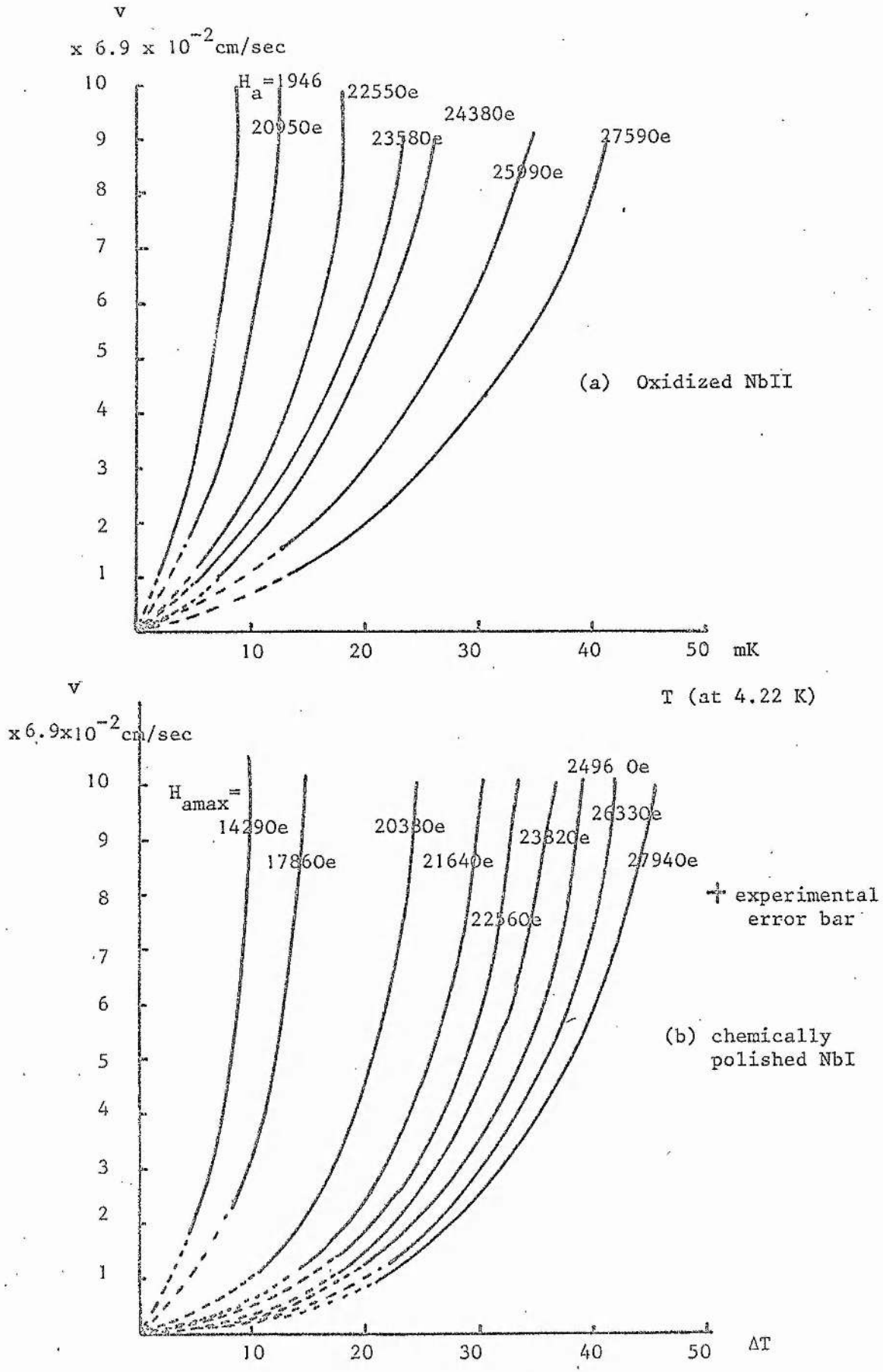

FIGURE 7.6 The maximum temperature rise, ΔT at 4.22 K, of the specimen as function of H_{amax} and sweeping with different speeds.

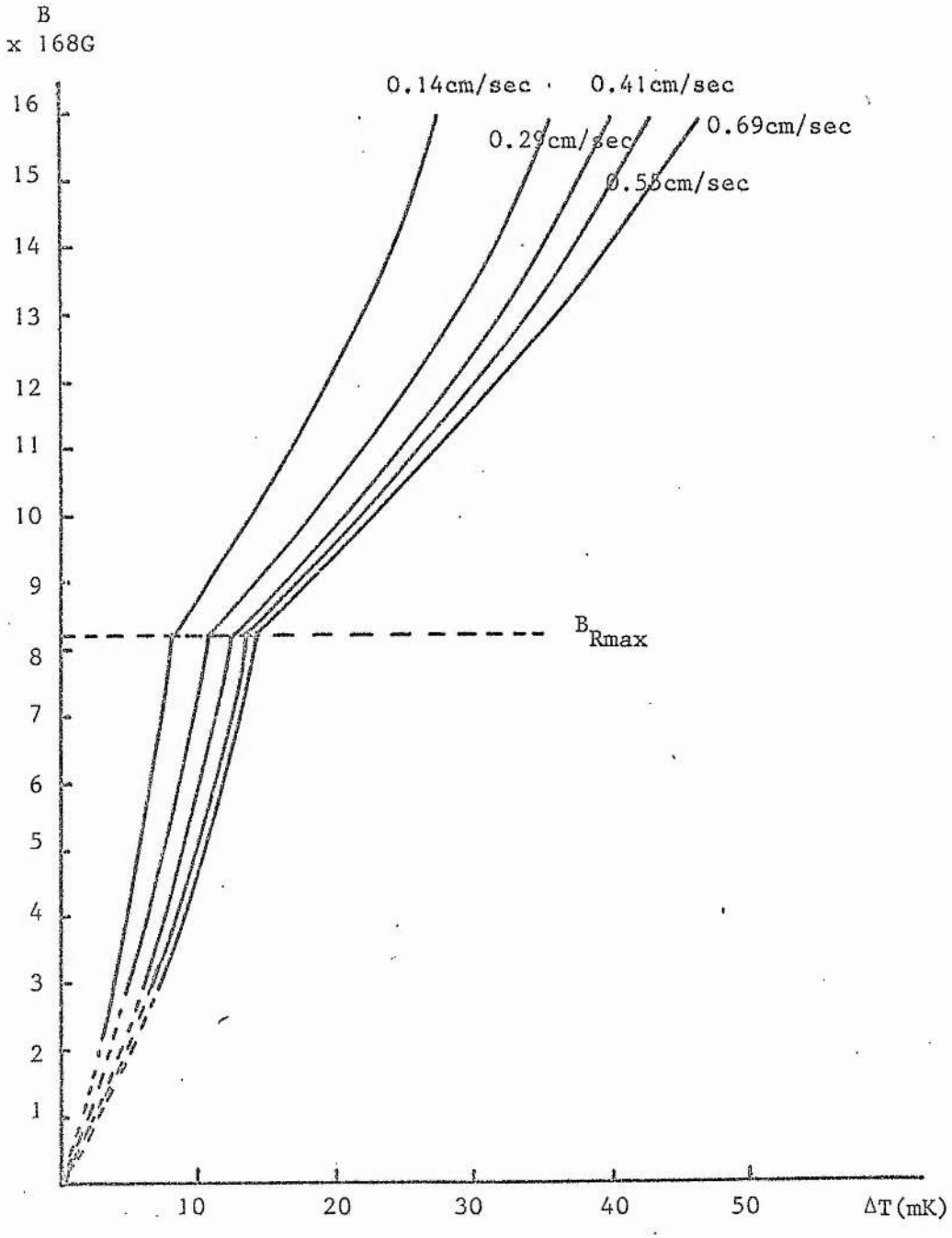

FIGURE 7.7 The maximum temperature variation ΔT of the oxidized NbII vs the magnetic induction B at different field sweeping speeds.

The above results clearly showed that there was heat dissipation associated with flux penetration and with the bulk pinning force F_p. Although the temperature change of the specimen was determined by following equation,

$$\int c \frac{dT}{dt} \cdot dt = \int -k \nabla^2 T \, dt + \int \dot{Q} \, dt, \qquad 7.3.2$$

since the heat leak of the system was quite large and the value of k was unknown (c being a parameter involved in a non-equilibrium state) we were not able to solve this equation. Instead, we have assumed that since the temperature rise was always less than 0.05 K, any change in specific heat with temperature could be ignored and it depended only on B. For a constant H_{amax}, the amount of heat generated during one field passage was proportional to the area under the recorded temperature variation curves. Evaluating those areas, we found that they were approximately the same for different sweep speeds. The small difference observed could be due either to evaluation error or to the flux penetration speeds being different. That the total heat dissipated did not depend on the field sweep speed was in agreement with the observation that the mechanical work done via torque arising from the pinning force was independent of the field sweep speed.

The maximum temperature rise ΔT of the specimen at high sweep speeds took place in a relatively shorter time interval than the heat diffusive time of the specimen. We have therefore used these maximum rises to calculate the amount of heat generated Q(B) in the specimen as function of B with the help of the estimate of the specific heat from Equation 5.2.20. The results of Q(B) calculated from $C(B) \Delta T$ and from $C(B>B_{Rmax}) \Delta T = C(B_{Rmax}) \Delta T$ are plotted in Figure 7.8. We do not know which value of C(B) should be taken; the former one is the specific heat of a specimen with magnetic induction $B(H_a)$ and the latter is based on the knowledge that the

amount of magnetic induction in the specimen was B_{Rmax} after the field $H_a > H_{Rmax}$ had swept through the specimen. Nevertheless, both of these curves in Figure 7.8 and the temperature variation curves of Figure 7.7 showed that the dependence on B of heat generation above B_{Rmax} was qualitatively different from that for B below B_{Rmax}. This difference may be caused by increased flux flow after all of the pinning sites in the specimen have been occupied. The amount of heat dissipation when calculated from the mechanical work of the torque measurement is also plotted in Figure 7.8 curves (a) and (b). The difference between the mechanical work and the thermally calculated heat suggest that the viscous dissipation becomes significant in the higher field region.

(b) NbIIa

The original idea of this experiment was to create a temperature gradient along the "Bitter Pancake" annular specimen in order to study the dissipation in this specimen, but because time for heat diffusion was shorter than the rate of heat generation, no constant temperature gradient could be established along the specimen. In Figure 7.9 we have shown the temperature variation of the specimen during the pinning force measurement under non-isothermal conditions. It showed that there was dissipation associated with every pinning force of the specimen. In Figure 7.10 we have plotted the maximum temperature rise of the specimen as a function of the field H_{amax}. This curve can be fitted to following equation:

$$\Delta T = 0.014 \ (H-H_{c1}^{*})^{0.37} \ ,$$

where ΔT is in K and H is in Oe. In Figure 7.11 we have plotted the maximum temperature rise of the specimen as a function of the corresponding pinning force. This curve can be represented by

$$\Delta T = 0.35 \ F_p^{\ 0.16}$$

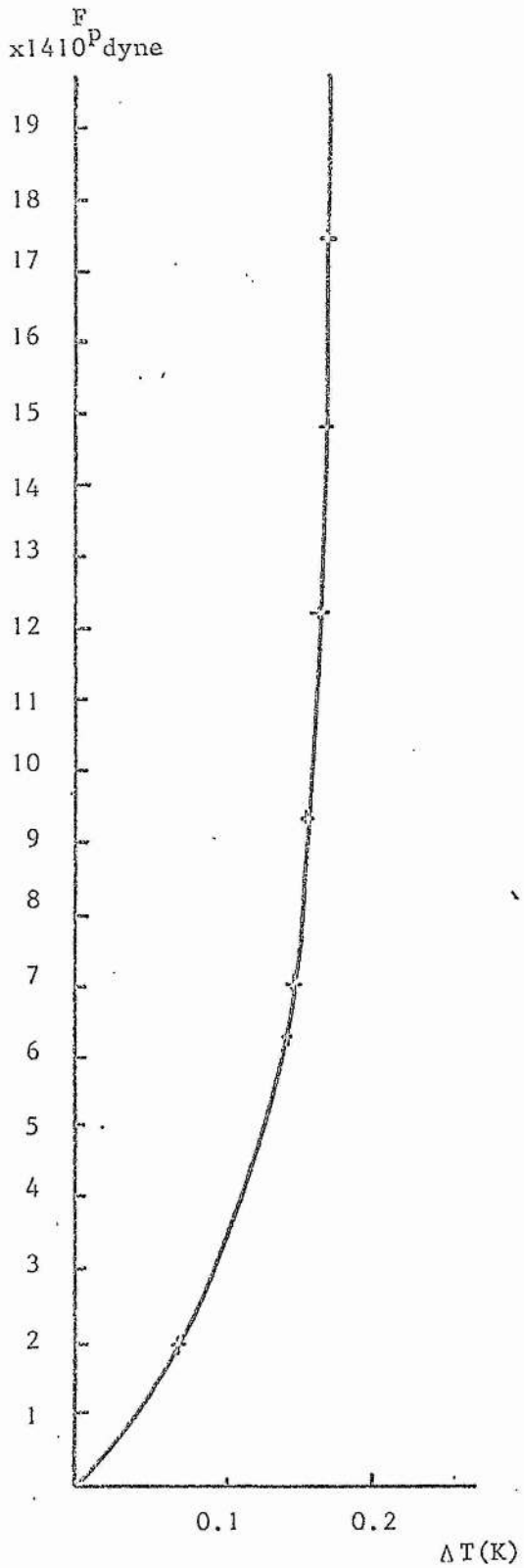

Figure 7.11 The maximum temperature rise of the NbIIIa specimen as function of the corresponding pinning force.

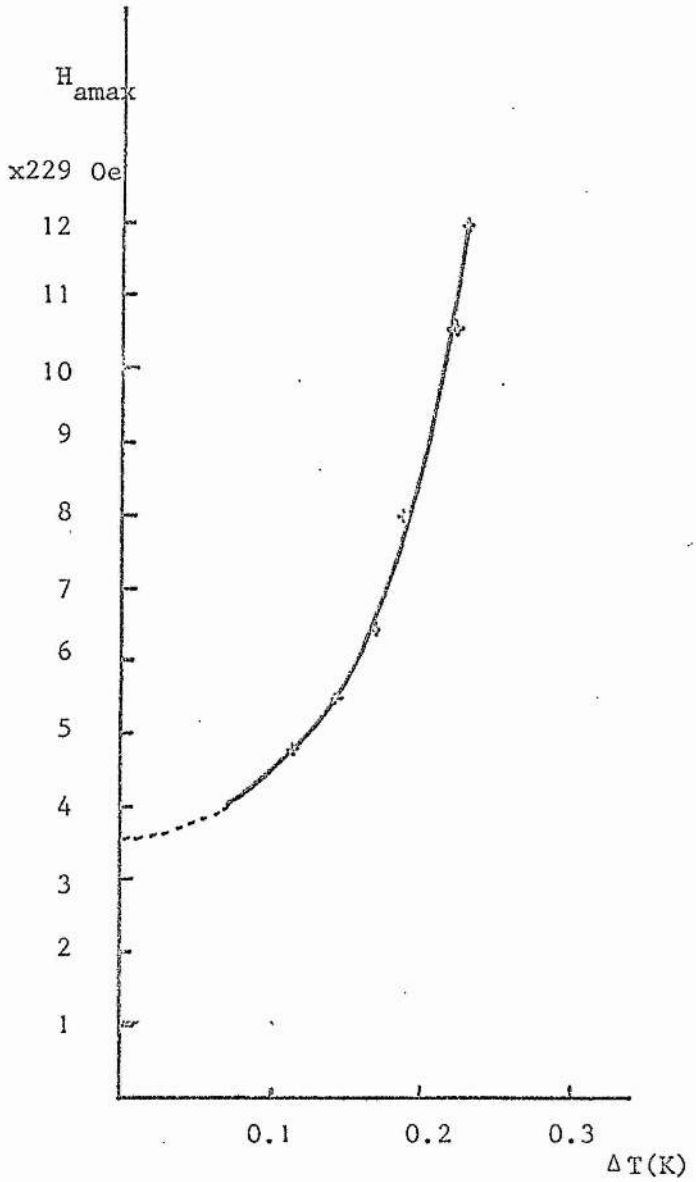

Figure 7.10 The maximum temperature rise of the NbIIIa specimen as function of the field H_{amax}.

above F_p = 2800 dynes, with ΔT in K and F_p in dynes.

Since we do not have knowledge of the microstructure of the specimen we were not able to calculate the actual amount of heat associated with each temperature rise. What these measurements did show was that the distribution of pinning sites in the specimen was not uniform and that different pinning sites had different pinning forces and gave different magnitudes of dissipation.

The experiment also suggested that in V-I measurements in a long specimen, the critical current J_c of the specimen will depend on the position of the voltage probe, and this will give different values of J_c for the same material.

If we could determine the distribution of pinning sites and were able to measure the speed of flow of flux lines just after release from pinning sites, such an experiment would provide a useful way to study the nature of the pinning force.

CHAPTER VIII

THE EFFECT ON A SUPERCONDUCTOR OF BEING SUBJECTED TO A 'MOVING' BUT UNIFORM FIELD

CHAPTER VIII The effect on a superconductor of being subjected to a 'moving' but uniform field

8.1 Introduction

In this chapter we discuss observations made on a superconductor when it is placed in a 'rotating' uniform field. The reason for doing the experiment was to make a sensitive test as to whether one can continue to speak of 'flux lines' if a magnetic field is uniform.

The concept of 'lines of magnetic flux' being associated with magnetic field is well-known and is frequently employed in discussions about induction.

If a flux line actually exists then it will be attached to its magnetic source; e.g. magnet, even in the case of a uniform field. Therefore it should be possible to move the flux line either by bodily moving the source of uniform field over a probe or by moving the probe through the uniform field.

A magnetic field can exist inside a superconductor in the form of normal laminar regions in the intermediate state of type I, and in the form of normal fluxons in the mixed state of type II materials. As we have shown in Chapters VI and VII, we can move these normal regions when the source of a non-uniform magnetic field is passed over them. Thus one can regard a particular normal region in a superconductor as being fixed relative to the field source. The idea occurred that we could make a sensitive test of the flux line concept of field by using the superconducting specimen as a probe in the completely uniform field of a permanent magnet of such a shape that the field stays constant in the probe as the magnet is rotated over it. If there is such a thing as a flux line in an absolutely uniform field, then movement of the magnet should be accompanied by movement of the normal region in the superconductor. We have shown in Chapters VI and VII that motion of

the normal region in a superconductor will cause dissipation and consequent temperature variation of the specimen if the conditions are adiabatic. We have here a very sensitive means of determining the reality of flux lines.

8.2 Experimental detail and results

A schematic diagram of the experimental arrangement is shown in Figure 8.1. A carbon thermometer was mounted on the bottom surface of the specimen and a pick-up coil was placed round the specimen. The sensitivity of the temperature and magnetic flux measurements were better than 0.1 m K and 5×10^{-9} weber/sec, respectively. The experiment was repeated at two different field strengths - 754 Oe and 542 Oe, and for three specimens, over the temperature range 1.6 K - 4.2 K so that the Meissner state, the intermediate state and the mixed state were all covered.

The specimens were the short cylinders described in Chapter III. These were suspended by cotton threads in vacuum. A uniform axial magnetic field was produced by mounting permanent magnets above and below the specimen. The magnets could be rotated at speeds between 0.5 and 10 r.p.m.

Neither the temperature of the specimen nor the pick-up coil voltage showed any change while the magnets were rotating, over periods of several minutes and under nearly perfect adiabatic conditions.

When an 80 Oe field gradient was superimposed over 10% of the circumference to give a maximum increase from 542 to 620 Oe, the temperature of the specimen was observed to rise during each passage of the hump in the field, as is shown in Figure 8.2 for two starting temperatures of the specimen $Pb_{94}In_6$, 4.22 K and 1.80 K. The dependence of the temperature rise on magnet rotation speed is shown for the same specimen in Figure 8.3.

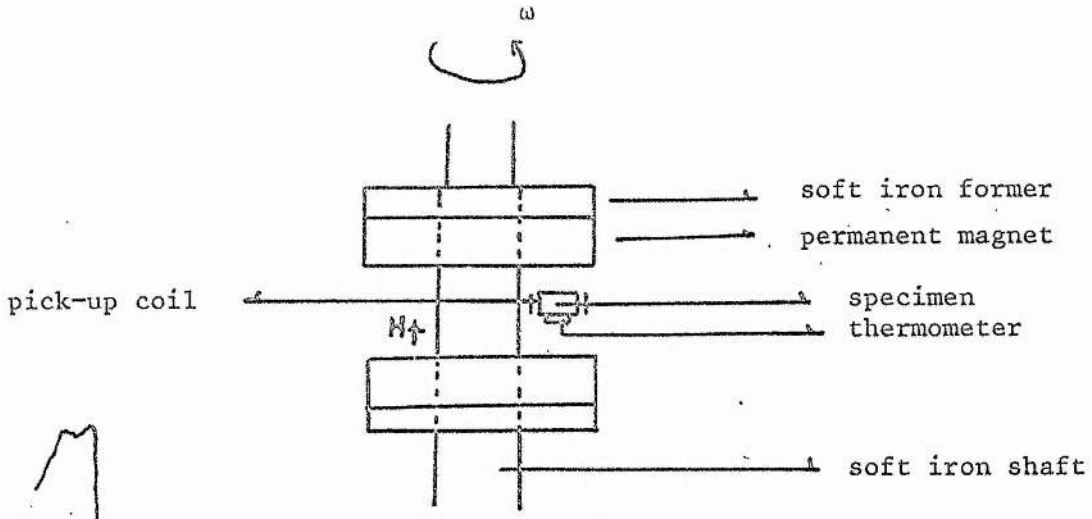

FIGURE 8.1 Schematic diagram of experimental arrangement

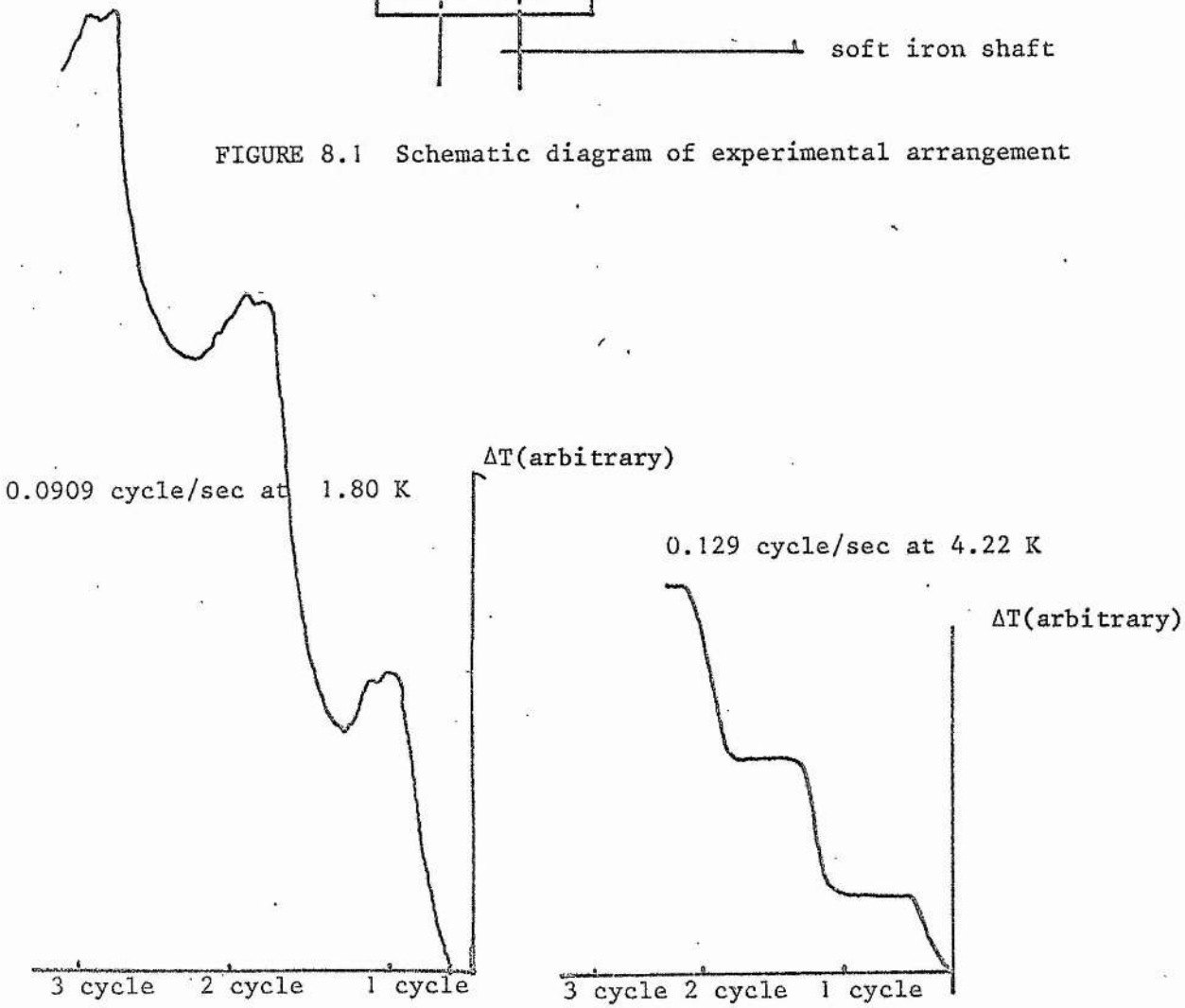

FIGURE 8.2 The temperature rise of the $Pb_{94}In_6$ at each field passage

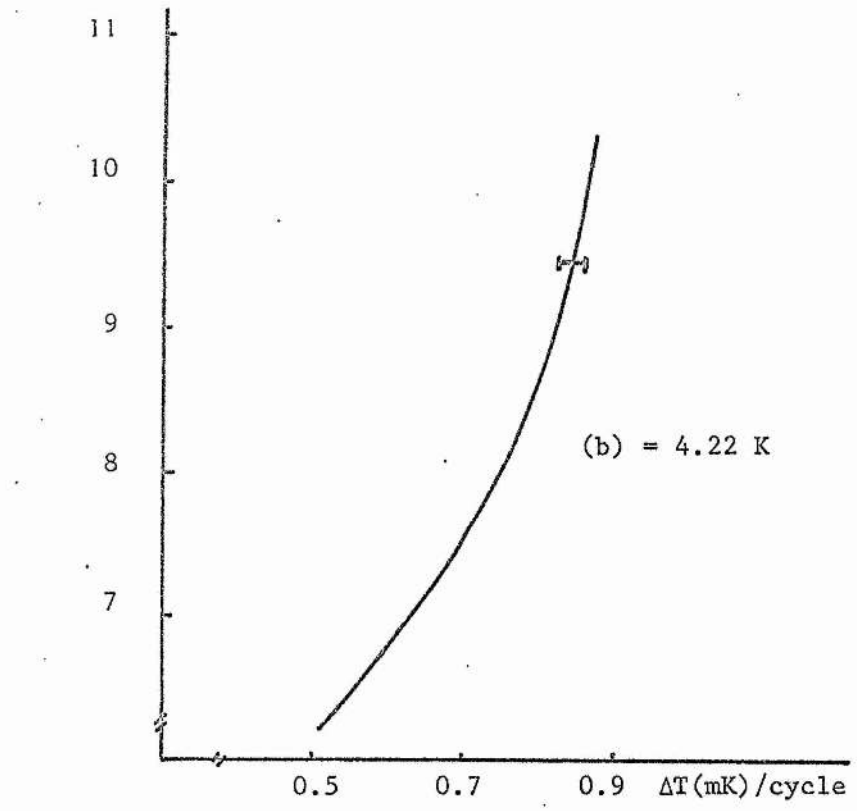

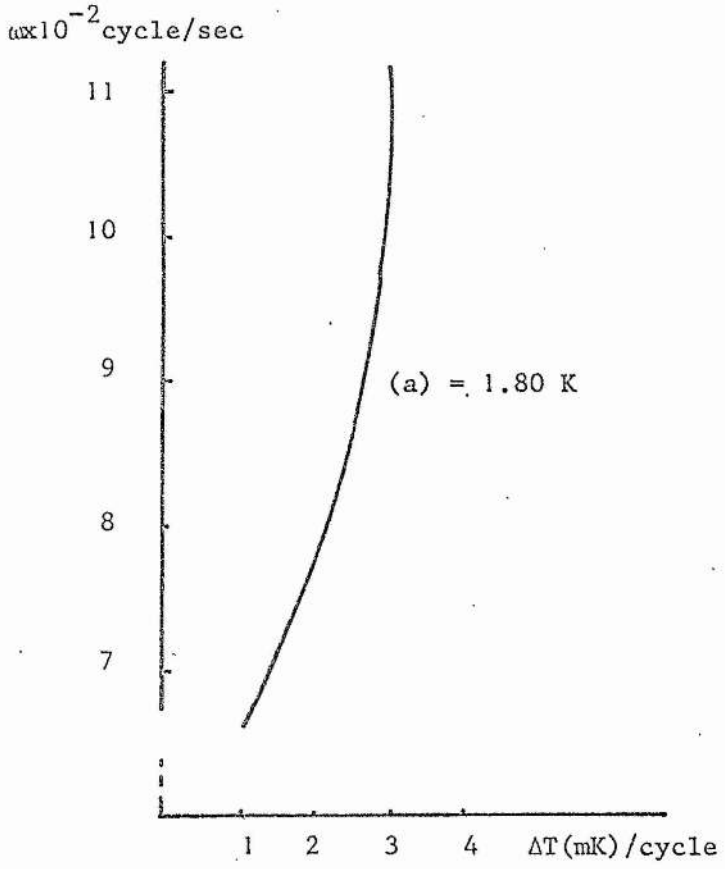

FIGURE 8.3 Temperature rise of the $Pb_{94}In_6$ per field passage at (a) 1.80 K and (b) 4.22 K vs the magnet rotation speed.

8.3 Conclusion

In the uniform field case, the total number of fluxons and their distribution in the specimen remained unchanged during the experiment, and there is no observed magnetic force created since the currents circulating round the normal regions were not affected by the rotation of the magnet and maintained their value. From the experimental results, we conclude that for a uniform magnetic field it is not possible to deduce the motion of the source of the field, and that the concept of 'flux lines' is only valid when speaking of a field which varies either in time or space.

CHAPTER IX

SUMMARY

CHAPTER IX Summary

9.1 Introduction

The work reported in the preceding chapters was concerned with the thermal and magnetic properties of Pb-In, Pb-Tl and Nb type II superconductors. They are:

(1) The magneto-caloric effect and the specific heat of Nb

(2) The magnetic properties of Pb-In, Pb-Tl alloys and of Nb

(3) The pinning forces in the Nb and Pb-In specimens

(4) The dissipation effects in the Nb, Pb-In and Pb-Tl specimens

(5) The concept of magnetic flux line in a uniform field.

In this final chapter, we summarize the results of the present research, we discuss the performance of the experimental techniques which we used, we survey the problems left unresolved, and we suggest some experiments to study the dynamic properties of a type II superconductor which may be done in the future.

9.2 Summary of the experimental results and apparatus performance

9.2.1 The magneto-caloric effect and the specific heat of a Nb Specimen

(a) The magneto-caloric effect: the reversible magneto-caloric effect,

$$T \left(\frac{\partial S}{\partial H}\right)_T = -C \left(\frac{\partial T}{\partial H}\right)_S \quad , \qquad 5.2.21$$

is obstructed by heating due to the irreversible processes which occur during the transit from the Meissner state to the mixed state. The experimental results on the disc and on the rod niobium specimen showed that the entropy production was closely associated with the flux penetration rate and the flux density which both determine the fluxon flow velocity.

(b) The specific heat : the results of the specific heats of the Nb rod in the superconducting and in the normal states were in agreement with the well-known expression,

$$C_n = \gamma T + \beta T^3,$$

and

$$C_s = \beta_1 T^3 ,$$

where $\gamma = 7.85$ mJ mole^{-1} K^{-2}, $\beta = 0.22$ mJ mole K^{-4} and $\beta_1 = 0.5$ mJ mole K^{-4} for this Nb specimen. The mixed state specific heat C_m of the Nb rod was determined thermally by

$$C_{mT} = \frac{1}{n} \frac{dQ}{dT} ,$$

and also from the magnetic induction of the specimen via a 'two-fluid'-type phenomenological equation,

$$C_{mB}(H,T) = \gamma T + \beta T^3 + \frac{H_c^2(o)}{2\pi T_c^2} \left(\frac{3T^3}{T_c^2} - T\right) - \frac{H_c^2(o)}{2\pi T_c^2} \left(\frac{3T^3}{T_c^2} - T\right) \frac{B(H,T)}{H_{c2}(T)} +$$

$$+ \frac{H_c^2(o)}{2\pi T_c^2} \left(T^2 - \frac{T^4}{T_c^2}\right) \left(\frac{\partial [B(H,T)/H_{c2}(T)]}{\partial T}\right)_H . \qquad 5.2.18$$

We have assumed that the difference between C_{mT} and C_{mB} was due to the magneto-caloric effect of the specimen. After defining

$$C_m = \frac{\Delta Q_i}{\Delta T} ,$$

where $\Delta Qi = \Delta Q + \Delta Q_{ir} + \Delta Q_r$, and having derived some values of ΔQ_i from the magneto-caloric measurements, we found that C_m is in agreement with C_{mB}.

Although we have not measured the specific heat of a reversible type II superconductor, we expect that its specific heat will be in agreement with that calculated from Equation 5.2.18. This would provide a crucial

check of the validity of the equation.

The specific heat change of the specimen during the transition from the Meissner state to the mixed state and from the mixed state to the normal state were also investigated. The results of the latter were in agreement with Maki's theoretical work, although the specific heat change at H_{c1} was not conclusively determined.

With the present experimental set up, it took too long to pump the exchange gas out to get a reasonable thermal vacuum. It would be more convenient to cool the specimen with a cold finger. Direct contact heat conduction takes a much shorter time, and also allows one to achieve a better vacuum. This kind of arrangement could possibly be done by using a 'screw' system driven by our 'indirect magnetic-coupling rotating arrangement.'

9.2.2 The magnetic properties of Pb-In, Pb-Tl and Nb specimens

We have determined the critical fields H^{*}_{c1}, H_{c1}, H_c and H_{c2} of the Pb-In, Pb-Tl and Nb specimens from their magnetization curves, although a method of finding H_{c1} of a specimen which gives better accuracy has been suggested. The characteristic lengths λ, ξ, and the Ginzburg-Landau parameters $\kappa_1(t)$, $\kappa_2(t)$ for the above specimens have also been determined. These results have been compared with several theories; e.g. the reversible magnetization curve of the Abrikosov theory, the temperature dependence of H_{c2} in comparison with Gorter-Casimir, Bardeen-Ginzburg and Gorkov's predictions and the temperature dependence of the κ_1, κ_2 parameters.

The demagnetization effect on a short cylindrical specimen, e.g. NbI, has been taken into account in the magnetic induction of the specimen through a phenomelogical "shifting" method, and experimentally

examined, with results which were quite satisfactory.

We have introduced a method by which we can separate the surface contribution in the remanence field of the specimen from its magnetization curve. The method again was tested experimentally, and found to be applicable.

The values of B_{Rmax}, H_{Rmax} for specimens were determined, and both of these quantities have the same temperature dependence for a particular specimen, and hence their ratio remained constant at different temperatures for a particular specimen.

The experimental set up which we used for the magnetization curve measurement performed very well indeed, as is shown in the magnetization curves in Chapter IV. The sensitivity of the system could be increased if desired, with the noise of the system still remaining small.

9.2.3 Pinning forces in Pb-In and Nb specimens

In this measurement, we were able to measure the F_s force due to the interaction between the shielding Meissner current of the specimen with the external field, the F_A force due to the interaction between the trapped flux lines and the external field, and also the pinning force of the bulk material with good accuracy. The relation between F_s and H_{amax} acting on a 'virgin' superconductor can be expressed by

$$F_{sp} = n H_{amax} ,$$

where n is a constant which varies from specimen to specimen.

The magnitude of F_s acting on a superconductor with some remanent field was determined by the Gibb's free energy acting on the surface,

$$g(x) = E(x) + E_R(x) + \sum_{ij} U_{ij} , \qquad 6.4.5$$

where $E(x)$ is the attractive energy due to the attractive interaction between the trapped flux line and the surface, and $E_R(x)$ is the repulsive energy due to the repulsive interaction of the Lorentz force exerted by the Meissner current of the external field, and $\sum_{ij} U_{ij}$ is the repulsive energy due to the interaction between the flux lattice and the entering flux lines.

The results of the F_p force can be well represented by the Irie-Yamafuji model

$$F_p = \alpha B^{\gamma},$$

where γ was determined from the ratio of B_{Rmax}/H_{Rmax} via Equation 6.3.26. The value of γ of a particular specimen did not depend on the temperature but did depend on the distribution and the nature of the pinning sites of the specimen. The value of α of a particular specimen increased as the temperature decreased.

The temperature dependence of F_p was derived by extending Anderson's potential well model, and gave

$$F_p(T) = F_p(o)\ (1 - \frac{T}{T_c}) \quad , \qquad 6.5.6$$

Equation 6.5.6 is well in agreement with our experimental results in different Nb and Pb-In specimens.

The results of the measurement of F_s and F_p showed that these forces were reduced after a mechanically polished specimen had been oxidized, and then further reduced after it has been chemically polished. This suggested that surface pinning also plays a very important role in the magnitude of the critical current of the specimen, as long as the pinned flux lines were initially parallel to the field and perpendicular to the current.

The magnitudes of F_A, F_s and F_p were not affected by the sweeping speeds of the magnet. This suggested that these forces were not dependent on the flux flow velocity.

This system was very convenient for the measurement of pinning forces although the accuracy of the measurement could be improved by using a pair of more sensitive springs. It would be even better if one could use some kind of feedback system in which the specimen remained stationary during the measurement. With little modification, one could place a pick-up coil onthe solenoid holder at the same distance from the rotation shaft as the specimen and far away from the solenoid. This coil would pick up the remanent field in the specimen during each field passage, which would provide a more precise relation between the remanent field B_R and the sweep field H_{amax}.

A major disadvantage of the present system was that it was limited in temperature to the liquid helium region, whereas T_c for Nb is 9.28 K and for our Pb-In alloys about 6.5 K.

9.2.4 The dissipation mechanism in Pb-In, Pb-Tl and Nb

We have investigated the possibility of making a refrigerator using the motion of the flux lines to transfer heat. The experimental results on the Pb-In and Pb-Tl annular specimens showed that the heating due to pinning dissipation in the mixed state dominated and destroyed the cooling over most of the temperature range apart from that near T_c. Near T_c, the cooling effect might have shown up but since the entropy difference between the superconducting and the normal state is small there, the cooling is also small.

In a specimen in the mixed state the dissipation in flux flow is determined by

$$Q - (Q_{el} + Q_{th}) - Q_p - k\nabla T = 0, \qquad 7.2.34$$

where Q is the heat absorbed by the vortices which are added to the superconductor. The Q_{el}, Q_{th}, Q_p and $k\nabla T$ terms of Equation 7.2.34 were the heating due to eddy current, irreversible entropy production (due to the local temperature gradient of the core), the pinning dissipation, and the heat conductions of the specimen, respectively. The results of the temperature variation of the Pb-Tl specimen showed that at low values of the sweep field the pinning dissipation dominated over the heating effect, and the Q_{el} and Q_{th} terms were relatively smaller than Q_p. In this situation, the heat generation rate in Pb-Tl can be represented by

$$Q = [\, F_p\,(o)\,(1-t) - bt^2\,]\, v_\phi\,, \qquad 7.3.1$$

with $F_p(o) = 2312$ dyne and $b = 446$ erg v^{-1}. This result was in agreement with

$$\nabla T = \frac{1}{k}\Big[\Big(\frac{T\,n\,\phi_o\{S_n(T)-S_s(T)\}}{H_{c2}(T)} - \alpha B^\gamma\Big]\, v_\phi +$$

$$- n\Big[\frac{\phi_o H_{c2}(o)}{\rho_n} + \frac{\phi_o T\,\{S_n(T) - S_s(T)\}^2}{2\,H_{c2}(T)(k_s+k_n)}\Big)_{T=T_o}\Big]\, v_\phi^2\,, \qquad 7.2.35$$

with the last terms being small.

The temperature variation of the specimen during the pinning force measurement, under semi-adiabatic conditions, on NbI, NbII and NbIIIa showed that there was temperature rise (heat dissipation) associated with the release of flux lines from the pinning sites. There was heat generation

observed when the flux lines start to penetrate the specimen. The magnitude of the temperature rise was dependent on the magnet sweep speed. The total amount of heat generated during each field passage was evaluated and found to be approximately the same for the same H_{amax} at different sweep speeds.

We have calculated the amount of heat generation in NbI and NbII from the temperature rise of the specimen at different H_{amax} with the highest sweep speed. At high speed the period of heat generation was much shorter than the heat diffusion time. In the calculation we have estimated the possible value of the specific heat C(B) of the specimen. The result was compared with the heat calculated from the mechanical work of the torque measurement. It showed that at low fields the difference between the two values was small, but gradually becoming larger as the field became larger so long as B was below B_{Rmax}. Above B_{Rmax} the heat generation became much larger, which might have been due to increased flux flow.

Lack of knowledge both of the heat leak of the system and of the microstructure of the specimen limited further analysis of the experimental results.

The experimental set-up was not ideal for the study of dissipation. The small experimental space available for mounting the specimen made it difficult to get good thermal isolation. This meant that attempts to solve the exact thermodynamic state of the specimen became very difficult.

The large return rotation of the specimen, produced by the action of the spring, which followed the release of the flux lines from the pinning sites probably affected the actual velocity of the flux lines inside the specimen. This could be avoided in future by using a system which allowed

the specimen to remain stationary, and measuring the torque by a feedback loop.

9.2.5 The concept of a magnetic flux line in a uniform field

We have measured the thermal and magnetic behaviour of a superconductor in a 'rotating' uniform field in order to make a sensitive test as to whether one can continue to speak of 'flux lines' if the magnetic field is uniform. The experimental results on superconductors in various states, Meissner intermediate and mixed, showed that the profile condition of the field inside the specimen was not affected in any way by the rotating magnet which was subjecting the specimen to a 'moving' uniform field. This enabled us to conclude that a 'flux line' is a concept which should be limited strictly to discussion of a non-uniform field.

9.3 Discussion

Most of our experimental results can be explained on the basis of different phenomenological theories. The magnetization measurement only provides the average value of B of the specimen, and did not give the actual flux configuration or field profile in the specimen. Therefore the pinning force of the specimen has to be interpreted in terms of an average pinning strength density of a specimen. This is clearly not true as shown in 7.3.3(b); pinning force measurement on NbIIa showed that the pinning sites were not uniformly distributed and therefore that the heat

which accompanied flux flow is not uniformly dissipated. In order to determine the precise nature of pinning force and the heat dissipation in a type II superconductor, we need to know its microstructure. Our measurements of the temperature dependence of the pinning force for the bulk material suggested that Anderson's potential well model may be the right kind of mechanism for flux pinning.

However, even if we did have precise knowledge of the microstructure, it would still probably be very difficult to calculate the pinning strength and other useful parameters of the specimen.

The maximum pinning force which we observed did not depend on the sweep speed of the field, therefore the mechanical work due to pinning was also independent of sweep speed. However, the heat dissipation was dependent on the sweep speed of the field; this was because the flux flow speed after it was released from the pinning sites was affected by the flux density and the flux lattice of the specimen, and the flux lattice flow velocity was affected by the magnet rotation speed over most of the range of sweep speeds of the magnet. We found that the heat generation rate due to the pinning dissipation was proportional to the speed, but at high speed (>8 r.p.m.) there seemed to exist a critical velocity limit to flux flow, and heat rate became constant. This was not investigated in detail since the heat diffusion time became comparable to the rotation interval. It is particularly important to know the velocity/velocities of flow of flux lines in order to study the dissipation and the stability of the flux lattic in a superconductor.

We finish this thesis with Figure 9.1, in which we have outlined the experiments which we think are important for the study of the hysteresis properties of a type II superconductor. Some of these experiments we have done in this thesis and others we wish we had had

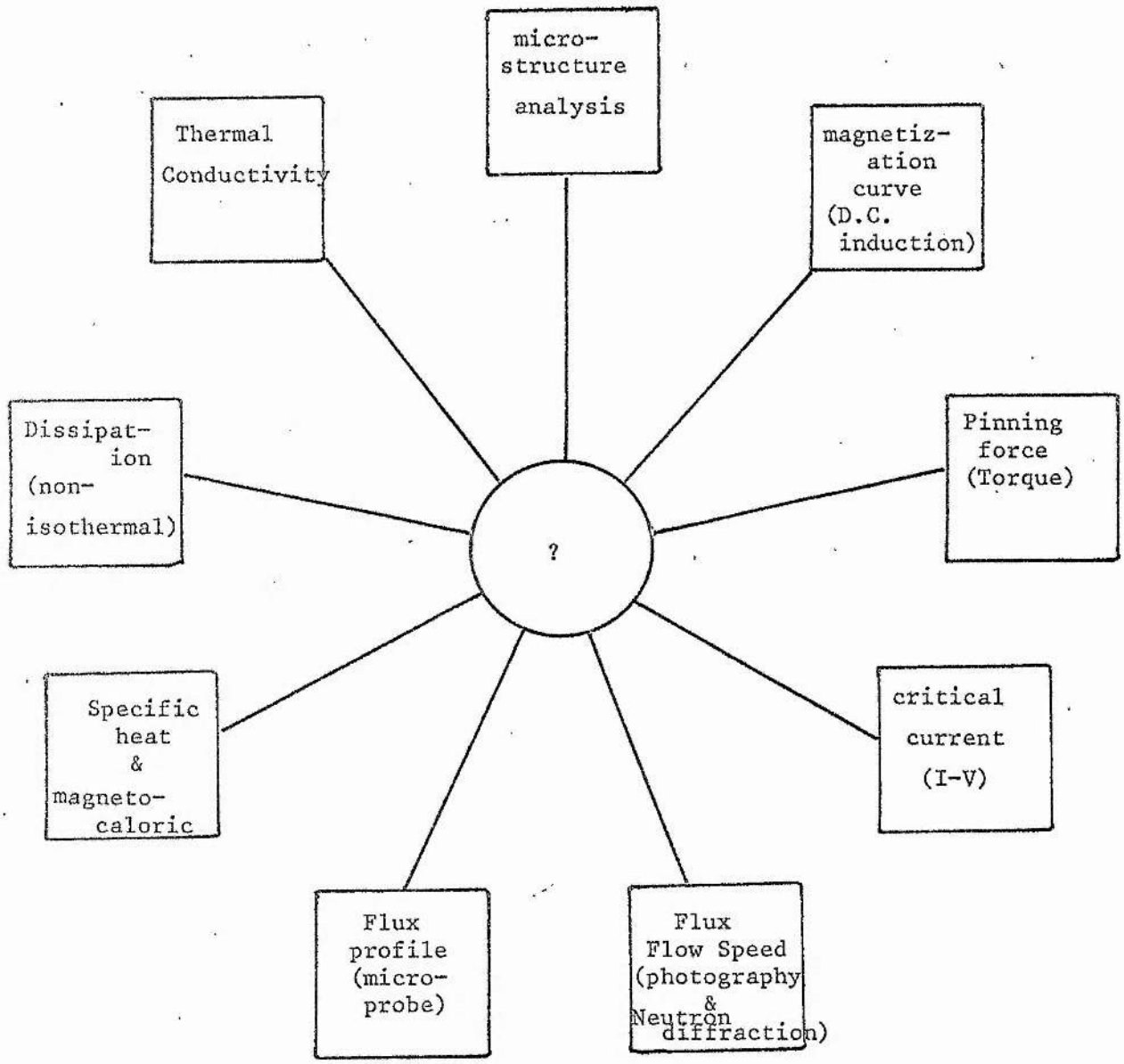

FIGURE 9.1 Essential experiments for the study of the magneto-dynamic properties of a type II superconductor.

time to do and have simply mentioned possible methods except for the case of the flux flow velocity measurements. The flux flow velocity can be measured by methods of neutron diffraction (Schelten and Lippmann 1975), measuring the depolarization of a polarized atomic beam (Brown and King 1971), measuring the rotational NMR line, and using FASTAX high speed photography (Wertheimer and Gilchrist 1967). Among these we think the photography method would provide more detailed information about the flux flow speed, although being a surface powder method this might still not give the true flux flow speed. However, it might be of assistance in further analysis of our results.

If we do all the experiments of Figure 9.1, between them we can check the different parameters determined from one experiment with the same parameters determined from another experiment. From these might emerge a satisfactory model of the magneto-dynamic state of a type II superconductor.

REFERENCES

Abrikosov A A, JETP 5 1174 1957

Abrikosov A A and Gor'kov L P, JETP 12 1243 1961

Alden T H and Livingston J D, J Appl Phys 37 3551 1966

Anderson A C and O'Hara S G, J Low Temp Phys 15 323 1974

Anderson P W, Phys Rev Lett 9 309 1962

Anderson P W and Rowell J M, Phys Rev Lett 10 230 1963

Andronikashvili E L, Chivinadze J G, Kerr R M, Lowell J, Mendelssohn K and Tsakadze J S, Cryogenics 9 119 1969

Arkadiev V, J Phys USSR 9 148 1945

Bardeen J, Phys Rev 94 554 1954

Bardeen J, Cooper L N and Schrieffer J R, Phys Rev 108 1175 1957

Bardeen J, Rickayzen G and Tewordt L, Phys Rev 113 982 1959

Bardeen J and Stephen M J, Phys Rev 140A 1197 1965

Bean C P, Phys Rev Lett 8 250 1962
Rev Mod Phys 36 32 1964

Bean C P and Livingston J D, Phys Rev Lett 12 14 1964

Becker R, Heller G and Sauter F, Z Phys 85 772 1933

Bohm D and Pines D, Phys Rev 92 609 1953

Born M and Cheng K C, Nature 161 968 1948

Brandt U, Pesch W and Tewordt L, Z Phys 201 209 1967

Brown T R and King J G, Phys Rev Lett 26 969 1971

Campbell A M, Proc Int Discussion Meeting on Flux Pinning in Superconductors p47 1974. Eds: P Haason and H C Freyhardt

Campbell A M and Evetts J E, Adv Phys 21 199 1972

Campbell A M, Evetts J E and Dew-Hughes D, Phil Mag 10 333 1964
Phil Mag 18 313 1968

Caroli C, de Gennes P G and Matricon J, Phys Condensed Matter 1 176 1963

Caroli C and Maki K, Phys Rev 164 591 1967

Clem J R, Phys Rev Lett 20 735 1968

Coffey H T, Cryogenics 7 73 1967
Phys Rev 166 447 1968

Cooper L N, Phys Rev 104 1189 1956

Corak W S, Goodman B B, Satterthwaite C B and Wexler A,
Phys Rev 96 1442 1954
Phys Rev 102 656 1956

Deaver B S and Fairbank W M, Phys Rev Lett 7 43 1961

de Gennes P G, Phys Cond Matter 3 79 1964
Superconductivity of Metals and Alloys p180 1966

de Gennes P G and Matricon J, Rev Mod Phys 36 45 1964

de Lange O L and Otter Jr F A, J Phys Chem Solids 33 157 1972

Delrieu J M, J Phys F 3 893 1973

de Sorbo W, Phys Rev 130 2177 1963
Phys Rev 132 107 1963
Phys Rev 134 1119 1964

Dew-Hughes D, Rep Prog Phys 34 821 1971

Eilenberger G, Phys Rev 153 584 1967

Doll R and Näbauer M, Phys Rev Lett 7 51 1961

Ekin J W and Clem J R, Phys Rev B12 1753 1975

Essmann U, Proc Int Discussion Meeting on Flux Pinning in Superconductors p23 1974. Eds: P Haasen and H C Freyhardt

Ferreira da Silva J, Burgemeister E A and Dokoupil Z, Physica 41 409 1969

Ferreira da Silva J, Van Duykeren N W J and Dokoupil Z, Leiden Comm 348 1253 1966

Fetter A L, Phys Rev 147 153 1966

Feynman R P, Phys Rev 94 262 1954

Fietz W A, Beasley M R, Silcox J and Webb W W, Phys Rev 136A 335 1964

Fietz W A and Webb W W, Phys Rev 178 657 1969

Finnemore D K, Stromberg T F and Swenson C A, Phys Rev 148 231 1966

Fiory A T and Serin B, Phys Rev Lett 16 308 1966
Physica 55 73 1971

Friedel J, de Gennes P G and Matricon J, Appl Phys Lett 2 119 1963

Fröhlich H, Phys Rev 79 845 1950

Fuhrmans M and Heiden C, Proc Int Discussion Meeting on Flux Pinning in Superconductors p223 1974. Eds: P Haason and H C Freyhardt

Giaever I, Phys Rev Lett 5 147 1960

Gifkins K J, Malseed C and Rachinger W A, Scripta Metall 2 141 1968

Ginzburg V L, JETP 3 621 1956

Ginzburg V L and Landau L D, JETP 20 1064 1950

Goedemoed S H, Kes P H, Jacobs F T A and de Klerk D, Physica 35 273 1967

Goodmann B B, Phys Lett 1 215 1962

Gor'kov L P, JETP 7 505 1958
JETP 9 1364 1959
JETP 10 593 1960

Gorter C J, Arch Teyler 7 387 1933
Physica 23 45 1957
Phys Lett 1 69 1962
Phys Lett 2 26 1962a

Gorter C J and Casimir H B G, Phys Z 35 963 1934
Z Tech Phys 15 539 1934a

Grover F W, Inductance Calculations p143, D van Nostrand Co NY 1946

Habermeier H U, Proc Int Discussion Meeting on Flux Pinning in Superconductors p317 1974. Eds: P Haason and H C Freyhardt

Hampshire R G and Taylor M T, J Phys F 2 89 1972

Harrison R B, Wright L S and Wertheimer M R, Phys Rev B7 1864 1973

Hill D C, Morrison D D and Rose R M, Phys Lett A29 482 1969
J Appl Phys 40 5160 1969

Hirshfeld A T, Leupold H A and Boorse H A, Phys Rev 127 1501 1962

Houston W V and Smith D R, Phys Rev Lett 16 516 1966
Phys Rev 163 431 1967

Hu C R, Proc Int Conf on Low Temp Phys LT14 2 297 1975 Ed: M Krusius and M Vuorio

Irie F and Yamafuji K, J Phys Soc Japan 23 255 1967

Josephson B D, Phys Lett 1 251 1962

Kammerer U, Phys Stat Sol 34 81 1969

Keesom W H, Discussion 4e Congress Physique Solvay p289 1924

Kim Y B, Hempstead C F and Strnad A R, Phys Rev Lett 9 306 1962
Phys Rev 129 528 1963
Phys Rev 131 2486 1963a

Kleiner W H, Roth L M and Autler S H, Phys Rev 133A 1226 1964

Kramer E J, J Appl Phys 44 1360 1973

Kramer L, Pesch W and Watts-Tobin R J, J Low Temp Phys 14 29 1974

Kronmuller H, Proc Int Discussion Meeting on Flux Pinning in Superconductors p1 1974. Eds: P Haason and H C Freyhardt

Kronmuller H and Seeger A, Phys Stat Sol 34 781 1969

Kulik I O, JETP Lett 3 259 1966

Labush R, Phys Stat Sol 19 715 1967
Phys Rev 170 470 1968
Phys Stat Sol 32 439 1969

Landau L D, JETP 5 71 1941
JETP 11 91 1947

Lerski R A, St Andrews Univ PhD Thesis (unpublished) 1974

Livingston J D, Phys Rev 129 1943 1963
J Appl Phys 34 3028 1963
Acta Metall 11 1371 1963
Appl Phys Lett 8 319 1966

London F, Superfluids Vol 1 p86 John Wiley & Sons NY 1950

London H, Proc Roy Soc A152 650 1935
Phys Lett 6 162 1963

Love G R, Phil Mag 21 1003 1970

Lowell J, J Phys C 3 712 1970

Lowell J, Munoz J S and Sousa J, Phys Lett 24A 376 1967

Maki K, Physics 1 127 1964
Physics 1 201 1964
Phys Rev 139A 702 1964
Phys Rev Lett 21 1755 1965
J Low Temp Phys 1 45 1969
Prog Theor Phys 41 902 1969a

Marcus P M, Bull Am Phys Soc II 9 438 1964

Meissner W and Ochsenfeld R, Naturw 21 787 1933

Mendelssohn K, Proc Roy Soc A152 34 1935

Mendelssohn K and Moore J R, Nature 135 826 1935

Montgomery D B, Solenoid Magnet Design: The Magnetic and Mechanical Aspects of Resistive and Superconducting Systems, NY 1969

Nabarro F R N, Theory of Crystal Dislocation, Oxford 1967

Nicholson J E, Cort B S and Cort G P, J Low Temp Phys 26 69 1977

Ogg R A, Phys Rev 69 243 1946
Phys Rev 69 544 1946

Olafsson R, St Andrews Univ PhD Thesis (unpublished) 1971

Olafsson R and Allen J F, J Phys F 2 123 1972

Olsen J L and Rosenberg H M, Adv Phys 2 28 1953

Onnes H K, Leiden Comm 122b 124c 1911
Leiden Comm Suppl 34 1913

Onsager L, (see V L Ginzburg Doklady Akad Nauk 69 161 1949)

Otter F A and Solomon P R, Phys Rev Lett 16 681 1966

Pippard A B, Proc Roy Soc A203 210 1950
Proc Camb Phil Soc 47 617 1951
Proc Roy Soc A216 547 1953

Reynolds C A, Serin S, Wright W H and Nesbitt L B, Phys Rev 78 487 1950

Rollins R W, Kuper H and Gey W, J Appl Phys 45 5392 1974

Rosenblum B and Cardona M, Phys Rev Lett 12 657 1964

Rutgers A J, Physica 1 1055 1934

Saint-James D and de Gennes P G, Phys Lett 7 306 1963

Schelten J and Lippmann G, Proc Int Conf Low Temp Phys LT14 2 341 1975
Eds: M Krusius and M Vuorio

Seeger A and Kronmuller H, Phys Stat Sol 27 371 1968

Shmidt V V and Mkrtchyan G S, Sov Phys Uspekhi 17 170 1975

Shoenberg D, Superconductivity Camb Univ Press 1952

Silsbee F B, J Wash Acad Sci 6 597 1916

Silcox J and Rollins R W, Appl Phys Lett 2 231 1963
Rev Mod Phys 36 52 1964

Stephen M J, Phys Rev Lett 16 801 1966

Thompson R S, Phys Rev B1 327 1970
Phys Rev B2 1433 1970

Tinkham M, Phys Rev 129 2413 1963

Träuble H and Essman U, Phys Stat Sol 18 813 1966
Phys Stat Sol 25 373 1968
J Appl Phys 39 4052 1968

van Vijfeijken A G, Philip Res Rep Suppl No8 1 1968

Volger J, Quantum Fluids p128 Ed: Brewer 1966

Wada Y and Tamura Y, Prog Theor Phys 50 1194 1973

Weber H W and Riegler R, Sol Stat Comm 12 121 1973

Wertheimer M R and Gilchrist J le G, J Phys Chem Sol 28 2509 1967

Wilkinson M K, Shull C G, Roberts L D and Bernstein S, Phys Rev 97 889 1955

Yasukochi K, Ogasawara T, Usui N and Ushio S, J Phys Soc Japan 19 1649 1964